ESPOO 2004 VTT SYMPOSIUM 235

URSI/IEEE XXIX Convention on Radio Science

Espoo, Finland, November 1–2, 2004

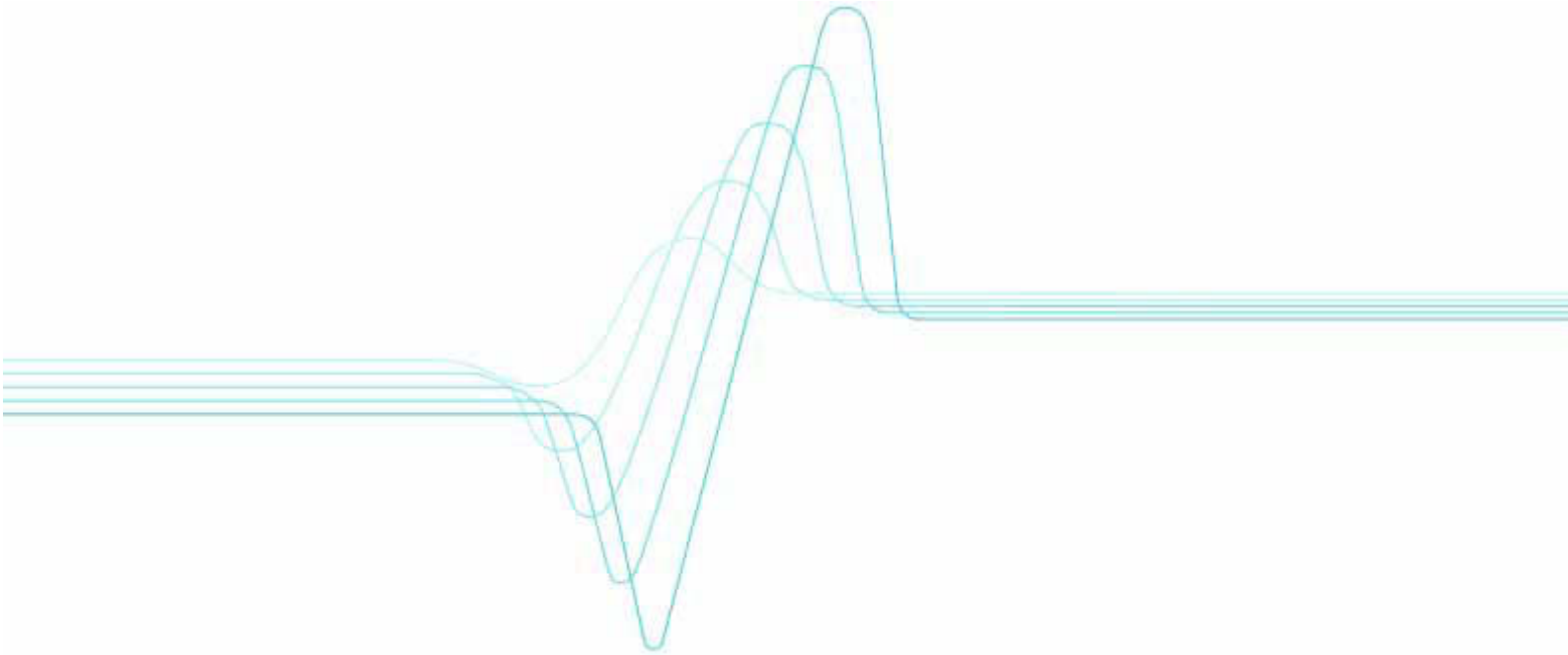

VTT

VTT SYMPOSIUM 235

Keywords:
communication technology, remote sensing, antennas, electromagnetic theory, electromagnetic materials, circuits and components, wireless communications, sensors, defence and security

URSI/IEEE XXIX Convention on Radio Science

Espoo, Finland, November 1–2, 2004

Edited by

Manu Lahdes

Organised by

VTT Information Technology
Finnish National Committee of URSI

ISBN 951–38–6295–X (soft back ed.)
ISSN 0357–9387 (soft back ed.)

ISBN 951–38–6296–8 (URL:http://www.vtt.fi/inf/pdf/; CD-rom)
ISSN 1455–0873 (URL: http://www.vtt.fi/inf/pdf/; CD-rom)

JULKAISIJA – UTGIVARE – PUBLISHER

VTT, Vuorimiehentie 5, PL 2000, 02044 VTT
puh. vaihde (09) 4561, faksi 456 4374

VTT, Bergsmansvägen 5, PB 2000, 02044 VTT
tel. växel (09) 4561, fax 456 4374

VTT Technical Research Centre of Finland
Vuorimiehentie 5, P.O.Box 2000, FIN–02044 VTT, Finland
phone internat. + 358 9 4561, fax + 358 9 456 4374

VTT Tietotekniikka, Tietotie 3, PL 12021, 02044 VTT
puh. vaihde (09) 4561, faksi (09) 456 7012

VTT Informationsteknik, Datavägen 3, PB 12021, 02044 VTT
tel. växel (09) 4561, fax (09) 456 7012

VTT Information Technology, Tietotie 3, P.O.Box 12021, FIN–02044 VTT, Finland
phone internat. + 358 9 4561, fax + 358 9 456 7012

Otamedia Oy, Espoo 2004

Preface

On behalf of VTT Information Technology, I wish to welcome the Finnish radio science and technology community to the XXIX URSI Convention on Radio Science.

This year the convention is hosted by VTT Information Technology. I want to express my sincere thanks to the Conference Secretary, Mr Manu Lahdes, and others at VTT who have participated in the organizing work. Special thanks are also due to Professor Pekka Eskelinen from Helsinki University of Technology, Institute of Digital Communications, for his solid involvement in the preparation process.

The convention was organized in co-operation with the Finnish National Committee of URSI represented by Professor Martti Hallikainen and Mr Jaan Praks, and with the Finland IEEE Section. It provides a forum for discussion of advances in the broad field of radio science and radio communications. The program will include contributed and invited presentations in all relevant fields. To all speakers, invited speakers and presenters of submitted papers, chairpersons and sponsors (Nokia Research Centre, IEEE Finland Section) I wish to give my warmest thanks for their contributions. Together we all make a convention to be remembered.

Markku Sipilä

Chairman of the Organizing Committee

Organizing Committee

Markku Sipilä (chairman)
Pekka Eskelinen
Jaan Praks
Markku Jenu
Jussi Tuovinen
Jouko Aurisalo
Manu Lahdes (secretary)

Conference Program

Monday 1. November

9:00–10:00	**Registration and Coffee**	
10:00–10:10	**Opening** Location: 4A/4B Martti Hallikainen, (Finnish URSI Committee), HUT Space Lab Markku Sipilä (Organizing Committee), VTT	
	Session 1a: Future Communications Technologies Chair: M. Sipilä, VTT	
10:10–10:45	H. Kattelus (Invited): *Amorphous Metals for RF-Mems,* VTT	
10:45–11:20	H. Kauppinen (Invited): *Spectrum sharing and flexible spectrum use*, Nokia	
11:20–11:40	T. Vähä-Heikkilä	
11:40–12:00	A. Hottinen	
12:00–13:00	**Lunch**	
	Session 2a: Remote Sensing I Location: 4A Chair: M. Hallikainen, HUT Space Lab	**Session 2b: Antennas I** Location: 4B Chair: A. Tuohimaa, PvTT
13:00–13:20	K. Rautiainen	I. Salonen
13:20–13:40	P. Lahtinen	M. Hirvonen
13:40–14:00	M. Mäkynen	A. Viitanen
14:00–14:20	J.-P. Kärnä	M. E. Ermutlu
14:20–14:50	**Coffee Break**	
	Session 3a: Electromagnetic Theory and Materials Location: 4A Chair: I. Lindell, HUT Electromagnetics Lab	**Session 3b: Circuits and Components** Location: 4 B Chair: V. Porra, HUT ECDL
14:50–15:10	R. M. Mäkinen	H. Eskelinen
15:10–15:30	T. Dufva	T. Häkkilä
15:30–15:50	K.-P. Lätti	H. Salminen
15:50–16:10	L. Jylhä	K. Kalliomäki
16:10–16:30	I. S. Nefedov	V. Saari
17:00–20:30	**Reception**	

Tuesday 2. November

	Session 4a: Defence and Security
	Location: 4B
	Chair: Arvi Serkola, PvTT
9:00–9:30	J. Ruoskanen (invited): *Radar Signal Processing*, PvTT
9:30–9:50	E. Korpela
9:50–10:10	P. Kuosmanen
10:10–10:40	**Coffee Break**
	Session 5a: Antennas II and Wireless Communications
	Location: 4B
	Chair: Hannu Kauppinen, Nokia
10:40–11:00	P. Pursula
11:00–11:20	T. Koskinen
11:20–11:40	J. Mallat
11:40–12:00	L.Viggiano
12:00–13:00	**Lunch**
	Session 6a: Sensors and Applications
	Location: 4B
	Chair: Antti Räisänen, HUT Radio Lab
13:00–13:30	P. Jukkala (invited): *Planck – Mission and Technology*
13:30–13:50	M. Kantanen
13:50–14:10	J. S. Penttilä
14:10–14:30	**Coffee Break**
	Session 7a: Remote Sensing II
	Location: 4B
	Chair: Tuomas Häme, VTT
14:30–14:50	K. Luojus
14:50–15:10	M. Takala
15:10–15:30	K.-A. Hovitie
15:30–15:50	**Closing and Young Scientist Award**

Contents

Session 1a:
Future Communications Technologies

Amorphous Metals for RF-MEMS

H. Kattelus, M. Ylönen, and T. Vähä-Heikkilä

VTT Information Technology
Tietotie 3, Espoo,
Finland
Email: Hannu.Kattelus@vtt.fi

Abstract
Several RF-MEMS devices can benefit from metallic micromachining processes in comparison to the conventional silicon-based MEMS technologies for various reasons. A variety of metallic materials and their fabrication techniques have indeed been tested in the laboratory but commercial volume manufacturing processes for RF-MEMS devices are almost non-existent. Good conductors such as copper and gold do not perform optimally as structural materials during extended cycling. This report describes a new group of materials for RF-MEMS: amorphous metals. In terms of electrical conductivity amorphous metals are intermediate between elemental metals and semiconductors but they can fulfil the mechanical function of the devices despite of their conductivity limitation.

Keywords: Amorphous metals, metallic micromachining, RF-MEMS, RF-switch, MEMS varactor.

1. INTRODUCTION

Metallic micromachining possesses inherent advantages over silicon-based MEMS technology. The thermal budget of the complete fabrication cycle is very low, and the devices can be integrated over the IC without causing circuit malfunction. Polymeric materials can be used for the sacrificial layer for the same reason. The devices can thus be diced and mounted in package prior to sacrificial layer removal, which is performed in an oxygen plasma as the very final step before enclosing the capsule. Elemental metals suffer from microstructural variations within the fabrication batch increasing the fabrication tolerances and cutting down yield. Making the metal amorphous through proper alloying reduces scatter of data.

2. EXPERIMENT

Sputter-deposited molybdenum-nitrogen and molybdenum-silicon-nitrogen alloys are used for the structural material in our RF-MEMS processes. If the sheet resistance needs to be locally reduced, a shunting layer of aluminium is patterned on top. The merits and limitations of such materials and processes are described. 1 – 50 GHz switches and varactors are prepared for test vehicles, whose electrical properties are characterized.

3. RESULTS

The electrical conductivity of Mo-N is between 100 – 200 μΩcm, and that for Mo-Si-N about 1000 μΩcm. The former is X-ray amorphous but contains nanocrystallites resulting in stress gradients. Ternary Mo-Si-N is more completely amorphized and shows smaller gradients than Mo-N. Both materials have been used for demonstrating RF-MEMS devices successfully, and show promise for commercial applications. 20 million cycles of switching show practically no instability in electrical device characteristics.

4. CONCLUSION

Amorphous metals constitute a new group of materials showing promise for RF as well as low-frequency MEMS. The mechanical properties are stable up to at least 20 million switching cycles in laboratory environment without a protective package. The membranes and switches are not prone to stiction.

Multi-Band and Reconfigurable Radio Systems Based on MEMS Circuits

Tauno Vähä-Heikkilä, Markus Rintamäki, Jussi Varis, and Jussi Tuovinen

Millimeter Wave Laboratory of Finland - MilliLab,
VTT Information Technology
P.O.BOX 12021, 02044 VTT, Finland
Email: tauno.vaha-heikkila@vtt.fi

Abstract
Novel circuits and methods are presented to develop multi-band and reconfigurable radio systems. Reconfigurable MEMS based matching networks are found to be very suitable for power amplifier matching applications being very linear, having low loss and good power handling capabilities.

Keywords: Reconfigurable systems, RF MEMS, matching network, impedance tuner

1. INTRODUCTION

Portable handsets are using already now multiple frequency bands since they need to be functional in many countries with different frequency allocation. Also, the number of frequency bands is expected to be increased in the near future since new applications (GPS, WLAN etc.) are integrated to handsets currently. Also at microwave (3-30 GHz) and millimeter wave (30-300 GHz) frequencies, radio links are using many frequency bands including bands around 7, 8, 13, 15, 18, 23, 26, 28, 38, 42, and 58 GHz.

Other types of problems that exist both in single and multi-band systems are changing conditions. For example, changing antenna impedance creates mismatch between a power amplifier (PA) and the antenna reducing the output power. This could be avoided by using a reconfigurable matching network between the PA and antenna.

To minimize the number of components in multi-band systems and to develop reconfigurable systems, reconfigurable and tunable components and circuits are needed. Tunability is usually done with varactor diodes or transistors. These are lossy components having reasonable high resistance. Also, their nonlinearities decrease the system performance. MEMS (microelectromechanical systems) based components and circuits have very low intermodulation products and low loss [1]. Different ways to get more efficient systems based on tunable and reconfigurable circuits are presented in this paper.

2. RECONFIGURABLE TELECOMMUNICATION SYSTEMS

Conventional and reconfigurable multi-band front-ends are shown schematically in Figure 1. Number of active and passive devices can be reduced using tunable and reconfigurable filters, matching networks, and wideband thru type power sensors.

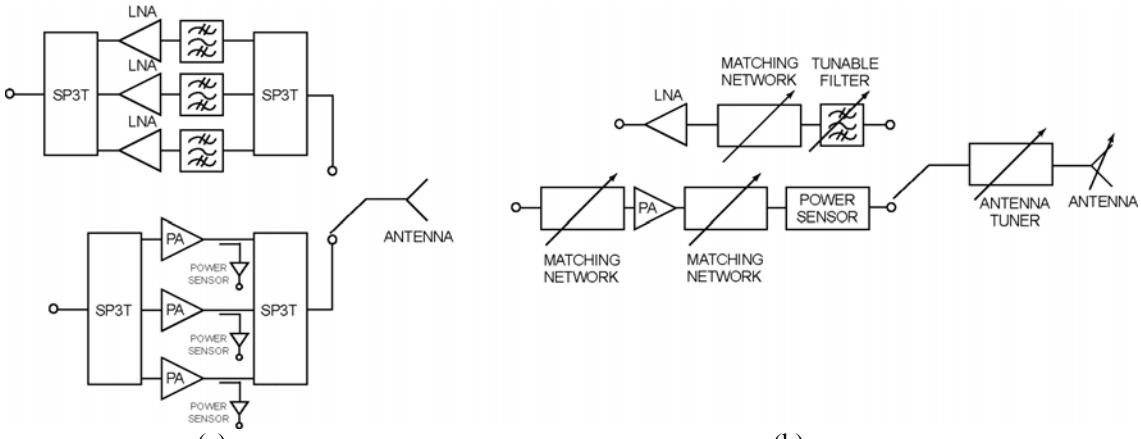

(a) (b)

Fig. 1. a) Conventional and b) reconfigurable multi-band front-end.

One very challenging problem in current and future radios is how to make small and multi-band handset antennas. Other application area is in wireless local area networks (WLAN), where reconfigurable base station antennas can be used for improving the system performance. Antennas can be made reconfigurable and/or multi-band using MEMS switches and varactors. As an example of reconfigurable antenna at WLAN frequencies, the University of Rennes with several partners have developed a 5.7 GHz reflect-array unit cell consisting in a set of six switchable dipoles placed at different angles, only one of them being switched on at a time (Figure 2) [2]. We have developed matching networks/impedance tuners that were optimized for matching an antenna with changing impedance to a power amplifier [3-5]. This kind of matching networks are needed both in reconfigurable antennas and in antennas where their impedance changes because the impedance seen by the antenna changes. This is a typical problem in mobile phones. A mobile phone can be, for example, on a metal table or next to a human body and the impedance seen by the antenna changes. This causes mismatch between the antenna and PA affecting RF power loss in the system. If a reconfigurable matching network is used with the antenna, maximum power transfer can be ensured in different output impedance conditions.

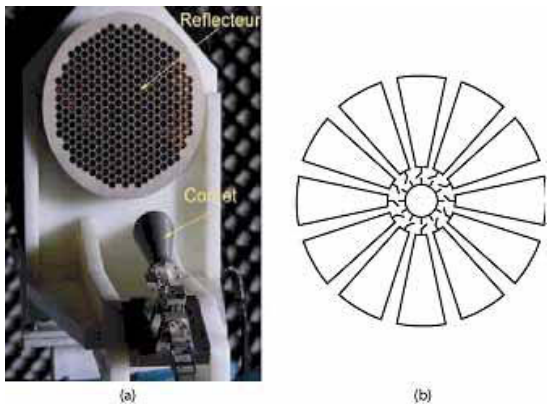

Fig. 2. Example of MEMS-reconfigurable reflect-array. a) Photograph of the system and b) detail of the unit cell [2].

Power amplifiers have usually low output impedance and are mismatched in 50 Ω systems. These can be matched in narrow frequency band using a fixed matching network at the output of the PA and in multi-band systems, different power amplifiers are needed in different frequency bands (like in Figure 1). Using a reconfigurable matching network, a PA can be matched to an antenna in different frequency bands and only one PA is needed in a multi-band system. Reconfigurable matching networks can be realized with stub-based [4] or distributed topologies [3,5]. Stub-based matching networks are usual in microwave engineering [6], and can be easily applied reconfigurable systems. The electrical length and impedance of stubs and electrical distance between them can be changed using capacitive loading [4]. Schematic of a 6-20 GHz reconfigurable triple-stub impedance tuner with its impedance coverage at 14 GHz are shown in Figure 3 [4]. Almost the whole Smith chart can be covered with the tuner. The electrical tuning is realized with 11 switched capacitors that can be controlled separately. Impedance, phase delay, and the effective dielectric constant of the transmission line are changed by changing the loading capacitance. The switched capacitor is a series combination of a MEMS switch and fixed metal-air-metal (MAM) capacitor, and its capacitance ratio can be designed to be 1.5-30:1 being 4.9:1 in this work. Using 11 switched capacitors, 2048 (2^{11}) different impedances can be generated with the tuner. Stub-based impedance matching networks are quite large in size since the electrical length of the stubs and distance between them are proportional to wavelength. For example, the area of the 6-20 GHz triple-stub tuner is about 7.3 mm x 7.3 mm on a glass substrate (ε_r=4.6). We have also developed novel reconfigurable matching networks that are based on distributed topology [3,5]. Schematic of a distributed matching network based on four switched capacitors is shown in Figure 4. When the switched capacitors are in the state C1 (lower capacitance state, C = 81.2 fF), the impedance of the matching network is close to 50 Ω. Putting more and more switched capacitors to the state C2 (higher capacitance state, C = 398 fF), the loading of the line is increased and the impedance is lowered to the region of the output impedance of power amplifiers. Distributed nature of the network ensures wideband operation. We have demonstrated that the distributed type reconfigurable 4-18 GHz matching networks can handle more than 1 W RF power at 8 GHz and the third order intercept point (IIP3) of the networks is better than +45 dBm with 100

kHz signal separation (Δf) at 8 GHz, and is expected to be better than +70 dBm with signal separation greater than 1 MHz.

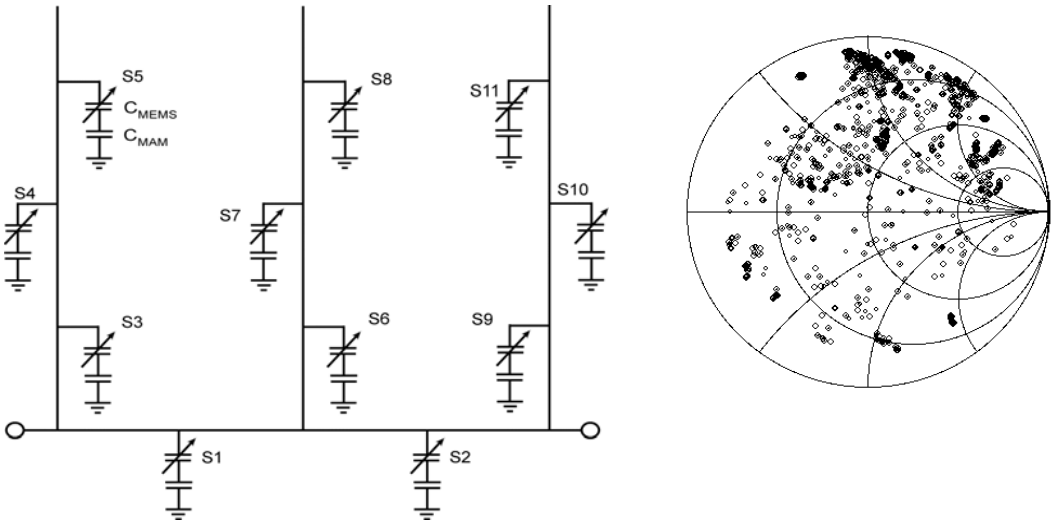

(a) (b)

Fig. 3. a) Schematic of a reconfigurable triple-stub impedance tuner based on 11 switched capacitors and b) its impedance coverage at 14 GHz [4].

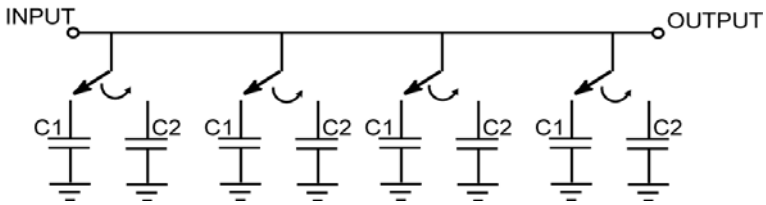

Fig. 4. a) Schematic of a distributed type reconfigurable matching optimized for power amplifier applications.

RF power measurement and control is needed in radio transmitter. RF power sensors are connected to transmitters with couplers in conventional radio systems. Couplers limit the bandwidth of transmitters since they are narrowband wavelength dependent components. Also, they are large in size. We have developed thru type RF power sensors based on MEMS technology [7-8]. These are small and wideband and neither couplers nor diode based power sensors are not needed anymore.

CONCLUSIONS

Radio system performance can be improved with MEMS based components and circuits. We have showed alternative methods both at system and circuit level for improving radios. As an example of reconfigurable microwave circuits, we have presented our wideband reconfigurable matching networks with good performance (IIP>+70 dBm @ Δf=1 MHz, power handling > 1W @ 8GHz) and impedance tuners covering almost the whole Smith chart.

ACKNOWLEDGEMENTS

This work was supported by the European Space Agency (ESA/ESTEC) contract no. 1655/95/NL/MV and the Graduate School GETA, Finland.

REFERENCES

[1] G. M. Rebeiz: "RF MEMS Theory, Design, and Technology," John Wiley & Sons, New York, 2003.

[2] H. Legay, B. Pinte, M. Charrier, A. Ziaei, E. Girard, R. Gillard, “A steerable reflectarray antenna with MEMS controls,” 2003 IEEE Int. Symp. on Phased Array Systems and Technology, 14-17 oct. 2003, pp. 494-499.

[3] T. Vähä-Heikkilä, G. M. Rebeiz:" A 4-18 GHz Reconfigurable RF MEMS Matching Network For Power Amplifier Applications," *RF applications of MEMS and micromachining special issue on International Journal of RF and Microwave Computer-Aided Engineering*," vol. 14, Issue 4, July, 2004.pp. 356-372.

[4] T. Vähä-Heikkilä, J. Varis, J. Tuovinen, and G. M. Rebeiz, "A Reconfigurable 6-20 GHz RF MEMS Impedance Tuner," *IEEE MTT-S International Microwave Symposium digest,* Forth Worth, TX, USA, 2004, pp. 729-732.

[5] T. Vähä-Heikkilä, and G. M. Rebeiz, "A 20-50 GHz Reconfigurable Matching Network for Power Amplifier Applications," *IEEE MTT-S International Microwave Symposium digest,* Forth Worth, TX, USA, 2004, pp. 717-721.

[6] R. E. Collin: "Foundations For Microwave Engineering," 2nd edition, New York, McGraw-Hill, 1992.

[7] T. Vähä-Heikkilä, J. Kyynäräinen, A. Oja, J. Varis, and H. Seppä.: ”Capacitive MEMS power sensor”, *Proceedings of 3rd workshop on MEMS for millimeter wave communications – MEMSWAVE*, Heraklion, Greece, 2002.

[8] T. Vähä-Heikkilä, J. Kyynäräinen, A. Oja, J. Varis, and H. Seppä, "Design of Capacitive RF MEMS Power Sensor", URSI/IEEE XXVII Convention on Radio Science, Espoo Finland, Oct. 17-18, 2002.

Channel Reciprocity for FDD Systems using Duplex Hopping

Ari Hottinen

Nokia Research Center
P.O. Box 407, Nokia Group 00045, Finland
Email: ari.hottinen@nokia.com

Abstract
This paper proposes a new duplexing solution for paired frequency bands employing frequency division duplexing (FDD). The proposed method, duplex hopping, captures channel reciprocity in a manner analogous to time division duplexing systems, and thus enables channel-aware transmission methods. It is shown, in particular, that the proposed method can be used effectively with multi-antenna transmission with very high spectral efficiencies.

Keywords: Duplexing, channel reciprocity, MIMO, channel-aware transmission,4G

1. INTRODUCTION

Channel-aware transmission methods have become increasingly attractive recently. It is well-known that Channel State Information (CSI) can be used e.g. to increase the efficienc y of transmit beamforming, scheduling, coding and modulation, among other things. As an example, the WCDMA Release 5 employs adaptive coding and modulation (ACM), multiuser scheduling, and closed-loop transmit diversity [2], all of which require some form of CSI for efficient operation. CSI at transmitter is therein obtained with a feedback channel and used to increase system performance. While capacity enhancement is relevant for any wireless system, other objectives are also of interest. In 4G systems where the channel bandwidth may be up to 100 MHz, CSI could be used also as means to simplify receiver signal processing algorithms. Decreasing the computational burden of the receiver by moving it to the transmitter can be done efficiently with the aid of CSI. Indeed, the potential MIMO capacity gains can be achieved by a simple linear receiver provided that the transmitter has complete channel knowledge.

The examples given above motivate both the study of feedback channels for conveying the CSI to the transmitter, and the study novel solutions for inherently conveying CSI to the transmitter. Bearing in mind that the frequency-division-duplexing (FDD) and related paired regulatory bandwidth allocations will remain dominant for some years, it is of interest to provide efficient means for providing CSI for FDD systems. In this paper, a solution is provided where explicit feedback channel are not needed, and thus the current paired radio spectrum allocations could potentially used for future high capacity radio air interfaces. The proposed solution may avoid feedback channels in FDD systems by inherent channel reciprocity.

2. DUPLEX HOPPING

Conventionally, Channel State Information (CSI) is available inherently in TDD systems, but in FDD systems an explicit feedback channel is needed. This approach is used e.g. in WCDMA standard, where TXAA (Closed-loop transmit diversity) is controlled by receiver feedback with 1.5 kbps/Hz uplink signalling channel. In this case the feedback link supports two transmit antennas. If more than two antennas or more than two beams would need to be supported e.g. in multiple-Input Multiple-Output (MIMO) channels the feedback link capacity would have to be increased accordingly.

Since the explicit signalling channel may be difficult to devise for arbitrary antenna and transmission con gurations, we propose herein an alternative approach, coined as *duplex hopping* [5]. With FDD the concept operates as follows:

- at least two (sub)carrier frequencies f_1 and f_2, and
- f_1 is used for uplink transmission during slot t_1 and
- f_1 is used for downlink transmission at t_2. Simultaneously,
- f_2 is used for downlink transmission at t_1 and

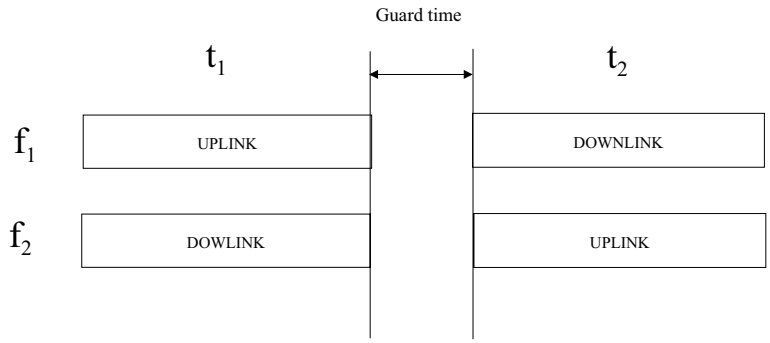

Figure 1: Duplex hopping with two carriers f_1 and f_2 and two time slots t_1 and t_2. Guard interval may be placed between hops.

- f_2 is used for uplink at t_2.

Clearly, orthogonality across duplex frequencies is preserved if the carriers do not overlap. Therefore, due to implementation imperfections, there we may need to define a guard band between f_1 and f_2, and a guard time between t_1 and t_2.

In the context of cellular networks, rst and second duplex direction may refer to uplink and downlink directions respectively. Using this approach, the channel used in reception during slot t_1 (t_2) is used for transmission during slot t_2 (t_1), as shown in Fig. 1, and channel reciprocity akin to that obtained via Time Division Duplex (TDD) is available. A guard interval may be placed between the slots to ease the power ampli er design problem.

The advantages obtained with this solution include

- Inherent channel reciprocity, provided that duplex times t_1 and t_2 are suf ciently close to each other (within time coherence). Channel reciprocity may be used to
  - determine communication parameters for transmission (beam coefficients, coding/modulation options, power control, rate control, scheduling, etc.)
  - Simplify reception complexity, when by using pre-rake combining, or transmit beamforming, or precoding.
  - reduce the control channel capacity (e.g. for adaptive modulation).
- Improved diversity, when duplex (frequency) distance is sufficiently large, as consecutive slots are transmitted in different frequencies.

The diversity benefit may be utilized by coding across multiple duplex frequencies. This is applicable even if CSI is not used or is not accurate enough in the transmitter. This may be the case e.g. due to complexity constraints or due to short channel coherence time (e.g. in the presence of very large Doppler spreads).

The duplex hopping concept is easiest to adopt in systems where the network is synchronized, such the cdma2000, or in 4G systems. If the network is not synchronized the a terminal (e.g. at cell edge) may attempt transmission while another terminal in reception mode.

3. APPLICATION TO CLOSED-LOOP MIMO

The signal model used to represent the key concepts described below is given by [2]

$$\underset{T\times N_{\mathrm{r}}}{\mathbf{Y}} = \underset{T\times N_{\mathrm{b}}}{\mathbf{X}}\ \underset{N_{\mathrm{b}}\times N_{\mathrm{t}}}{\mathbf{W}}\ \underset{N_{\mathrm{t}}\times N_{\mathrm{r}}}{\mathbf{H}} + \underset{T\times N_{\mathrm{r}}}{\mathrm{noise}} \tag{1}$$

Above, N_{r} designates the number of receive antennas, $\mathbf{Y}$ is a $T \times N_{\mathrm{r}}$ received signal matrix, $\mathbf{X}$ is a $T \times N_{\mathrm{b}}$ modulation matrix and $\mathbf{W}$ is a $N_{\mathrm{b}} \times N_{\mathrm{t}}$ beam-forming matrix. The columns of the channel

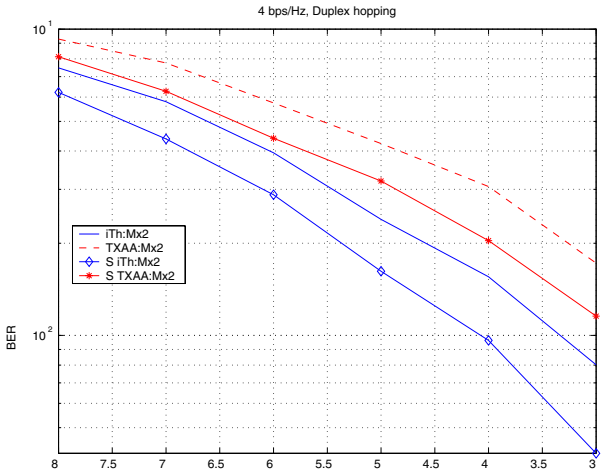

Figure 2: Duplex-hopping based FDD system with $N_{\mathrm{t}} = 8$ transmit and $N_{\mathrm{t}} = 2$ receive antennas. Single-stream (TX-AA) and 2×2 matrix modulation (using i-threaded transmission).

matrix $\mathbf{H}$ designate channel vectors from N_{t} transmit antennas to different receive antennas,

$$\mathbf{H} = \begin{bmatrix} h_{11} & h_{12} & \dots & h_{1N_{\mathrm{r}}} \\ h_{21} & h_{22} & \dots & h_{2N_{\mathrm{r}}} \\ \vdots & \vdots & \ddots & \vdots \\ h_{N_{\mathrm{t}}1} & h_{N_{\mathrm{t}}2} & \dots & h_{N_{\mathrm{t}}N_{\mathrm{r}}} \end{bmatrix}. \tag{2}$$

In vector modulation $\mathbf{X}$ is an N_{b}-vector ($N_{\mathrm{b}} > 1$), while in matrix modulation $N_{\mathrm{b}} > 1, T > 1$[2].

Consider BER performance of different transmission methods as a function of transmitter E_b/N_0, where N_0 refers to noise power at a representative receive antenna and E_b is the transmit energy per bit per channel use. Assume a at fading channel with $N_{\mathrm{t}} = 8$ transmit antennas and and $N_{\mathrm{r}} = 2$ receive antennas. Matrix modulator $\mathbf{X}$ is de ned as the threaded or i-threaded symbol rate two modulator as de ned in [3]. For closed-loop MIMO the beam-forming matrix $\mathbf{W}$ is defined to comprise two dominant eigenbeams of the channel correlation matrix $\mathbf{H}\mathbf{H}^{\dagger}$.

In the presence of a feedback-based solution, the dominant feedback beam uses 8PSK quantization constellation for the $N_{\mathrm{t}} - 1$ coordinates of the dominant beam and the secondary beam uses 4PSK. This requires $(N_{\mathrm{t}} - 1)(q_1 + q_2)$ feedback bits, where q_1 and q_2 designate the number of bits used to represent one (complex) coordinate of a given beam. With 4 tx antennas and two beams (with 8PSK and 4PSK constellations) this gives a feedback word of length 30 bits. The feedback bits are sent to the transmitter and they are receiver error-free.

With duplex hopping, the beamforming matrix is computed as above as dominant eigenbeams, but without quantization, as it determined at the transmitter based on channel estimates. For both concepts, the channel estimates are assumed to be perfect. We notice from Figures 2 and 3 that the duplex hopping based feedback improves performance by about 1.5-2 dB over a feedback scheme involving as many as 30 feedback bits. Note that the use of as many as 30 feedback bits per one downlink transmission packet may be not be feasible in practice (e.g. WCDMA uses only 1 bit per feedback slot, since feedback capacity is limited).

The gures with legends “i-Th" are with two QPSK modulated streams with i-Threaded matrix modulation [3], whereas TX-AA refers to single-stream transmission using only one eigenbeam and 16QAM to attain the same spectral efficiency. The gures also indicate performance where the transmission is carried out in better duplex frequency (f_1 or f_2), as selected using channel state information. When the duplex selection is used legends “S-TXAA" and “S-iTh" are adopted for the corresponding gures.

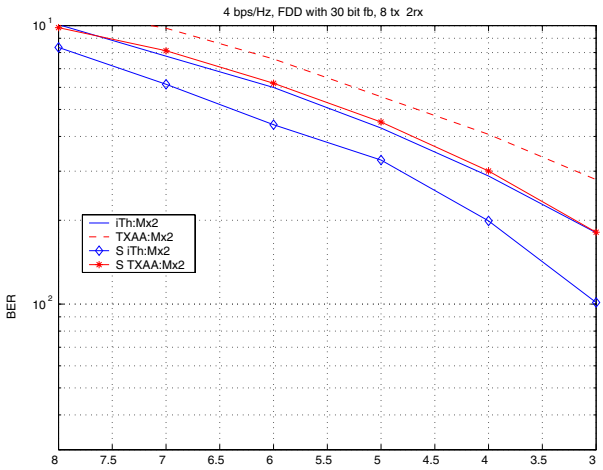

Figure 3: Conventional FDD system with $N_{\mathrm{t}} = 8$ transmit and $N_{\mathrm{t}} = 2$ receive antennas, with 30 bits used for beamforming.

4. CONCLUSION

A new method called duplex hopping was introduced to enable CSI for paired spectrum allocations. The benefits were highlighted from the point of view of diversity, MIMO transmission, and beamforming, in various combinations. Additional potential applications include multiuser scheduling [4, 1]. A simple and efficient way to convey channel state information to the transmitter is likely to be crucial for future (evolutions of) wireless systems, in particular for multi-antenna systems and for systems using other channel-aware transmission schemes.

References

[1] R.W. Heath Jr., M. Airy and A. Paulraj, "Multiuser diversity for MIMO wireless systems with linear receivers," in *Proc. Thirty-Fifth Asilomar Conference on Signals, Systems and Computers*, Vol. 2, 4-7 Nov. 2001, pp. 1194 -1199.

[2] A. Hottinen, O. Tirkkonen and R. Wichman, *Multi-antenna transceiver techniques for 3G and beyond,* John Wiley & Sons, 2003.

[3] A. Hottinen and O. Tirkkonen, "Precoder designs for high rate space–time block codes," in *P*roc. Conf. Inf. Sci. Syst. (CISS 2004), Princeton, NJ, USA, March 2004

[4] R. Knopp and P. Humblet, "Information capacity and power control in single cell multiuser communications," *P*roc. IEEE ICC, Seattle, WA, June 1995.

[5] A. Hottinen, *Linear space–time modulation in multiple-antenna channels*, unpublished manuscript (June 7, 2004)

Session 2a:
Remote Sensing I

First Remote Sensing Images from the HUT Airborne L-band Aperture Synthesis Radiometer

Kimmo Rautiainen, Robert Butora, Martti Hallikainen, Simo Tauriainen

Helsinki University of Technology
Laboratory of Space Technology
P.O.Box 3000
02015 HUT
Finland
Email: kimmo.rautiainen@hut.fi

Abstract
Helsinki University of Technology, Laboratory of Space Technology is finishing the manufacture of an airborne L-band radiometer based on two-dimensional aperture synthesis technology, referred as HUT-2D hereafter. The concept is new in remote sensing, although a similar approach has been successfully used in radioastronomy. In this paper we present the results of the first test flight with a sub-unit of the complete HUT-2D instrument.

Keywords: Aperture synthesis, radiometry, airborne

1. INTRODUCTION

Aperture synthesis is a solution for achieving a relatively good geometric resolution for L-band passive measurements required for the global monitoring of soil moisture (SM) and sea surface salinity (SSS). The European Space Agency (ESA) is currently developing a space-borne instrument based on this technology. The mission is referred to as SMOS (Soil Moisture and Ocean Salinity).

Helsinki University of Technology, Laboratory of Space Technology is participating in the SMOS mission, especially by designing the calibration subsystem of the satellite. Additionally, the laboratory is building an airborne version of the instrument called HUT-2D: a two-dimensional aperture synthesis radiometer for imaging in L-band. The instrument has characteristics similar to those of the SMOS mission sensor and applies the same calibration technology as the satellite and thus also serves as a proof of concept.

The HUT-2D instrument technology has been tested in various ground-based and laboratory measurements using a four-receiver sub-unit. After the encouraging tests results obtained from the EMC chamber measurements, the sub-unit was flown over the coastal region and open sea in December 2003. The main purpose of the flight was to examine interference from the aircraft. As no significant interference was observed in the cross-correlation channels, an attempt was made to retrieve images from the data taken during the flight. The flight track was in the costal area around Helsinki, rich in archipelagos, which providedgood contrast between the low brightness temperatures of the sea (~100 K) and the high temperatures of the ground (~250 K).

2. HUT-2D INSTRUMENT

The HUT-2D instrument will consist of 36 receivers in U-shaped geometry with associated calibration subsystem and a digital correlator unit based on programmable logic circuit technology. Block level configuration is seen in Fig. 1. Each receiver has two outputs: the in-phase (I) and the 90 degrees phase shifted quadrature (Q). The outputs are one-bit digitised and send to the correlator through fibre optic harness. Additionally, an on-board calibration subsystem is required to calibrate the receiver phase errors.

Each receiver pair, referred as baseline hereafter, forms an interferometer producing as an output a complex correlation of the scene in the field of view of the antenna. The image of the target is in ideal case formed from the complex correlations of the baselines using inverse Fourier transformation.

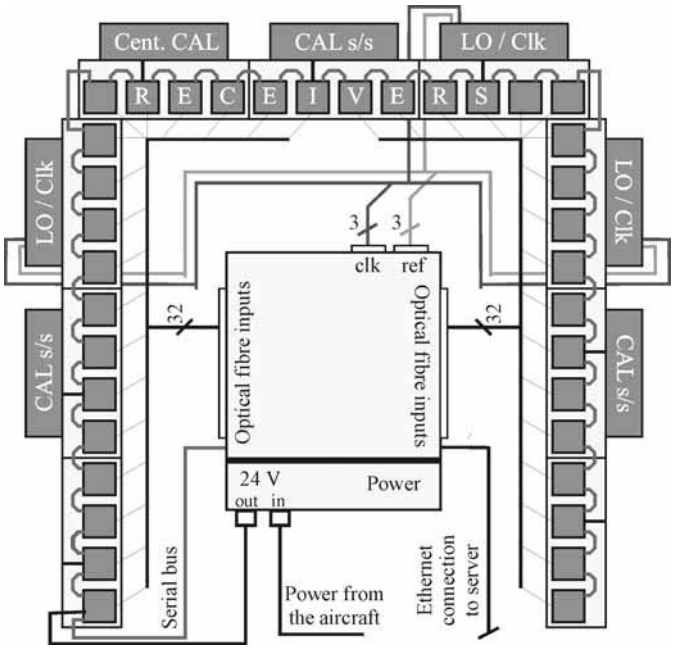

Fig 1**.** The HUT-2D aperture synthesis radiometer.

3. CALIBRATION

The instrument error correction is divided into (1) on-ground characterization, including antenna voltage pattern and the characterization of the on-board calibration network itself, and (2) on-board calibration. The on-board calibration is performed to eliminate the effect of the correlation offset and the receiver errors, including the phase errors and the amplitude errors.

3.1 Offset correction

The offset error is mainly due to the threshold voltage of the zero point comparators used for one-bit digitising of the analogue receiver output signal. The error is systematic and can be corrected by applying additional correlation channels into the digital correlator between a continuous stream of ones or zeros and each receiver I and Q output. The resulting correlation becomes zero independent of the input source when no comparator threshold errors are present i.e. the two comparator input voltage levels are equal over a longer period (integration time). The method for the correction is given in [1].

3.2 Receiver phase error correction

The receiver phase error correction algorithm is similar to the SMOS instrument calibration. The quadrature errors are solved from each receiver I and Q output correlation result (self-correlation). Independently of the input signal, the self-correlation becomes zero in ideal case due to the 90 degree I/Q demodulator. The quadrature error can be solved in a straightforward manner from the measured self-correlation result taking the arc sinus of the measured self-correlation. The receiver phase errors are further solved based on injecting correlated noise into the receiver inputs. The imaginary part of the correlation becomes zero and the real part is the ratio between the correlated noise and the total noise. All deviations from the expected results are due to the phase errors and can be solved as described in [2].

3.3 Amplitude calibration

The offset and phase error corrected correlations result in a normalised visibility map. For the conversion to the brightness temperature the system noise temperature (antenna and receiver noise temperature) information is needed. Accurate antenna temperature information requires use of a continuously calibrated on-board reference receiver. During the four-unit subassembly test flight no reference receivers

were available. The amplitude calibration was performed using correlating receiver's total power output information. Two known targets – open water and snow-covered ground area – were used as calibration references. The brightness temperatures of the selected targets were determined using a HUT emission model [3]. For the large real aperture of the instrument antennas the hot and cold target brightness temperatures were 240 K and 70 K for H-polarisation and 250 K and 130 K for the V-polarisation, respectively. The estimated error of the above values due to the lack of proper ground truth data is ±5 K.

4. TEST FLIGHT RESULTS

The sub-unit used in the first test flight consists of four receivers in a line. Only the cross-track dimension was synthetic with a resolution of ~20°. The resolution along the track is provided by a combination of the real antenna pattern and the dependence of the emissivity on the incidence angle on the ground, as the instrument is mounted 45° tilted. The image reconstruction formula for the points across the track is obtained with the Discrete Fourier Transform as

$$\tilde{T}_B(\xi_i) = \frac{d}{\lambda} \cdot \frac{\Omega_A \sqrt{1-\xi_i^2}}{\left|F_\eta(\xi_i)\right|^2} \cdot \sum_k V(u_k,0) \cdot e^{j2\pi \cdot u_k \xi_i} \qquad (1)$$

where V is the measured visibility map (offset and phase corrected correlation result of the target),
$\xi = \sin\theta\cos\phi$ is the direction cosine along the cross-track direction,
F is the voltage pattern of the antennas,
Ω_A is the solid angle of the antennas, and
$d/\lambda = \Delta u$ is the relative distance between the receivers.

The $\tilde{T}_B(\xi_i)$ represents one line in cross-track. At each integration time (0.25 sec) one such line is obtained. With the speed of the aircraft being ~60 m/sec, there is at each ~15 m one 'snap-shot' line.

The array consists of rectangular patch antennas with two orthogonal probes. The model of the antenna pattern is based on measurements of an antenna of the same type as those used in the array. The patterns were measured in two orthogonal cuts yielding the half power beam widths: HPBW≈75° along the array's line and HPBW≈65° across the array. We used a simple antenna pattern model

$$F(\phi,\theta) = \cos^2\phi \cdot \cos^{n_1}\theta + \sin^2\phi \cdot \cos^{n_2}\theta \qquad (2)$$

where n_1, n_2 correspond to the beam widths.

The images obtained during the first test flight are presented in Fig. 2. The flight was performed in December 2003 in the coastal area of Helsinki. The instrument was mounted to the back-door of the aircraft and tilted 45°, looking backwards (opposite to the direction of the flight). The average speed was 60 m/sec at the altitude of 300 m. The high contrast areas are clearly visible and the measured results coincide well with the target.

6. CONCLUSION

This paper presents the first images from the HUT-2D aperture synthetic radiometer four-receiver sub-unit test flight. The images provide support to the feasibility of the chosen technology and demonstrate proper operation of the instrument. The information and experience from this test flight will be used in preparation for a flight with the full two-dimensional instrument in the near future.

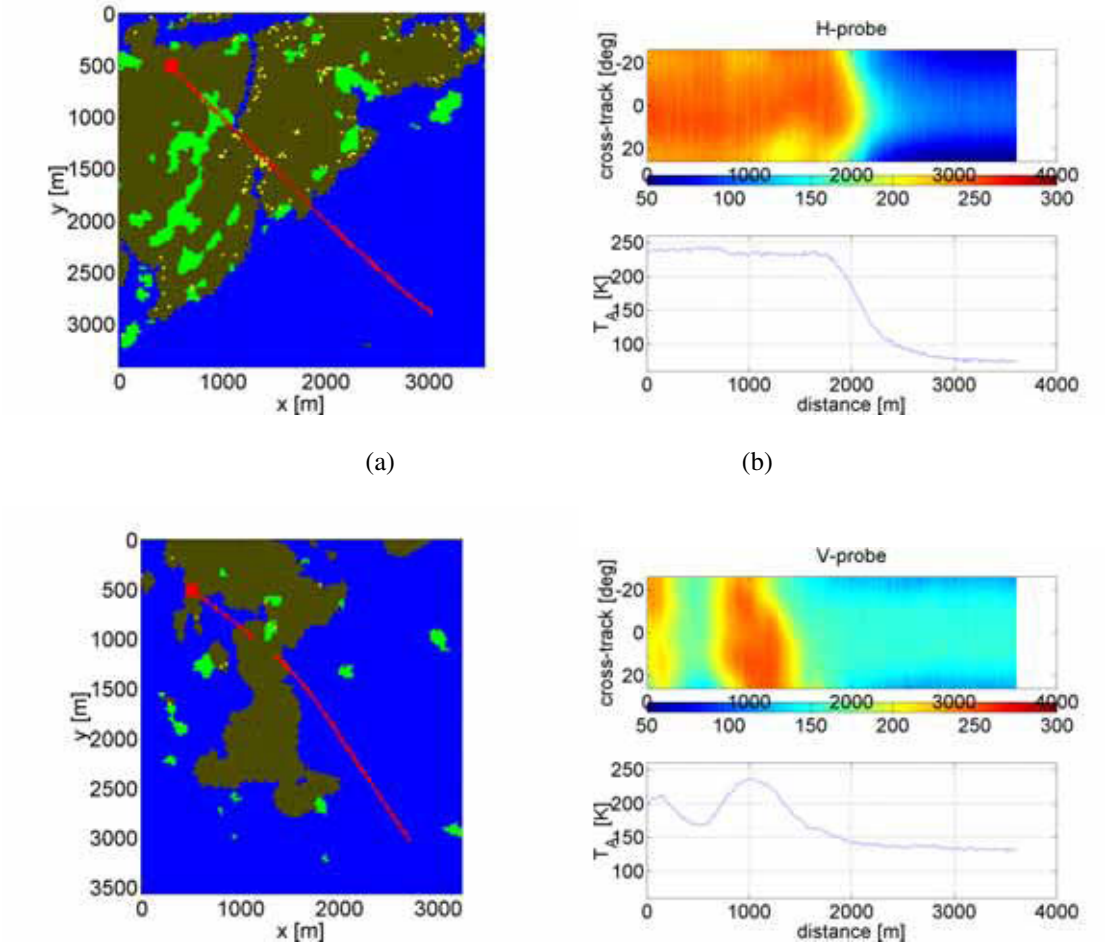

Figure 2 (a)-(d): First flight results. Left images are data from a coverage database with the following colour coding: blue – sea, green – fields and brown – forest. The red line is the flight track with the rectangle corresponding to distance zero in the images on the right side. The negative values of the cross-track look angles correspond to the left side of the flight track.

5. REFERENCES

[1] M. Martin-Neira, S. Ribo, K. Rautiainen, *0-1 correction of comparator threshold in 1-bit interferometric radiometers*, in 8th Specialist Meeting on Microwave Radiometry and Remote Sensing Applications – μRad 2004, La Sapienza University, Rome24-27 February 2004, p. 93.

[2] F. Torres, A. Camps, J. Bara, I. Corbella, R. Ferrero, *On-board phase and modulus calibration of large aperture synthesis radiometers: study applied to MIRAS*, IEEE Trans. Geoscience and Remote Sensing, vol. GRS-34, no. 4, pp. 1000-1009, July 1996.

[3] J. Pulliainen, K. Tigerstedt, H. Wang, M. Hallikainen, C. Mätzler, A. Wiesmann, U. Wegmuller, *Retrieval of Geophysical Parameters with Integrated Modeling of Land Surfaces and Atmosphere (Models/Inversion Algorithms)*, Final Report, ESA/ESTEC Contract 11706/95/NL/NB(SC), ISBN 951-22-4322-9.

Application of Seawinds Catterometer Remote Sensing of snow

Panu Lahtinen[(1)], **Martti Hallikainen**[(2)]

[(1),(2)] ***Helsinki University of Technology***
Laboratory of Space Technology
P.O. Box 3000
FIN-02015 HUT Finland

[(1)] ***Email: palahtin@cc.hut.fi***
[(2)] ***Email: Martti.Hallikainen@hut.fi***

Abstract

The purpose of this paper is to study the feasibility of SeaWinds K_u-band scatterometer onboard QuikSCAT satellite for remote sensing of snow.

QuikSCAT/SeaWinds is a K_u-band (13.4 GHz) scatterometer designed for wind speed retrieval near the ocean surface. However, NASA Scatterometer Climate Record Pathfinder (SCP) provides also image data with backscattering coefficients (σ°). The satellite data used in this study are in 'gridded' format with a pixel resolution of 22.25 km. In situ data from Finnish Meteorological Institute (FMI) consist of daily temperatures, snow depth and rainfall measurements from nine different weather stations. Daily snow water equivalent (SWE) maps were obtained from Finnish Environment Insitute (SYKE). **Keywords:** scatterometry, Ku-band, snow

1. INTRODUCTION

The use of spaceborne remote sensing instruments can give us a way to monitor Earth frequently and with good coverage. However, most of the sensors either measure a narrow swath or their orbit around Earth does not allow them to cover the whole surface in a reasonable time frame. QuikSCAT/SeaWinds has a very broad swath (1400 km for H-pol and 1800 km for V-pol) and Sun-synchronous near polar orbit with an orbital time of 101 minutes, thus covering aproximately 90% of the Earth surface each day. Latitudes over 40° are covered twice a day, so areas typically covered by seasonal snow which can be monitored very effectively.

2. FINDING THE SNOWMELT PERIODS

According to previous studies by Nghiem and Tsai [1] it is possible to detect snowmelt with a K_u-band scatterometer. As Figure 1 shows, this is true also for QuikSCAT/SeaWinds.

The thick black lines in top of every plot in Figure 1 represent the instants when the maximum temperature has risen above the freezing point ($0\ ^\circ C$). The vertical lines in SWE and Snow Depth plots mark the snowmelt periods determined from the differential backscatter coefficient (σ°) data. The vertical dashed lines mark the beginning of the snowmelt period and the solid lines the end of the snowmelt.

The procedure presented here is based entirely on observations made from relations between aforementioned data sets, thus being empirical.

2.1. The Procedure

To detect snowmelt, we first have to determine if the ground is snow covered. This is done by finding empirical thresholds for both H- and V-polarizations. When the snowmelt begins, σ° decreases due to wet snow [2]. This is easily seen by comparing the plots in Fig. 1.

The detection of the end of the snowmelt is done by following the trends in σ° values. The first option is that the σ° value exceeds the initial level of snow covered ground. The others determine whether the ground is snow free. Wet ground free from snow has a low and quite stable backscattering characteristics, thus providing good base for determining the end of the melting season.

3. DETECTING SNOW COVERED GROUND

When we compare maps based on σ° values with maps with measured (SYKE) SWE values, we can see that the needed SWE value to detect dry snow is somewhere around 10 mm. This can be seen in Figs. 2 and 3. Fig. 2 shows pixel values of satellite data on H-pol exceeding -9.5 dB in white (H-pol) and values below that in gray. White areas in Fig. 3 have SWE larger than 10 mm. Black areas in both figures are either sea or outside the Finnish borders.

3.1. Retrieval of Snow Water Equivivalent

Figure 4 is a scatterplot of 192 measurements made during winters 1999-2000, 2000-2001 and 2001-2002 for two test sites near municipality of Multia. The measurements were selected to represent backscattering from dry snow. The criteria for dry snow was that the maximum air temperature had to be below -2 $^\circ C$ for five consecutive days before the selected measurements. The curve fitted in the scatterplot is a second degree polynomial. When compared to interpolation represented by Nghiem and Tsai in [1], we can see that the fitted curves are quite similar even if the SWE values in used dataset represent only the lower end of the interpolated curve.

Part of the relatively high scatter in Fig. 4 is caused by the varying atzimuthal angle, since the amount of snow seen differs when the azimuthal angle changes (overshadowing by surface topology, man-made structures and also vegetation to some extent).

4. PROBLEMATIC AREAS

The map in Figure 5 reveals two problematic types of terrain in satellite-based σ° data. Large water-covered areas such as seas and large lakes have a very low level of backscattering. This affects the ability to detect first snow because lakes tend to freeze well after the snow cover.

Another obstacle for detecting the initial snow cover arrival are urban areas (mainly greater Helsinki area). Part of the explanation for the high backscattering characteristics may be the buildings forming corner reflectors.

5. CONCLUSIONS

As this study shows, K_u-band scatterometers, such as QuikSCAT/SeaWinds, can be used for remote sensing of snow, given some restrictions. Retrieval of snowmelt phases works quite well in most areas. The most problematic areas have a high backscattering signature (eg. greater Helsinki

area and some fjelds in central Lappland). The high backscattering signature of large built-up areas also deteriorate the ability to identify initial snow from bare ground.

6. REFERENCES

References

[1] Nghiem, Son V. and Tsai, Wu-Yang, "Global Snow Cover Monitoring With Spaceborne Ku-band Scatterometer," *IEEE Transactions on Geoscience and Remote Sensing*, vol. 39, pp. 2118–2134, October 2001.

[2] A. K. Fung, *Microwave Scattering and Emission Models and Their Applications.* Boston, London: Artech House, 1994.

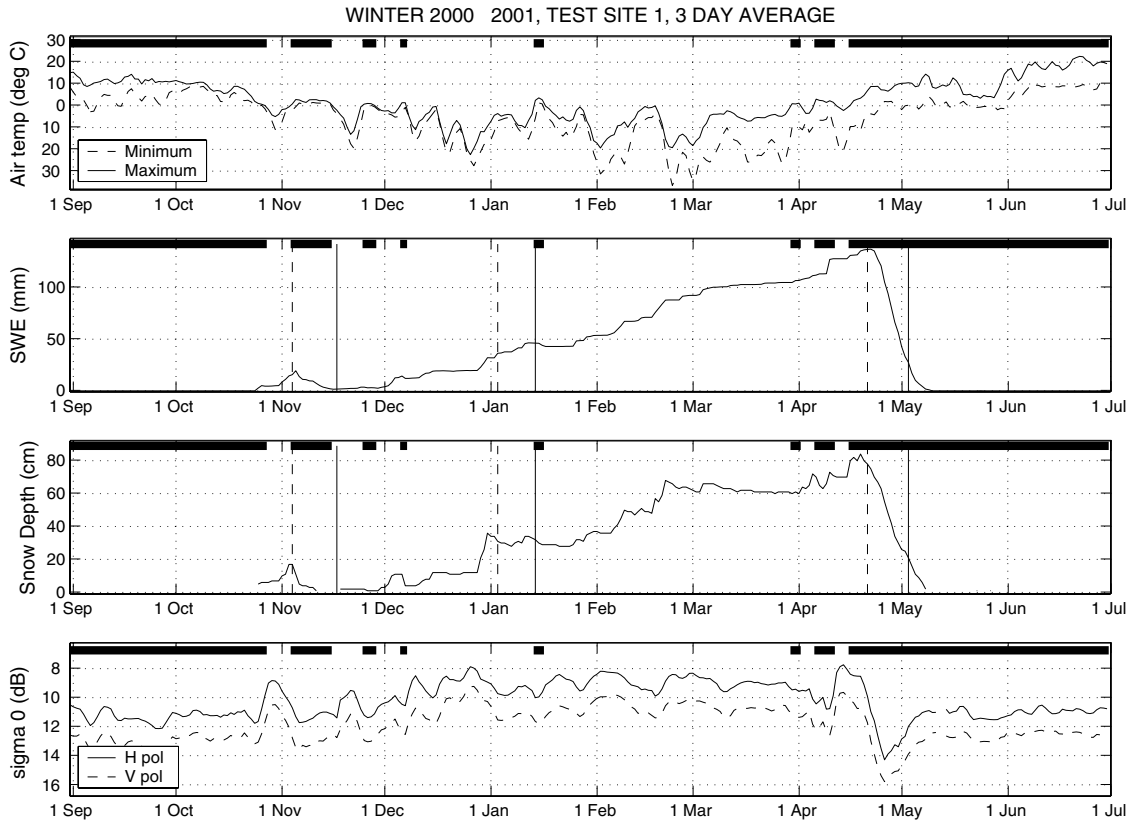

Figure 1: Winter 2000-2001 on Sodankyla test site, three day averaging for σ° data.

Figure 2: Areas where σ° is over -9.5 dB on H-pol.

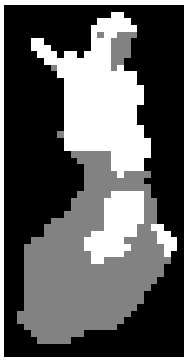

Figure 3: Areas where SWE is over 10 mm based on maps by SYKE.

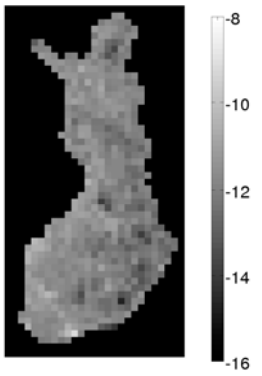

Figure 5: Backscattering on June 7, 2000 on H-pol.

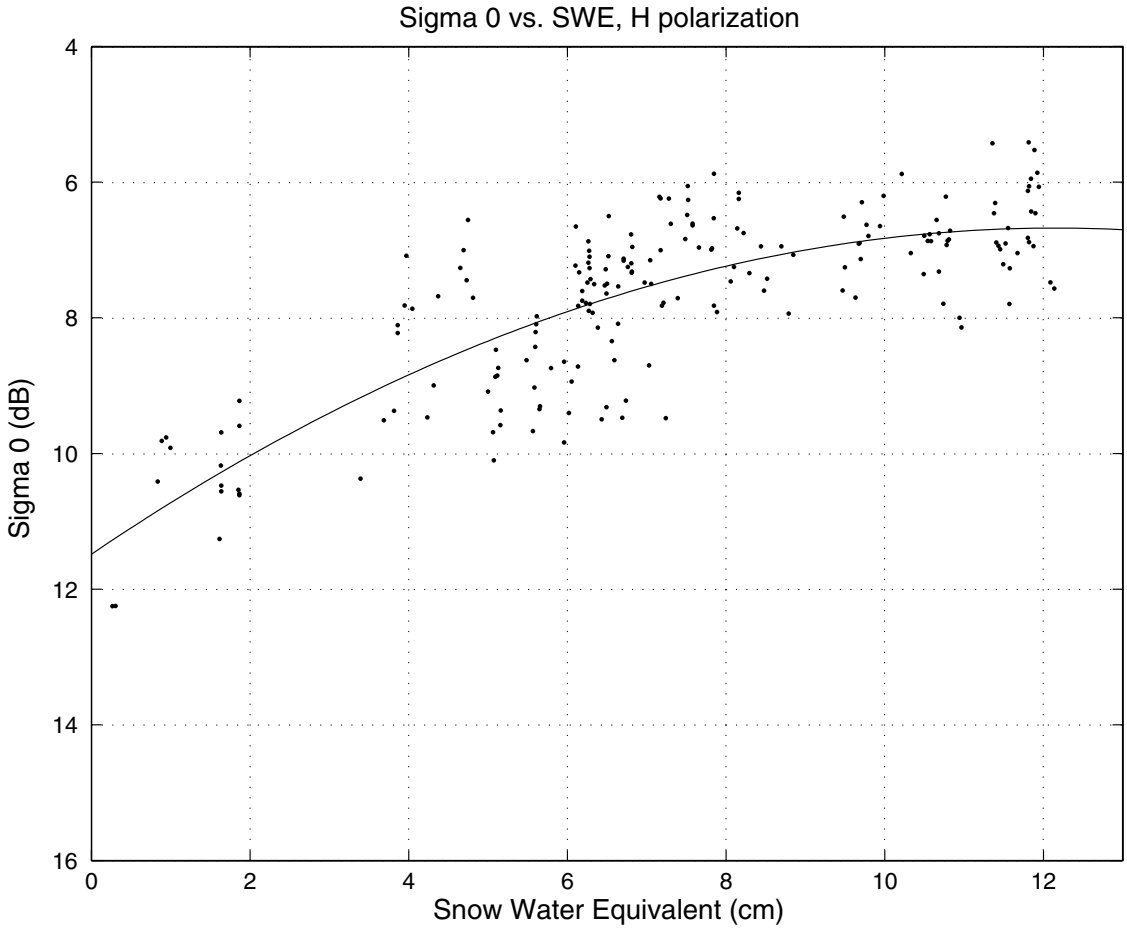

Figure 4: Scatterplot of σ° values as a function of SWE. Data are from three winters in 1999–2002.

DEPENDENCE BETWEEN SPATIAL STATISTICS AND MEASUREMENT LENGTH FOR C-BAND BACKSCATTERING SIGNATURES OF THE BALTIC SEA ICE

Marko Mäkynen[(1)], Terhikki Manninen[(2)], Markku Similä [(3)] , Juha Karvonen [(3)], Martti Hallikainen[(1)]

[(1)] Laboratory of Space Technology, Helsinki University of Technology
P.O. Box 3000, FIN-02015 HUT, Finland
Email:makynen@avasun.hut.fi

[(2)] Finnish Meteorological Institute

[(3)] Finnish Institute of Marine Research

Abstract
We have studied using C-band one-dimensional helicopter scatterometer data and ENVISAT SAR images, the dependence between measurement length l and standard deviation (std) and correlation length L for the Baltic Sea ice backscattering coefficient (σ°). The results with both data sets indicate strong linear dependence between $\ln(l)$ and $\ln(\mathrm{std}(\sigma^\circ))$ up to a distance of at least few kilometers. The dependence between l and L is non-existent as the radar signal fading destroys the textural correlation in the σ° data. The regression coefficients describing the dependency of $\ln(l)$ vs. $\ln(\mathrm{std}(\sigma^\circ))$ do not discriminate various ice types better than just mean and standard deviation of σ°. However, the use of the regression coefficients instead of mean and std is preferred due to the scale invariant comparability with the results of other studies.

Keywords: Fractals, sea ice, statistics, synthetic aperture radar.

1. INTRODUCTION

Surface roughness measurements of various Baltic Sea ice types have indicated fractal-like nature of the ice surface [1]. We have studied by means of data analysis if this fractal-like nature extends from a property of surface to a property of backscattering coefficient (σ°). Our aim in data analysis was to determine the dependence of the rms variation and correlation length of the Baltic Sea ice σ° data on the length of measurement, and, if this dependence is found, then assess its usability for sea ice classification. The analysis was conducted using C-band data acquired with the helicopter-borne non-imaging Helsinki University of Technology Scatterometer (HUTSCAT) and ENVISAT SAR images.

2. HUTSCAT INSTRUMENT AND DATA SETS

2.1 HUTSCAT Instrument

The HUTSCAT is a helicopter-borne non-imaging FW-CW scatterometer that operates simultaneously at 5.4 and 9.8 GHz (C- and X-band) with all four linear polarizations [2]. At each channel, 20 backscattered power spectra per second are measured. The range resolution of the spectra is 0.68 m. Simultaneously with the backscattering measurements, the target is recorded by a video camera. A typical flight altitude is 100 m and the flight speed is 25 m/s. At 5.4 GHz the 90% confidence interval of the absolute σ° is better than ±0.8 dB. The noise equivalent σ° at 5.4 GHz is less than -28 dB at co- and less than -44 dB at cross-polarizations.

2.2 HUTSCAT Data Set

HUTSCAT data were acquired during seven ice research campaigns at the Baltic Sea in 1992-2003. HUTSCAT measurements were conducted at incidence angles of 23 and 45 degrees along selected test lines that included various ice types. HUTSCAT data was assigned into various ice type classes by video imagery. The ice type classes are: nilas (NI) is a general term for recently formed ice which is usually less than 10 cm thick. Smooth level ice (SLI) is almost unaffected by deformation, only cracking or finger rafting may occur. Rough level ice (RLI) has protruding ice blocks and floe edges and low uneven surface

areas and it has typically broken and frozen several times. Slightly deformed ice (SDI) consists of ice ridges, uneven surfaces and level ice areas, the sizes of which are usually larger than the pixel size in SAR images. The average size of level ice areas in highly deformed ice (HDI) is usually smaller than the pixel size and the proportion of level ice areas is smaller than in SDI, i.e. the degree of deformation is higher. Loose and frozen brash ice (LBI, FBI) are accumulations of ice fragments not more than 2 m across. They are wreckage of other forms of ice.
The ground truth data provided further classification into the following snow cover categories: (1) dry snow, (2) moist snow (volumetric wetness < 1%) and (3) wet snow (wetness > 1%).

2.3 ENVISAT Data Set

During a sea ice field campaign in February 2003 two ENVISAT SAR image mode precision (IMP) images at HH-polarization and two alternating polarization precision (APP) images at HH/HV-polarization were acquired over the northern part of the Bay of Bothnia. The images were block averaged from the original pixel size of 12.5 m to a pixel size of 37.5 m so that the neighboring pixels are not correlated. The noise equivalent σ° at HH/HV-polarization is below -22 dB.

3. ANALYSIS METHODS OF SPATIAL STATISTICS

For a Brownian fractal profile, the surface correlation length L is linearly dependent on the measurement length l [3]:

$$L = k_0 l \tag{1}$$

and the logarithm of the standard deviation σ is linearly dependent on the logarithm of the measurement length [3]:

$$\ln(\sigma) = a + b\ln(l). \tag{2}$$

The coefficient a is related to the actual profile level, whereas b describes the variation of the profile with spatial frequency and it is related to the fractal dimension $D = 2 - b$. In the following, the use of (1) and (2) for the HUTSCAT and ENVISAT data are explained.

3.1 HUTSCAT Data

At first the HUTSCAT data were averaged to a resolution of 12.5 m which compares to the pixel size of many SAR images. Averaged data has around 50 independent samples in each σ° (i.e. fading < 0.62 dB).

Std(σ°) and L as a function of l were calculated in the following steps: 1) a measurement line is divided into disjoint segments consisting of 20 consecutive pixels (σ° values). 2) A window of length d is slid through a segment by one pixel steps. In every allowed window position the σ° values are first rectified using linear regression and then std(σ°) and autocorrelation function $\rho(x)$ of σ° are computed. This yields m distinct values for these statistics for every segment. 3) Statistics over the m values are averaged for each segment separately. L is determined as the first discrete x value where $\langle\rho(x)\rangle < \exp(-1)$. 4) The steps 2) and 3) are repeated when d increases from the minimum to the maximum length. 5) (1) and (2) are fitted for each segment using d as the explaining variable. In step 4), the minimum length d for std(σ°) and $\rho(x)$ is 3 and 5 pixels, respectively. Because of the restricting effect of the finite length on the variation, the maximum measurement length was chosen to be at most 60% of the segment length [4].

The chosen segment length is a compromise between of a long segment for large number points in (1) and (2) and a short segment for large set of regression coefficients for statistical studies.

3.2 ENVISAT data

Several rectangular areas representing level ice, deformed ice and highly deformed ice were visually selected from each SAR image. A typical area of a rectangle was 6.9 km^2. Within each rectangle 10 windows of size 20 by 20 pixels (750 by 750 m) were selected at random locations. The average number of windows for each ice type is around 400. Equations (1) and (2) were used as in the case of the HUTSCAT data, but the averages were calculated separately for horizontal and vertical direction and then these two estimates were averaged.

4. RESULTS AND DISCUSSION

4.1 Standard deviation of σ°

The results with the both data sets indicate strong linear dependence between $\ln(l)$ and $\ln(\mathrm{std}(\sigma^\circ))$: in the HUTSCAT data the average coefficient of determination (r^2) is 0.91 and only 11% of the total of 7167 r^2 values are below 0.80. For the ENVISAT data the average r^2 is 0.93, and only 11% of the total of 3520 r^2 values are below 0.90. Dependence between $\ln(l)$ and $\ln(\mathrm{std}(\sigma^\circ))$ for those HUTSCAT segments of 20 pixels where r^2 has its maximum or minimum value for each ice type is shown in Fig. 1 at 5.4 GHz HH-polarization. When the HUTSCAT measurement lines of various ice types are used in their full length (max 60% length 6.5 km, average 650 m) in the analysis, the average r^2 is still high, 0.88. There is no correlation between r^2 and the length of the measurement. The results suggest increase of $\mathrm{std}(\sigma^\circ)$ as a function of l up to a distance of at least few kilometers.

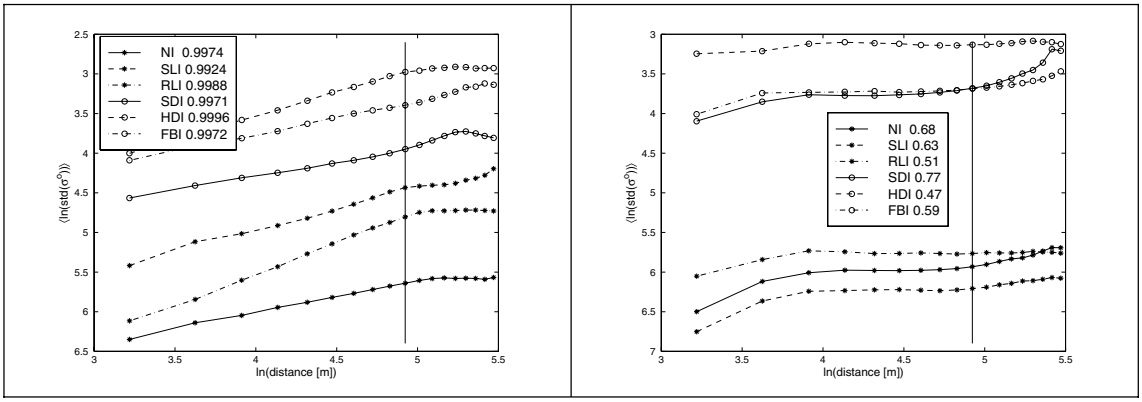

Fig. 1. The strongest (a) and the weakest (b) dependence between $\ln(l)$ and $\ln(\mathrm{std}(\sigma^\circ))$ for various ice types using HUTSCAT 5.4 GHz HH-polarization dry snow data. The incidence angle is 23° and the data were averaged to a resolution of 12.5 m. The maximum and minimum coefficient of determination for each ice type is given. The vertical line shows to the maximum l according to the 60% rule used in (2).

The average b depends on ice type, polarization, incidence angle and snow cover wetness, e.g. in the HUTSCAT data the average b is usually the largest for slightly deformed ice (SDI) (from 0.357 to 0.563) and the smallest for frozen brash ice (FBI) (from 0.296 to 0.402). The smaller b the more uniformly and densely distributed the significant changes in the σ° level are. FBI is very homogeneous in its surface structure and thus its σ° has most likely small textural variations without any large scale patterns. The addition of multiplicative fading yields abrupt local σ° variations which results in a small b value. Whereas in the case of SDI, the overall level of the σ° intensity may remain low (or high) on a relatively long interval before a large jump. The large scale variation for SDI due to the ridging intensity variation is greater than the local variation due to the small scale texture and the fading. This property is reflected in the large b.

The regression coefficients describing the dependency of $\ln(l)$ vs. $\ln(\mathrm{std}(\sigma^\circ))$ do not discriminate various ice types better than just mean and std of σ°, see Fig. 2. However, the disadvantage of using the

mean and std values is that they are fixed for a certain distance, so that direct comparison of corresponding values of other studies is not possible if the l used for their determination is not equal.

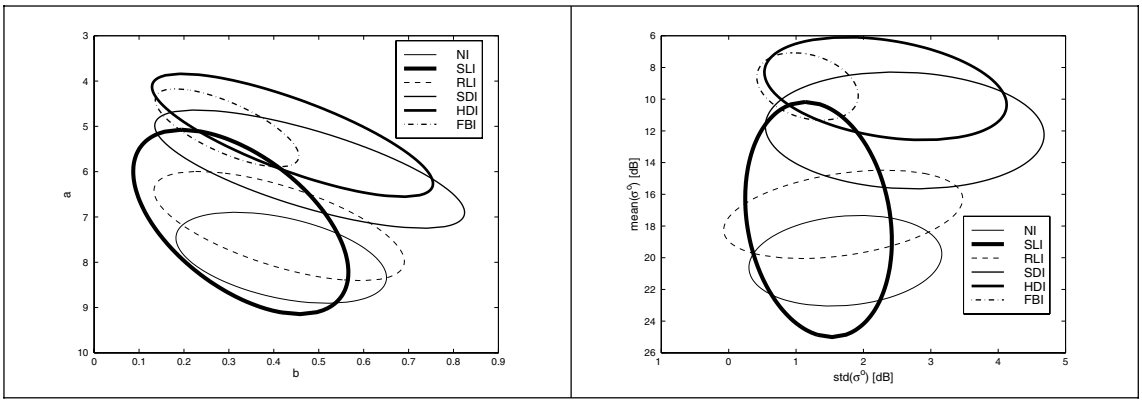

Fig. 2. The variation of (a) the regression coefficients a and b of (2) and (b) the mean and standard deviation for a section of 20 σ° values (length of 237.5 m) of various ice types using HUTSCAT 5.4 GHz HH-polarization dry snow data. The incidence angle is 23° and the data was averaged to a resolution of 12.5 m. The ellipses represent 90% confidence limits.

4.2 Correlation length of σ°

There is no linear dependence between l and L in both data sets. L is always very short, only a distance corresponding to one or two pixel shift at the distance of 137.5 m which corresponds to the 60% rule. This is very likely due to the radar signal fading destroying the textural correlation in the σ° data yielding always very small L values regardless of the length of the measurement.

5. CONCLUSIONS

We have studied using C-band HUTSCAT scatterometer data and ENVISAT SAR images, the dependence between measurement length l and standard deviation (std) and correlation length L for the Baltic Sea ice σ°. The results indicate strong linear dependence between $\ln(l)$ and $\ln(\mathrm{std}(\sigma^\circ))$ up to a distance of at least few kilometers. The linear dependence between $\ln(l)$ and $\ln(\mathrm{std}(\sigma^\circ))$ is a property of fractional Brownian motion, but based on our analysis it is not possible to determine whether the σ° variation as function of l is truly fractal-like or not. The dependence between l and L is non-existent as the radar signal fading destroys the textural correlation in the σ° data.

The regression coefficients describing the dependency of $\ln(l)$ vs. $\ln(\mathrm{std}(\sigma^\circ))$ do not discriminate various ice types better than just mean and std of σ°. However, the use of the regression coefficients instead of mean and std is preferred due to the scale invariant comparability with the results of other studies. It is also possible that a relation exists between b and degree of large scale ice deformation. This assumption could only be studied with quantitative ground truth data describing ice deformation.

6. REFERENCES

[1] A.T. Manninen, "Surface roughness of Baltic Sea ice*," J. Geophys. Res.*, vol. 102, no. C1, pp. 1119-1139, 1997.

[2] M. Hallikainen, J. Hyyppä, J. Haapanen, T. Tares, P. Ahola, J. Pulliainen, and M. Toikka, "A helicopter-borne eight-channel ranging scatterometer for remote sensing - Part I: system description," *IEEE Trans. Geosci. Remote Sensing*, vol. 31, no. 1, pp. 161-169, 1993.

[3] E.L. Church, "Fractal surface finish," *Applied Optics*, vol. 27, no. 8, pp. 1518-1526, 1988.

[4] A.T. Manninen et al., "Multiscale surface roughness description for scattering modelling of bare soil," *Physica A*, vol. 319, March 1, pp. 535-551, 2003.

Mapping of Snow Covered Area Using Combined SAR and Optical Data

Juha-Petri Kärnä[(1)], **Jouni Pulliainen**[(1)], **Sari Metsämäki**[(2)], **Markus Huttunen**[(2)], **Martti Hallikainen**[(1)]

[(1)] ***Laboratory of Space Technology, Helsinki University of Technology***

P.O. Box 3000, 02015 HUT, FINLAND

E-mail: Juha-Petri.Karna@hut.

[(2)] ***Finnish Environment Institute***

P.O. Box 140, 00251, Helsinki, FINLAND

Abstract

A Bayesian inversion method for deriving Snow Covered Area (SCA) using combined SAR and optical data is introduced. SCA estimation is done for over 2000 sub drainage areas covering the whole Northern Finland using RADARSAT and NOAA AVHRR images. The applied inversion method used takes into account the statistical accuracies of the two data sources, optical and SAR images.

Keywords: remote sensing of snow, RADARSAT, SAR, SCA

1 INTRODUCTION

Hydrological processes in boreal forest zone are highly affected by the seasonal snow cover. Thus, hydrological models operationally used for run-off and river discharge forecasting employ spatially distributed information on physical snow pack characteristics, and on the extent of snow. In Finland, the most important period is the spring melt season and the snow parameters essential for forecasts include the fraction of snow-covered area (SCA) and snow liquid water content (snow wetness). This information is required in a spatial scale from a few to several kilometer s corresponding to sizes of sub-basins. The Finnish forecasting system applies snow information interpolated from weather stations and snow gauging network. However, its spatial accuracy is relatively poor. Moreover, measurements on some important parameters, such as snow liquid water content, are not carried out operationally. Space-borne observations can be used to overcome these problems. The operational system already applies SCA-estimates derived from optical satellite images during the spring melt period, but they are only available under non-cloudy conditions. Space-borne SAR provides information that can be used for the mapping of SCA regardless of cloud cover. SAR measurements can be also used to retrieve information on snow wetness.

2 DATA AND TEST SITE

Investigations are carried out using both SAR and optical data. The SAR data consists of RADARSAT images from the year 2004 covering the whole Northern Finland (Fig. 1). Also several ERS-2 SAR images from years 1997-2002, and Envisat ASAR images from the year 2003 are used. The backscattering coefficients are classified into five classes based on the forest stem volume information. The optical data used is NOAA AVHRR images from years 2001-2004 and some Envisat MODIS images.

The area used in the study is the whole Northern Finland containing over 2000 sub drainage areas (Fig. 1).

3 METHOD

A Bayesian inversion method for deriving SCA using combined SAR and optical data is used. The inversion method used takes into account the statistical accuracies of the two data sources, optical and SAR images.

The backscattering model used is the semi-empirical HUT backscattering model [2], which describes the average backscattering coefficient of forested terrain as a function of forest stem volume. The backscattering equation can be given as a function of forest stem volume V, scalar variable χ, and SCA:

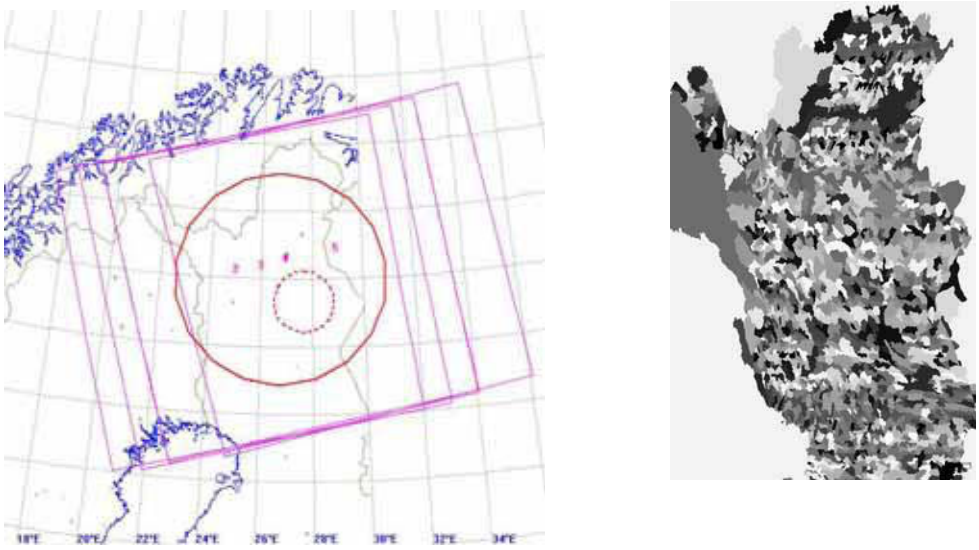

Figure 1: The coverage of the RADARSAT images (left), and sub drainage areas of the Northern Finland (right).

$$\sigma^o(V,\chi,SCA) = \left[SCA \cdot \sigma^o_{snow} + (1-SCA)\cdot \sigma^o_{ground}\right] \cdot t(V,\chi)^2 + \sigma^o_{canopy}(V,\chi) \quad (1)$$

where σ^o_{snow} is the backscattering coefficient of snow covered ground and σ^o_{ground} is that of snow-free ground surface. The model requires the reference values for backscattering coefficient for the 100 % wet snow cover and totally snow-free conditions.

An analogous model for optical reflectance [1] is used:

$$\rho(SCA) = (1-t^2)\cdot \rho_{forest} + t^2 \cdot [SCA \cdot \rho_{snow} + (1-SCA)\cdot \rho_{ground}] \quad (2)$$

where ρ_{forest}, ρ_{snow}, and ρ_{ground} are the reflectances for forest canopy, wet snow and snow-free ground, respectively. The value t is empirically determined apparent forest transmissivity for each sub-drainage area.

The assimilation is done by minimizing the following equation

$$J(\chi, SCA) = \sum_i w_1(\sigma^o_{model}(i) - \sigma^o_{SAR}(i))^2 + w_2(\rho_{model} - \rho_{AVHRR})^2 \quad (3)$$

where $\sigma^o_{model}(i)$ is the calculated and $\sigma^o_{SAR}(i)$ is the measured backscattering coefficient for the forest stem class i. Similarily, ρ_{model} is the calculated and ρ_{AVHRR} the measured reflectance of the sub drainage area. Weighting factors w_1 and w_2 represent the accuracy of the corresponding values.

The SCA estimation is done for over 2000 sub-drainage areas in Northern Finland.

4 RESULTS

The performance of SCA estimation is analyzed by comparing the obtained estimates with independent SCA reference data sources: (a) the WSFS hydrological model [3] predictions, (b) observations at weather stations. The obtained results indicate that the SCA mapping accuracy of C-band SAR is around 20 % while the accuracy of optical images is around 15 %. As optical images are not always available due to cloud cover, SAR data can be applied for those cases.

REFERENCES

[1] S. Metsämäki, M. Huttunen, and S. Anttila. The operative remote sensing of snow covered area in a service of hydrological modelling in Finland. In *Proceedings of the 23rd EARSel Symposium on Remote Sensing*, Ghent, Belgium, June 2003.

[2] J. Pulliainen, J. Koskinen, and M. Hallikainen. Compensation of forest canopy effects in the estimation of snow covered area from SAR data. In *IEEE 2001 International Geoscience and Remote Sensing Symposium (IGARSS 2001)*, Sydney, Australia, July 2001.

[3] B. Vehviläinen. The watershed simulation and forecasting system in the National Board of Waters and Environment. Publications of the Water and Environment Research Institute No. 17, National Board of Waters and the Environment, Helsinki, 1994.

Session 2b:
Antennas I

Microstrip Antenna Circuit Model and Linear Pattern Correction

Ilkka Salonen[(1)] and Pertti Vainikainen[(1)]

[(1)] IDC, SMARAD, Radio Laboratory, Helsinki University of Technology (HUT), Finland
P.O.Box 3000, 02015HUT, Finland
Email Address: ilkka.salonen@hut.fi, pertti.vainikainen@hut.fi

Abstract
Mutual coupling and other effects cause that the element patterns in an array are different. In the practical (adaptive) use of the array identical element patterns are usually expected. A matrix pattern correction method can be used to correct the array element inputs/outputs. A multiport model for microstrip array with parallel circuit model with voltage input for antenna element is searched for pattern correction beginning from the measured scattering matrix.

1. INTRODUCTION

Mutual coupling distorts antenna array element patterns. A matrix method can be used for correction of the array inputs/outputs [1,2]. In addition to mutual coupling also the groung plane edge effect should be included in the correction of a microstrip array [3,4]. If the radiation of an antenna element is defined basically with a value of current or voltage, then the array pattern correction can be done with the impedance or admittance matrix [1,4]. A circuit model for an antenna array would be of interest for mutual coupling compensation [3]. When only the measured scattering matrix is known, this is a reverse problem.

2. THEORY AND RESULTS

Mutual coupling in multiport devices can be presented with impedance (**Z**), admittance (**Y**) or scattering matrix (**S**). For this work scattering matrices of microstrip antenna arrays are measured. Impedance matrix elements for a given port are defined as the ratio of output voltage in each port to input current in the given port when all other ports are open circuited with zero input currents. In the admittance matrix measurement the input is voltage and outputs are

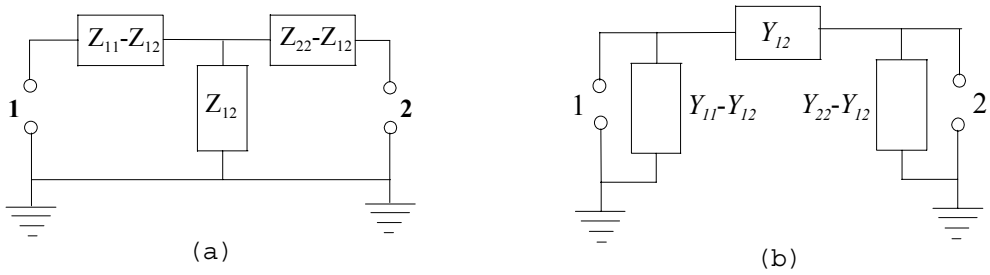

Fig. 1. Two-port circuit model of an antenna pair a) for impedance matrix with a T-circuit [6] and b) for an admittance matrix with a π-circuit. Impedances Z_{11} and Z_{12} are defined with input current in port 1 with port 2 opened, without a current. Admittances Y_{11} and Y_{12} are defined with input voltage in port 1 and port 2 short circuited with zero voltage.

currents when other ports are short circuited with zero input voltages [5]. In Fig. 1 we see equivalent circuits for two-element impedance and admittance matrix measurements [6-7]. It is simple to proof, that these circuits are in accordance with impedance and admittance matrix definitions and can be both presented a priori as model circuit for a linear passive two-port. These models explain for a given port the open- or short-circuited condition of the other port as "neutral", without mutual coupling [1,6]. In general, the components of these circuits can be different, also complicated circuit structures. One complication to real linear circuit is, that the mutual component can have as well an unphysical negative resistance as a positive one [6]. Because the circuit is passive the mutual components are only explaining the balance in the system and do not have any independent explanation.

Where is the signal? Without mutual coupling the RF signal vector to/from an antenna array can be as well the voltage ($\vec{\mathbf{V}}$), current ($\vec{\mathbf{I}}$) or voltage wave vector ($\vec{\mathbf{V}}^+$). In that case these parameters at a given port depend only on each others and the corresponding matrix dependency between corresponding signal vectors

($\vec{\mathbf{V}}$, $\vec{\mathbf{I}}$, $\vec{\mathbf{V}}^{+}$) is a diagonal matrix. In the case of mutual coupling the matrix dependency of a pair of different signal vectors is not a diagonal one. For an antenna array, the signal is usually the current or voltage (field) in the antenna element of the array. When the RF signals to/from array ports are in the form of a voltage wave vector $\mathbf{V}^{+}$ the input coefficients can be corrected to the voltages or currents by multiplying with corresponding correction matrices [2,4,7,8]

$$\vec{\mathbf{V}}^{+}_{correct} = (\mathbf{I}+\mathbf{S})^{-1}\vec{\mathbf{V}}_{wanted} = (\mathbf{I}+\mathbf{y})\vec{\mathbf{V}}_{wanted} / 2 \quad (1)$$

$$\vec{\mathbf{V}}^{+}_{correct} = (\mathbf{I}-\mathbf{S})^{-1}Z_0\vec{\mathbf{I}}_{wanted} = (\mathbf{I}+\mathbf{z})Z_0\vec{\mathbf{I}}_{wanted} / 2 \quad (2)$$

In (1) and (2) it is assumed, that the wanted input vectors are the wanted complex weights of the uncoupled element patterns, defined without taking into account the mutual coupling in the antenna array. We see, that the corrections with (1) and (2) have opposite effects on the inputs/outputs. The mutual coupling compensation removes internal reflections, which cause ripples in the antenna element patterns. If the input/output RF signal are the currents and they should be voltages in the array (or vice versa) then the impedance (admittance) matrix of the array is the corresponding correction matrix. The impedance, admittance and scattering matrices are related to each other with [5]

$$\mathbf{z} = \left(\mathbf{I}+\mathbf{S}\right)\cdot\left(\mathbf{I}-\mathbf{S}\right)^{-1} \quad (3)$$

$$\mathbf{S} = \left(\mathbf{z}+\mathbf{I}\right)^{-1}\cdot\left(\mathbf{z}-\mathbf{I}\right) \quad (4)$$

$$\mathbf{y} = Z_0\mathbf{Y} = Z_0\mathbf{Z}^{-1} = \mathbf{z}^{-1} \quad (5)$$

In modern antenna technology the antenna elements and the input ports have dimensions that are not small compared with the wavelength. In this case the feed should also be presented as an input circuit to be extracted from the array multiport circuit. When higher frequencies with increased bandwidth are used (which is the tendency of radio system evolution), then the problems with input circuits will grow. If there are well known and well modeled feed structures for the antenna elements, then they can be easily extracted. If we have scattering matrix measurements, then we should change to **z**-matrix presentation to subtract an impedance component at input and to **y**-matrix presentation to subtract an admittance component at input,

$$\mathbf{y}_i = \mathbf{y}^{in}_{i+1} + \mathbf{y}_{i+1} \quad (6)$$

$$\mathbf{z}_k = \mathbf{z}^{in}_{k+1} + \mathbf{z}_{k+1}, \quad \text{where } k \neq i, \quad (7)$$

where $\mathbf{y}_i$ and $\mathbf{z}_k$ are the admittance and impedance matrices at extracting step i and k, the input admittance and impedance matrices $\mathbf{y}^{in}$ and $\mathbf{z}^{in}$ are diagonal ones and are to be subtracted, and $\mathbf{y}_{i+1}$ and $\mathbf{z}_{k+1}$ are the admittance and impedance matrices after extracting an input component. After subtracting an input circuit element the remaining multiport circuit should be closer to an ideal voltage/current driven array. Stepwise we can subtract whole input circuit changing between **y**- and **z**-presentations, in analog to working with the Smith chart, and then use finally the required correction by (1) or (2). After that we should go stepwise backward to the original measurement reference points defining a new correction matrix at each step using dependencies in formulas (3)-(6) to obtain the final correction matrix for the reference planes of the measured scattering matrix. The reference plane in the input line for the original measurement is usually at the array connectors.

In Fig. 2 we see a multiport circuit model for an admittance matrix, which is in accordance with admittance matrix definition. The principle is that each port is connected to all other ports and that the admittance at the given port is the self-admittance of the port minus all mutual admittances for that port. The corresponding circuit model for the impedance matrix is not found when the number of ports is more than two. In [9] is presented a 3x3 multiport, which is not symmetric and cannot explain all mutual components with the impedance matrix measurement. Also the simplification with a common mutual component in [9] has no sense for a linear array. We can assume, that the topography/structure in Fig. 2 is the only one explaining mutual coupling in a passive multiport. Thus the same structure should be needed also for the impedance matrix and it might be done by the dualism of electromagnetics using magnetic circuits [10-13]. Another alternative would be to use mutual components parametrically as is done traditionally with mutual inductance or capacitance, and use even mutual resistances [14]. The mutual component can be presented for **y**- and **z**-matrices as an internal source of current or voltage depending parametrically on the input to another port. A disadvantage of the continuous circuit models in Figs. 1 and 2 is, that the mutual component appears there three times.

Because the model in Fig.2 is the model explaining the admittance matrix measurement there is no simpler circuit models in the general case. When two elements are far from each other the mutual admittance between them can be ignored compared with other connections and the model can be simplified. Each measurement of impedance matrix component can be modeled with the circuit in Fig. 1a with other ports open-circuited, but these measurements cannot to be collected to a multiport model. This is a serious limitation, because in a linear array there is usually two neighbors for an antenna element.

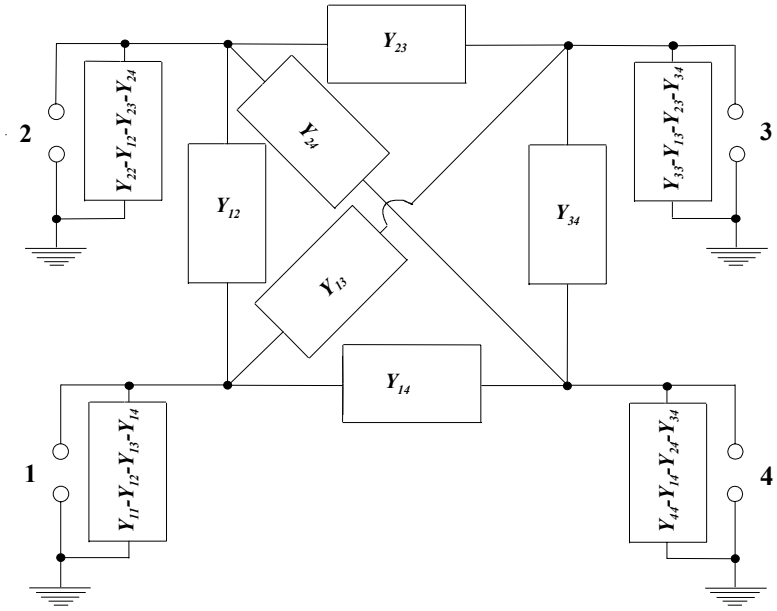

Fig. 2. A multiport circuit model defining admittance matrix. In this example admittance matrix is a 4x4-matrix.

A parallel resonator model has been used to explain the behavior of microstrip antenna elements [15-18]. The correction results in [3] using (1) are in accordance with the parallel model. In Fig. 3 we see the measured resonators, when the scattering matrix reference point is at the beginning of the feed probe of a coaxial SMA connector. In the correction done in [3] the reference point is shifted further from the level presented in figure 23° towards the array with a 45° shift on the Smith diagram. The position of the circle of the ideal admittance resonator is also shown. In the first case of Fig. 3a the measured S_{ii}:s are presented. The frequency range is 3 … 6 GHz. The frequency of 5.3 GHz is shown for each resonance with a little circle. $S_i(y_{ii})$ and $S_i(z_{ii})$ are the reflection coefficients corresponding to diagonal element values of **y** and **z** calculated as in one-dimensional case. We see, that these resonators of **z**-presentations are less ideal than the others. This shows, that the **y**-presentation is potentially better for the correction. For an array with element spacing 0.3λ this effect is more pronounced, which shows the importance of the resonators as well as the near ideal eigenvalue-resonances detected in [4].

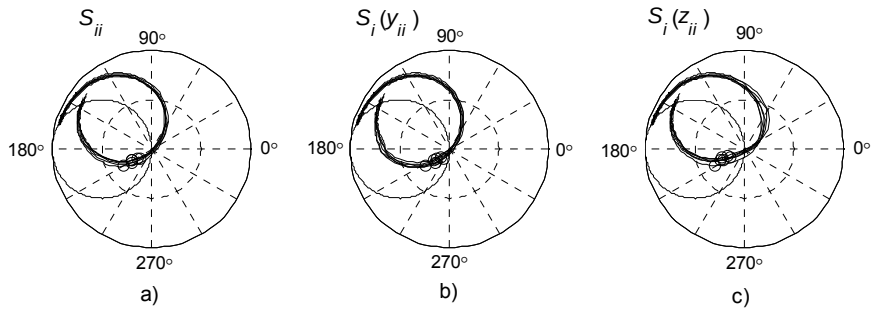

Fig. 3. The resonator behavior of an 6-element microstrip array with element spacing of 0.4λ. Measured S_{ii}:s are in a and in b) and c) are the calculated S_i:s calculated as in one-dimensional case depending on the diagonals of y- and z-presentations, respectively.

Further an input circuit to be extracted has been searched. The criterion for a good input circuit can be, that after extraction the remaining $S_i(y_{ii})$-resonators are identical and they are close to the circle of ideal resonator (see Fig. 3). Different lumped elements up to 6 are proved to be extracted. A simple alternative for input circuit is detected

to be a circuit with a series inductor and a parallel capacitor. However, any significant improvement in the correction results has not been detected compared with those in [3] and [4], using scattering matrix or its eigenstructure, when the reference plane is redefined. The input inductance in the best case does not differ much from that reported in [3]. Also the series inductance and parallel capacitance are similar to the impedance line reference plane shift done in [3], which is much simpler to do. The correction of element patterns is not a good criterion for input circuit finding, because a false input circuit can also give good correction results.

Another criterion additional to the resonator behavior is the behavior of the mutual components. For example, the y_{ij}:s should oscillate regularly [6] and the phases of S_{ij} should change about linearly for elements placed far from each other. The identity of mutual admittances for elements with equal distance in the array is also used as a criterion for input circuit finding. The criterion of identity of the resonators have a tendency to give small final point-like resonator circles on the Smith chart, if any counterpart is not used. The progress using the presented and also some other ideas for pattern correction is yet poor using admittance matrix with input circuit extraction, and also the complexity of this method exceeds the complexity of the earlier correction using scattering matrix [3,4].

3. CONCLUSIONS

It is demonstrated, that the matrix correction of array can be done easily, if the array circuit model is one of the idealized models with voltage or current driven antenna elements. When there is an input circuit, it can be extracted. Further, even in the best case of ideal model with impedance matrix the linear electric circuit model cannot be found and an additional magnetic circuit model might be needed to explain array with mutual coupling. The finding of new reference plane for scattering matrix using input circuit extracting has not yet given better results than reached earlier in [3] and [4].

4. REFERENCES

[1] I. Gupta and A. Ksienski., "Effect of mutual coupling on the performance of adaptive arrays", *IEEE Trans. Antennas Propagat.*, vol. AP–31, pp. 785–791, Sep. 1983.

[2] H. Steyskal and J. Herd, "Mutual coupling compensation in small array antennas", *IEEE Trans. Antennas Propagat.*, vol. 38, pp. 1971–75, Dec. 1990.

[3] I. Salonen, "*Pattern distortion and impedance mismatch in small microstrip antenna arrays*", Licentiate Thesis, Helsinki University of Technology, Department of Electrical and Communications Engineering, 2002, 170 p.

[4] I. Salonen, A. Toropainen, and P.Vainikainen, "Linear pattern correction in a small microstrip antenna array," *IEEE Trans. Antennas Propagat.*, Vol. 52, No. 2, Feb. 2004, pp. 578-586.

[5] Pozar, D., M*., Microwave engineering*, New York, John Wiley & Sons inc., 1998, 716 p.

[6] Kraus, J., D., *Antennas*, McGraw-Hill book company, second edition, New York 1988, 892 p.

[7] W. K. Kahn, "Impedance-match and element-pattern constraints for finite arrays", *IEEE Trans. Antennas Propagat.*, vol. AP–25, pp. 747–755, Nov. 1977.

[8] L. Pettersson, M. Danestig, and U. Sjöström, "An experimental S-band digital beamforming antenna", *IEEE AES Systems Magazine*, pp. 19–27, Nov. 1997.

[9] R. Levy, "Derivation of equivalent circuits of mictowave structures using numerical techniques", *IEEE Transactions on microwave theory and techniques*, Vol. 47, No. 9, Sep 1999, pp. 1688-1695.

[10] N. C. Cheung, and K. K-C. Chan, "Magnetic modeling of a mutually coupled variable reluctance gripper", 28th annual conference of the Industrial electronics society (IECON 2002), Vol. 4, pp. 2733-2738.

[11] M. A. Preston, J. P. Lyons, "A switched reluctance motor model with mutual coupling and multi-phase excitation", *IEEE Transactions on magnetics*, Vol. 27, pp. 5423-5425.

[12] L. J. Giacoletto, "Magnetic circuits analysis using electronic circuit analysis program", Proceedings of conference on Power electronics in transportation, Dearnborn, MI USA, 1994, pp. 91-94.

[13] A. H. Mohammadian, N. M. Martin, and D., W. Griffin, "A theoretical and experimental study of mutual coupling in microstrip antenna arrays", *IEEE Transactions on antennas and propagation*, Vol. 37, Oct. 1989, pp. 1217-1223.

[14] H. Ymeri, B. Nauwelaers, K. Maex, S. Vanderberghe, and David de Roest, "New analytical expressions for mutual inductance and resistance of coupled interconnects on lossy silicon substrate", *Digest of Papers of 2001 Topical Meeting on Silicon Monolithic Integrated Circuits in RF Systems*, Ann Arbor, MI USA, 2001, pp. 192-200.

[15] K. R. Carver and J. W. Mink, "Microstrip antenna technology", *IEEE Trans. Antennas Propagat.*, vol. AP–29, pp. 3–25, Jan. 1981.

[16] W. F. Richards and Y. T. Lo, "An improved theory for microstrip antennas and applications", *IEEE Trans. Antennas Propagat.*, vol. AP–29, pp. 38–46, Jan. 1981.

[17] B. Robert, T. Razban, and A. Papiernik, "Capasitors provide input matching of microstrip antennas", *Microwaves & RF*, vol. 33, pp. 103–106, July 1994.

[18] V. Voipio, J. Ollikainen, and P. Vainikainen, "Quarter-wave patch antenna with 35% bandwidth", *IEEE Antennas and Propagation Soc. Int. Symposium*, 1988, pp. 790-793.

Platform Tolerant Planar Inverted F-antenna

Mervi Hirvonen[(1)], Johan C.-E. Sten[(1)], Pekka Pursula[(1)]

[(1)]VTT information Technology
P.O.Box 1202, 02044 VTT Finland
Email: Mervi.Hirvonen@vtt.fi

Abstract
A small and low-cost planar inverted F-antenna solution applicable in many different environments is presented. Attention is paid to the immunity of the antenna input impedance to the platform. A theoretical study of the effects of the platform is presented by analyzing the decay of surface currents caused by vertical and horizontal point sources. The design and measurement results of an example platform tolerant PIFA are reported and discussed.

Keywords: PIFA, finite size ground plane, RFID

1. INTRODUCTION

Different platforms tend to affect the characteristics of the antenna. The radiation pattern, bandwidth and input impedance are typically highly platform dependent. In most applications the platform is fixed and thus, can be considered already in antenna planning. However, there are applications were the platform of the antenna is not fixed. Especially in RFID applications the same antenna type may be attached directly on top of different kinds of objects.

Since in practice metallic platforms or objects near the antenna affect the characteristics the most, the problem of different platforms can be reduced to the effects of different sizes of ground planes. These effects to antenna performance have been studied since the 1950's [1]-[3]. These studies concern vertical monopoles mounted on circular ground. According to these studies a ground plane of wavelengths in size is needed to stabilize the input impedance of the monopole. Also results concerning circular microstrip antennas have been reported [4]. The study shows that a ground plane radius beyond 1.3 times the patch radius is enough to stabilize the input impedance. A similar study concerning PIFA structure has been reported also [5]. In the study the ground plane less than about 0.3 λ in size had an impact on the input impedance.

Traditionally, the effects of the platform are decreased by using as large ground planes as possible in the antenna structure. However, usually in modern applications the overall antenna structure has to be very small compared to the wavelength. Also, the impedance variation due to platform may be stabilized by exploiting broad bandwidth. However, in small antenna structures like PIFAs broad bandwidth usually means large size and more importantly, high profile. On the other hand, for example in RFID applications both small size and low profile are key issues. In this paper small and platform tolerant PIFA applicable in different RFID environments is discussed.

2. THEORY

To study the effects of the ground plane to antenna input impedance surface currents caused by a simple antenna model were analysed. An electronically small antenna brought to radiate at a small distance *h* from conducting surface of infinite extent is considered. The antenna current is decomposed into a vertical (*z*-directed) and a horizontal (*x*-directed) current. By evaluating the magnetic field **H** radiated by the antenna element and by using the relationship $\mathbf{J}_s = \mathbf{n} \times \mathbf{H}$, where **n** is surface normal, the surface current may be presented in spherical coordinates as

$$J_r(r,\varphi) = -\frac{je^{-jkr}(kr-j)}{2\pi r^2}\left[[Il]_z + [Il]_x \frac{h}{r}\cos\varphi\right] \tag{1}$$

$$J_\varphi(r,\varphi) = \frac{je^{-jkr}(kr-j)}{2\pi r^2}[Il]_x \frac{h}{r}\sin\varphi \tag{2}$$

where $[Il]_z$ and $[Il]_x$ are the respective current moments. As can be seen from equations 1 and 2 vertical source induces radial current and horizontal source both radial and circulating currents. The surface current caused by the vertical current moment decays at far distances roughly as $1/r$. On the other hand the surface current caused by the horizontal moment decays roughly as $1/r^2$. As a result dominating vertical current source in the antenna element leads to more sensitive impedance behaviour as a function of the ground plane size and shape than horizontal one.

In Fig. 1 the surface currents of vertical and horizontal point sources of same magnitude located at the same distance from the conducting surface are illustrated. The scale of the contour lines is the same in both cases. As can be seen from Fig. 1 the surface current induced by the horizontal source decays more rapidly than current induced by the vertical source.

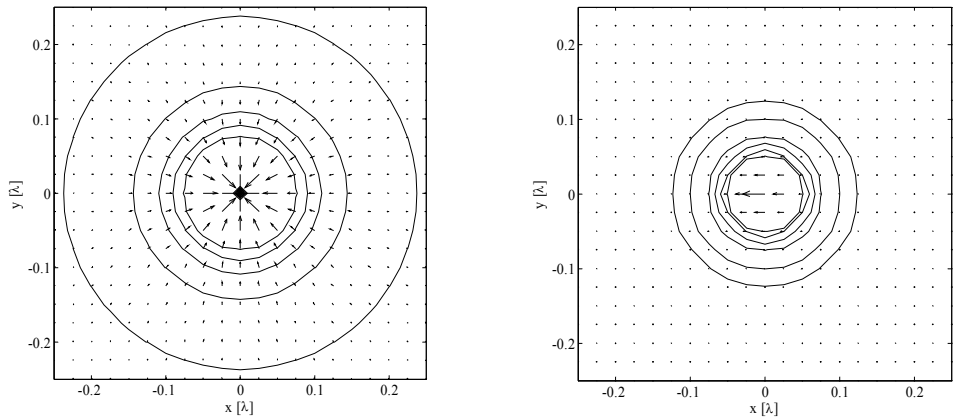

Fig. 1. Surface currents of vertical (left) and horizontal (right) point sources located at height 0.03 λ from the conducting surface.

3. DESING AND MEASUREMENTS

The geometry of the developed platform tolerant planar inverted F-antenna is presented in Fig. 2. At the operation frequency of 869 MHz the antenna is only 3 mm (0.009λ) high and the patch is 45 mm (0.13λ) wide. The patch and the ground plane are square in shape. The antenna is filled with polyethylene substrate in the area under the patch.

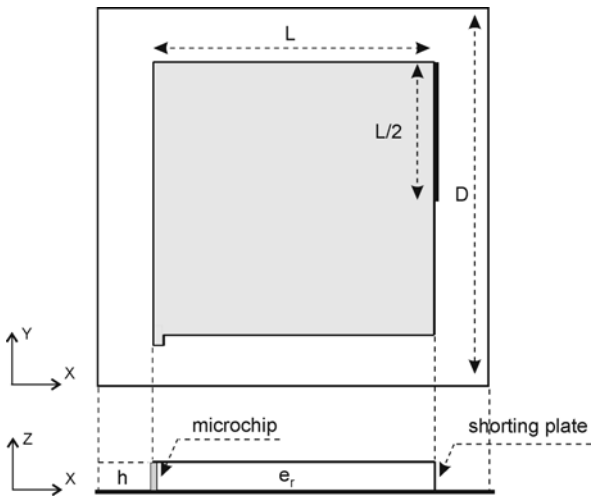

Fig. 2. Antenna design.

The antenna is designed for RFID applications, when the feed of the antenna is a microchip. The microchip feed is placed in one corner of the patch and the shorting plate is half of the width of the of the patch edge. In this case the impedance of the antenna is matched to (7 - j170) Ω. The ground plane is optimised to be as small as possible (59 mm or 0.17λ), while still providing the impedance tolerance to the platform. As the antenna is very low in profile and the main current flows horizontally a rather stable impedance behavior is achieved.

The antenna performance was verified with a scattering measurement technique. A microchip with an input impedance of (7 - j170) Ω was attached as a feed of the antenna. The chip contains a 200 kHz oscillator which modulates the input reactance of the chip, causing a phase modulation of the backscattered signal. The modulation starts if the chip is fed at least with 16 µW of input RF power. As the limiting power is known, the transmitted power P_{tx} needed to wake up the chip is measured as a function of the frequency to determine the antenna bandwidth. In other words, the effective antenna aperture including mismatch is measured. Both the input impedance and the required power level of the chip are similar to that of the RFID chip in the passive long distance multiple access UHF RFID (PALOMAR) system [6].

The performance of the antenna was studied with different platforms. The results of the bandwidth measurements are presented in Fig. 3 and in Table 1. In Fig. 3 all the peaks have been scaled to 0 dB. The bandwidth is defined as the half-power bandwidth of the antenna aperture, which is equivalent to +3 dB in required transmitted power P_{tx}. As seen from Fig. 3 and Table 1, the centre frequency varies only ±1 MHz around the operation frequency of 869 MHz. Also, the bandwidth varies only from 15 to 17 MHz. It is clear that the impedance and bandwidth variance as a function of different platforms is minimal indicating very good tolerance to different platforms.

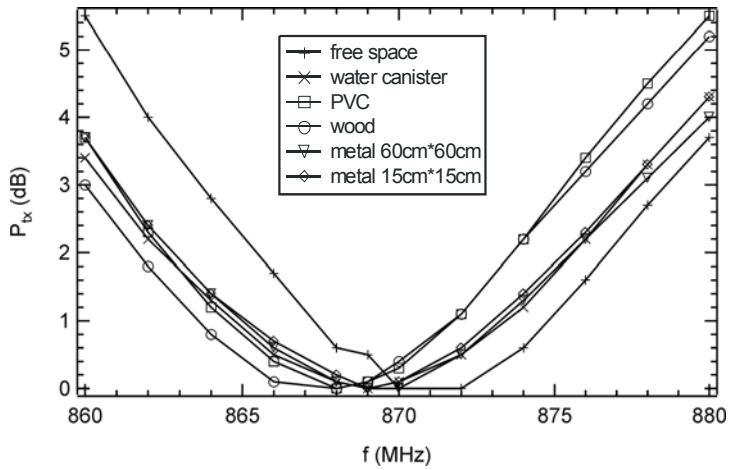

Fig. 3. Results of the bandwidth measurement

Table 1. Measured centre frequencies and bandwidths

platform	centre frequency [MHz]	half-power bandwidth [MHz]
free-space	870	15
metal 150x150 mm	869	17
metal 600x600 mm	869	17
wood	868	16
PVC plastic	868	15
water canister	869	17

4. CONCLUSIONS

A compact and low-cost platform tolerant PIFA structure has been developed. It has been found that surface currents induced by horizontal current sources decay more rapidly than those induced by vertical sources. In the developed structure main current flow is horizontal, which has lead to tolerant impedance behaviour. The developed PIFA is applicable in different RFID environments and may be mounted directly on different materials, for example on metal, wood or plastic.

Acknowledgments

This work has been supported by Tekes, The National Technology Agency of Finland.

References

[1] A. S. Meier and W. P. Summers, “Measured impedance of vertical antennas over finite ground planes,” Proc. IEEE, vol. 37, pp. 609-616, June 1949.
[2] K. H. Awadalla and T. S. M Maclean, “Input impedance of a monopole antenna at the center of a finite ground plane,” IEEE Trans. Antennas Propagat., vol AP-26, no. 2, pp. 244-248, Mar. 1978.
[3] J. H. Richmond, “Monopole antenna on circular disk,” IEEE Trans. Antennas Propagat. vol. AP-32, no. 12, pp.1282-1287, Dec. 1984
[4] K. Antoszkiewicz and L. Shafai, “Impedance Characteristics of Circular Microstrip Patches,” IEEE Trans. Antennas Propagat., vol AP-38, no. 6, pp. 942-946, June. 1990.
[5] M.–C. Huynh and W. Stutzman, “Ground plane effects on planar inverted-F antenna (PIFA) performance,” IEE Proc. –Microw. Antennas Propag., vol. 150, no. 4, August 2003.
[6] The Palomar project: 'Passive Long Distance Multiple Access UHF RFID system', European Commission, Public Report, Project Number IST1999-10339, Nov. 2002.

WAVEGUIDING PROPERTIES OF GROUNDED DIPOLE LINE ARRAYS

Ari Viitanen[(1)], **Sergei Tretyakov**[(2)]

[(1)] ***Electromagnetics Laboratory,***
Department of Electrical and Communications Engineering,
Helsinki University of Technology, P.O. Box 3000, FI-02015 HUT, Finland
Email: ari.viitanen@hut.fi

[(2)] ***Radio Laboratory/SMARAD,***
Department of Electrical and Communications Engineering,
Helsinki University of Technology, P.O. Box 3000, FI-02015 HUT, Finland
Email: sergei.tretyakov@hut.fi

Abstract
Periodical arrangements of longitudinally directed dipole particles over an infinite metal plane are considered. The dipole particles are along a straight line and are close to each other, forming a dense dipole array construction. These kind of structures, also called metawaveguides, are recently intensively studied in optical and in mm-wave frequency ranges because these systems can be used as transmission lines with exotic and controllable properties. The dipole inclusions may be plasmon resonant particles (optics) or small loaded wire antennas (microwaves). In this study an analytical solution for waves propagating along the infinite dipole line structure is presented.

Keywords: waveguides, dipole arrays, metawaveguides

1. INTRODUCTION

Properties of periodical structures such as photonic crystals, have been recently intensively studied because of new interesting phenomena and possible new applications in microwave engineering. Linear periodical arrangements of small inhomogeneities have been studied experimentally with interesting resonance effects in [1, 2]. In [3, 4] an analytical approach for such structures has been developed and a dipole line arrays are theoretically considered in [5, 6]. It is well known that strong spatial dispersion effects occur when the wavelength of the electromagnetic waves propagating in a periodical structure is comparable to the period. At certain frequency ranges there can be stop bands typically for photonic band gap structures. Also planar periodical arrangements of inclusions are of interest for special applications and for easy and low cost manufacturing techniques.
Usually, periodical structures are studied using numerical techniques which makes it difficult to understand the physical phenomena and find conditions for realization and control of desired effects. In this study we consider a simple periodic system, periodically positioned dipole inclusions over a conducting plane for studying wave propagation characteristics with analytical methods. The solution depends on the properties of the array elements, the geometry and the frequency. In this theoretical study we assume that every inclusion can be modeled as an electric dipole, that is, the geometrical size of every separate inclusion is small compared to the wavelength. To control their properties, the dipoles can be loaded by passive loads. These can be capasitive or inductive bulk loads, or resonant circuits. This artificial waveguiding structure that we introduce and theoretically study here can be considered as an artificial metawaveguide. Although the particles forming the array are modeled as electric dipoles, it is assummed that they can exhibit strong and resonant electromagnetic response. Especially, the effects of particle frequency resonances, for example using plasmon resonant particles in optical region, leads to very unusual and interesting electromagnetic properties of the structure.

2. EIGENVALUE EQUATION

To find the eigenfield solutions we need to study field interactions between dipoles in a grounded line array. The polarizability of a small dipole particle is denoted by α. Dipoles are longitudinally directed, i.e., in the z direction, along a straight line as shown in Figure 1.

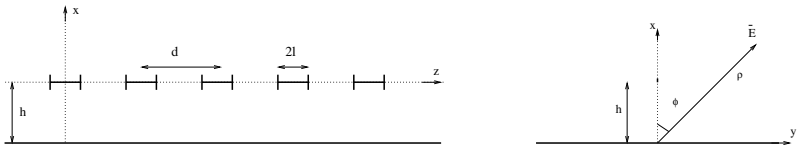

Figure 1: Loaded dipole line array over metal plane

Considering as an example the microwave and millimeter wave realizations, the particles can be short metal wire or strip dipoles. For example, for a short unloaded wire dipole of length $2l$ and wire radius r_o, the real part of the inverse of the polarizability is $\frac{\ln(2l/r_o)}{\epsilon_o \pi l^3}$ and the corresponding imaginary part is $\frac{k^3}{6\pi\epsilon_o}$ [3, 4]. The distance between the dipole particles is denoted by d. In this study it is assumed that the structure is in free space, although the theory is not restricted to the free space background. For the dipole at position $z = 0$, the induced dipole moment (also in the z direction) is

$$\mathbf{p}(0) = \alpha \mathbf{E}_{\text{loc}} \tag{1}$$

where $\mathbf{E}_{\text{loc}}$ is the local field created by the external field $\mathbf{E}_{\text{ext}}$ and all the other dipole particles:

$$\mathbf{E}_{\text{loc}} = \mathbf{E}_{\text{ext}} + \sum_{n=-\infty, n\neq 0}^{\infty} \beta(nd)\mathbf{p}(nd) \tag{2}$$

$\beta(nd)$ is the interaction constant which takes into account the influence of the other dipoles. It consists of the dipole line part and the image dipole line part

$$\begin{aligned}\beta(nd) = {} & \frac{1}{2\pi\epsilon_o}\left(\frac{1}{(|n|d)^3} + \frac{jk}{(nd)^2}\right)e^{-j|n|kd} - \frac{1}{4\pi\epsilon_o}\left[\frac{k^2}{2h} - \frac{jk}{(2h)^2} - \frac{1}{(2h)^3}\right]e^{-jk2h} \\ & -\frac{1}{4\pi\epsilon_o}\left[\frac{k^2(2h)^2}{[(2h)^2+(nd)^2]^{3/2}} + \left(\frac{3(nd)^2}{(2h)^2+(nd)^2} - 1\right)\times \right. \\ & \left.\left(\frac{1}{[(2h)^2+(nd)^2]^{3/2}} + \frac{jk}{(2h)^2+(nd)^2}\right)\right]e^{-jk\sqrt{(2h)^2+(nd)^2}}\end{aligned} \tag{3}$$

Assuming that the external field $\mathbf{E}_{\text{ext}}$ is a plane wave, or there is no external field, and knowing that the structure is periodical in the z direction we can write, according to the Floquet theorem,

$$\mathbf{p}(nd) = e^{-jqnd}\mathbf{p}(0) \tag{4}$$

where q is the propagation factor along the line structure. Eliminating the fields in the above equations (1) - (4), one obtains the eigenvalue equation for the propagation factor q:

$$\begin{aligned}\frac{1}{\alpha} = {} & \frac{1}{4\pi\epsilon_o}\left[\frac{1}{(2h)^3} + \frac{jk}{(2h)^2} - \frac{k^2}{2h}\right]e^{-jk2h} \\ & +\frac{1}{4\pi\epsilon_o}\sum_{n=-\infty, n\neq 0}^{\infty}\left(2\left[\frac{1}{(|n|d)^3} + \frac{jk}{(nd)^2}\right]e^{-jk|n|d}\right. \\ & -\left[\frac{k^2(2h)^2}{[(2h)^2+(nd)^2]^{3/2}} + \left(\frac{3(nd)^2}{(2h)^2+(nd)^2} - 1\right)\right. \\ & \left.\left.\left(\frac{1}{[(2h)^2+(nd)^2]^{3/2}} + \frac{jk}{(2h)^2+(nd)^2}\right)\right]e^{-jk\sqrt{(2h)^2+(nd)^2}}\right)e^{-jqnd}\end{aligned} \tag{5}$$

This complex valued equation should be solved separately for the real and imaginary parts. The first and the last terms inside the sum cancels each other with large index values n making the summation to converge fast. The imaginary part of the eigenvalue equation is related to the power conservation, as considered in [5]. The imaginary part gives us the guided-wave and leaky-wave regions, and the real part of the eigenvalue equation gives us finally the dispersion relation.

3. DISPERSION RELATION

For lossless particles the imaginary part of the polarizability factor and the interaction constant are related through the power conservation. That relation has a simple physical explanation: the power received by inclusions is radiated by the line array structure. Actually, the real part of the eigenvalue equation gives us the dispersion relation which is evaluated numerically. The result is shown in Figure 2 with one chosen geometry and varying bulk load capasitance.

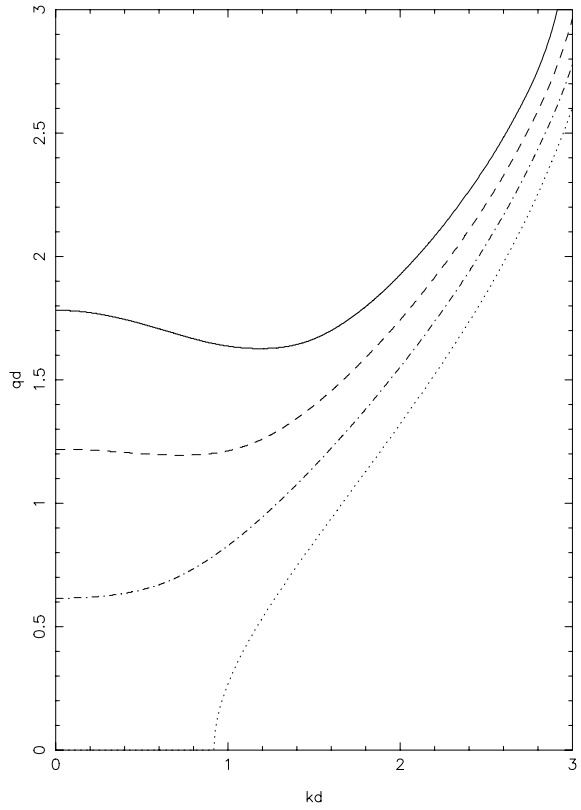

Figure 2: Dispersion curves with different values of $\pi\epsilon_o d^3 \mathrm{Re}\{1/\alpha\}$: solid line (0.0), dashed line (0.5), dotted-dash line (1.0), dotted line (1.5) and $d/h = 2$.

These curves show dispersion curves in case of a constant $\mathrm{Re}\{1/\alpha\}$. There are bandgaps which are typical for periodic structures. When considering an unloaded short metal wire dipole, the corresponding value of $\mathrm{Re}\{1/\alpha\}$ is very large, and there is no solution for guided waves. To achieve guided wave solutions, the wire dipoles must be loaded. It is found that guided waves exist at low frequencies when this value is small enough. Also the results show that there are large qd values even at low frequency and in a wide frequency band, thus making strong spatial variations in fields along the line array structure. These high qd values are obtained by using capacitive loads. In a radiation region the construction supports leaky waves. The leakage of the power can be controlled by the height of the dipole line array from the ground plane. By changing loading, and also changing the height of the line array it is possible to tune the optimum guided wave performance. With a very small height the radiated power is small and the structure is like a quasi-TEM transmission line.

4. CONCLUSIONS

Conditions for guided wave solutions with dispersion curves of a line of dipole particles over a metal plane are presented. Microstrip line with cut and loaded metal strips would be one practical realization of this kind of slow-wave structure. In a given example, bulk capasitive load is used which results in wide band waveguiding properties. Instead, using resonant loading, for example series or parallel resonant circuits as loads in millimeter wave region, the propagation characteristics change dramatically near the inclusion resonance frequency. In optical region, the dipole particles could be plasmon resonant particles. Such structures can offer potential applications in imaging and detection techniques and are intensively studied nowadays. In certain frequency regions the introduced structure supports backward waves as seen in Figure 2 (solid line). Backward waves exist in periodical structures with period comparable to wavelength and in left-handed structures. The known realization of a left-handed waveguiding structure at low frequencies consists of a series of lumped LC cells [7]. In this study introduced construction offers an alternative realization of the left-handed structure.

References

[1] M.A.G. Laso, M.J. Erro, D. Benito, M.J. Garde, T. Lopetegi, F. Falcone, M. Sorolla, Analysis and design of 1-D photonic bandgap microstrip structures using a fiber grating model, *Microw. Optical Technol. Lett.,* vol. 22, no. 4, pp. 223-226, 1999.

[2] F. Falcone, T. Lopetegi, M. Sorolla, 1-D and 2-D photonic bandgap structures, *Microw. Optical Technol. Lett.,* vol. 22, no. 6, pp. 411-412, 1999.

[3] S.I. Maslovski, S.A. Tretyakov, Full-wave interaction field in two-dimensional arrays of dipole scatterers, *Int. J. Electron. Commun. (AEÜ)*, vol. 53, no. 3, pp. 135-139, 1999.

[4] S. A. Tretyakov, A. J. Viitanen, S. I. Maslovski, I. E. Saarela, Impedance boundary conditions for regular dense arrays of dipole scatterers. *IEEE Trans. Antennas and Propagation,* vol. 51, no. 8, pp. 2073-2078, August 2003.

[5] S. A. Tretyakov, A.J. Viitanen, Line of periodically arranged passive dipole scatterers. *Electrical Engineering, Archiv für Elektrotechnik,* vol. 82, no. 6, pp. 353-361, November 2000.

[6] A.D. Yaghjian, Scattering-matrix analysis of linear periodic arrays. *IEEE Trans. Antennas and Propagation,* vol. 50, no. 8, pp. 1050-1064, August 2002.

[7] C. Caloz, T. Itoh, Transmission line approach of left-handed (LH) materials and microstrip implementation of an artificial LH transmission line, *IEEE Trans. Antennas and Propagation,* vol. 52, no. 5, pp. 1159-1166, May 2004.

Transmission Line Model of a Patch Aantenna Loaded With Dispersive Double Negative Material

Murat Emre Ermutlu [(1)] **Sergei Tretyakov** [(2)]

[(1)] ***Affiliation***
Radio Laboratory, Helsinki University of Technology, P.O. Box 3000, FIN-02015 HUT Finland
Nokia Networks, P.O. Box 301, FIN-00045, Finland
Email: murat.ermutlu@hut. and murat.ermutlu@nokia.com

[(2)] ***Affiliation***
Radio Laboratory, Helsinki University of Technology, P.O. Box 3000, FIN-02015 HUT Finland
Email: sergei.tretyakov@hut.

Abstract
In this work a transmission line model for a patch antenna where a half of the patch is loaded with a dispersive double negative material is used to show its resonance characteristics. Resonant properties of the patch antenna are compared when the material properties of the loaded part is a dispersive material and $\epsilon = -\epsilon_0$, $\mu = -\mu_0$ with the unloaded case. Two important properties of the antenna, return loss and efficiency are numerically calculated.

Keywords: patch antenna, metamaterials, double-negative materials, Veselago media

1. INTRODUCTION

After Veselago theoretically investigated plane wave propagation in media whose material parameters, permittivity and permeability, are negative [1] and Smith *et al.* [2] constructed such a composite medium for microwave regime, double-negative media have been a subject of much research. It has been suggested that these media could be used to built small resonators and antennas [3, 4]. This is done by having two media in a resonator where one of the medium is a metamaterial having negative permittivity and permeability compared with the first medium. In this configuration they are perfectly matched regardless of the frequency for lossless media. This idea has been questioned by Tretyakov *et al.* [5] and Shen *et al.* [6] since a double negative material must be dispersive.

Here we study a patch antenna as a resonator to show the antenna performance when the antenna is partially filled with a double negative material like suggested in [3, 4]. But for the material parameters, dispersive models are used for permittivity and permeability, like suggested in [7].

2. TRANSMISSION LINE FORMULATION

The transmission line model of a patch antenna which is partially filled with air and partially with a dispersive medium is shown in Fig. 1, where Y_0 and Y_w are the characteristic admittances, β and β_0 are the phase constants, $l_0 + l_1 = l$ is the length of the patch antenna, and Y_r is the load admittance. In the transmission line model $Y_r = G_r + jB_r$ is thought of as two load admittances connected to each other in parallel via a microstrip transmission line. Here we neglect the imaginary part of the admittance and assume that both sides of the transmission line are loaded by the same conductance G_r which is given in many antenna books, e.g. [8]:

$$G_r = \frac{1}{90}\left(\frac{l}{\lambda_0}\right)^2 \tag{1}$$

for $l \ll \lambda_0$ and for $h \ll \lambda_0$.

The input admittance Y_{in} of the structure can be written as

$$Y_{in} = Y_r + Y_0 \frac{Y_{in1} + jY_0 \tan(\beta_0 l_0)}{Y_0 + jY_{in1} \tan(\beta_0 l_0)}, \tag{2}$$

where the input admittance of the first part

$$Y_{in1} = Y_w \frac{Y_r + jY_w \tan(\beta l_1)}{Y_w + jY_r \tan(\beta l_1)}, \tag{3}$$

the phase constants of the transmission lines $\beta_0 = \omega\sqrt{\epsilon_0}\sqrt{\mu_0}$ and $\beta = \omega\sqrt{\epsilon}\sqrt{\mu}$, the characteristic admittance of the transmission lines $Y_o = \frac{l_0}{h}\frac{\sqrt{\epsilon_0}}{\sqrt{\mu_0}}$ and $Y_w = \frac{l_1}{h}\frac{\sqrt{\epsilon}}{\sqrt{\mu}}$, the radian frequency $\omega = 2\pi f$, the frequency $f = c/\lambda_0$, λ_0 is the wavelength, and c is the speed of light ($c = 1/\sqrt{\epsilon_0\mu_0}$).

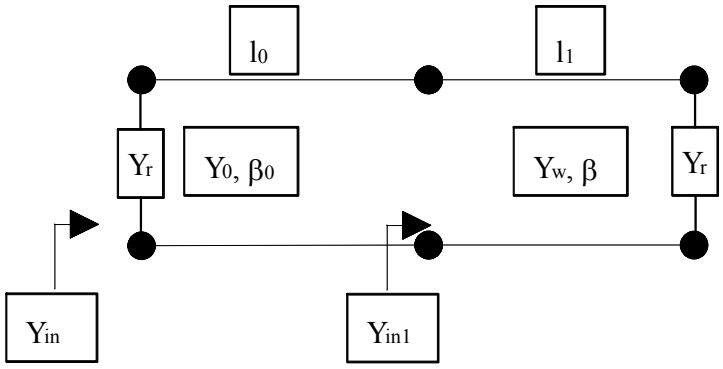

Figure 1: Transmission line model with two media.

3. DISPERSIVE MEDIA

For dispersive media the following models are used for the permittivity and permeability (e.g. [7]):

$$\epsilon = \epsilon_0 \left(1 + \frac{\omega_p^2}{\omega_{o\epsilon}^2 - \omega^2 + j\omega\gamma}\right) \tag{4}$$

$$\mu = \mu_0 \left(1 + \frac{A\omega^2}{\omega_{o\mu}^2 - \omega^2 + j\omega\gamma}\right) \tag{5}$$

The $\omega_{o\epsilon}$ and $\omega_{0\mu}$ are the resonant frequencies of the permittivity and permeability, A is the magnitude factor, γ is the loss factor, and ω_p is the *plasma frequency*. The total length of the transmission line is set to $\lambda/2$ at 1 GHz. In order to use the idea of an ideal resonator at 1 GHz, the material parameters are set to *negative* values of the transmission line itself. In order to have *negative* material parameters, the resonant frequencies of the permittivity and permeability $\omega_{o\epsilon}$ and $\omega_{o\mu}$ are set to 0.7 GHz, which is less than the resonant frequency of the antenna without any material. Then proper *plasma frequency* ω_p and the magnitude factor A have been found in order to get the *negative* material values at 1 GHz. For $\epsilon = \epsilon_0\,(-1 - j0.025)$ and $\mu = \mu_0\,(-1 - j0.0125)$ the plasma frequency ω_p is found to be $\sqrt{2.082}\omega_{0e}$, and the magnitude factor is $A = 1.02005$.

4. NUMERICAL RESULTS

It is assumed that the antenna is fed with a transmission line that is perfectly matched to the antenna at 1 GHz ($Z = 174\ \Omega$). The reflection coefficients of the antenna in dB are calculated for when $\epsilon = \epsilon_0\,(1 - j0.025)$ and $\mu = \mu_0\,(1 - j0.0125)$, $\epsilon = -\epsilon_0\,(1 + j0.025)$ and $\mu = -\mu_0\,(1 + j0.0125)$ and for the dispersive medium. The length of the both media are same $l_0 = l_1 = \lambda/4$.

As seen from Fig. 2, the dispersive medium does not improve the antenna matching in wide ranges of frequency. It has even narrower band than the air-filled antenna at 1 GHz. On the other hand, if we set the loading medium parameters to $-\epsilon_0$ and $-\mu_0$, it matches the antenna at every frequency, so that it has a very large bandwidth. The antenna filled by the dispersive medium has many resonances around 07 GHz. Also the resonant frequency of the antenna is reduced due to a dielectric and magnetic loading.

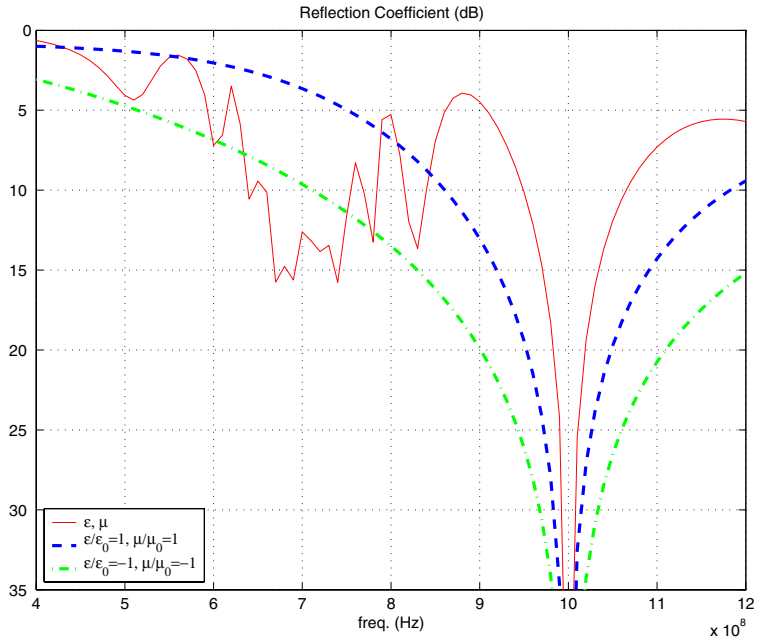

Figure 2: Reflection coefficient of the patch antenna partially filled by a dispersive medium (solid), $\epsilon = \epsilon_0\,(1 - j0.025)$, $\mu = \mu_0\,(1 - +j0.0125)$ (dashed), and $\epsilon = -\epsilon_0\,(1 + 0.025)$, $\mu = -\mu_0\,(1 + j0.0125)$ (dot dashed) for $l_0 = l_1 = \lambda/4$.

5. ANTENNA EFFICIENCY

Another important antenna performance parameter is the antenna efficiency. Antenna efficiency is defined as the ratio of the radiated power to the input power. One of the antenna efficiency measurement technique is the Wheeler cap method [11]. This method has been discussed recently due the increase in the design of small antennas in radio communications [12, 13, 14]. In the Wheeler cap method, the input impedance of the antenna is measured when the antenna is in the normal working conditions and enclosed with a conducting sphere. When the antenna is enclosed, the radiation conductance is eliminated ($Y_r = 0$) and only the losses of the antenna could be seen when Y_{in} is calculated (G_{in}). So the efficiency of the antenna can be calculated as

$$\eta = 1 - \frac{R_{cap}}{R_{nocap}}. \tag{6}$$

The numerical solution of the antenna efficiency is given in Fig. 3, where $Y_r = 5 \quad \times 10^{-5}$ for the dispersive medium, air and $\epsilon = -\epsilon_0$, $\mu = -\mu_0$ when $l_0 = l_1 = 0.25\lambda$. It is clearly seen that the antenna with a dispersive medium has a good efficiency at 1 GHz, but it is not working as efficiently at other frequencies.

References

[1] V.G. Veselago, "The electrodynamics of substances with simultaneously negative values of ϵ and μ", *Soviet Physics Uspekhi,* vol. 10, pp. 509-514, 1968. (originally in Russian in *Uspekhi Fizicheskikh Nauk,* vol. 92, no. 3, pp. 517-526, July 1967).

[2] R.A. Shelby, D.R. Smith and S. Schultz, "Experimental verification of a negative index of refraction", *Science*, vol. 292, pp. 77-79, 2001.

[3] N. Engheta "An Idea for Thin Subwavelength Cavity Resonators Using Metamaterials with Negative Permittivity and Permeability", *IEEE Antennas and Wireless Propagation Letters*, vol. 1, pp. 10-13, 2002.

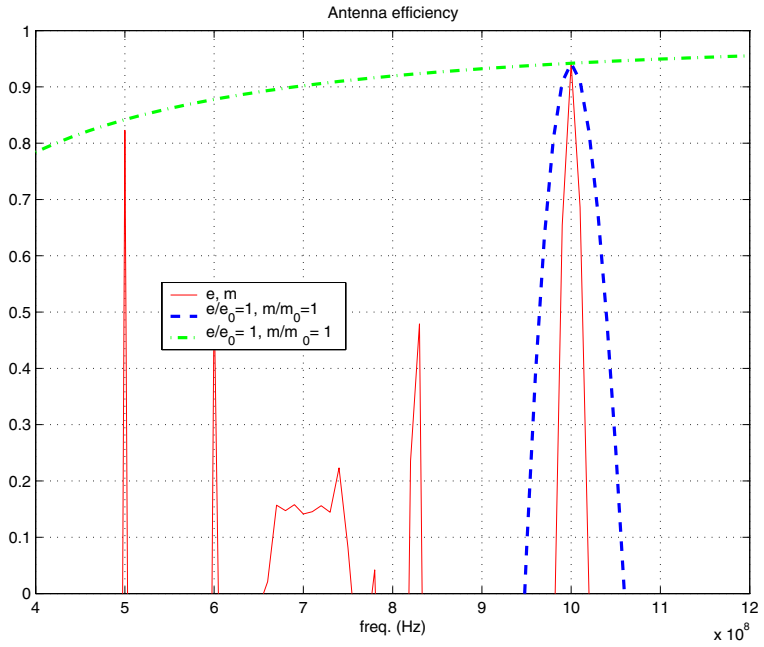

Figure 3: Antenna efficiency for the dispersive medium (solid), $\epsilon = \epsilon_0 \ (1 - j0.025)$, $\mu = \mu_0 \, (1 - + j0.0125)$ (dashed), and $\epsilon = -\epsilon_0 \, (1 + 0.025)$, $\mu = -\mu_0 \, (1 + j0.0125)$ (dot dashed) when $l_0 = l_1 = 0.25\lambda$.

[4] S.F. Mahmoud, "New Miniaturized Annular Ring Patch Resonator Partially Loaded by a Metamaterial Ring With Negative Permeability and Pemittivity", *IEEE Antennas and Wireless Propagation Letters*, vol. 3, pp. 19-22, 2004.

[5] S.A. Tretyakov, S.I. Maslovski, I.S. Nefedov, and M.K. Kärkkäinen, "Evanescent modes stored in cavity resonators with backward-wave slabs," *Microwave and Optical Technology Letters,* vol. 38, no. 2, pp. 153-157, 2003.

[6] L. Shen, S. He, and S. Xiao, "Stability and quality factor of a one-dimensional subwavelength cavity resonator containing a left-handed material", *Phys. Rev. B*, vol. 69, pp. 115111(1-6), 2004.

[7] S. Tretyakov, "Field energy density in artificial microwave materials with negative parameters", submitted to *Phys. Rev. E,* preprint http://arxiv.org/pdf/cond-mat/0409351.

[8] C.A. Balanis, *Antenna theory: Analysis and design*, John Wiley & Sons, Inc., 2nd ed. 1997.

[9] S.A. Tretyakov, I.S. Nefedov, C.R. Simovski, and S.I. Maslovski, "Modelling and microwave properties of artificial materials with negative parameters", in *Advances in electromagnetics of complex media and meta-materials*, S. Zouhdi, A. Sihvola and M. Arsalane (eds), NATO Series II, vol. 89, Kluwer Academic Publishers, pp. 99-122, 2002.

[10] S.A. Tretyakov, *Analytical modelling in applied electromagnetics*, Artech House, Boston–London, 2003.

[11] H.A. Wheeler, "The radian sphere around a small antenna", *Proc. IRE,* pp. 1325-1331, August 1959.

[12] E. H. Newman, P. Bohley, and C.H. Walter, "Two methods for the measurement of antenna effi - ciency", *IEEE Trans. Antennas and Propagation,* vol. AP-23, pp. 457-461, July 1975.

[13] D. M. Pozar and B. Kaufman, "Comparison of three methods for the measurement of printed antenna efficiency", *IEEE Trans. Antennas and Propagation,* vol. AP-36, pp. 136-139, Jan. 1988.

[14] M. Geissler, O. Litschke, D. Heberling, P. Waldow, and I. Wolff, "An improved method for measuring the radiation efficiency of mobile devices", *IEEE Antennas and Propagation Society International Symposium,* vol. 4, pp. 743-746, 22-27 June 2003.

Session 3a:
Electromagnetic Theory and Materials

Frequency- and tieme-domain formulations of an impedance-boundary condition in the finite-integration technique

Riku M. Mäkinen[(1)], Herbert De Gersem[(1)], Thomas Weiland[(1)]

[(1)]Institut für Theorie Elektromagnetischer Felder, Technische Universität Darmstadt
Schlossgartenstrasse 8, D-64289 Darmstadt, Deutschland
Email: maekinen@temf.tu-darmstadt.de

Abstract
Frequency- and time-domain formulations of a standard impedance-boundary condition (SIBC) are presented in the context of the finite-integration technique (FIT). The SIBC is formulated as a non-linear passive lumped element connected in parallel to the cell, alleviating the spatial and temporal discretization errors present in typical finite-difference time-domain (FDTD) implementations of first-order SIBCs. The spatial discretization scheme of the formulation is shown to be energy conserving. In time-domain, a recursive implementation of the convolution integral related to the nonlinear impedance is used. The formulations are validated for a three-dimensional (3-D) case.

Keywords: Finite-integration technique, first-order impedance-boundary condition, lumped parameter element

1. INTRODUCTION

Surface-impedance concept [1] is used to simplify electromagnetic field simulations, e.g., by avoiding calculation of fields inside conductors. A typical application for a standard impedance boundary condition (SIBC) is the modeling of the skin effect in metals without resorting to a large number of small cells in order to capture the rapid field variation inside the metal. In this work, a first-order SIBC is formulated as a non-linear passive lumped element and implemented in frequency- and time domain in the context of the finite-integration technique (FIT) [2]. The formulation alleviates the spatial and temporal discretization error between the magnetic and electric fields, typically ignored in the implementation of a SIBC. In frequency domain, the SIBC is included in the curl-curl equation for the electric field (a driven problem). Based on the energy-conservation properties of the FIT [3], the formulation is shown to be consistent. In time domain, the impedance function is approximated in the frequency domain by a series of first-order rational functions allowing a recursive implementation of the convolution integral in time domain [4].

1.2. Notation and Some Properties of FIT

The FI technique is based on discretization of Maxwell's equations in integral form on two staggered grids, the primary grid G and the dual grid $\tilde{G}$ [2]. The edges, facets and volumes on G and $\tilde{G}$ are denoted with L_i, S_i, V_i and $\tilde{L}_i$, $\tilde{S}_i$, $\tilde{V}_i$, respectively. The FIT state variables (electric and magnetic voltages and fluxes), current and charge are defined as [2]

$$\begin{aligned} \hat{e}_i &= \int_{L_i} \mathbf{E}\cdot d\mathbf{s}, \quad \hat{\tilde{d}}_i = \int_{\tilde{A}_i} \mathbf{D}\cdot d\mathbf{A}, \quad q_i = \int_{\tilde{V}_i} \rho dV, \\ \hat{h}_i &= \int_{\tilde{L}_i} \mathbf{H}\cdot d\mathbf{s}, \quad \hat{\tilde{b}}_i = \int_{A_i} \mathbf{B}\cdot d\mathbf{A}, \quad \hat{\tilde{j}}_i = \int_{\tilde{A}_i} \mathbf{J}\cdot d\mathbf{A}. \end{aligned} \tag{1}$$

The Maxwell's grid equations in the vector form are given by [2]

$$\tilde{\mathbf{C}}\hat{\mathbf{h}} = d/dt\,\hat{\tilde{\mathbf{d}}} + \hat{\tilde{\mathbf{j}}}, \quad \mathbf{C}\hat{\mathbf{e}} = -d/dt\,\hat{\tilde{\mathbf{b}}}, \quad \mathbf{S}\hat{\tilde{\mathbf{b}}} = 0, \quad \tilde{\mathbf{S}}\hat{\tilde{\mathbf{d}}} = \mathbf{q}, \tag{2}$$

where the discrete curl matrix $\mathbf{C}$ relates voltages on primary edges to fluxes on primary facets, and the discrete divergence matrix $\mathbf{S}$ relates fluxes on primary facets to charges in primary volumes. The dual curl $\tilde{\mathbf{C}}$ and divergence $\tilde{\mathbf{S}}$ matrices act analogously on the dual grid. The discrete operators satisfy fundamental topological relations $\tilde{\mathbf{C}} = \mathbf{C}^T$, $\mathbf{SC} = 0$, $\tilde{\mathbf{S}}\tilde{\mathbf{C}} = 0$ [2]. The constitutive relations are given by

$$\hat{\tilde{\mathbf{d}}} = \mathbf{M}_\varepsilon \hat{\mathbf{e}}, \quad \hat{\mathbf{h}} = \mathbf{M}_\nu \hat{\tilde{\mathbf{b}}}, \quad \hat{\tilde{\mathbf{j}}}_e = \mathbf{M}_\kappa \hat{\mathbf{e}}, \tag{3}$$

where the generalized material operators $\mathbf{M}_\varepsilon$ (permittivity), $\mathbf{M}_\nu$ (inverse of permeability) and $\mathbf{M}_\kappa$ (electrical conductivity) introduce metric information into the system [2]. In an orthogonal grid system, where the primary (dual) edges are normal to the dual (primary) facets, the material matrices $\mathbf{M}_\varepsilon$, $\mathbf{M}_\nu$ and $\mathbf{M}_\kappa$ are diagonal. For positive material parameters, the material matrices are positive semidefinite.

2. LUMPED-ELEMENT FORMULATION OF A SIBC

A first-order SIBC relates the tangential field components at the boundary [1]. For FIT state variables,

$$\mathbf{n}\times\hat{\mathbf{e}} = Z(L_i / \tilde{L}'_j)\mathbf{n}\times\mathbf{n}\times\hat{\mathbf{h}} = Z(L_i / \tilde{L}'_j)\mathbf{n}\times\hat{\tilde{\mathbf{j}}}_{BC} \tag{4}$$

where $\mathbf{n}$ is outward pointing normal, Z is the scalar surface impedance scaled by appropriate edge lengths, and $\hat{\tilde{\mathbf{j}}}_{BC}$ is the surface current. Consider the PEC boundary in Fig. 1. (a). Ampere's law over $\tilde{A}_i$ gives

$$\tilde{\mathbf{C}}\hat{\mathbf{h}}\Big|_{\tilde{A}_i,PEC} = -\hat{h}_{x_1} + \hat{h}_{z_1} - \hat{h}_{z_2} = j\omega\mathbf{M}_{\varepsilon,ii}\hat{e}_y + \mathbf{M}_{\kappa,ii}\hat{e}_y . \tag{5}$$

A virtual layer shown in Fig. 1. (b) carrying the current due to the SIBC is then added. The magnetic field $\hat{h}'_{x2}$ is calculated using (4), resulting in $-\hat{h}'_{x2} = +\hat{\tilde{j}}_{BC,y} = [Z(L_i / \tilde{L}'_j)]^{-1}\hat{e}_y$. The current through $\tilde{A}_i$ is now

$$\tilde{\mathbf{C}}\hat{\mathbf{h}}\Big|_{\tilde{A}_i} = -\hat{h}_{x_1} + \hat{h}_{z_1} - \hat{h}_{z_2} + \hat{h}'_{x_2} = \tilde{\mathbf{C}}\hat{\mathbf{h}}\Big|_{\tilde{A}_i,PEC} - [Z(L_i / \tilde{L}_j)]^{-1}\hat{e}_y = j\omega\mathbf{M}_{\varepsilon,ii}\hat{e}_y + \mathbf{M}_{\kappa,ii}\hat{e}_y . \tag{6}$$

The current term due to the SIBC depends on the analytical impedance Z (scaled by the edge lengths) and the tangential electric field at the boundary. Moving the SIBC current term in (6) to the right-hand side gives Ampere's law for the PEC condition with an additional lumped SIBC current term added to the total current. Note that for each tangential electric field at the boundary there is exactly one SIBC current term in the direction of the electric field. It is therefore possible to construct a diagonal impedance matrix.

3. SIBC IN FREQUENCY DOMAIN

Maxwell's curl equations can be combined to result in the so-called curl-curl equation for the electric field, given in the time-harmonic case by

$$\tilde{\mathbf{C}}\mathbf{M}_\nu\mathbf{C}\hat{\mathbf{e}} - \omega^2\mathbf{M}_\varepsilon\hat{\mathbf{e}} + j\omega\mathbf{M}_\kappa\hat{\mathbf{e}} + j\omega\mathbf{Q}^T\mathbf{Z}^{-1}\mathbf{Q}\hat{\mathbf{e}} = -j\omega\hat{\tilde{\mathbf{j}}}_s \tag{7}$$

where $\hat{\tilde{\mathbf{j}}}_s$ is the excitation current and $\hat{\tilde{\mathbf{j}}}_{BC} = \mathbf{Q}^T\mathbf{Z}^{-1}\mathbf{Q}\hat{\mathbf{e}}$ is the current due to the SIBC. The selector $\mathbf{Q}$ selects the primary grid edges at the SIBC boundary, $\mathbf{Z}$ is the diagonal surface impedance matrix (including the scaling by appropriate primary and dual edge lengths), and $\mathbf{Q}^T$ places the current due to the surface impedance at appropriate dual facets.

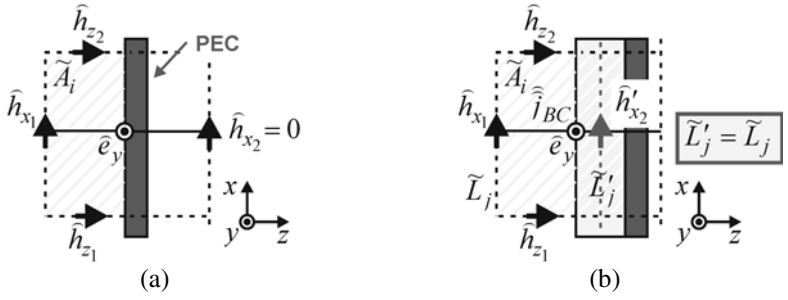

Fig. 1. Derivation of the SIBC. (a) PEC boundary. (b) Virtual layer supporting SIBC current.

To investigate the consistency of a time-harmonic formulation, it suffices to consider the conservation of energy of the spatial discretization scheme. In a loss-free case, the system must be energy conserving and in a lossy case the losses must be positive, i.e., the matrix $\mathbf{M}_\kappa$ must be positive semidefinite. To this end, let us first consider a homogeneous loss-free eigenvalue problem. Using the duality of the curl operators ($\tilde{\mathbf{C}} = \mathbf{C}^T$) and assuming positive definite material matrices $\mathbf{M}_\varepsilon = \mathbf{M}_\varepsilon^{1/2}\mathbf{M}_\varepsilon^{1/2}$ and $\mathbf{M}_\nu = \mathbf{M}_\nu^{1/2}\mathbf{M}_\nu^{1/2}$, the system can be symmetrized by introducing a normalized the electric field $\hat{\mathbf{e}}' = \mathbf{M}_\varepsilon^{1/2}\hat{\mathbf{e}}$, resulting in [3]

$$(\mathbf{M}_\nu^{1/2}\mathbf{C}\mathbf{M}_\varepsilon^{-1/2})^T(\mathbf{M}_\nu^{1/2}\mathbf{C}\mathbf{M}_\varepsilon^{-1/2})\,\hat{\mathbf{e}}' = \omega^2\hat{\mathbf{e}}'. \tag{8}$$

The system matrix is positive semidefinite. The eigenvalues ω^2 are thus real-valued and non-negative, correspondig either to static solutions ($\omega^2 = 0$) or to oscillations at constant amplitudes ($\omega^2 > 0$). In FIT, a sufficient condition for the system to be energy conserving is that $\mathbf{M}_\varepsilon$, $\mathbf{M}_\nu$ are positive definite [3].

Let us consider the surface admittance matrix $\mathbf{Q}^T\mathbf{Z}^{-1}\mathbf{Q}$. For positive values for the conductivity, the matrix $\mathrm{Re}\{\mathbf{Q}^T\mathbf{Z}^{-1}\mathbf{Q}\}$ is positive semidefinite, and can be combined with the conductivity matrix $\mathbf{M}_\kappa$

$$\mathbf{M}_\kappa' = \mathbf{M}_\kappa + \mathrm{Re}\{\mathbf{Q}^T\mathbf{Z}^{-1}\mathbf{Q}\}, \tag{9}$$

where $\mathbf{M}_\kappa'$ is positive semidefinite. For the imaginary part of $\mathbf{Q}^T\mathbf{Z}^{-1}\mathbf{Q}$, two different cases are considered. In case of a capacitive surface impedance, the imaginary part of the admittance is positive. Therefore, the matrix $\mathrm{Im}\{\mathbf{Q}^T\mathbf{Z}^{-1}\mathbf{Q}\}$ is positive semidefinite, and can be combined with the permittivity matrix $\mathbf{M}_\varepsilon$ resulting in a positive definite matrix

$$\mathbf{M}_\varepsilon' = \mathbf{M}_\varepsilon + \mathrm{Im}\{\mathbf{Q}^T\mathbf{Z}^{-1}\mathbf{Q}\}/\omega. \tag{10}$$

For an inductive surface impedance, the imaginary part of the admittance is negative. In this case, $-\mathrm{Im}\{\mathbf{Q}^T\mathbf{Z}^{-1}\mathbf{Q}\} > 0$, and can be combined with the inductive part of the system, i.e., the curl-curl part:

$$(\tilde{\mathbf{C}}\mathbf{M}_\nu\mathbf{C})' = \tilde{\mathbf{C}}\mathbf{M}_\nu\mathbf{C} - \omega\,\mathrm{Im}\{\mathbf{Q}^T\mathbf{Z}^{-1}\mathbf{Q}\}, \tag{11}$$

where $(\tilde{\mathbf{C}}\mathbf{M}_\nu\mathbf{C})'$ is a positive semidefinite matrix. The matrix $-\omega\,\mathrm{Im}\{\mathbf{Q}^T\mathbf{Z}^{-1}\mathbf{Q}\}$ is diagonal thus preserving the symmetry of the system matrix. Therefore, the consistency of the system is preserved.

4. SIBC IN TIME DOMAIN

Also in time domain the SIBC is implemented by adding a current term due to the SIBC in Ampere's law

$$\tilde{\mathbf{C}}\hat{\mathbf{h}}^{n+1/2} = \mathbf{M}_\varepsilon(\hat{\mathbf{e}}^{n+1} - \hat{\mathbf{e}}^n)/\Delta t + \mathbf{M}_\kappa(\hat{\mathbf{e}}^{n+1} + \hat{\mathbf{e}}^n)/2 + (\hat{\tilde{\mathbf{j}}}_{BC}^{n+1} + \hat{\tilde{\mathbf{j}}}_{BC}^{n})/2, \tag{12}$$

where the semi-implicit approximation in time has been used for the electric voltage and the SIBC current at time step *n*+1/2. Unlike standard FDTD implementations incorporating a SIBC, (12) avoids relating the tangential electric field at the boundary to the tangential magnetic field half a cell inside the domain and at half a time step time offset. The current due to the SIBC is given by a convolution integral [4].

To be able to optimize the accuracy of the SIBC over a desired frequency range, the surface admittance is approximated in the Laplace domain using a series of first-order rational functions [4]. The approximation is calculated using the vector-fitting technique [5]. The first-order rational functions transform into exponential functions in time domain leading to a recursive expression for the convolution integral. Assuming the fields piecewise linear in time [4], the current is given by

$$\hat{\tilde{\mathbf{j}}}_{BC}^{n+1} = C_0\hat{\mathbf{e}}^{n+1} + \sum_{p=1}^{P}\boldsymbol{\chi}_p^{n+1}, \tag{13}$$

where P is the number of first-order rational functions used in the approximation and

$$\boldsymbol{\chi}_p^{n+1} = e^{-\alpha_p \Delta t}\boldsymbol{\chi}_p^n + \frac{C_p}{\alpha_p}[1+\frac{(e^{-\alpha_p\Delta t}-1)}{\alpha_p\Delta t}]\hat{\mathbf{e}}^{n+1} + \frac{C_p}{\alpha_p}[\frac{1}{\alpha_p\Delta t} - e^{-\alpha_p\Delta t}(1+\frac{1}{\alpha_p\Delta t})]\hat{\mathbf{e}}^n, \tag{14}$$

where α_p and C_p are the poles and coefficients of the rational approximation, respectively. Substituting the expressions (13), (14) at time step n+1 in (12) and solving for $\hat{\mathbf{e}}^{n+1}$ results in an explicit update equation for the electric field. Only the field values at the previous time step ($\boldsymbol{\chi}_p^n$, $\hat{\mathbf{e}}^n$, $\hat{\mathbf{h}}^{n+1/2}$) are needed in the update equation. No reduction in the time step from the Courant limit is required.

5. NUMERICAL RESULTS

A 20x25x30-mm rectangular cavity resonator with lossy walls is used as a test structure. Reference results (MWS 1, MWS 2) are calculated with CST Microwave Studio™ using the eigenmode solver and utilizing the perturbation technique in the post-processing phase to calculate the wall losses. In frequency domain, the biconjugate-gradient (BICG) algorithm with Jacobi preconditioning is used. In time domain, 6- and 4-term approximations for $Z^{-1}(s)$ were used for copper and platinum, respectively. The simulation was continued for 40960 time steps and the resonance frequency f_0 and Q value were computed using the Prony's method. The resonance frequencies and Q values calculated in frequency- (sibc fd) and time domain (sibc td) are collected in Table 1. The reference MWS 1 is calculated using a 49x61x73-cell grid, others with a 17x21x25-cell grid. The results indicate validity of the present formulation of a SIBC.

Table 1. Quality factor of the cavity resonator.

	Wall conductivity σ = 5.8e7 S/m (copper)						**Wall conductivity σ = 0.94e7 S/m (platinum)**					
	TE_{011} mode		**TE_{101} mode**		**TE_{110} mode**		**TE_{011} mode**		**TE_{101} mode**		**TE_{110} mode**	
	f_0/GHz	Q	f_0/GHz	Q	f_0/GHz	Q	f_0/GHz	Q	f_0/GHz	Q	f_0/GHz	Q
MWS 1	7.8041	10740	9.0063	11078	9.5966	11820	7.8041	4323.8	9.0063	4459.9	9.5966	4758.4
MWS 2	7.7978	10786	8.9957	11152	9.5848	11899	7.7978	4342.3	8.9957	4489.4	9.5848	4790.3
sibc fd	7.7975	10765	8.9953	11127	9.5844	11876	7.7969	4333.8	8.9947	4479.3	9.5838	4781.0
sibc td	7.8020	10732	9.0022	11083	9.5928	11814	7.8014	4309.7	9.0015	4439.3	9.5921	4729.5

6. CONCLUSION

A formulation of the SIBC as a non-linear passive lumped element is presented in both frequency- and time domain. The formulation avoids spatial and temporal discretization errors typically associated with FDTD implementations of first-order SIBCs. The approach can also be extended to transition conditions to model transparent surfaces. Further, extension to triangular fillings to model cylindrical structures is possible. However, the applicability of a first-order SIBC is limited to the modeling of good conductors.

7. ACKNOWLEDGEMENT

This work is supported by the Academy of Finland under grant no. 207626.

8. REFERENCES

[1] T. B. A Senior and J. L. Volakis, *Approximate boundary conditions in electromagnetics*: The Institute of Electrical Engineers, London, 1995.

[2] T. Weiland, "Time Domain Electromagnetic Field Computation with Finite Difference Methods," *International Journal of Numerical Modelling*, vol. 9, pp. 295-319, 1996.

[3] R. Schuhmann and T. Weiland, "Conservation of Discrete Energy and Related Laws in the Finite Integration Technique," *Progress in Electromagnetics Research*, PIER 32, pp. 301-316, 2001.

[4] K. S. Oh and J. E. Schutt-Aine, "An efficient implementation of surface impedance boundary conditions for the finite-difference time-domain method," *IEEE Trans. Antennas Propagat.*, vol 43, no. 7, pp. 660-666, July. 1995.

[5] B. Gustavsen and A. Semlyen, "Rational approximation of frequency domain responses by vector fitting," *IEEE Trans. Power Delivery*, vol. 14, no. 3, pp. 1052–1061, Jul. 1999.

Generic Circuit Model for Multilayer Spiral Inductors and Transformers

Tommi Dufva [1] **Juha Volotinen** [1] **Johan Sten** [1]

[1] ***VTT Technical Research Centre of Finland***
VTT Information Technology
P.O. Box 1202, FIN-02044 VTT, Finland
rstna me.lastname@vtt.

Abstract
The paper reports the theoretical development of a new generic circuit model for multilayer spiral inductors and transformers and its implementation into the APLAC circuit simulator. Also, a numerical example is presented in order to prove the accuracy of the model.

Keywords: Spiral inductor, transformer, multilayer, circuit model, APLAC.

1. INTRODUCTION

This paper reports the development of a new generic circuit model for multilayer spiral inductors and transformers. Unlike conventional circuit models, which are often based on simulated or measured data and fitted polynomials, this model solves electro- and magnetostatic fields in an approximated geometry, extracts capacitances and inductances of the structure and then creates an equivalent circuit. Thus, the model is more like a small EM-simulator — heavier than a conventional model but more flexible.

The model enables any number of spirals and substrate layers. As geometric limitations, the spirals must be round, share a common axis and turn into the same direction with the same rate of change of radius.

The model was implemented into the APLAC circuit simulator which provides an excellent development platform for a device modeling. The object oriented software technology used in APLAC provides predefined interfaces for device models and simulation methods which speeds up the model implementation work.

In the following, the methods used in the theoretical modeling and the APLAC model implementation work are described. Also, a numerical example is presented in order to prove the accuracy of the model.

2. MODELING METHODS

The modeled structure consists of one or several planar spiral conductors on a common vertical axis. Together these spirals may form a multilayer inductor, transformer etc. The medium below, between and above the spirals may consists of any number of homogeneous layers with permittivities $\epsilon_1, \epsilon_2, \ldots, \epsilon_L$ and permeabilities $\mu_1, \mu_2, \ldots, \mu_L$. The conductors are assumed indefinitely thin.

The electromagnetic analysis of the structure is simplified via two sequential approximations:

1. The low-frequency assumption: an angular segment of the structure is interpreted as a block of curved conductors within which the field can be assumed quasi-static.
2. The geometry approximation: the curved conductors within the block are averaged with annular ring conductors.

Consequently, the analysis is reduced to a treatment of rotationally symmetric electro- and magnetostatic problems which give the capacitances and inductances needed for the equivalent circuit.

In the electrostatic problem the unknowns are the charge distributions $\varrho_1, \varrho_2, \ldots, \varrho_P$ on the surfaces $S_1, S_2, \ldots, S_P$ of the rings that establish given constant potentials $U_1, U_2, \ldots, U_P$ upon them:

$$\sum_{p'=1}^{P} \int_{S_{p'}} G_{ll'}(|\boldsymbol{\rho} - \boldsymbol{\rho}'|)\, \varrho_{p'}(\rho')\, dS(\boldsymbol{\rho}') = U_p, \quad \boldsymbol{\rho} \in S_p \quad (p = 1, 2, \ldots, P). \tag{1}$$

In the magnetostatic problem the unknowns are the current distributions $J_1, J_2, \ldots, J_P$ that induce vector potentials inversely proportional to ρ upon the rings. Moreover, a line integral of the vector potential along the pth ring should equal a given value of the magnetic flux ψ_p passing through the particular ring:

$$\sum_{p'=1}^{P} \int_{S_{p'}} \cos(\varphi - \varphi') G_{ll'}(|\boldsymbol{\rho} - \boldsymbol{\rho}'|) J_{p'}(\rho')\, dS(\boldsymbol{\rho}') = \frac{\psi_p}{2\pi\rho}, \quad \boldsymbol{\rho} \in S_p \quad (p = 1, 2, \ldots, P). \tag{2}$$

In both cases $G_{ll'}$ represents the Green's function of the respective problem.

The integral equations (1) and (2) are solved by using the variational method together with the Rayleigh-Ritz procedure. By estimating the charge distributions as $\varrho_p(\rho) = \sum_i c_i f_i(\rho)$, and the current distribution similarily, one ends up then to the system of equations

$$[a_{ii'}][c_{i'}] = [b_i]. \tag{3}$$

The coupling terms

$$a_{ii'} = 4\pi^2 \int_0^\infty \widetilde{f}_i(m; k_\rho) \widetilde{G}_{ll'}(0; k_\rho) \widetilde{f}_{i'}(m; k_\rho) k_\rho \, dk_\rho \quad (i, i' = 1, 2, \ldots, PN) \tag{4}$$

between the basis functions f_i and $f_{i'}$ are written in the spectral domain in order to simplify the solution of the Green's functions. Above, $\widetilde{f}_i(m; k_\rho)$ represents the Hankel transform of $f_i(\rho)$ of order m etc. In the electrostatic case $m = 0$ while in the magnetostatic case $m = 1$.

The elements of the vector $[b_i]$ are calculated simply in the spatial domain. In the electrostatic case they are

$$b_i = U_p \int_{S_p} f_i(\rho)\, dS(\boldsymbol{\rho}) \quad (i = 1, 2, \ldots, PN) \tag{5}$$

while in the magnetostatic case

$$b_i = \psi_p \int_{\boldsymbol{\rho} \in S_p} f_i(\rho)\, d\rho \quad (i = 1, 2, \ldots, PN). \tag{6}$$

The basis functions $f_1, f_2, \ldots, f_{PN}$ are of entire-domain-type forming an orthogonal base over each conductor and including the physically correct edge behaviour. Thus, they constitute a quickly converging expansion for the charge and current distributions on the rings.

For more detailed description of the methods, see [1].

3. IMPLEMENTATION OF THE MODEL INTO APLAC

The APLAC circuit simulator program provides a versatile simulation and programming platform for complex circuit design tasks. The object oriented software technology used in APLAC makes model development straightforward. The model code is separated from the analyzer code by using constant and voltage controlled current sources as an interface between the device model and analyzer. Thus, the analyzer and model codes are independent and can be developed separately.

The APLAC model is based on the equivalent circuit of the modeled device. The electrical characteristics of the element in the equivalent circuit is represented using the element specific model equation. The model equations are coded into the access functions that provide also some utility functionality, for example parameter checks and calculation control. The equivalent circuit is created during the model construction phase when data structures are also initialized.

The capacitance and inductance matrices are calculated in one access function. Capacitances and inductances, including mutual couplings, are parsed from the calculated matrices into value vectors. These vectors are used to transfer individual inductance and capacitance values into the each element of the equivalent circuit. Vectors are updated automatically when needed.

In the present model, each turn of a spiral is modelled with one or more π-circuit having series inductance and shunt capacitances. Each block is also electromagnetically coupled to other blocks and this coupling is modelled using mutual inductances and coupling capacitances.

As the model constractor is executed only once, the equivalent circuit can not be changed during the simulation. So the number of layers and turns can not be changed during the simulations.

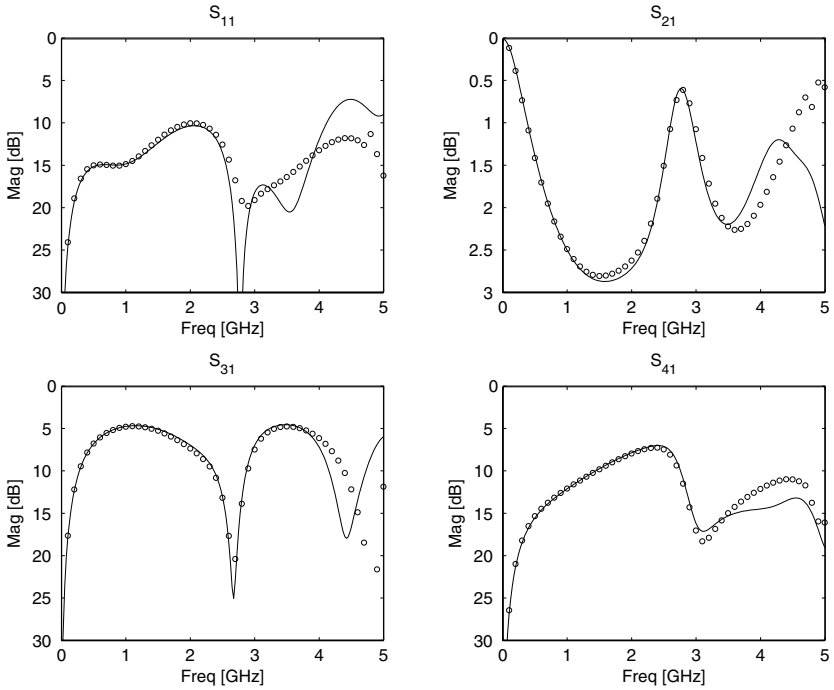

Figure 1: The magnitudes of the S-parameters of the transformer in the numerical example. The solid line corresponds to the circuit model and the dots to the field simulator.

4. NUMERICAL EXAMPLE

As a numerical example a transformer constituting of two three-turn spirals was simulated by using the developed APLAC model, and the accuracy of the result was verified against an electromagnetic field simulator IE3D. Every half turn in the spirals was modelled with a π-circuit. The resulting equivalent circuit included then 12 inductances, 30 mutual inductances, 54 capacitances and 15 nodes including the ground node.

The graphs in Figs. 1 and 2 show an excellent correspondence at the low-frequency regime. However, the difference grows at higher frequencies as the quasi-static approximation becomes invalid.

5. CONCLUSION

The development of a new circuit model for multilayer spiral inductors and transformers and its implementation into the APLAC circuit simulator has been described. The model enables an efficient and accurate low-frequency analysis of inductors and transformers with certain geometric limitations.

The efficiency of the method is based on the use of entire-domain basis functions for describing the charge and current distributions on the conductors. Benefit is also drawn from the nearly-cylindrical symmetry of the structure and the stratification of the medium which allow the problem to be cast in the Hankel transformed domain.

The model will be developed further by

- improving the accuracy at higher frequencies,
- taking different loss-mechanisms into account,
- enabling thick conductors and
- enabling spirals on different vertical axes.

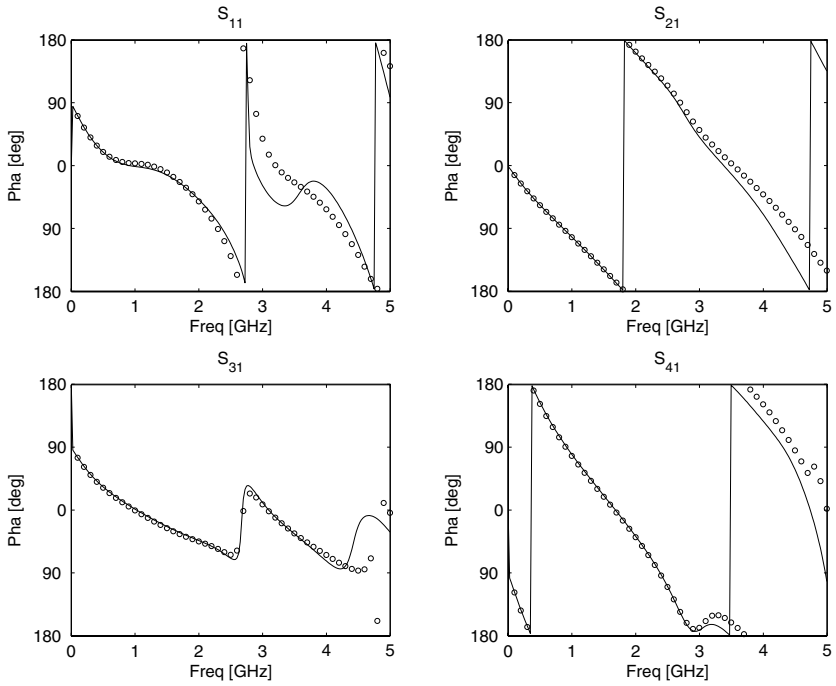

Figure 2: The phases of the S-parameters of the transformer in the numerical example. The solid line corresponds to the circuit model and the dots to the field simulator.

6. ACKNOWLEDGEMENT

This work has been supported in part by Tekes, the National Technology Agency, Finland.

References

[1] T. J. Dufva and J. C.-E. Sten, "Quasi-static variational analysis of planar spiral conductors," *J. of Electromagn. Waves and Appl.*, Vol. 16, No.7, 957–976, 2002.

A Novel Strip Line Test Method for Relative Permittivity and Dissipation Factor of Printed Circuit Board Substrates

Kare-Petri Lätti, Janne-Matti Heinola, Marko Kettunen, Juha-Pekka Ström, Pertti Silventoinen

Lappeenranta University of Technology
P.O. Box 20, Lappeenranta
FIN-53851, Finland
Email: kare.latti@lut.fi

Abstract
This paper introduces the strip line T-pattern resonator method for relative permittivity and dissipation factor of printed circuit board substrates at frequency range from 0,5 GHz to 9,5 GHz. The design of the T-resonator is presented and the used calculation methods are introduced. Functionality of the method is investigated experimentally with one FR-4 type material. The method is based on a simple strip line structure, which can be manufactured in normal printed circuit board multilayer manufacturing process. The results from this test method agree with the results from other test methods and known material data.

Keywords: Stripline T-pattern resonator, T-resonator, relative permittivity, dissipation factor.

1. INTRODUCTION

The frequencies in electronic applications continue to increase, and the characteristics of the printed circuit board materials become more important. The more accurate data of electrical properties of the laminate materials are therefore needed at microwave frequencies. Different methods to determine dielectric constant and dissipation factor of the printed circuit board materials are presented in the literature, but they are often very complicated and have disadvantages.

The strip line T-pattern resonator or T-resonator is a simple configuration, which provides numerous data points over a broad frequency range and is simple to fabricate. With the strip line structure no microstrip dispersion or radiation occurs. Thus dispersion and radiation can be ignored simplifying the calculation. Strip line T-resonator has also no gaps, like measurement structures of other methods often have. The gaps can have an effect to the determined results, and experimental testing of gap length is often needed.

2. DESIGN OF THE TEST STRUCTURE

T-resonator is a parallel resonator, which operates like a notch filter having a resonant null in resonance frequencies. The length of T-resonator's arm is a quarter wavelength. It represents an open-end transmission line stub and resonates at odd integer multiplies of quarter wavelength frequency. The conductor pattern of the strip line T-resonator is a simple T-pattern with same line widths in all branches.

The characteristic impedance of the strip line is designed to be 50 Ohms. The design is carried out with commercial software as EEsof Linecalc. The T-resonator test sample is designed to have the primary resonance frequency at 0.5 GHz. The basic equation to calculate the length of the T-resonator's stub is shown below:

$$L_{\mathrm{el}} = \frac{nc}{4f\sqrt{\varepsilon_{\mathrm{r}}}}, \tag{1}$$

where n is the order of the resonance (in this case n=1), c is the speed of light in vacuum, f is frequency, ε_{r} is the estimated dielectric constant and L_{el} is electrical length of the stub. The basic dimensioning of the stub can be carried out with (1), but in order to get the first resonance frequency as accurately as possible at 0.5 GHz, the corrections for open-end and T-junction effects must be used. The accurate designing makes it possible to have data points at desired frequencies, and to see directly from the measurements, if the estimated dielectric constant equals the value calculated from the measurements.

While the open-end extends the stub, the T-junction foreshortens it. The open-end effect is taken into account with the method presented by Altschuler and Oliner [2] as follows:

$$l_{\mathrm{eo}} = \frac{\lambda_{\mathrm{g}}}{2\pi}\cot^{-1}\left(\frac{4d+2w}{d+2w}\cot\left(\frac{2\pi}{\lambda_{\mathrm{g}}}d\right)\right), \tag{2}$$

where $d = (h \ln 2)/\pi$, h is the height of the substrate, w is the width of the line and λ_{g} is the wavelength in the medium. The strip line T-junction discontinuity is only studied in few papers and there are only approximations for the effect of the T-junction. The T-junction effect is taken into account with the experimentally established curves presented by Franco and Oliner [3]. The physical length of the stub is calculated from the (1) with the open-end and T-junction corrections. After all dimensions are determined, the test samples can be manufactured by traditional multilayer manufacturing steps, just like any other application.

3. MEASUREMENTS

The frequency response of the 2-port strip line T-resonator is measured with network analyzer. The calibration of the network analyzer is carried out with TRL-calibration in order to take into account the attenuation caused by measurement cables and connector interfaces. The TRL calibration kit is manufactured into same kind of printed circuit board multilayer structure as the measurement structures, and the same kind of connector interfaces are used. The implementation of the TRL calibration is introduced in [4]. The resonance frequencies and 3 dB bandwidths are measured on narrow enough spans to achieve adequate frequency resolution. The critical dimensions of the measurement structures, as substrate height and line width, are verified by microsections.

4. CALCULATION

4.1 Relative Permittivity Calculation

The dielectric constant of the laminate material is calculated from the resonance frequencies, which are extracted from the frequency response of the T-resonator. The basic idea of determining the material dielectric constant is to design a strip line T-resonator to a particular base frequency. The design is carried out based on the estimated material dielectric constant value. If the measured resonance frequencies deviate from the designed frequencies, the material dielectric constant deviates from the estimated values.

When the dimensions from the microsections are known, the material dielectric constant is calculated based on the resonance frequencies:

$$\varepsilon_{\mathrm{r}}(n) = \left(\frac{nc}{4\left(L_{\mathrm{fys}} + \frac{w}{2} + l_{\mathrm{eo}} - d_2\right)f(n)}\right)^2, \tag{3}$$

where n is the order of the resonance (n=1,3,5,…), w is the width of the line, l_{eo} is the equivalent extra length of the strip line stub [2], d_2 is the displacement of the reference plane for the stub [3], and $f(n)$ are the measured resonance frequencies for n=1,3,5,... . The original reference plane of the stub is in the middle of the feed lines, therefore term (w/2) is added to the stub length in (3).

4.2 Dissipation Factor Calculation

Dissipation factor is calculated from the quality factor of each resonant null. The loaded quality factor Q_L is determined from the measured resonance frequencies $f(n)$ and 3 dB bandwidths BW_{3dB} of the resonance frequencies. The unloaded quality factor Q_0 is calculated from the loaded quality factor as follows: [5]

$$Q_L = \frac{f}{BW_{3dB}}, \qquad Q_0 = Q_L \Big/ \sqrt{1 - 2 \cdot 10^{-(L_A/10)}}, \tag{3), (4}$$

where L_A is the insertion loss in dB at the resonance. With strip line T-resonator structures, two types of losses occur: dielectric losses and conductor losses. The total losses are the sum of the loss components, so the unloaded quality factor includes the effects of dielectric and conductor losses:

$$\frac{1}{Q_0} = \frac{1}{Q_d} + \frac{1}{Q_c}, \tag{6}$$

where Q_d is quality factor due to dielectric losses and Q_c is the quality factor due to conductor losses. Conductor losses are calculated with $Q_c = \pi/(\alpha_c \lambda_g)$ as presented by Cohn [6], where λ_g is wavelength in strip line and α_c is conductor attenuation constant in nepers per length unit. The conductor attenuation constant is calculated as follows:

$$\alpha_c = \frac{4 R_s \varepsilon_r Z_0}{376.6^2 h}\left[X + \left(\frac{2wX^2}{h}\right) + \left(\frac{X^2}{\pi}\left(1 + \frac{t}{h}\right)\ln\left(\frac{X+1}{X-1}\right)\right)\right], \tag{8}$$

where $X = 1/(1 - t/h)$, R_s is the surface resistivity of conductor and t is the resonator conductor thickness. Material dissipation factor i.e. material loss tangent is calculated from unloaded quality factor and quality factor due to conductor losses as shown below:

$$\tan\delta = \frac{1}{Q_0} - \frac{1}{Q_c}. \tag{9}$$

5. EXPERIMENTAL RESEARCH

The experimental research was carried out with one FR-4 type printed circuit board substrate material. The connector interface was carried out with SMA connectors. The center conductor of the SMA connector was soldered, and the ground plane of the connector was attached to ground plane of the printed circuit board with screws. The ground planes of the printed circuit board were connected by vias.

The measurements were carried out with HP8720D network analyzer and the calibration with a TRL calibration kit. A strip line T-resonator test sample with 0.5 GHz base frequency and typical frequency response of the strip line T-resonator are shown in Fig. 1. The results from the experimental determination of relative permittivity and dissipation factor are shown in Fig. 2. The results agree with the results from strip line and microstrip ring resonator methods [4], [7] and with known material data.

The strip line T-resonator method is shown to be valid with the high loss materials up to 10 GHz. With high loss materials, the use of the T-resonator in higher frequencies is restricted by low magnitude of the resonance peaks. The used connector interface is suitable up to 10 GHz, but if the method is used with low loss materials and over 10 GHz frequencies, the connector interface must be reselected or impedance matching should be improved. There is a lack of research concerning the discontinuities in strip line, hence additional research of strip line discontinuities, especially of strip line T-junction, would result in better accuracy of the method.

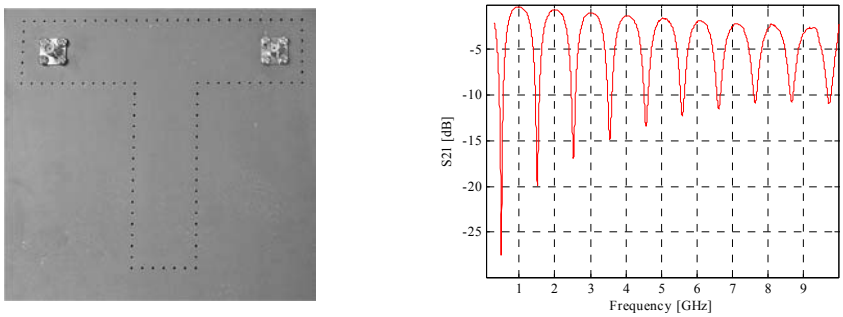

Fig. 1. A strip line T-resonator test sample with 0.5 GHz base frequency and typical frequency response of a strip line T-resonator in one FR-4 type printed circuit board material.

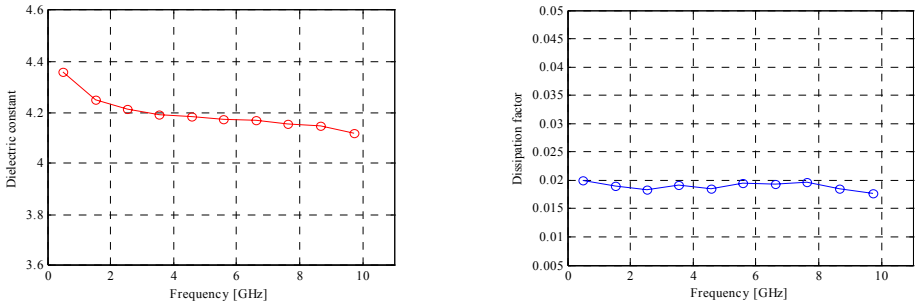

Fig. 2. Relative permittivity and dissipation factor of one FR-4 type substrate material in function of frequency from 0.5 GHz to 10 GHz.

6. CONCLUSION

The presented method is valid for determining the relative permittivity and dissipation factor of printed circuit board materials in function of frequency at wide frequency range from 0.5 to 9.5 GHz. The strip line T-resonator can be manufactured in normal printed circuit board manufacturing process. Data points over a broad frequency range can be achieved with a single structure. The calculation in the strip line T-resonator method is simple, because no microstrip dispersion or radiation occurs. The results agree with results from other test methods.

7. REFERENCES

[1] H. A. Wheeler, "Transmission-Line Properties of a Strip Line Between Parallel Planes," *IEEE Trans. Microwave Theory and Techniques*, vol. MTT-26, November, 1978, pp. 866-876.

[2] H. M. Altschuler and A. A. Oliner, "Discontinuities in the Center Conductor of Symmetric Strip Transmission Line," *IRE Trans. Microwave Theory Tech*., vol MTT-8, pp. 328-339, May 1960.

[3] A. G. Franco and A. A. Oliner, "Symmetric Strip Transmission Line Tee Junction," *IRE Trans. Microwave Theory Tech*, vol. MTT-10, pp. 118-124, March 1962.

[4] J-M. Heinola, K-P. Lätti, J-P. Ström, M. Kettunen and P. Silventoinen, "A Strip Line Ring Resonator Method for Determination of Dielectric Properties of Printed Circuit Board Material in Function of Freqyency," *IEEE Conf. on Electrical Insulation and Dielectric Phenomena*, *Colorado*, October 2004.

[5] J. Carroll, M. Li, K. and K. Chang, "New Technique to Measure Transmission Line Attenuation," *IEEE Trans. Microwave Theory and Techniques,* vol. 43, No. 1, pp. 219-222, January 1995.

[6] S. B. Cohn, "Problems in Strip Transmission Lines," *IRE Trans. Microwave Theory and Techniques*, Vol. MTT-3, March, 1955, pp. 119-126.

[7] J-M. Heinola, K-P. Lätti, J-P. Ström, M. Kettunen and P. Silventoinen, "A New Method to Measure Dielectric Constant and Dissipation Factor of Printed Circuit Board Laminate Material in Function of Temperature and Frequency," *Proc. International Symposium on Advanced Packaging Materials, Atlanta,* March 2004. pp. 235-240.

Effective Permittivity of Ceramic-polymer Composites: Study of Elementary Shape

[1]*Liisi Jylhä,* [2]*Johanna Honkamo,* [2]*Heli Jantunen and* [1]*Ari Sihvola*

[1] *Electromagnetics Laboratory, P.O. Box 3000, Helsinki University of Technology, Finland*
liisi.jylha@hut.fi, ari.sihvola@hut.fi

[2] *Microelectronics and Materials Physics Laboratories, P.O. Box 4500, University of Oulu, Finland*
jhonkamo@ee.oulu.fi, heja@ee.oulu.fi

Abstract:
This study considers modeling of macroscopic permittivity of composites that consist of different amounts of TiO_2 powder dispersed in a continous epoxy matrix (0-3 composites). The composites researched have no closed form solutions predicting their effective permittivity because the phases used have very different relative permittivity values and the inclusions can be very densely packed. The study demonstrates a method which enables fast and accurate modeling for relative permittivity values by using electrostatic Monte-Carlo simulations by three different runs for every sample with orthogonal field directions. Numerical simulations are in very good agreement with measured permittivities. Same method can be used for other materials as well. The presented method can be used for other materials as well because the modeling is based on the microstructure of the mixture.

1. INTRODUCTION

Ceramic-polymer composites, consisting of ceramic crystal particles in an amorphous background material, have several interesting properties. Their electrical properties, for example effective permittivity, can be adjusted by changing the fractions of the constituents. Furthermore, materials have plastic-like non-fragile structure and are suitable for multilayer structures even in curved shape. Because the mixing theories, however, fail to predict the effective permittivity, the correct mixing ratio has to be found experimentally, which can be very laborious. Furthermore, an effective modeling method could be used as a tool for designing materials. In this study, the effective permittivity of TiO_2/epoxy type 0-3 composites is modeled and measured for volume fractions of TiO_2 particles up to 30%. Titanium dioxide is anisotropic ceramic material with relative permittivity of ϵ_r=114 in a frequency range 100 kHz – 1 MHz [1-2]. Epoxy is an amorphic isotropic material with permittivity ϵ_r = 4.0 – 3.7 in the same frequency range.

2. PROPERTIES OF EXPERIMENTAL SAMPLES

Titanium dioxide, with composition of minimum 97% rutile phase (Merck), was used with a solution of epoxy (Bisphenol-A) and curing agent (triethylenetetramine) (Struers) as starting materials to form slurry for bulk composite samples. Five parallel samples of each mixing ratio 10-30 vol.% of TiO_2, were pre-

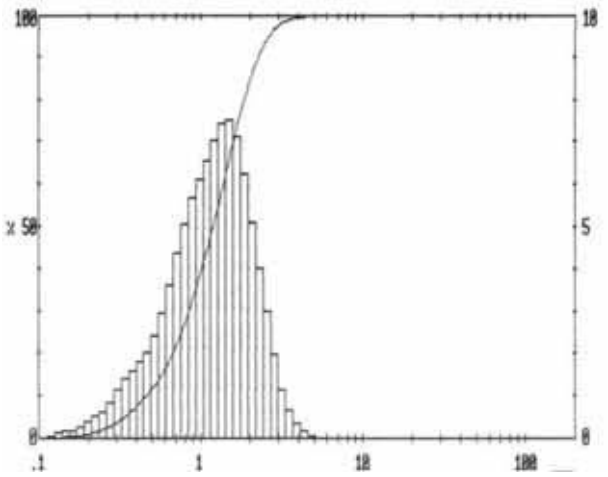

Particle size (μm)

Figure 1: The particle size distribution of TiO_2 powder.

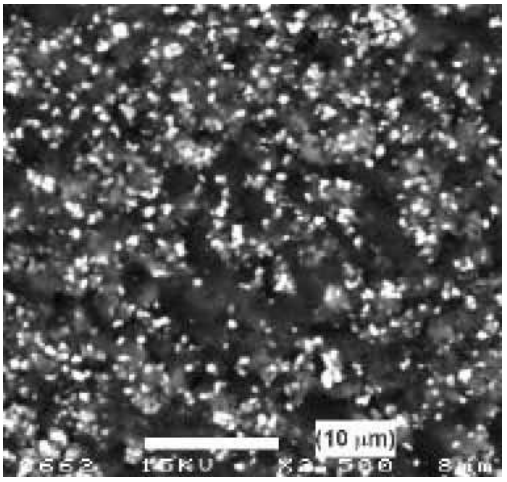

Figure 2: A scanning electron microscope image of the composite with the ceramic loading of 10 vol.%.

pared by weighing titanium dioxide powder and measuring epoxy resin by syringe. After mixing and vacuum treatment the slurry was poured into cylindrical molds. Composite samples were cured in air for 24 hours. Densities of composites were estimated from the physical dimensions and weights of the polished samples. Electrodes were painted on both sides of the cylinders by using conductive silver paint (Electrolube). Relative permittivities were measured by a HP4284A precision LCR meter (Hewlett-Packard, USA) in the frequency range of 100 Hz - 1 MHz.

Particle size distribution of the titanium dioxide powder was measured by Malvern Mastersizer (MS1002, Malvern Instruments Ltd., Malvern, UK). The microstructures of the composites were studied with a scanning electron microscope, SEM (Jeol JEM-6400, Tokyo, Japan).

The results showed that the TiO_2 powder with D_{50} value of 1.18 μm had large size deviation (Fig. 1). The microstructure of a compostie with 10 vol. % loading of TiO_2 is shown in Fig. 2. The white areas represent titanium dioxide particles on the surface of the sample, the dark areas corresponds to epoxy resin and the grey areas embedded TiO_2 particles. The gure shows that TiO_2 particles are well dispersed. Permittivities of pure epoxy and bulk composites with ceramic loading 10, 20 and 30 vol.% were measured.

Figure 2 shows the microstructure of the composite material with TiO_2 loading 10 vol.%. The white color represents titanium dioxide phase while dark areas correspond to epoxy resin. The gure shows that TiO_2 particles are well dispersed. Permittivities of pure epoxy and bulk composites with ceramic loading 10, 20 and 30 vol.% were measured. The results show that the TiO_2 powder effectively modifies the permittivity value of epoxy. At 1 MHz 30 vol.% ceramic loading e.g. increases the value of pure epoxy from 3.7 to 11.0. The same trend could be seen at all frequencies.

3. MODELING

The classical mixing theories [3] fail to predict the effective permittivity of TiO_2/epoxy composite, because the electrical constrast is large and the shape of elementary inclusions is far from the assuptions of mixing formulas, which assume well separated spherical inclusions.

Different numerical approaches have been developed to predict the effective permittivity of disordered mixtures [4-6]. None of these methods models correctly the fine structure of a mixture. In [5] the mixture is modeled with a cubic lattice of aligned cylinders. The model involves several parameters, which are fitted to get a match with the measurements. This method gives a good agreement with the measured data, but it does not predict the effective permittivity if the incredients of the mixture are changed. In [4] and [6] much attention is focused on the avoiding of the effect of the periodicity. The mixture consists of a three dimensional chess-board type of strucure, where elementary cubes are filled with inclusion or background material. The computation domain contains a large number of inclusions, and because of that the fine structure can not be modeled realistically. In [6] the error between measurements and simulations is about 10%-35% and in [4] no experimental verifications is made.

In this study, the aim is to model the effective permittivity of the mixture by modeling the fine structure of the material. The effect of particle size distribution, shown in Fig. 1, was ignored because the wavelength is much longer than the size of particles. The effective permittivity of a mixture is calculated using Monte Carlo simulations. Inclusions occupy the homogenous cubical environment in a random positions. The incident static electric field is applied with a voltage over opposite sides of the cube. The computation domain represents an ideal conductor and the effective permittivity of the mixture inside can be calculated easily after solving the Laplace equation in a whole domain. The problem was solved using FEM-based Electromagnetic software Opera in CSC. The number of elements is about 30 000 in every simulation and only quadratic elements are used.

In this type of numerical simulations, the boundary conditions makes the structure periodical. The length of a pseudorandom period is the side of the computation domain b. The modeled real-life mixture is isotropic and homogeneous in a large scale, but it has granular nonhomogenous microstructure. A pseudorandom mixture is anisotropic, which means it has different permittivites as calculated using three runs with orthogonal field directions parallel to x, y or z-axis. The effect of anisotropy can be effectively compensated by calculating an average over ϵ_x, ϵ_y and ϵ_z, which are calculated using these field directions. In [7] it has been shown, that for spherical inclusions which are allowed to overlap the boundaries and each other, the effect of the periodicity is negligible, if this method of three separate runs for each sample with field parallel to x, y or z-axis is used. It has been shown that the diameter of inclusions a can be as large as $a = 0.4b$, where b is the side of the cubical domain. With this averaging method, the deviation of results for inclusions $a = 0.2b$ or $a = 0.4b$ was the same. Accordingly, equally good results can be reached using significantly smaller simulations than previously.

The shape of elementary inclusions in simulations is the most important parameter, because the effect of the periodicity is shown to be negligible with the averaging method. Because titanium dioxide in a rutile phase has a regular lattice structure [2] (Fig. 3), an assumption of the elementary shape of titanium dioxide particles can be made. The smallest elementary cell, which contains one titanium dioxide molecule has diameters as presented in Fig. 3, where a=4.59 A, c/a=0.64. Let us assume that the lattice will break or crystallize most easily along its symmetry lines, where the separation between neighboring atoms is the greatest. This leads to a brick with dimensions $a : a : c/2$, accordingly $1 : 1 : 0.32$. This is the basic shape of inclusions in the numerical simulations. In order to be able to simulate large volume fraction of inclusions, the dimensions of elementary shape are allowed to vary with deviation $0.07n$, where n is the side of the brick. The expectation values for diameters are $1 : 1 : 0.32$, but they can vary separately. The deviation is allowed to cover also high volume fraction of inclusions, because inclusions are not allowed to cross each other. According to [7] the expectation value for diameter of inclusions was chosen to be $a = 0.4b$.

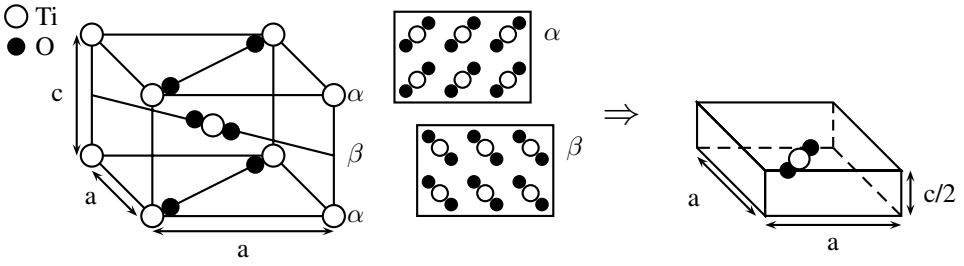

Figure 3: The lattice structure of TiO_2 in a rutile phase [2] is presented on the left. The planes α and β are identical with a rotation $\pi/2$. The smallest cell which contains a titanium atom and two oxygen atoms is presented on the right.

4. RESULTS

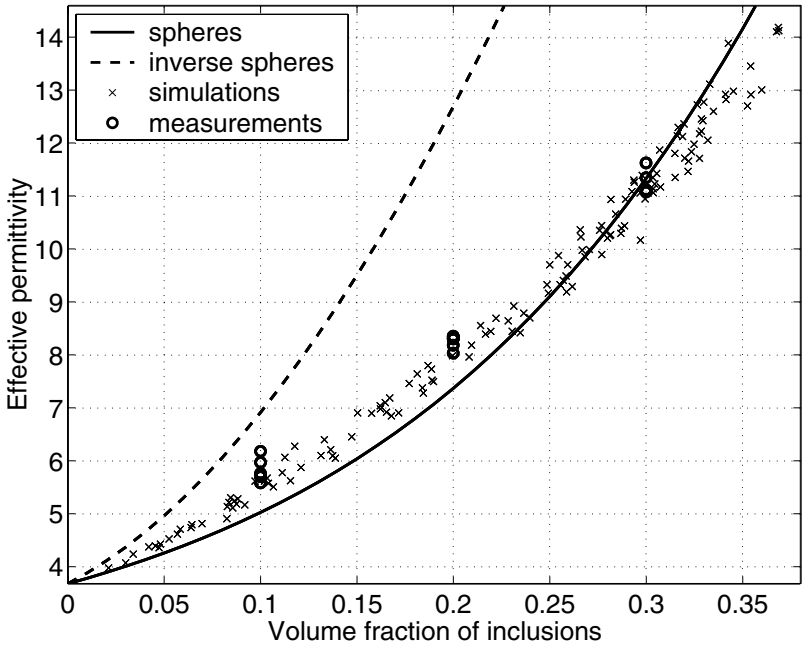

Figure 4: The effective permittivity of the mixture as a function of volume fraction of TiO_2 powder. Simulations are presented with dots and measurements with circles. Measurements were achieved by manufacturing several samples for every volume fractions of inclusions.

The simulations and the measurements are presented in Fig. 4. Simulations are presented after averaging over three permittivities ϵ_x, ϵ_y and ϵ_z [7]. The number of inclusions vary from 2 to 36. As a comparison a regression model for two different elementary shapes are presented, which are a result of a numerical study [8] using nite difference method and a large amount of Monte Carlo samples. In a mixture consisting of spheres, TiO_2 particles are assumed spherical and they can overlap each other and the boundaries of the domain. The position of spheres is random in every sample. In the mixture labelled "inverse spheres" the TiO_2 particles are modeled as an inversion of overlapping sphers. Then the epoxy between inclusions have a spherical shape. It can be seen, that the shape of elementary inclusions is an essential parameter. The good match in all volume fraction of inclusions implies, that the ne structure is modeled correctly in this study. Numerical results presented in this study describes the effective permittivity of the mixture best in all volume fraction of TiO_2.

5. CONCLUSIONS

It has been shown that ceramic-polymer composites can be modeled from the microstructure. The computational domain, i.e. the size of the bounding box b compared to the size of inclusions a, can be as small as $a = 0.4b$, but only if the averaging method presented in [7] is used. The correlation between measurements and simulations is very good across the whole volume fraction of TiO_2. The model uses elementary shapes derived from the lattice structure of TiO_2, therefore it is possible to use the similar method also for modeling mixtures without experimental verification of effective permittivity. It was shown that the shape of elementary inclusions is an essential parameter as modeling the effective permittivity of mixtures. The modeling method is useful for the design of composite-materials, but it can also be used for remote sensing applications.

6. REFERENCES

[1] N. Klein, C. Zuccaro, U. Dähne, H. Schulz, N. Tellmann, R. Kutzner, A. G. Zaitsev and R. Wördenweber. *Dielectric properites of rutile and its use in high temperature superconducting resonators*, J. Appl. Phys. 78(11), 1995, pp. 6683-6686.

[2] R. Parker "Lorentz corrections in rutile" in *Physical Review*, vol 124, no. 6, 1961.

[3] A. Sihvola. *Electromagnetic mixing formulas and applications*, IEE Electromagnetic Wave Series 47, The Institution of Electrical Engineers, 1999.

[4] B. Sareni, L. Krähenbühl and A. Beroual "Effective dielectric constant of random composite materials" *J. Appl. Phys.* 81(5), pp. 2375-2383, 1997.

[5] S. Orlowska, A. Beroual and J. Fleszynski "Barium titanate particle model inquiry through effective permittivity measurements and boundary integral equation method based simulations ot the $BaTiO_3$-epoxy resin composite material" in *J. Phys. D: Appl. Phys.* 35, pp. 2656-2660, 2002.

[6] Y. Wu, X. Zhao, F. Lei and Z. Fan "Evaluation of mixing rules for dielectric constants of composite dielectrics by MC-FEM calculation on 3D cubic lattice" in *J. Electroceramics*,11, pp. 227-239, 2003.

[7] L. Jylhä and A. Sihvola "Numerical modeling of disordered mixture using pseudorandom simulations" in *IEEE Trans. on Geosci. and Rem. Sens.*, in press.

[8] K. Kärkkäinen, A. Sihvola and K. Nikoskinen "Effective permittivity of mixtures: numerical validation by the FDTD method",*IEEE Trans. on Geosci. and Rem. Sens.*,vol.38, no.3, 2000.

On Possible Use of Metamaterials in Broadband Phase Shifters

Igor S. Nefedov **Sergei A. Tretyakov**

Radiolaboratory / SMARAD Center of Excellence
Helsinki University of TechnologyP.O. Box 3000, FI-02015 HUT, Finland
Email:igor.nefedov@hut. Email:sergei.tretyak ov@hut.

Abstract
A possibility to design phase shifters with reduced frequency dispersion, using combined sections of forward-wave and backward-wave transmission lines (TL) is discussed. It is shown that inclusion of backward-wave sections into a transmission line always increases the total dispersion. On the other hand, we show that dispersion can be reduced by means of lines with positive anomalous dispersion and provide an example of such line.

Keywords: Metamaterials, Backward waves

1. INTRODUCTION

Recent years have witnessed growing interest in metamaterials and complex transmission lines supporting propagation of backward waves at microwave frequencies. Different terms are used for these metamaterials: left-handed media, Veselago media, backward-wave (BW) media, media with negative refractive index or with negative permittivity and permeability, lines with negative dispersion. Several new application ideas have been proposed. Most of them utilize the effect of anomalous refraction at an interface between a forward-wave (FW) and a BW medium and on phase compensation, taking place when a wave propagates across slabs of FW and BW materials. The first idea belongs to V. Veselago, who published pioneer work on electrodynamics of media with negative parameters and discussed a design of a planar lens [1]. This idea was developed by many authors, who considered wave focusing, including sub-wavelength imaging [2], wave leakage (a new type of leaky-wave antennas) [3], *etc.* The design of three-dimensional BW media with the use of resonant particles like split-ring resonators [8] is difficult due to high losses in these resonant structures. Two-dimensional structures for the microwave range can be realized without any resonant elements, periodically loading two-dimensional transmission lines with lumped element series capacitors and shunt inductors [4].

The phase compensation idea was proposed by N. Engheta [5], who suggested a sub-wavelength cavity resonator formed by two adjacent material slabs that support forward and backward waves. However, as has been shown in [6], this structure in fact exhibits resonant response only due to the resonant behavior of the filling material.

The idea of phase compensation was further extended to the design of phase shifters in [7]. That paper discusses a broadband phase shifter formed by connected transmission-line sections with forward and backward waves. This design allows to realize negative values of phase shift in comparatively short sections of transmission lines. A natural question arises: Is it possible to reduce the frequency dispersion of phase shifters using this approach, in addition to achieving negative phase shifts? And if possible, what kind of transmission line or filling metamaterial is required? These are the questions that we address in this paper.

2. POSITIVE AND NEGATIVE, NORMAL AND ANOMALOUS KINDS OF DISPERSION

In this introductory section we give definitions of various dispersion types to be used in the following discussion and explain how these various dispersion laws can be realized in artificial transmission lines. Characterizing dispersion of media or transmission lines with negligible losses that support waves with the propagation constant β at frequency ω, two terms are commonly used: *positive* dispersion, when $\beta d\beta/d\omega > 0$ and *negative* dispersion, when $\beta d\beta/d\omega < 0$. Sometimes negative dispersion is referred to as *anomalous* dispersion, which is not quite correct because this term originates from optics, where "anomalous dispersion" is understood as positive dispersion in the case when the real part of the refractive index n decreases with the frequency. This usually takes place within narrow frequency bands close to the resonant frequencies of molecules. Identifying anomalous and negative dispersion we lose some important details of the dispersion laws.

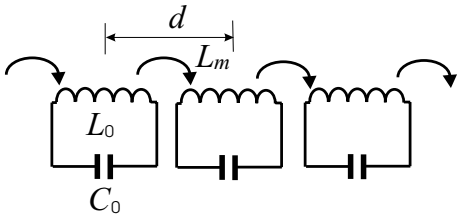

Figure 1: A chain of resonators coupled via mutual inductance L_m.

For more complete description of dispersion of metamaterials one can additionally consider the frequency dependence of the slow-wave factor (refractive index) $n = \beta/k_0$, where k_0 is the wavenumber in free space. In this paper we will use the following definitions: dispersion is *normal*, if $ndn/d\omega > 0$ and *anomalous*, if $ndn/d\omega < 0$. The notions of positive, negative, normal and anomalous dispersion are not independent, and the relation is different for forward and backward waves. Indeed, because

$$\beta\frac{d\beta}{d\omega} = \frac{n}{c}\left(n + \omega\frac{dn}{d\omega}\right)k_0 = \frac{n}{c}\left(n - \lambda\frac{dn}{d\lambda}\right)k_0, \tag{1}$$

where c is the speed of light, we see that normal dispersion is always positive, but anomalous dispersion can be either positive or negative.

Let us demonstrate here, how three kinds of dispersion can be observed in a certain periodical structure formed by a chain of lumped inductances and capacities (see Fig. 1). The cells are coupled by a mutual inductance L_m, and the coupling coefficient $\kappa = L_m/L_0$ can be either positive or negative. This periodical structure is described in detail in [4]. More recently, waves in one-, two-, and three-dimensional chains of capacitively loaded and magnetically coupled loops were investigated in [9, 10]. These waves are referred by these authors as "magnetoinductive waves". However, negative coupling coefficients between inductive elements have not been considered by Shamonina, Wiltshire, *et al.*

The dispersion equation for this structure can be written as [4]:

$$\lambda/\lambda_r = \sqrt{1 - 2\kappa\cos\psi}, \tag{2}$$

where $\psi = \beta d$ is the phase shift per period d, λ is the wavelength in free space, and the resonant wavelength λ_r is defined as $\lambda_r = 2\pi c\sqrt{L_0 C_0}$. It is more convenient to illustrate different kinds of dispersion in the (λ, n) coordinates, than in the (ω, β) coordinates, see Fig. 2. Here the straight lines are the lines of constant phase shift per period, because $n = \psi\lambda/(2\pi d)$. Depending on the value of the coupling coefficient κ, dispersion may be normal positive (curve 1), anomalous positive (curve 2), and anomalous negative (curve 3). According to Raley's formula

$$n_{\rm gr} = n - \lambda\frac{dn}{d\lambda}, \tag{3}$$

in the (λ, n) coordinate system the group slow-wave factor $n_{\rm gr}$ (normalized as $n_{\rm gr}d/\lambda_r$ in our case) for some point P_i at a dispersion curve is shown as intersection of the ordinate axis and the tangent to the dispersion curve at point P_i. The pass band of the chain lies in the limits [4]

$$\lambda_r\sqrt{1 - 2\kappa} \le \lambda \le \lambda_r\sqrt{1 + 2\kappa}. \tag{4}$$

As is seen from the plot in Fig. 2 and formula (1), waves along structures with $\kappa > 0$ are backward waves with negative dispersion. If $\kappa < 0$, we have forward waves with positive dispersion. Positive anomalous dispersion can be observed at $\psi > \pi/2$ if $\kappa < 0$ and it can be rather large in the absolute value.

3. APPLICATION OF TL WITH POSITIVE ANOMALOUS DISPERSION

In this section we consider a possibility to broaden the working frequency range of phase shifters, namely, the use of transmission-line sections with positive anomalous dispersion. If the frequency is changed with a small increment $\Delta\omega$, the corresponding phase shift change is

$$\Delta\psi_0 = \frac{\Delta\omega}{c}\left(n_1 + \omega\frac{dn_1}{d\omega}\right)d_0, \tag{5}$$

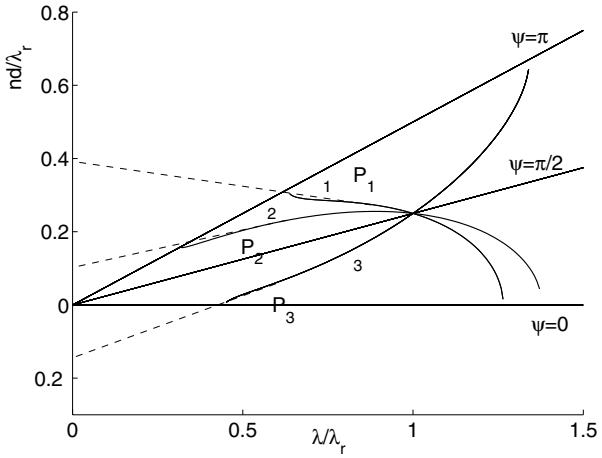

Figure 2: Dispersion characteristics of the structure shown in Fig. 1. Curves 1,2, and 3 correspond to the values of the mutual coupling coefficient $\kappa = -0.3$, $\kappa = -0.45$, and $\kappa = 0.4$, respectively.

According to formula (5), we can expect a reduction of the phase shift variation $\Delta\psi_0$ if we utilize a TL with $nd\,n/d\,\lambda > 0$, but $\beta d\,\beta/d\,\lambda < 0$. The last condition imposes the following restriction:

$$\lambda \left| \frac{dn}{d\lambda} \right| < n, \tag{6}$$

otherwise we have negative dispersion (a backward-wave line).

In Section 2 we demonstrated, that positive anomalous dispersion may be observed in unit cells, shown in Fig. 1, but at large phase shifts. Fig. 3 provides a comparison of the phase shift increments $\Delta\psi_0$ throughout the pass band $F_{\min} = 1.9$ GHz, $F_{\max} = 2.2$ GHz in a one-stage structure considered in Section 2 (solid curve), and in a transmission line with a constant slow-wave factor (dashed curve). The total phase shift per a period is close to π, parameters of the cell are taken following: $\kappa = -0.48$ and the resonant frequency $f_r = 0.559$ GHz. The difference in the phase shift within interval $[F_{min}, F_{max}]$ is $\Delta\psi_0 = 4.94^\circ$ for the structure with anomalous dispersion and $\Delta\psi_{TL} = 24.16^\circ$ for a transmission-line segment, having length d (the period of the first structure) and a constant slow-wave factor, if the phase shifts for both structures are equal in the middle of the considered pass band.

However, such a promising result can be obtained only near the total phase shift $\psi = \pi$. When the phase shift changes from $\psi = \pi$ to $\psi = \pi/2$, the difference in the phase shift variation becomes smaller.

4. CONCLUSION

We have shown that some reduction of frequency dispersion can be attained using transmission-line sections with positive anomalous dispersion. However, we are restricted here by relation (6), which makes it easer to obtain positive anomalous dispersion at large phase shifts ψ per period. An example in Section 3, where positive anomalous dispersion is observed between phase shifts $\pi/2$ and π, does not imply impossibility of existence of such dispersion at smaller ψ. In any case one cannot consider a series of cascaded unit cells with positive anomalous dispersion as an effective homogeneous transmission line, because the Bloch propagation constant $\beta_{\rm Bloch}$ cannot satisfy the condition $\beta_{Bloch} d \ll 1$.

Acknowledgements

This work has been supported by the *Metamorphose* Network of Excellence and partially funded by the Academy of Finland and TEKES through the Center-of-Excellence program.

References

[1] V.G. Veselago, "The electrodynamics of substances with simultaneously negative values of ε and μ," *Soviet Physics Uspekhi*, no. 10, pp. 509-514, 1968.

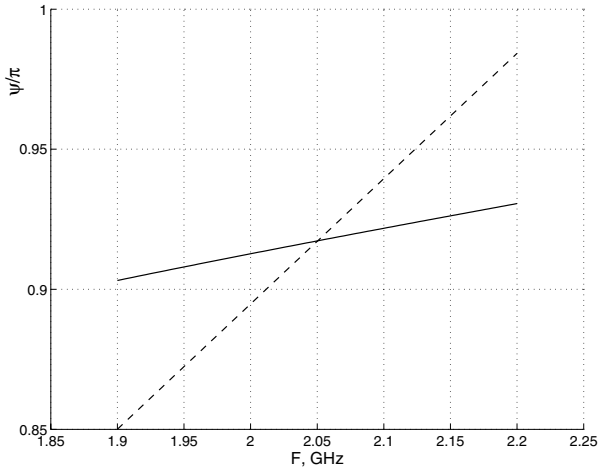

Figure 3: Frequency dependence of the phase shift per period for the structure with anomalous dispersion (solid curve) in comparison with a conventional TL (dashed curve).

[2] J.B. Pendry, "Negative refraction makes a perfect lens," *Phys. Rev. Lett.*, vol. 55, pp. 3966-3969, October 2000.

[3] A. Grbic and G.V. Elefthrediades, "Experimental verification of backward-wave radiation from a negative refraction index metamaterial," *J. Appl. Phys.*, vol. 92, pp. 5930-5935, November 2002.

[4] R.A. Silin and V.P. Sazonow, *Slow-wave structure*, Staschera, Boston-SPA Eng., National-Landing Science and Technology, 1971. Translated from Russian: R.A. Silin. *Slow-Wave structures*, Moscow: Sovetskoe Radio, 1966; R.A. Silin. *Periodic Waveguides*, Moscow: Phasis, 2002 (in Russian).

[5] N. Engheta, "An idea for thin subwavelenght cavity resonators using metamaterials with negative permittivity and permeability," *IEEE Antennas Wireless Propagat. Lett.*, vol. 1, pp. 10-13, 2002.

[6] S.A. Tretyakov, S.I. Maslovski, I.S. Nefedov, and M.K. Kärkkäinen, "Evanescent modes stored in cavity resonators with backward-wave slabs," *Microwave and Optical Technology Letters,* vol. 38, pp. 153-157, 2003.

[7] M.A. Antoniades and G.V. Eleftheriades, "Compact Linear Lead/Lag Metamaterial Phase Shifters for Broadband Applications", *IEEE Antennas and Wireless Propagation Letters*, vol. 2, pp. 103-106, 2003.

[8] D.R. Smith, W.J. Padilla, D.C. Vier, S.C. Nemat-Nasser, and S. Schultz, "Composite Medium with Simultaneously Negative Permeability and Permittivity," *Phys. Rev. Lett.*, vol. 84, 4184-4187, 2000.

[9] E. Shamonina, V.A. Kalinin, K.H. Ringhofer, and L. Solymar, "Magnetoinductive waves in one, two, and three dimensions," *J. Appl. Phys.*, vol. 92, pp. 6252-6251, 2002.

[10] M.C.K. Wiltshire, E. Shamonina, I.R. Young, and L. Solymar, "Dispersion characteristics of magneto-inductive waves: comparison between theory and experiment," *Electron. Lett.*, vol. 39, pp. 215-217, 2003.

Session 3b:
Circuits and Components

Utilizing Probability Distributions of Manufacturing Accuracy of Low Loss Band Pass Filter to Support System Design

Harri Eskelinen [(1)], Janne Heinola [(2)]

[(1)] Lappeenranta University of Technology
Department of Mechanical Engineering
PO. BOX 20, FIN-53851 LAPPEENRANTA, FINLAND
Email: harri.eskelinen@lut.fi

[(2)] Lappeenranta University of Technology
Department of Electrical Engineering
PO. BOX 20, FIN-53851 LAPPEENRANTA, FINLAND
Email: janne.heinola@lut.fi

Abstract
In many RF- and MW-applications the performance of a low loss band pass filter is in key role when designers carry out the system design task. When low loss filters are used no electrical tuning is reasonable because that would destroy the goal of minimized losses. Also the mechanical tuning of the filter is in many cases time and money consuming and it might lead to difficult iterations with various tuning and measuring stages. To avoid this we discuss in this paper about the possibility to utilize probability distributions of manufacturing accuracy of the filter to support the system design by substituting the results of the probability analysis into the iterative design functions of the low loss filter.

Keywords: low loss filter, system design, manufacturing accuracy

1. INTRODUCTION

The electrical behavior of a microwave device very often relies on the special boundary conditions defined by the mechanical structure surrounding the actual wave. A generalized way is to describe the associated magnetic and electric field vectors separately and to use perfectly conducting materials to restrict the volume of propagation. Based on these assumptions, the electric field vector turns to be perpendicular to a conducting wall. Imperfections in the material or the shape will thus immediately alter the field direction or pattern. For these reasons [1], it is necessary to take into account the importance of dimensional accuracy and to integrate the system design process into DFMA -approach (Design for Manufacturing and Assembly).

When we are integrating the design rules based on the physical and mathematical theory of microwaves propagation with the computer aided mechanical design we can use five tools like presented earlier in [2]. In [3] we have discussed about high power RF applications, which cannot use passive constructions based on printed circuit board solutions due to excessive losses. In [3] we have shown the importance of the mechanical aspects as guidelines for the system design. In this paper this research will be continued.

2. TESTED LOWLOSS FILTER

The case example is a milled sixth order interdigital Tshebyscheff band pass filter, which bandwidth is 10% and the attenuation ripple is 0.1 dB. Dimensions and the CAD-illustration of the center conductor are presented in Fig. 1. The results of similar designs in [4] suggest a residual attenuation 0.4 - 0.5 dB, 3/60 dB bandwidth ratio of 1 : 3 and an input VSWR between 1.1 and 1.3. Manufacturing tolerances were set to meet the IT-grade 5 [2]. For this filter we used high-strength ALUMEC -alloy to ensure the post-milling perpendicularity and straightness of the rods. The material data is given in [2].

3. FORMULATION OF DISTRIBUTIONS OF MANUFACTURING ACCURACY

In conventional manufacturing analysis the normal distributions are used to estimate the probability of the manufacturing accuracy. Designers can utilize the whole dimensional deviation area, according to the selected IT-grade. However, due to the high-accuracy milling process, which is used to manufacture the parts of this filter, it is possible to ensure that no under sized dimensions are allowed. This means that the milled dimensions are inside the positive allowed deviations of the tolerance grade IT5. Only this reason alone would give us a good reason to assume that the probability distribution of the expected deviations is far from the traditional normal distribution. In addition to this, the modern quality management

technology of CNC-machines gives the possibility to control e.g. tool wearing and machining parameters so that no under sized dimensions are possible. And finally, as shown in Fig. 1, the construction of the filter is designed so that either the accumulation of manufacturing deviations is positive or equal to zero. For these three reasons it is more appropriate to describe the probability of manufacturing accuracy by using Weibull- distribution instead of normal distribution (see Fig. 2)

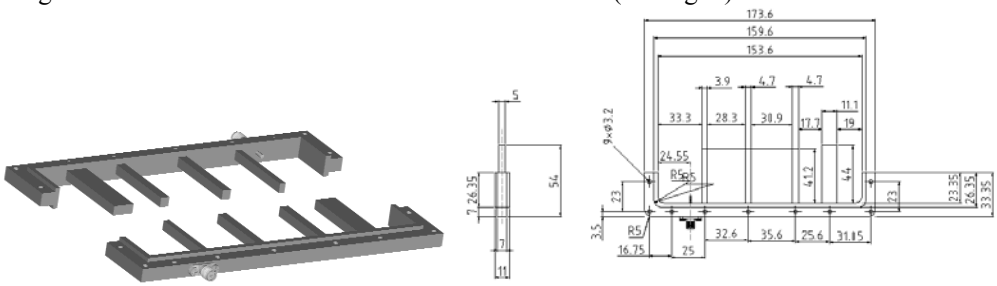

Fig. 1. The CAD-illustration and dimensions of the critical center conductor [2].

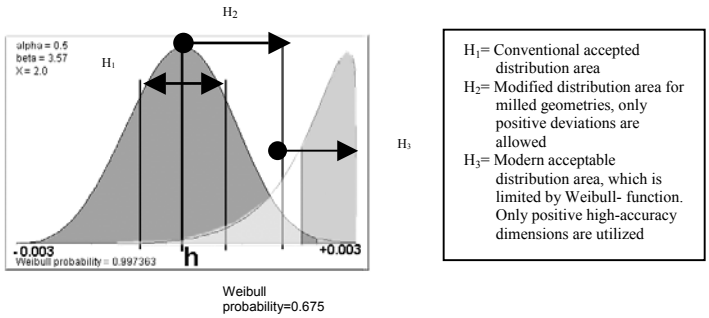

Fig. 2. Illustration of the acceptable rods height values "h" according to different distribution functions. In this case the height of the rod will be between 5.002…5.003 with Weibull probability of 0.67. Notice that if three parameter Weibull function gets value beta=3.57 it leads to normal distribution.

4. WAVE PROPAGATION CONDITIONS RELATED TO GEOMETRICAL TOLERANCES

Like shown in [2] and [5] there is the crucial importance of the possible difference in the dimensioned and milled lengths of the individual resonators to the performance of the filter. The most important aspect is to establish the length of the resonators perpendicular projection against to the adjacent resonator rod and the projection distance of the end of the rods from the opposite filter wall. The results are illustrated with the Smith chart (see Fig. 3), which shows the complex impedance matching of the two filter ports as a function of frequency.

Fig. 3. The Smith chart presentation of S11 shows that the two filters with ultimately sharp resonator roots give a good impedance match over the entire pass band (left). The track of the milling tool is visible on the bottom. Surface roughness is 0.8 μm (middle). A photo of the resonator root, which width is 5 mm (right) [2] and [5].

If the selected milling method produces a curved resonator root, the accurate length is no more predictable by computation and part of the incident wave will be reflected. The same type of mistuning

would have been caused if the perpendicularity requirements of rods were not met. Also the possible error of parallelism of the rods with the covers of the filter will change the performance of the filter. The theoretical interpretation of these to the geometric tolerances is illustrated in Fig. 4. The results showed that resonators with these types of manufacturing inaccuracies produce a worse matching, which is observed as a greater radial distance from the chart center. During the manufacturing process the most critical aspect is to control the bending and twisting of each rod. Relative large amounts of the bulk are actually milled away and forces may be high. These may lead to deformations, which disturb the performance either because the depth of the air gap will be changed or because the construction is not dense after assembly.

4.1 Required Tolerances

The center conductor of the discussed filter includes several resonator rods, which are all machined from one part together with the body. If we require resonator straightness only, it is possible that we have exactly right dimensioned and correctly shaped rods but their position against the body and against the adjacent rod might be false. To avoid these faults we recommend that the requirement of perpendicularity is set. The filter body is a good datum plain if the manufacturing quality of the center conductor is checked before assembly. The allowed tolerance area for perpendicularity is an orthogon (see Fig. 4). To take care of the assembly accuracy we have to set also the requirement of parallelism of the rods with two filter covers. (see Fig. 4). Required tolerances for this specific filter design are presented in Fig. 4.

Tolerance	Allowed deviations [mm]
Length	+/- 0.0065
Air gap	+/- 0.006
Longitudinal perpendicularity	0.016
Transversal perpendicularity	0.012
Width	+/- 0.004
Height	+/- 0.003
Parallelism	0.006
General tolerance	IT 5
Surface roughness	0.008

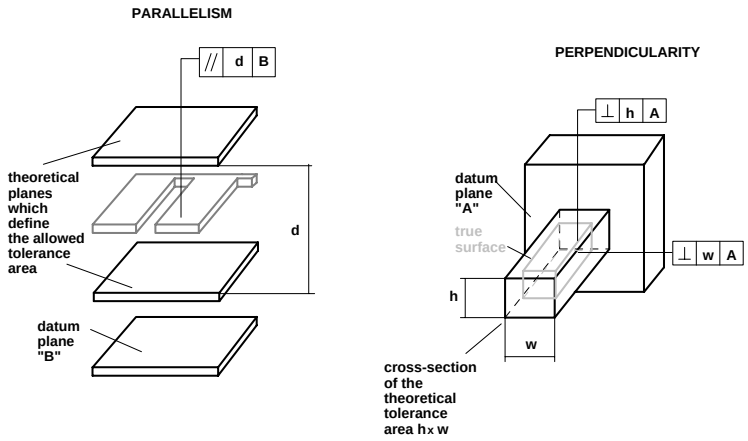

Fig. 4. Values for required tolerances of the rods of the center conductor (left). Requirement of parallelism is d=0.006 mm (middle) to ensure that the correctly shaped rods are positioned in an acceptable way against the body and against the adjacent rod perpendicularity must be required. The corresponding values for perpendicularity are= 0.012 mm and w=0.016 mm (right). [6].

5. ASPECTS OF SYSTEM DESIGN

For system design it is important to notice that the required tolerance grade (IT-grade) depends mostly on the operating frequency range of the device or the system. Further on the dimensional tolerances, geometric tolerances and required surface roughness depend from each other due to used manufacturing technology. If the construction material is known it is possible to select the most appropriate machining parameters beforehand and to model the surface geometry and roughness by using computer-aided simulation. This gives also the possibility to summarize the probability distributions of these three mechanical properties and estimate their affects to the system design. For this application the possibility to utilize previously described probability distributions of manufacturing accuracy of the filter is in key role.

The length of the resonator rod is the most important parameter for ensuring the expected performance of the filter. The distance between the sidewalls of the resonator is dimensioned to be quarter-wavelength at the center frequency of the filter. The lengths of the resonator rods are foreshortened because of the open-end capacitances. A possible mistuning of the open-end capacitances or changes in the resonator rod lengths mights cause shifting of the pass-band center frequency compared to the designed value. In addition, the pass-band response of the filter will be asymmetric if one or several of the open-end capacitances of the resonator rods are mistuned compared to others. The open-end capacitances can be

tuned by using tuning screws. Tuning mechanisms must be avoided when designing high power applications are designed or manufacturing costs or losses of the filter must be minimized.

In our case the distributions of the manufacturing accuracy are used to support system design by substituting the results of the probability analysis into the iterative design functions of the resonator rod. Therefore it is possible to get prepared to the expected performance deviations of the filter during the system design. Alternatively to ensure the adequate performance of the filter, the mechanical requirements can be set to the desired level. Cloete [7] has presented an approximation for calculation of resonance frequency of the interdigital filter. The approximation can be used for iteration of the effects of the manufacturing tolerances in the presented case. The resonance condition for the rectangular resonator rod is satisfied when

$$2\pi f_0 C_g = 1/\left\{Z_0 \tan\left(2\pi f_0 (l-g)/\left(c/\sqrt{\varepsilon_r}\right)\right)\right\}, \quad (1)$$

where f_0 is the resonance frequency, C_g is the gap capacitance, Z_0 is the characteristic impedance of the rod, l is the length of the resonator rod, g is the gap between the rod and the sidewall of the resonator, c is the velocity of light and ε_r is the dielectric constant of medium. An approximation for the gap capacitance of the resonator rod located between two adjacent resonators is

$$C_g \cong 2wC'_{fo}(2g/b, t/b) + tC'_{fo}(2g/(p_1+w), w/(p_1+w)) + tC'_{fo}(2g/(p_2+w), w/(p_2+w)) - \varepsilon\frac{wt}{g}, \quad (2)$$

where w is the width of the rod, C'_{fo} is the odd-mode fringing capacitance, b is the distance between the upper and the lower ground planes, p_1 and p_2 are the interconductor spacings associated with each of vertical edges and t is the thickness of the rod. The odd-mode capacitance can be found Fig 4, in [8]. For the resonator element that located between the input/output impedance transformer and other resonator element can the gap capacitance be calculated by using following approximation:

$$C_g \cong 2wC'_{fo}(2g/b, t/b) + tC'_{fo}(2g/(2s+w), w/(2s+w)) + tC'_{fo}(2g/(p+w), w/(p+w)) - \varepsilon\frac{wt}{g}, \quad (3)$$

where s is the distance between the impedance transformer and the resonator element.

6. CONCLUSIONS

By using the high-accuracy milling process for manufacturing the parts of the filter, it is possible to ensure that no under sized dimensions are allowed. This means that the milled dimensions are inside the positive allowed deviations of the selected tolerance grade. The construction of the filter is also designed so that either the accumulation of manufacturing deviations is positive or equal to zero. For these reasons it is more appropriate to describe the probability of manufacturing accuracy by using Weibull-distribution instead of normal distribution. The distributions of the manufacturing accuracy can be used to support system design by substituting the results of the probability analysis into the iterative design functions of the resonator rods.

7. REFERENCES

[1] H.Eskelinen,"Developing Computer Aided Design Environment for Microwave and Radio Frequency Mechanics Design," *Engineering Mechanics*, Vol 8, N. 5, 2001.

[2] H. Eskelinen, P. Eskelinen, K. Tiihonen, "Application of concurrent engineering in innovative manufacturing and design of a milled microwave filter construction ", *Proc. of the Managing Innovative Manufacturing MIM2000-conference*, Birmingham 17.-19.7.2000.

[3] H. Eskelinen, P.Eskelinen,"Manufacturability of all-metallic passive high power RF-components in volume production,"*Proc. of the URSI/IEEE XXIV Convention on Radio Science,* Turku 1999.

[4] G. Matthaei, L.Young, E. Jones*, Microwave Filters, Impedance, Matching Networks and Coupling Structures*, New York: McGraw Hill, 1964 (reprinted 1990).

[5] Eskelinen, H., "Developing Computer Aided Design Environment for Microwave and Radio Frequency Mechanics Design*," Engineering Mechanics*, Vol. 8, No. 5, 2001, pp. 343-351.

[6] H.Eskelinen, P.Eskelinen, *Microwave Mechanics Components*, New York, Artech House 2003.

[7] J.H. Cloete,"The Resonator Frequency of Rectangular Interdigital Filter Elements,"*IEEE Trans. on Microwave Theory & Tech.,* vol. MTT-31, NO 9, pp. 772-774, September 1983.

[8] W.J. Getsinger,"Coupled Rectangular Bars Between Paraller Plates,"*IRE Trans. on Microwave Theory & Tech.,* vol. MTT-10, NO 1, pp. 65-72, January 1962.

A Low Power Cryogenic L-band Amplifier Using GaAs HEMTs

Tommi Häkkilä[(1)], Jarno Järvinen[(2)], Esa Tjukanoff[(1)] and Sergey Vasiliev[(2)]

[(1)] Turku University, Department of Information Technology
[(2)] Turku University, Wihuri Physical Laboratory
FIN-20014 Turku, Finland
Email: **tomhak@utu.fi**

Abstract

The performance of a low noise L-band amplifier using commercially available packaged HEMTs is presented. The amplifier is designed to be the first intermediate frequency amplifier in a 128 GHz ESR spectrometer and it will be positioned at the 1 K plate of a dilution refrigerator. Two HEMTs are included in the device and its cryogenic part has a total power dissipation of 1mW. At a temperature of 4.2 K and a frequency of 1.05 GHz the gain of the amplifier is 24.5 dB and the noise temperature is 4 K.

Keywords: HEMT, Low Power, Cryogenic.

1. INTRODUCTION

The design of a new low noise amplifier (Fig. 1.) was stimulated by the requirement to observe atoms adsorbed to surfaces at subkelvin temperatures. This amplifier operates as the first intermediate frequency stage of a 128 GHz ESR spectrometer [1] positioned in a dilution refrigerator. The most natural place for the amplifier is at the 1 K plate. However, as the cooling capability there is only a few milliwatts the heat generation of the amplifier becomes a major issue (together with the noise capabilities). The design guideline was to use common low cost packaged HEMTs. With optimal bias these devices lead to a power consumption about an order of magnitude larger than our cooling capabilty. Our solution is to use a bias well below optimum and still achieve good results.

The spectrometer is a superheterodyne receiver with a schottky-diode mixer downconverting the millimeter wave signal to an intermediate frequency of about 1 GHz. The mixer is cooled to about 1 K in a dilution refrigerator. The downconversion mixer has a noise temperature of about 100 K so the IF stage noise will contribute directly to the system noise temperature. A noise temperature of below 10K would be low enough not to affect the system sensitivity too much.

HEMTs (High Electron Mobility Transistors) have commonly been used in cryogenic amplifiers on a wide spectrum of frequencies. Cryogenically cooled HEMTs can achieve extremely low noise temperatures.

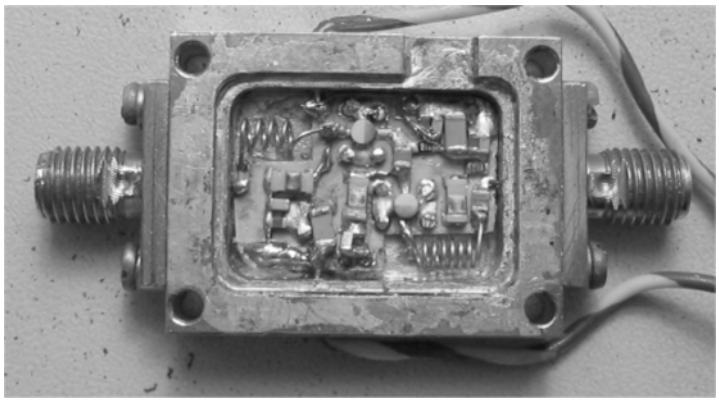

Fig. 1. Photograph of the amplifier.

The operation of GaAs based devices has been widely covered in several publications [2-7]. This earlier work concentrates mainly on presenting results on utilizing optimally biased transistors; ie the bias power is mostly around 15mW or more and the frequency band is typically around 4-8 GHz. We report on the performance of a GaAs HEMT amplifier biased well below optimum at about 1 mW and operating at a frequency of about 1 GHz.

2. DESIGN

The amplifier would have to withstand temperature cycling from 300K to 1K and back. It was decided to use a ceramically packaged device, due to easier availability and use as compared to a naked chip. Ceramically packaged transistors have been used often in cryogenic devices and were considered reliable. The HEMT chosen for this project was FHX35LG from Fujitsu. The passive components used were common chip components. The HEMTs were biased with a conventional operational amplifier-based active biasing circuit to regulate the amplifier bias conditions over the wide temperature range. All the components whose temperature dependence might significantly affect the amplifier bias conditions were placed on a separate bias board in room temperature. This also has the advantage of further reducing the power dissipated in the cold part. The FHX35LG has a nominal bias point of 3V and 10mA at room temperature.

The simulations using a manufacturer provided Materka model showed the room temperature gain to stay above 18dB down to about 0.5mW of DC power, but the measurements showed the gain to drop steeply as the bias power was reduced below about 3mW. An experimental value of transconductance was obtained to be used in constructing a Pospieszalski noise model, the other characteristics of which were obtained by matching the noise model with the Materka model. The device performance was simulated with a bias value of 0.65V and 3.1mA, equalling 2mW of DC power.

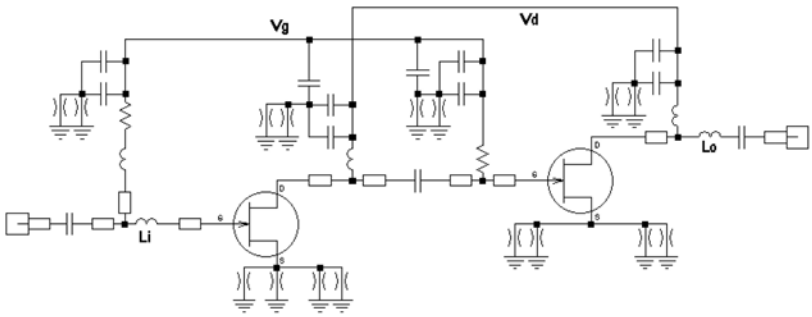

Fig. 2. Schematic of the amplifier

It is reasonable to assume that during cooling the changes in the reactive components in the HEMT small signal model would be small enough to be neglected. The resistive components and the transconductance would change somewhat, as well as the equivalent noise temperatures of the intrinsic resistances. These effects are well covered in the literature [8-11]. A prototype based on the simulations was made and matched for peak performance with 50 Ω port impedances at 1.15GHz in room temperature with two air core inductors, one at input (Li), the other at output (Lo), cf Fig. 2. The matching coils are the only critical components in the cold part of the amplifier. The simulations showed the performance not to change very much with different port impedances. It was found that the input and output reflection coefficients had moderately deep notches at the optimum matching points and their frequencies could be tuned independently of each other over a moderately wide range of frequencies, if a different optimum frequency was required.

3. RESULTS

The prototype was cooled to 4.2 K by dipping it into liquid helium in a helium-gas filled dipstick. The gain vs. bias was measured and the bias point of 0.25 V and 4 mA for both stages together was chosen as a compromise between gain and power consumption. At this bias point the device had a maximum gain of about 24.5 dB at 1.05 GHz, Fig 3*a*. The performance peak frequency changed by about 100 MHz as compared to the room temperature frequency due to the neglected changes in the model reactive components and, to a greater amount, the mechanical changes in the matching coils.

The noise temperature was measured at this bias point by heating a 50 Ω termination to several temperatures and measuring the resulting noise powers with a spectrum analyzer [7],[12]. The lowest value obtained with 1 mW of bias power was about 4 K, Fig. 3*b*. The measurement error was estimated to be 3 K. The amplifier had a -1dB gain compression point at –30 dBm at the input due to the very low bias point, but the power output of the schottky mixer should stay below –60 dBm. The gain at room temperature was about 19 dB at the same bias value and the frequency of 1.15 GHz. The noise temperature was measured to have a minimum of about 65 K at room temperature. The gain is higher than 20 dB for the required operating bandwidth of 850 MHz to 1.3 GHz and the noise temperature is below 10 K at 4.2 K. The input reflection coefficient (S_{11}) was measured to be better than 3 dB with a peak value of 8 dB and the output reflection coefficient (S_{22}) is 5 dB and 12 dB, respectively.

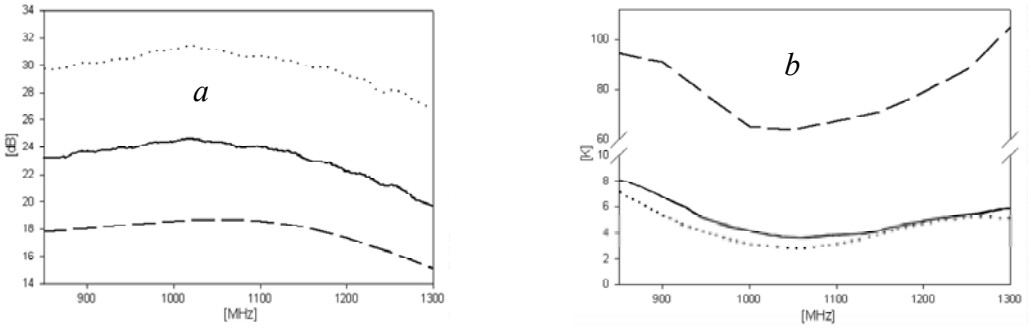

Fig. 3. *a*) Gain, *b*) Noise Temperature. Solid line = 4.2 K and 1 mW bias, Dashed line = Room temperature and 1 mW bias, Dotted line = 4.2 K and 4 mW bias

4. CONCLUSION

The performance of a cryogenically cooled low noise, low power L-band IF amplifier using commercial ceramically packaged GaAs HEMTs was presented. The amplifier used the HEMTs far below their nominal bias levels but still achieves a noise temperature of 4 K and a gain of 24.5 dB at the frequency of 1.05 GHz and a bias power of 1 mW at an amplifier temperature of 4.2 K. Raising the bias power to 4 mW (0.5 V and 8 mA) increased the gain to 31.5 dB and reduced the noise temperature to 3 K.

The increase in the amplifier gain versus temperature was larger than estimated and the noise temperature was slightly higher at room temperature but lower at the liquid helium temperature, which was to be expected due to the inaccuracies in the model at this low bias levels as well as the errors in the estimated temperature changes.

With a mixer noise temperature of around 100 K, achieving a noise temperature of less than 10 K for the IF amplifier should be good enough. Further reduction of the noise might be obtained by using InP-based HEMTs, when GaAs can be used to achieve low enough noise temperatures with low enough power dissipation.

5. ACKNOWLEDGEMENTS

The authors would like to thank prof Simo Jaakkola (University of Turku) for support and Viktor Sibakov (Helsinki Univeristy of Technology) for lending us a RF noise source.

6. REFERENCES

[1] S. Vasilyev, J. Järvinen, E. Tjukanoff, A.A. Kharitonov, and S. Jaakkola, Rev. Sci. Instr. 75, p 94, 2004.

[2] Stephen Padin and Gerardo G. Ortiz, "A Cooled 1-2GHz Balanced HEMT Amplifier", IEEE Transactions on Microwave Theory and Techniques, Vol. 39, No. 7, July 1991.

[3] Cristophe Risacher and Victor Belitsky, "GaAs HEMT Low-Noise Cryogenic Amplifiers From C-Band to X-Band With 0.7-K/GHz Noise Temperature", IEEE Microwave and Wireless Components Letters, Vol. 13, No 3, March 2003.

[4] S. Padin, D. P. Woody, J. A. Stern, H. G. LeDuc, R. Blundell, C.-Y. E. Tong and M. W. Pospieszalski, "An Integrated SIS Mixer and HEMT IF Amplifier", IEEE Transactions on Microwave Theory and Techniques, Vol. 44, No. 6, June 1996.

[5] Niklas Wadefalk, Anders Mellberg, Iltcho Angelov, Michael E. Barsky, Stacey Bui, Emmanuil Choumas, Ronald W. Grundbacher, Erik Ludvig Kollberg, Richard Lai, Niklas Rorsman, Piotr Starski, Jörgen Stenarson, Dwight C. Streit, and Herbert Zirath, "Cryogenic Wide-Band Ultra-Low-Noise IF Amplifiers Operating at Ultra-Low DC Power", IEEE Transactions on Microwave Theory and Techniques, Vol. 51, No. 6, June 2003.

[6] J. W. Kooi, "Cryogenic Low Noise Balanced I.F. Amplifiers", available at http:// www.submm.caltech.edu/cso/receivers/papers/ballna.pdf

[7] Cristophe Risacher and Victor Belitsky, "Low Noise Cryogenic IF Amplifiers for Super Heterodyne Radio Astronomy Receivers", Proceedings of the Thirteenth International Symposium on Space Terahertz Technology, March 2002.

[8] J. J. Bautista, J. Laskar, P. Szydlik, "On-Wafer, Cryogenic Characterization of Ultra-Low Noise HEMT Devices", TDA Progress Report 42-120 February 15, 1995 pp.104-120.

[9] I.Angelov, N.Wadefalk, J.Stenarson, E.Kollberg, P.Starski, H.Zirath "On the Performance of Low Noise, Low DC Power Consumption Cryogenic Amplifiers", presented at the IEEE MTT-s in 2000.

[10] Isaac López-Fernández, Juan Daniel Gallego Puyol, Otte J. Homan, and Alberto Barcia Cancio, "Low-Noise Cryogenic X-Band Amplifier Using Wet-Etched Hydrogen Passivated InP HEMT Devices", IEEE MICROWAVE AND GUIDED WAVE LETTERS, VOL. 9, NO. 10, OCTOBER 1999, pp. 413-415

[11] C.Risacher, M. Dahlgren, V.Belitsky, "A 3.4-4.6 GHz Low Noise Amplifier", Proceedings of Gigahertz 2001 Symposium, Lund, Sweden, November 26-27, 2001.

[12] Tom Lee, Stanford University Department of Electrical Engineering, CMOS RF Integrated Circuit Design course Handout 9, "Noise Figure Measurements", Winter 2003.

An Integrated Differential Single-chip VCO for S-band

Hannu Salminen[(1)], Pekka Eskelinen[(2)], Jan Holmberg[(1)]

[(1)]VTT Information Technology, PL 12021, 02044, VTT, FINLAND
Emails: hannu.salminen@vtt.fi, jan.holmberg@vtt.fi

[(2)]Helsinki University of Technology, Finland
Email: pekka.eskelinen@hut.fi

Abstract
A fully integrated 2.4 GHz differential voltage-controlled oscillator (VCO) is presented. The circuit can be tuned from 2.1 to 3.6 GHz without any component changes or re-dimensioning. The phase noise of the oscillator is -102 dBc/Hz at 1 MHz offset from 2.4 GHz. The design has been fabricated using a 0.35 µm SiGe BiCMOS process and the circuit area of the prototype is 0.9 mm^2 including on-chip inductors. The prototype chip draws 3.1 mA current from a 2 V supply.

Keywords: VCO, Differential oscillator, SiGe BiCMOS

1. INTRODUCTION

Many modern communication and radar systems utilize modulation and detection schemes, which are based on so-called I and Q signals, having a phase shift of 90 degrees. In some other designs, opposite phase signals are encountered. The efforts are targeted towards achieving an optimum balance between band usage and transmission capacity [1]. Of course, in radar the aim is to improve detection possibilities [2]. Regardless of application, these devices require local oscillators giving suitably phased outputs, for example in quadrature form [3]. Frequency agility is typically desired [4], whereby circuit topologies relying on inherently narrow-band external phase shifting networks are less favourable.

This paper describes an alternative approach of local oscillator source generation in the form of a single chip voltage controlled oscillator. A completely integrated design having no external components was selected. The prototype unit is manufactured with 0.35 µm SiGe BiCMOS process, which gives a reasonable compromise between a high cut-off frequency of 60 GHz and low manufacturing costs. It further supports relatively easy integration with common CMOS-type logic modules, as indicated e.g. in [5] and [6]. One of the greatest challenges was the low Q of substrate-based coils [7].

2. OSCILLATOR DESIGN AND SIMULATION

Figure 1 shows the simplified schematic of the voltage-controlled oscillator. The operational principle of the circuit is based on the cross-connected differential pair (Q1, Q2), which is connected to the LC-circuit. The negative resistance [8,9] of the differential pair is:

$$R_n = 2/g_m \tag{1}$$

Here g_m is the transconductance of the transistor. To maintain oscillation, the negative resistance compensates the loss in the LC resonator. For low phase noise, a high Q-factor of the resonator and high oscillation amplitude are required. Losses and the reduction in Q-factor are primarily due to substrate and metal losses of the inductor wirings. To reduce these problems small inductances and thick metal layer were used for inductors. Accumulation-mode MOS varactors [10] (X1, X2) are used for frequency control. Transistors Q3 and Q4 control the emitter current of the oscillator transistors. The output is taken from the collector of the transistors Q1 and Q2 and fed to a buffer stage. The realized buffer is an emitter follower (not shown in Fig. 1).

After the initial values were designed, the VCO circuit was simulated using commercial ADS and APLAC design tools. The simulated tuning range is 1.5 GHz and the current consumption 3.4 mA from a 2.0 V power supply. The simulated single-ended output power to a 50 Ω load equals -20 dBm.

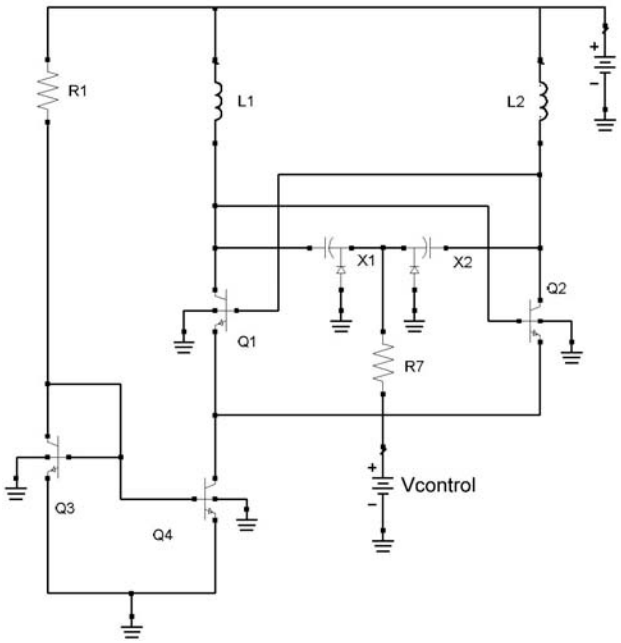

Fig. 1. Schematic of the basic VCO without emitter follower.

3. MEASUREMENTS

Critical RF parameters were measured with a Cascade Microtech probing system connected to a Rohde & Schwartz FSEM20 spectrum analyzer. The measurements were performed with a power supply voltage V_{dd} = 2.0 V. The VCO, however were able to work with V_{dd} as low as 1.5 V. The chip micrograph is shown in Figure 2. The measured frequency tuning range was 1.5 GHz and the tuning sensitivity 2 GHz/V at 2.8 GHz. Frequency pushing was observed to be 47 MHz/V. A fixed frequency comparison unit on the same wafer shows only 2 MHz/V. Frequency pulling was 4.3MHz at 12 dB return loss. Highest harmonic levels were below -18 dBc in all cases (Fig. 3). When the insertion losses of the cables and the HP 11612A blocking capacitor are taken into account, the real output power equals -20 dBm at nominal supply voltage.

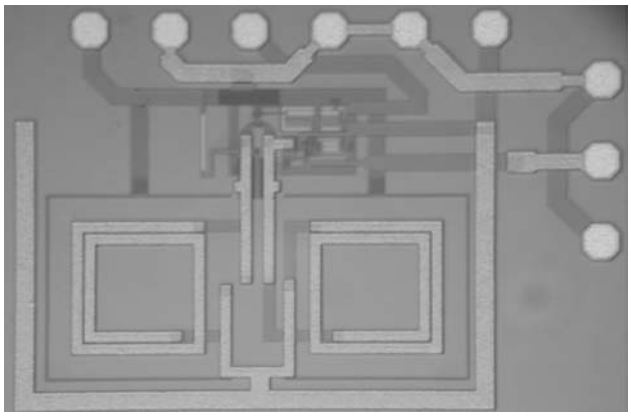

Fig. 2. Chip micrograph (0.7 mm x 1.2 mm).

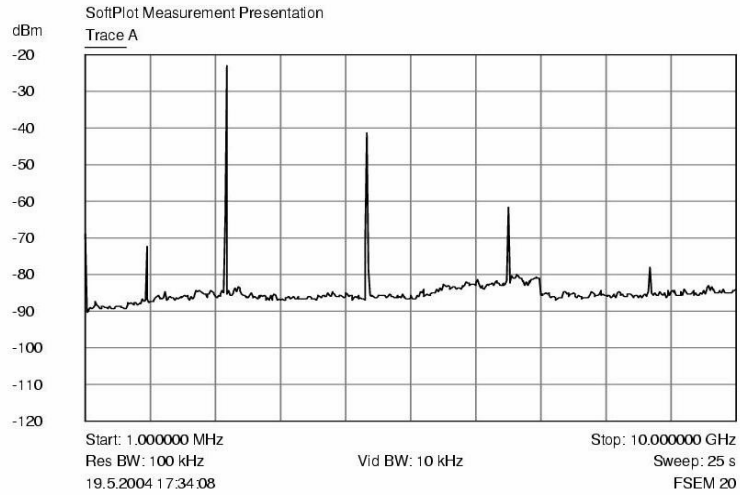

Fig. 3. The spectrum of the oscillator after emitter follower. All harmonics are less than -18 dBc.

At 1 MHz from the center frequency, the measured phase noise level was -102 dBc/Hz [11,12]. The measured and simulated values are shown in Fig. 4. The measured results are indicated with a solid line and the simulated curves with a dotted line. Here the simulated values agree from 100 kHz but show much too optimistic behaviour closer to the carrier.

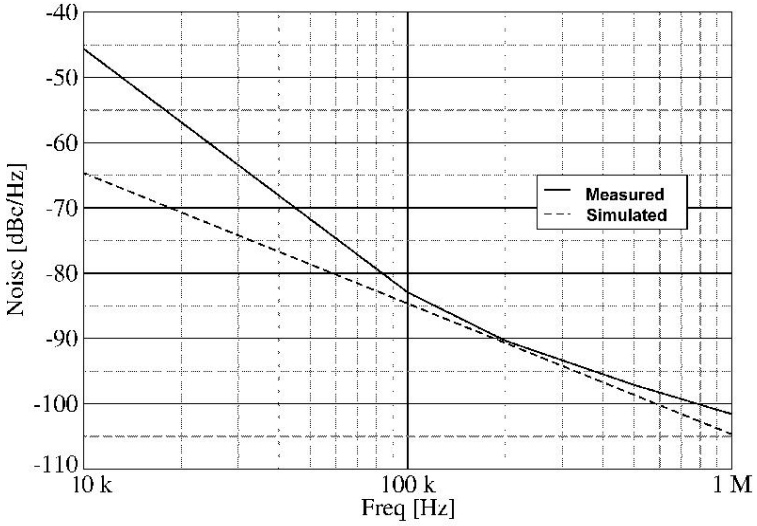

Fig. 4. Measured Phase noise is -102 dBc/Hz at 1 MHz offset.

3. CONCLUSIONS

The design of a differential VCO with fully integrated LC-tank fabricated in 0.35 μm SiGe BiCMOS process is demonstrated. MOS varactors are used as frequency control. The simulated and measured frequency ranges match quite closely. Further simulations indicate that the phase noise of the VCO can be improved by modifying the bias circuits of the oscillator transistors.

References

[1] R. Ludwig and P. Bretchko, *RF Circuit Design*, Prentice Hall, Upper Saddle River, 2000.

[2] P. Lacomme, J. Hardange, J. Marchais and E. Normant, *Air and Spaceborne Radar Systems*, William Andrew Publishing, Norwich, pp. 190-192, 2001.

[3] S. Hackl, J. Bock, G. Ritzberger, M. Wurzer and A. Scholtz, ”A 28 GHz Monolithic Integrated Quadrature Oscillator in SiGe Bipolar Technology,” *IEEE Journal of Solid State Circuits*, Vol. 38, No. 1, pp. 135-137, January 2003.

[4] M. Kihara, S. Ono and P. Eskelinen, *Digital Clocks for Synchronization and Communications*, Artech House, Norwood, pp. 222-229, 2003.

[5] D. Harame, D. Ahlgren, D. Coolbaugh, J. Dunn, G. Freeman, J. Gillis, R. Groves, G. Hendersen, R. Johnson, A. Joseph, S. Subbana, A. Victor, K. Watson, C. Webster and P. Zambardi, ”Current Status and Future Trends of SiGe BiCMOS Technology,” *IEEE Transactions on Electron Devices*, Vol. 48, No. 11, November, pp. 2575-2594, 2001.

[6] J. Cressler, ”SiGe HBT Technology: A New Contender for Si-Based RF and Microwave Circuit Applications,” *IEEE Transactions on Microwave Theory and Techniques*, Vol. 46, No. 5, pp. 572-589, May 1998.

[7] J. Burghartz, D. Edelstein, M. Soyuer, H. Ainspan and K. Jenkins, ”RF Circuit Design Aspects of Spiral Inductors on Silicon,” *IEEE Journal of Solid State Circuits,* Vol. 33, No.12, pp. 2028-2034, December 1998.

[8] Nhat M. Nguyen and Robert G. Meyer, ”Start-up and Frequency Stability in High-Frequency Oscillators, ” *IEEE Journal of Solid State Circuits*, Vol. 27, No. 5, pp. 810-820, May 1992.

[9] G. Konstanznig, T. Pappenreiter, L. Maurer, A.Springer, R.Weigel, "Design of a 1.5 V, 1.1 mA Fully Integrated LC-tuned Voltage Controlled Oscillator in the 4 GHz-band using a 0.12 μm CMOS-Process," Institute for Communication Engineering, University of Linz, Austria, pp. 1-4.

[10] Pietro Andreani and Sven Matisson,” On the Use of MOS Varactors in RF VCO's,” *IEEE Journal of Solid State Circuits*, Vol. 35, No. 6, pp. 905-910, June 2003.

[11] B. Neubig and W. Briese, *Das Grosse Quarzkochbuch*, Franzis’ Verlag, Feldkirchen, pp. 315-339, 1997.

[12] Ali Hajimiri and Thomas H. Lee, ” A General Theory of Phase Noise in Electrical Oscillator”, *IEEE Journal of Solid State Circuits*, Vol. 33, No. 2, pp. 179-194, February 1998.

25 MHz Standard Frequency and Time Transmitter of MIKES

Kalevi Kalliomäki, Tapio Mansten, Ilkka Iisakka

Centre for Metrology and Accreditation (MIKES), Otakaari 7 B, FI-02150 Espoo, Finland

Introduction

MIKES (earlier VTT/AUT) has taken care of Finnish official time and frequency since 1976. Finnish broadcasting company (YLE) as a partner disseminated time signal using audio channels and frequency with the aid on TV synchronisation signal. The accuracy of frequency obtained was better than 10^{-11} as a relative value.

Digitalisation of TV-links caused random delays at every link station and the accuracy of the frequency is now 100 times worse than earlier when analogue links were used. Calibration of high quality oscillators needs better easily available reference.
That is why MIKES has been designed and constructed an own transmitter and a suitable receiver.

Frequency selection

When looking tables of allocated frequencies for standard frequency transmitters, we selected 25 MHz (λ = 12 m) for several reasons. First, when using a high frequency the antenna size is convenient. Secondly, 25 MHz lies at short wave band, which means that one, can use cheap, commonly available receivers and transmitter components. Earlier (1977) we have tried to use 250 MHz, but with bad success due to lack of receivers. Third reason was that we could utilise 27 MHz citizen band components.

25 MHz Transmitter

Transmitter is now on air for test cycles to find a suitable format for time signal modulation. IRIG-B and DCF-77 code are considered. The latter is better for aural time signal reception because of one Herz (second tick) bit rate and easily recognisable minute mark.
Transmitter power is around 100 W and antenna (vertical ¾ λ dipole) gain near 10 dB. Antenna height during test cycles is 20 m above sea level but it will be 40 m next year.
The 25 MHz carrier comes from synthesised HP signal generator, which is locked to our atomic clock (Cs2). The relative accuracy of the carrier frequency is better than $1 \cdot 10^{-13}$. One of the above mentioned time codes amplitude modulates the carrier. Those codes include full time code consisting of day, hour, minute and second data.

Coverage area of the signal

The coverage area is estimated to be the circle inside kehä III when using outdoor antenna with preamplifier. At first tests signal level at Soukka, 12-km westward from MIKES seen to be 0,5 mV when using good outdoor antenna. The signal was traced at Lohja too, when using a sensitive receiving system.

Because of good conductivity of seawater, stable ground wave signal may be useable at Tallinn offering "international" frequency comparison. AS Metrosert in Tallinn, a corresponding organisation like MIKES, is interested to test this possibility.

25 MHz standard frequency receiver

As a diploma work a receiver for above mentioned signal, has been developed. It consists of standard components like a conventional short wave receiver; an oven controlled 10 MHz crystal oscillator (OCXO) and IRIG demodulator. Associated electronics takes care of phase locking etches.
Both received signal and OCXO reference signal, phase modulated at 2,5 kHz, pass the short wave receiver. Thus delays in receiver are mainly eliminated. Phase difference is measured by applying 2,5 kHz phase detection circuitry.

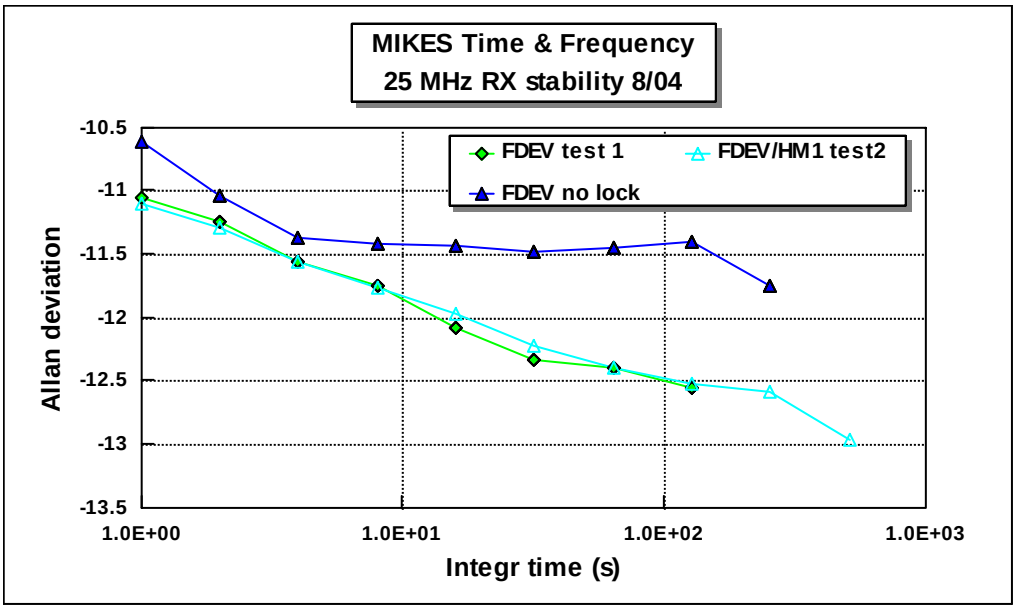

Fig 1 Allan frequency deviation of 10 MHz output of the receiver

Figure 1 shows the FDEV (Allan frequency deviation) of the 10 MHz output of the receiver. Test site with a indoor antenna was in a laboratory, within 50 meter from transmitter antenna. Thus the signal level was quite high, around 1 mV, but the received signal was suspect to laboratory interference. A special phase comparator,

capable to resolve $1 \cdot 10^{-13}$ just in one second, was used, Hydrogen maser (HM1) as a stable reference.
The uppermost curve shows the OCXO stability (no lock) and two lowermost curves stability in locked condition. One second frequency stability is better than $1 \cdot 10^{-11}$ (10 ps/s) . The stability is inversely proportional to the integration time and the the reference stability $1 \cdot 10^{-13}$ is gained on ten minutes.

Conclusions

The short-term frequency stability of the constructed receiver, at least near transmitter site, is about 100 times better than earlier TV-frequency standard before year 2001, when stable analog TV-links were used. Thus the constructed TX/RX system fulfils what is planned. Approximately 100 TV-standard units, produced by Jutel Oy, are still in use in whole Finland due to comprehensive coverage. Because the coverage are of the new system is the capital area only, we estimate that some 30 new receiver units are needed here.
Of course GPS is a competitor but US military authorities control it. In EU we can't trust that this service is always available, at lest free of charge. Therefore an independent service was needed.

An Integrated Class-S Modulator for 13.5 MHz

Ville Saari, Pasi Juurakko, Jussi Ryynänen, Kari Halonen

Helsinki University of Technology, Electronic Circuit Design Laboratory,
Espoo, P.O.Box 3000, 02015-HUT, Finland
Email: vsaari@ecdl.hut.fi

Abstract
An integrated 13.5 MHz class-S modulator for an EER transmitter is described. The modulator uses 3.3 V supply voltage and was fabricated using 0.18 µm CMOS technology. The measured output power was 22.8 dBm for a 10 MHz rectangle pulse input signal with 50 % duty cycle. The chip area is 1.6 mm^2.

Keywords: Integrated circuit, CMOS technology, class-S, EER technique

1. INTRODUCTION

Wideband multicarrier systems are needed in the future for high speed wireless LANs and digital television broadcasting. In these systems, the design of the power amplifier is one of the key blocks and has a high impact on the coverage, the product cost and the power consumption. Typically, the multicarrier signals have a high peak-to-average ratio caused by the large number of independent subcarriers which are added at the modulator in random phase and amplitude [1]. Although transmitter operates most of the time at the average power, it must be able to amplify the peak values of the signal without distortion. Therefore, linearity requirements for the transmitter are becoming stringent and it is likely, that the power amplifier linearisation methods must be used. To achieve low power consumption of the transmitter, it is prefer to use linearisation techniques which also improves efficiency. The envelope elimination and restoration (EER) technique is a promising choice, since its efficiency is largerly independent of signal level [2].

2. EER TRANSMITTER

The principle of an EER transmitter is to split the input signal into two paths. A baseband path contains the envelope of the input signal and a radio frequency (RF) path contains a constant-envelope phase modulated signal [3]. Fig. 1 a shows an EER transmitter, where signal separation is performed by the digital signal processing (DSP). With this concept it is possible to integrate the whole circuit on a single chip except the low-pass filter.

In the RF path, a constant-envelope phase modulated baseband signal $V_{phase}(t)$ is up-converted to radio frequency by a mixer and amplified by a high-efficient non-linear RF power amplifier. The low frequency envelope signal $V_{envelope}(t)$ can be amplified by a high-efficient class-S modulator and then applied as the bias voltage $V_{dd}(t)$ to the RF power amplifier after that [4]. Thus, the amplitude modulation to the output signal $V_{out}(t)$ is achieved through variation of the supply voltage.

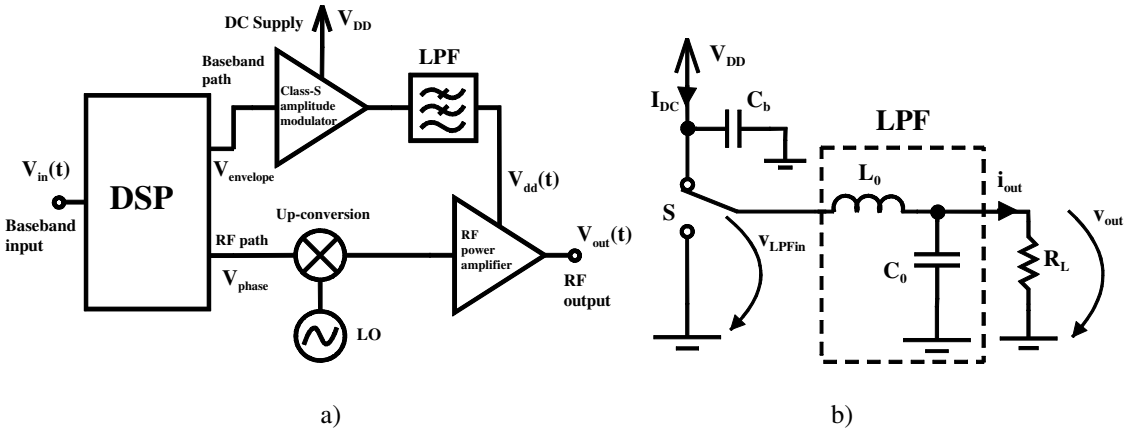

Fig. 1. a) EER transmitter and b) a simplified circuit for a voltage-switching class-S modulator.

3. CLASS-S MODULATOR

In a class-S modulator the transistors are used to form a switch shown in Fig. 1 b. A large capacitor C_b will bypass all ac signal components from V_{DD} to ground. The voltage v_{LPFin} applied to the low-pass filter is a square wave with levels 0 and $+V_{DD}$. The low-pass filter after switches allows the slowly varying average or the dc voltage component of the rectangular input voltage waveform to appear in the load R_L producing output voltage $v_{out}(t)$ and current $i_{out}(t)$.

By changing the pulse widths or the duty cycle of the voltage v_{LPFin} different average output voltage signals are produced. The input pulse width modulated (PWM) signal of the class-S modulator is generated by the DSP. PWM signal is a train of pulses whose width varies depending on the amplitude of the envelope signal [3]. The peak output power of a class-S modulator is $P_{out,peak} = V_{DD}^2 / R_L$. In the ideal case the output voltage and current are never nonzero simultaneously and therefore, the efficiency of an ideal class-S modulator is 100 % [3]. In practice, the efficiency reduces because of static and dynamic losses.

The static losses are associated with the nonzero saturation voltage and saturation resistance of the transistors as well as parasitic resistances in the interconnections, and parasitic resistances in the filter components. The efficiency degradation because of saturation voltage can be represent by using $V_{eff} = V_{DD} - V_{DS,sat}$ and the reduction caused by saturation resistance and parasitic resistances

$$V_{eff} = V_{DD} \cdot \frac{R_L}{R_L + R_{par}}. \tag{1}$$

The dynamic losses are associated with switching transitions. Real transistors have parasitic drain-source output capacitance. In addition, wide metal wiring must be used at the output of an integrated class-S modulator because of large transient currents adding parasitic shunt capacitance at the output of the circuit. Therefore, the total dynamic energy dissipation is $C_{shunt} \cdot V_{DD}^2$ per each cycle. Furthermore, real devices take a finite length of time to switch from a cutoff state to a saturated state and vice versa and this is an other dynamic loss mechanism [3]. At the turn-on instant, the voltage starts to fall from its initial value and the current starts to rise toward its final value. Thus, there is a finite crossover period when both the voltage and current are nonzero. The same is true at the turn-off instant [5].

4. DESIGN OF CLASS-S MODULATOR

In this work a class-S modulator was realised as a single chip integrated circuit using a 0.18 µm silicon CMOS technology. The switches were implemented using inverters. Altogether five inverters were cascaded in order to amplify the low level PWM input signal to desired level and on the other hand to accomplish low enough capacitive load to the DSP circuit.

It is well known fact that the mobilities of the PMOS and NMOS transistors are inherently unequal. The length of all transistor fingers were selected to be equal. Instead, based on process parameters and ELDO simulations the width of PMOS transistors was selected to be three times that of the NMOS transistors in this design. Each inverter stage was designed to be larger than the preceding stage approximately by a width factor *e* (i.e. base of natural logarithms), which minimises the total delay of the inverter chain.

Due to high output power and nonidealities discussed in Section 3 the layout design was critical. Six on-chip bonding pads, several stacked metal layers and wide metal wiring were used to distribute supply voltage efficiently. This is because the circuit draws large transient currents, over 300 mA, from the power supply during the switching instants. For the same reason several unit transistors were used in each cascaded inverters. To avoid heating unit transistors were separated from each other by 10–20 µm. Furthermore, NMOS unit transistors and three times wider PMOS unit transistors were placed symmetrically. Any additional parasitic capacitance and resistance were minimised in the signal interconnections as well as at the output of the circuit within the limits of the electromigration design rules. The microphotograph of the fabricated class-S modulator is shown in Fig. 3. The chip area is 1.6 mm^2.

For the off-chip low-pass filter, a fourth order Chebyshev prototype with 0.1 dB passband ripple and one transmission zero was selected. The –3 dB frequency of the filter was designed to be at 13.5 MHz. Ceramic surface mount chip capacitors and multi-layer chip inductors were used to implement the fourth order series inductor shunt capacitor type low-pass filter.

The modulator was designed to drive a low 10 Ω impedance, which represents the impedance seen from the drain of the class-E power amplifier.

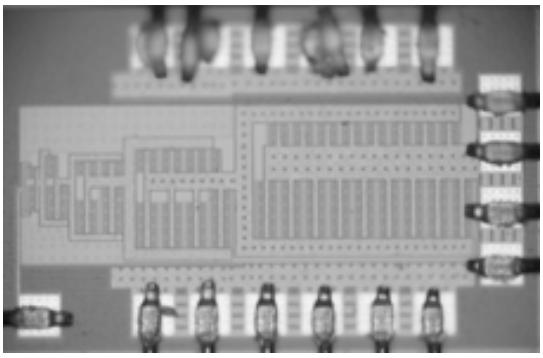

Fig. 3. Microphotograph of the fabricated class-S modulator.

5. SIMULATIONS AND MEASUREMENTS

The on-chip parasitic capacitances of the circuit were extracted from the layout and included in ELDO simulations. In addition, the resistances and reactances of the on-chip bonding pads and off-chip bonding wires as well as the parasitic components of the low-pass filter were taken into account in simulations.

As mentioned before, the low-pass filter was designed to have 10 Ω terminations. However, the implemented external low-pass filter had to be measured using a network analyzer with 50 Ω terminations. The measured frequency response is presented in Fig. 4 a together with a corresponding (i.e. 50 Ω terminations) simulation result. Due to accurate matching between these two curves, it can be assumed that the frequency response of the implemented low-pass filter in the case of 10 Ω terminations is in accordance with the prototype.

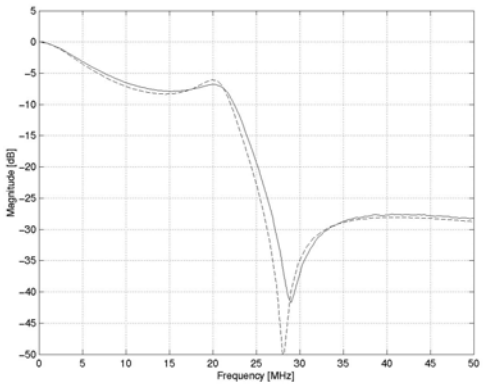

a)

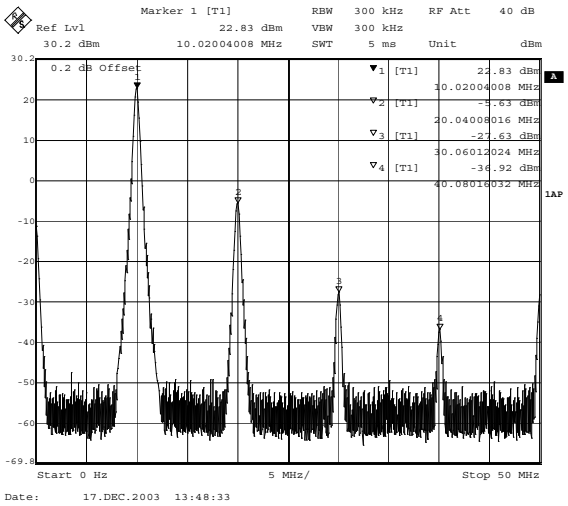

b)

Fig. 4. a) Measured frequency response (50 Ω terminations) of the implemented low-pass filter (solid line) and the simulated one (dashed line) and b) the measured output spectrum in case of a 10 MHz rectangle pulse input signal with 50 % duty cycle.

The class-S modulator measurements were performed in 50 Ω impedance environment. 3.3 V power supply voltage was used. Input rectangle pulse signals were generated by a pattern generator by setting 3.3 V voltage level for the logic one and 0 V for the logic zero. The measured output spectrum in case of a 10 MHz rectangle pulse input signal with 50 % duty cycle is shown in Fig. 4 b. As can be seen the output power at 10 MHz to 50 Ω load is 22.8 dBm. The corresponding simulation gave 20.6 dBm. The

measured dc current consumption was 115 mA and hence, the efficiency can be calculated to be 50.5 %. The measured output power level in case of 12 MHz rectangle pulse input signal was 23.5 dBm.

A pulse width modulated signal like pulse series was generated by the used pattern generator with time steps 5 ns. The measured output spectrum of the class-S modulator circuit in this case is shown in Fig. 5 a. The output power level at 10 MHz is 18.8 dBm. The measured current consumption was 61 mA, which corresponds to 38.5 % efficiency. Finally, a second order sigma-delta modulated (SDM) data (i.e. ones and zeros) was generated using MATLAB. This data was used as a square wave input signal and the measured output spectrum is shown in Fig. 5 b. The power level of the wanted 2 MHz signal is 9.7 dBm. The noise shaping of the sigma-delta modulator can be seen up to 20 MHz.

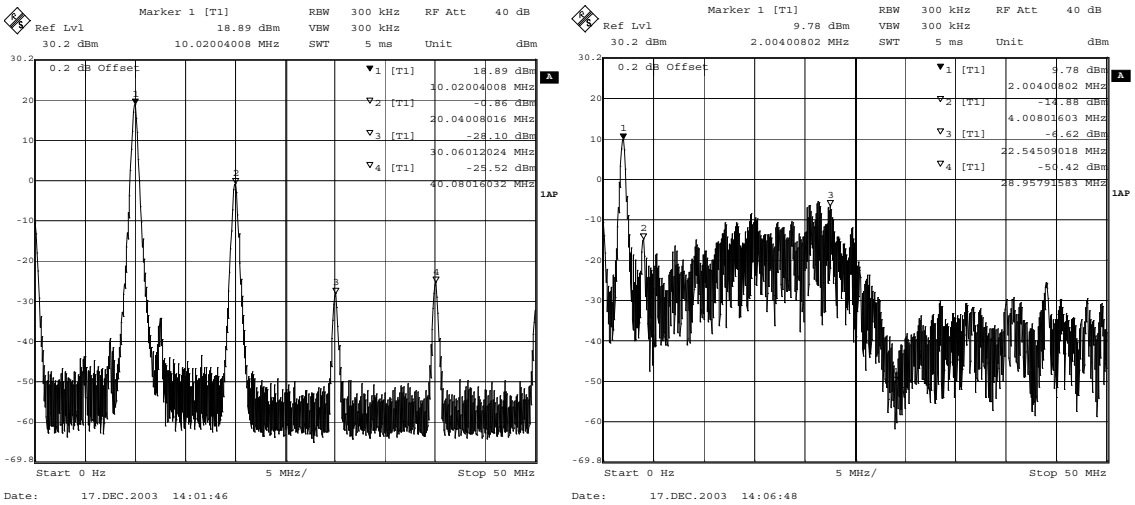

a) b)

Fig. 5. The measured output spectrum in case of a) a self-made PWM like input signal and b) a second order SDM input signal.

6. CONCLUSIONS

An integrated class-S modulator with an external low-pass filter for an EER system was implemented and measured. The modulator was designed to have a PWM input signal generated by a DSP circuit. Although the configuration is simple, the challenge is to modulate supply voltage of the RF power amplifier efficiently. Furthermore, as the output power level is increased, the transient currents in switches become larger. The measurement results shows that the modulator has a moderate efficiency and it can be used as one block with a class-E RF power amplifier in an EER transmitter.

7. ACKNOWLEDGEMENT

This work was supported by Finnish National Technology Agency and Spirea AB.

8. REFERENCES

[1] W. Liu, J. Lau and R. S. Cheng, “Considerations on Applying OFDM in a Highly Efficient Power Amplifier”, *IEEE Transactions on Circuits and Systems–II: Analog and Digital Signal Processing*, vol. 46, no. 11, November 1999, pp. 1329–1336.

[2] H. L. Krauss, C. W. Bostian and F. H. Raab, *Solid State Radio Engineering*, New York: Wiley, 1980.

[3] P. B. Kenington, *High-Linearity RF Amplifier Design*, Boston, London: Artech House 2000.

[4] J. Staudinger, B. Gilsdorf, D. Newman, G. Norris, G. Sadowniczak, R. Sherman, T. Quach and V. Wang, “800 MHz Power Amplifier Using Envelope Following Technique”, in *Proc. of Radio and Wireless Conference (RAWCON’99)*, August 1999, pp. 301–304.

[5] S. A. El-Hamamsy, “Design of High-Efficiency RF Class-D Power Amplifier”, *IEEE Transactions on Power Electronics*, vol. 9, no. 3, May 1994, pp. 297–308.

Session 4a:
Defence and Security

Rapid Prototyping of a Short-Range Radar with a Generic Reconfigurable Platform

Esa Korpela [1] **Juha Forsten** [1] **Antti Hämäläinen** [1] **Matti Tommiska** [1]
Jorma Skyttä [1] **Jukka Ruoskanen** [2] **Arvi Serkola** [2] **Pekka Eskelinen** [3]

[1] ***Signal Processing Laboratory***
Helsinki University of Technology
P.O. Box 3000
FIN–02015 TKK, Finland

[2] ***Electronics and Information Technology Division***
Finnish Defence Forces Technical Research Center
P.O. Box 10
FIN–11311 Riihimäki, Finland

[3] ***Institute of Digital Communications***
Helsinki University of Technology
P.O. Box 3000
FIN–02015 TKK, Finland

Abstract
This paper discusses the advantages of using a recon gurable FPGA (Field Programmable Gate Array) –based computing platform in rapid prototyping of a short–range radar system. The FPGA–based platform performs datastream compression and robust target recognition, and constructs a data structure suitable for an external display device. The FPGA–based computing platform is connected to a laptop computer with a USB (Universal Serial Bus) cord, thus enabling field tests. Although future work and research remains to be done, the usability of an FPGA–based computing platform in rapid prototyping and construction of a fully functional short–range radar test system has already been demonstrated.

Keywords: Short range radar, FPGA, rapid prototyping.

1. INTRODUCTION

Due to the continuing miniaturization in electronics manufacturing technology, it has become possible to implement modules and entire systems digitally. This trend is evident also in radar technology, where traditional analog technology is being replaced by digital implementations, especially in radar control, baseband processing and display devices. An ideal digital implementation has the benefits of the speed of hardware and the flexibility of software. This can be accomplished by implementing as many functions as possible with FPGAs. There are numerous published accounts on using FPGAs in radar signal processing, e.g. [1] [2].

2. THE SHORT–RANGE RADAR SYSTEM

A short-range radar front end with a known pulse repetition frequency (PRF) and corresponding maximum range, transmission power, relevant pulse characteristics and interfaces to the baseband units required field tests and echo signal recording for offline inspection. First attempts to interface the radar front end with a commercial off–the–shelf (COTS) data acquisition card to a host PC were not successful. The uncompressed data rate of 800 Mbps (megabits per second) quickly inundated the host computer, thus making both real–time radar display generation and datastream recording for offline analysis impossible.

The sampled datastream had to be compressed substantially, and an FPGA–based reconfigurable platform named SIG USB Card v2 [3], which was originally designed for another application, was taken into use. The goal was to transfer as much computation as possible onto the FPGA–based platform. A generic flow diagram of the short range radar system is presented in Fig. 1.

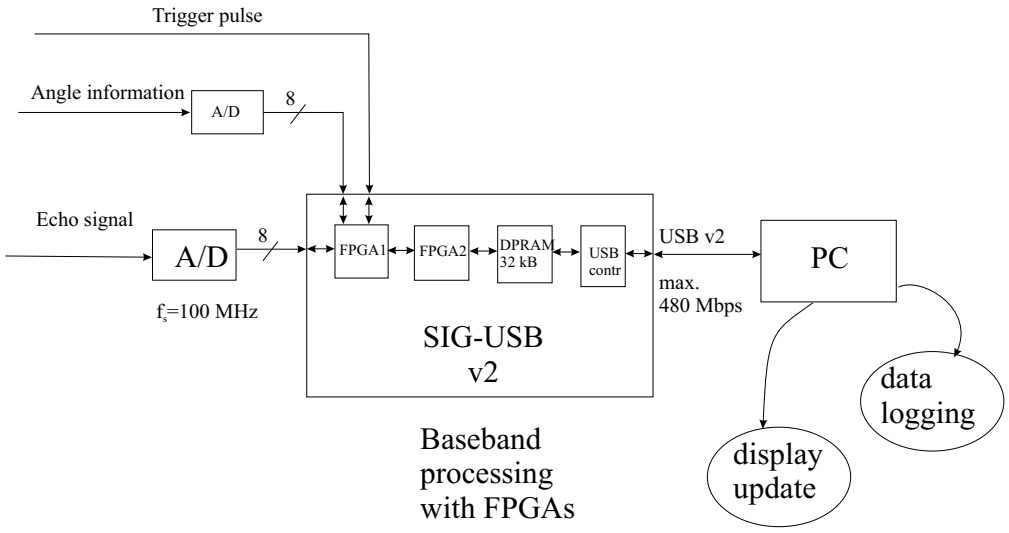

Figure 1: A flow chart of the baseband units in short–range radar system

3. GENERIC RECONFIGURABLE PLATFORM

The computing core of the short–range radar system is a custom designed FPGA–based reconfigurable platform called SIG USB Card v2. The card houses two large FPGA chips of Altera's Apex II device family [4], external connections, an SDRAM socket, 32 kilobytes of dual-port RAM, and an 8051 derivative with a USB controller and transceiver. Both FPGA devices can be reconfigured on the fly, which shortens system development time. The USB version 2.0 protocol was selected, as it is electrically simple with only four wires, has adequate transmission speed at maximum 480 Mbps, and is supported by laptop computers used in field tests.

The first target recognition algorithm was written in VHDL and was based on an algorithm used in a previous analog radar implementation. The incoming samples are compared to an on–the–fly adjustable threshold value, and if six of eight consecutive samples from the same distance element exceed the threshold, a target has been found. The FPGA constructs a data structure with appropriate header bits and stuffing and writes these values to the dual-port RAM. The data structure used for display generation is described in Fig. 2. There are four bits available for describing the amplitude of a target, which is sufficient for a visual inspection. A limiting factor is the dual–port RAM size of only 32 kilobytes, and it was decided to encode an entire display frame into this amount of memory. Naturally, there must be constant bookkeeping by the 8051–based USB controller to prevent overlaps in reads by the host PC and writes by the FPGA.

4. CONNECTIONS TO A/D CONVERTERS AND DISPLAY DEVICES

The SIG USB Card v2 is connected to two A/D converter boards with a flat cable. The first A/D converter is used for sampling the incoming echo signal at 100 MHz with an accuracy of 8 bits, and the second A/D converter samples the angle information with 781.25 kHz with an accuracy of 8 bits. At first sight, the granularity of angle information at 1.4 degrees $(360/2^8)$ may appear insufficient, but the laptop display accuracy did not improve with greater word lengths.

In addition to the two sampled bytes from A/D converters, a TTL pulse by the radar when a pulse is transmitted is an input to the FPGA devices (See also Fig. 1).

The display software runs at the host PC in two operating modes, an oscilloscope mode and a radar display mode. Depending on the mode selected by the user, the FPGA devices construct either the time domain datastream (oscilloscope) or describe an entire display frame that fits exactly into the 32 kilobytes large dual port RAM. In oscilloscope mode, the datastream can be saved to hard disk for offline inspection and algorithm verification.

The display software was developed with the OpenGL graphics library, which alleviated the load on the host processor by transferring the computation intensive graphics algorithms to the display card. For

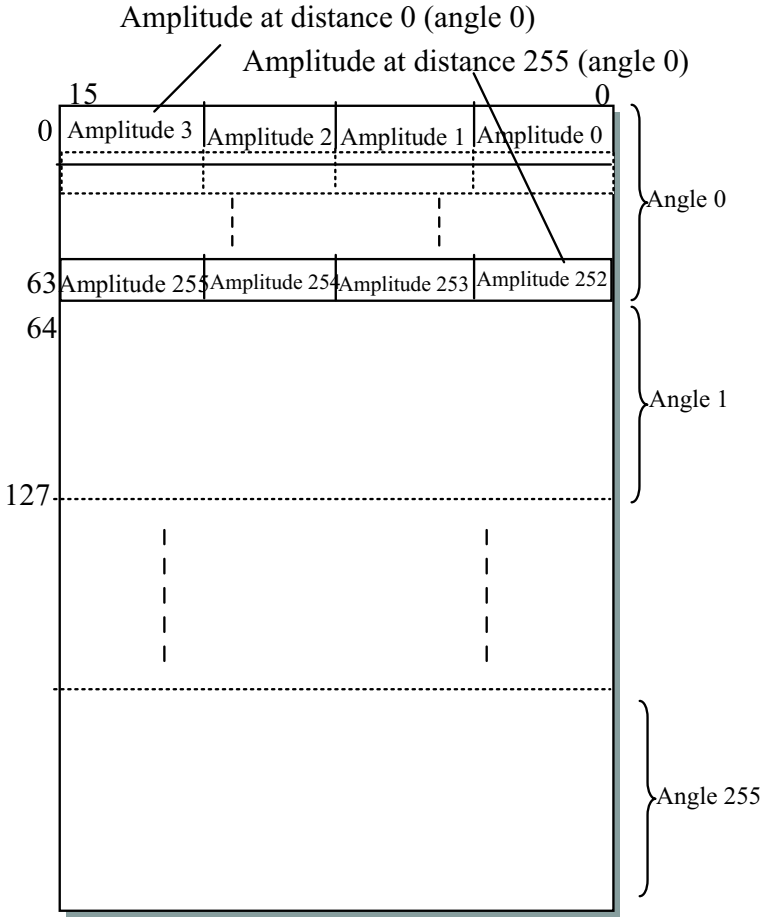

Figure 2: The 32 kB data structure used for displaying one radar frame. Angle and amplitude values are not physical quantities.

example, implementing after–glow is very efficient by simply decrementing a pixel value in the data structure. This is also in line with the applied design philosophy of transferring as much algorithmically demanding computation away from a general–purpose processor, which is most suitable for system–level bookkeeping and communications management.

5. ADVANTAGES OF FPGA–BASED PROTOTYPING AND FUTURE RESEARCH

The main benefits of using FPGA–based generic computing platforms are their reconfigurability on–the–fly, high throughput and rapid design cycles with parallel hardware and software development threads. Based on these characteristics, only twelve person–months were required from a three–man design team with no previous experience in baseband radar technology to implement the baseband and display units for a fully functional short–range radar test system.

The main contribution of this paper has been to demonstrate the practicality of using FPGAs for rapid prototyping. Gate counts in modern FPGAs are sufficient for computationally demanding algorithms, and in the particular application described in this paper, most of the logic remained unused as the target recognition algorithm was very robust.

Future plans include designing an FPGA-based computing platform specifically targeted for radar applications. An obvious bottleneck in the SIG USB v2 card is its dependence on the limited amount of

dual–port RAM, and this will be improved in the next version. The design emphasis will shift to developing algorithms for increased range and angular accuracy, taking into account the Doppler effects and implementing sliding–window techniques in target recognition, thus enabling motion detection.

6. REFERENCES

References

[1] R. Andraka and A. Berkun, "FPGAs Make a Radar Signal Processor on a Chip a Reality", in Proceedings of the 33rd Asilomar Conference on Signals, Systems and Computers, October 24–27, 1999, Monterey, California, United States, pp. 559–563.

[2] T. Moeller and D. Martinez: "Field Programmable Gate Array Based Radar Front-End Digital Signal Processing", in Proceedings of the Seventh Annual IEEE Symposium on Field–Programmable Custom Computing Machines, April 21–23, 1999, Napa, California, United States, pp. 178–187.

[3] E. Korpela: "Design of a Generic Reprogrammable Computing Platform", M.Sc. Thesis, Signal Processing Laboratory, Helsinki University of Technology, 2004.

[4] Altera: "APEX II Programmable Logic Device Family Data Sheet".

Universal Radar Antenna Stabilizer System for Vehicular Platforms

P. Kuosmanen[1], P. Makkonen[2], H. Heikkilä[3], P. Eskelinen[4]

[1]Helsinki University of Technology, P.O.Box 4100, FIN-02015 HUT, Finland
[2]Helsinki University of Technology, P.O.Box 4100, FIN-02015 HUT, Finland
[3]Armoured Brigade, P.O.Box 5, FIN-13701 Parolannummi, Finland
[4]Helsinki University of Technology, IDC, P.O.Box 3000, FIN-02015 HUT, Finland
email: petri.kuosmanen@hut.fi

Abstract: A universal antenna stabilizer and lifting system has been developed for different vehicular platforms, mainly with the focus at radar systems. The stabilizer arrangement is needed to compensate undesired movements caused by the platform and lifting system. In addition, the stabilizer enables high speed scanning and target tracking functions of the radar reflector antenna.

A systematic design process including clarification of the task, conceptual design and embodiment design have been applied throughout the task [1]. The behaviour of the selected vehicle platform was initially measured in true operating conditions. Finally, the performance of the developed design was simulated by multi body simulations using the measured source data.

Keywords: Radar, multi body simulation, modular design

1. Introduction

Antenna rotator mechanisms are as old and diverse as radars [2], but their performance requirements have been continuously increasing. The special requirement in the described project for the stabilizer system was applicability to different types of vehicular platforms, like ships and vehicles on wheels or on caterpillar chain. By definition, it should also contain a lifting system reaching up to 5 meters so that the radar can see its environment or targets without obstacles [3].

The design must tolerate loads caused by fire of the own platform and occasional collisions against small branches of trees. It must tolerate fire of rifle class guns. The operating temperature range is -40...+40°C. Of course, there is a pointing accuracy requirement as defined by the respective antenna pattern width [4]. Scanning speed and tracking performance are naturally combined as well [5].

2. Modular design

The structure is divided to two modules: lifting module and stabilizer module.

2.1 Lifting module

The lifting module has the following sub functions:

- Enable antenna mounting to the platform
- Carry the mechanical load
- Lift up and down
- Tolerate shocks
- Reduce vibrations

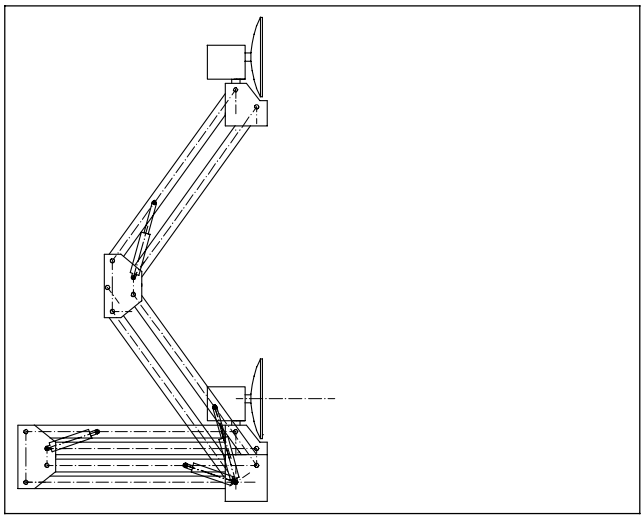

Figure 1 : Structure of the lifting module

2.2 Stabilisation module

The stabilisation module has following sub functions:

- Stabilize the antenna orientation
- Rotate the antenna

Orientation stabilization can further be divided into measurement and control of the momentary position. For position measurement is used encoder and

horizontal reference is measured by inclinometer. The position control is carried out with one servo hydraulic actuator.

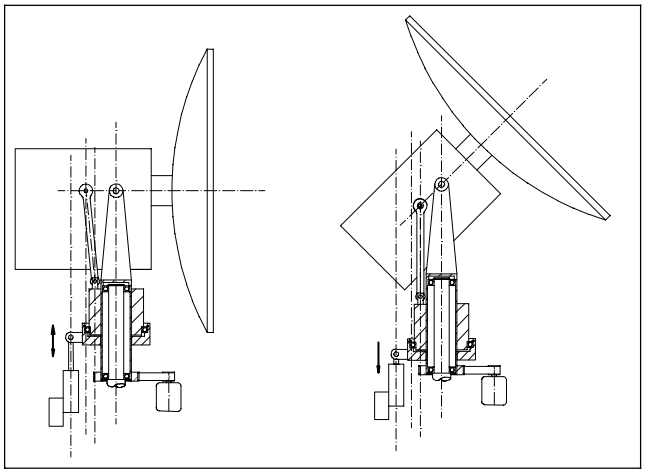

Figure 2 : Structure of the stabilizer module

4. Simulation model

A simulation model of the platform carrying the radar antenna was created with ADAMS 11.0 multi body systems program. The model was modular containing following submodules:

- 6 DOF vehicle model performing a driving path based on inertial navigation data measured in test drives.
- Modular mechanism model of the lifting module in figure 1. The beam structure was also modular enabling to change the rigid beam model with rigid-elastic lumped mass model with Timoshenko beams. The sub model can easily be changed to other structure.
- Rigid radar antenna stabilisation module containing horisontal and vertical direction mechanism for antenna stabilisation.

The vehicle model contained six accelometers which recorded the acceleration time history of the vehicle rigid body movement history in space. The function of the lifting mechanism is besides lifting the damping vibration of the vehicle. The damping is achieved with hydraulic cylinders controlled by semihydroactive steering by antenna position.
The mechanical vibration is damped in two stage approach. The low frequency translational motion of the platform is damped by the lifting mechanism. The high frequency vibration is damped by the antenna stabilisation module.

4. Results

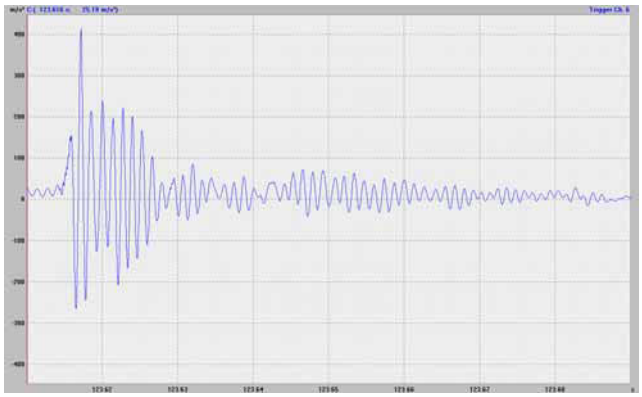

Figure 3 : Measured momentary acceleration, when the large caliber gun of the the platform is shooting

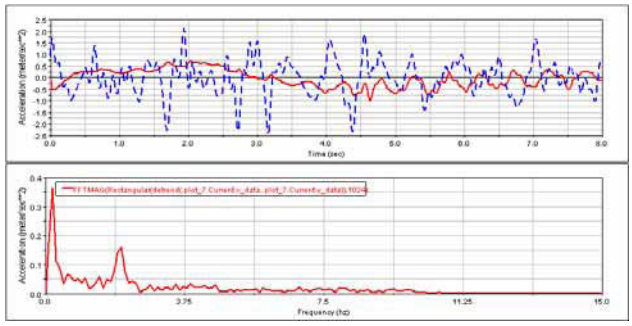

Figure 4 : MBS simulated vibration of the antenna in vertical direction when the platform is moving in operating environment.

In Fig. 4., the vertical translational vibration of the platform and radar stabilator unit is shown on the upper figure. The dotted line represents the platform vibration. The continuous line shows the antenna's damped vibration. The analysis shows, that maximum vertical vibration is damped with 64 %. The lower figure of Fig. 4 shows the Fast Fourtier transformed frequency domain signal from platform vertical vibration.

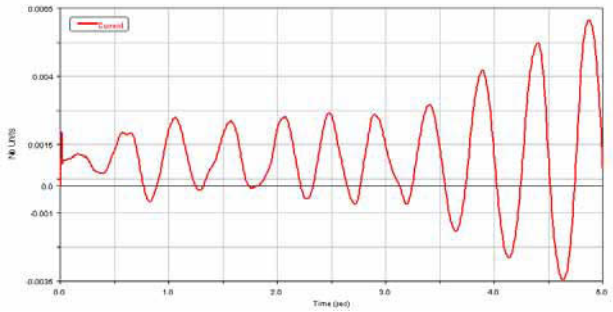

Figure 5. MBS simulated vertical variation of the radar mirror when the high frequency stabilisation is activated.

Fig. 5 shows the vertical variation of radar mirror elevation error from horisontal plane. The analysis shows mechanical accuracy of the radar mirror elevation adjustment, when absolute horisontal reference is obtainable for the system. The total variation of the elevation of the mirror keeps under 10 millidegrees if the platform elevation variation is under 15 degrees.

5. Conclusion

A universal radar antenna stabilizer and lifting system has been developed for different vehicular platforms. The behaviour of the selected vehicle platform was initially measured in true operating conditions. Finally, the performance of the developed design was simulated by multi body simulations using the measured source data.

The simulation shows that designed stabilizer system fullfills the pointing accuracy requirement defined by the antenna pattern width.

6. References

[1] Pahl, G., Beitz, W.: Engineering Design, Springer-Verlag, 1984.

[2] Delaney, W., Ward, W.: "Radar Development at Licoln Laboratory: An Overview of The First Fifty Years," MIT Lincoln Laboratory Journal, Vol 12, No 2, 2000, pp. 147-166

[3] Ruoskanen, J., Heikkilä, H., Eskelinen, P.: "Target Detection Trials with A Millimeter Wave Radar System", IEEE Aerospace and Electronics Systems Magazine. Vol. 18, 2003.

[4] Eskelinen, P., et al..: ”Test arrangements for a mobile millimeter wave battlefield radar,” Proceedings of URSI General Assembly 2002, Maastricht, August 19-24, 2002.

[5] Skolnik, M.: Radar Handbook, McGraw-Hill, New York, 1992

7. Glossary

MBS: Multi Body Simulation

DOF: Degree of Freedom

Session 5a:
Antennas II and Wireless Communications

Antenna radiation characterization by backscattering modulation

Pekka Pursula, Timo Varpula, Kaarle Jaakkola, Mervi Hirvonen

VTT Information Technology
PO.Box 1207, 02044 VTT, Finland
Email: Pekka.Pursula@vtt.

Abstract
The effective aperture of the antenna is determined using measured backscattering data. An oscillator with a known port impedance is connected to the antenna under test to modulate the backscattered radiation. The measurement is based on measuring the signal in the modulation sidebands. Using a simple circuit model for the antenna—oscillator system, the antenna effective aperture, bandwidth and radiation pattern can be determined. In this paper, theory for antenna aperture measurement is developed, and measurements with error considerations of an antenna with a highly reactive port impedance at the application frequency are presented. The results are compared to a traditional transmission measurement results.

Keywords: Antenna radiation patterns, antenna measurements, apertures, radar cross sections, UHF antennas, RFID.

1. INTRODUCTION

Several authors have demonstrated backscattering-based methods for measuring the antenna radiation pattern and gain (e.g. [1]) and the antenna drive port impedance (e.g. [2]). In most methods, the antenna under test is connected to known passive loads, but also negative resistance devices have been used [3]. Most methods require the measurement of the power level of the scattered signal at the transmitted frequency. Therefore environmental reflections limit the signal-to-noise ratio and accuracy of the measurement [2].

In this paper a completely new approach to backscatter measurement is taken. Instead of measuring the antenna radar cross section, the study concentrates on the effective antenna aperture (also antenna aperture, or aperture, in this paper). The antenna under test is connected to an oscillator circuit, which drives a small varactor in the input of the oscillator chip. The oscillator wakes up, when the antenna under test supplies it with high enough power. If this critical power is known, the effective antenna aperture can be measured. The method has been inspired by the need to characterize small RFID antennas, which are usually directly matched to a highly capacitive IC chip. The oscillator IC has same input impedance than the RFID chip, which the antenna will actually be used with.

The scattering methods are commonly agreed to give better measurement results than the transmission measurements in the case of small antennas, because the feedline connected to the antenna disturbs the antenna radiation in the transmission measurements. As an example of the aperture method, a small UHF RFID antenna, which has been designed to be mounted on metal surfaces, is measured. The measurements are carried out with the aperture and transmission methods on metal platforms of different sizes. Comparison of the results reveals the disturbing effect of the feedline in the transmission method.

2. THE LOADED SCATTERER MODEL

To study the scattering effects on a loaded antenna, the model presented in Fig. 1 is used. Both the antenna and the load are described as series resistances, R_A and R_L respectively, and reactances, X_A and X_L respectively. The antenna resistance consists of the radiation resistance R_R and the dissipations in the antenna R_D, i.e. $R_A = R_R + R_D$. The voltage V is the rms-value of the equivalent voltage generated by the incident wave.

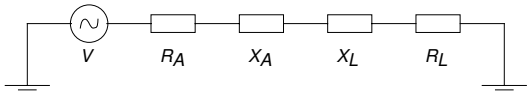

Figure 1: The series model of a loaded antenna.

Following the reasoning in [4] and [5] expressions for the effective aperture A_e and the radar cross section σ of the antenna can be derived. The rms-value of the RF current I in the circuit can be calculated as

$$I = \frac{V}{Z} = \frac{V}{(R_A + R_L) + j(X_A + X_L)}, \tag{1}$$

where Z is the impedance of the circuit. The effective aperture A_e is de ned as the ratio of the power dissipated in the load resistance R_L and the power intensity S of the incident wave. Similarly the radar cross section σ is defined as the power the antenna radiates, i.e power dissipated in the antenna resistance R_A times the gain G_A of the antenna, divided by the power intensity S. These definitions give

$$A_e = \frac{R_L|I|^2}{S} \quad \text{and} \quad \sigma = \frac{G_A R_A |I|^2}{S}, \tag{2}$$

where the antenna gain includes ohmic losses of the antenna. Assuming a perfect match between the antenna and the load, we have $Z_A = Z_L^*$ and the maximum power P_{max} transferred from the antenna to the load can be expressed as

$$P_{max} = \frac{V^2}{4R_{L,0}} = \frac{G_A \lambda^2}{4\pi} S, \tag{3}$$

where $R_{L,0}$ id the load resistance at perfect match. The latter equality arises from Friis transmission equation. Combining (1) – (3), expressions for the effective aperture A_e and the radar cross section σ become

$$\begin{aligned} A_e &= \frac{G_A \lambda^2}{4\pi} \frac{4R_L R_{L,0}}{(R_A + R_L)^2 + (X_A + X_L)^2}, \\ \sigma &= \frac{G_A^2 \lambda^2}{4\pi} \frac{4R_A R_{L,0}}{(R_A + R_L)^2 + (X_A + X_L)^2}. \end{aligned} \tag{4}$$

The equations consist of a common maximum aperture and a mismatch part. So far, most measurement methods have been based on measuring the radar cross section. A completely passive load has been used, and the backscattered power occurs at the same frequency than the transmitted power. On the other hand, antenna can be characterized also by measuring the antenna aperture. To do this, the antenna is connected to an oscillator chip, whose input impedance is known. The chip includes a rectifier, a low-frequency oscillator and a varactor. The chip has no battery, but has instead a voltage rectifier and extracts all the power it needs from the RF power transmitted by an illuminating antenna.

While the oscillator drives the varactor at the input of the IC chip, the backscattered signal is phase modulated, which is seen as a phase change in the equivalent circuit current in (1). By measuring the sidebands due to the modulation, a better signal-to-noise ratio in the receiver is achieved, because the only source of any signal in the sideband frequencies is the antenna under test. This reduces the errors caused by the environmental reflections. Hence the center frequency, bandwidth and normalized radiation pattern can be measured even in normal laboratory conditions. Of course, when the power intensity at the antenna under test has to be known, e.g. for antenna gain measurements, more accurate results can be achieved, if one uses an anechoic chamber, which minimizes the reflections.

The measurement proceeds as follows. The power in the sidebands is not directly measured, but the oscillator chip is designed so, that the RF power $P_{rf,0}$, which the chip needs to the backscatter modulation to wake up, is known. The oscillator-loaded antenna is illuminated with a transmitter. In measurements the transmitted power P_{tx} is increased until at some power level, the IC chip gets enough power to begin the modulation of the backscattering signal. When the modulation begins, sidebands appear to the signal in the receiver. This critical transmitted power $P_{tx,0}$ is recorded. A reference measurement on the power intensity S is required. The measurement links the intensity reference value to a transmit power value, i.e. $S_{ref} = S(P_{tx} = P_{tx,ref})$. The effective aperture A_e can now be calculated based on its definition as the ratio of power transferred to the load P_{rf} and power intensity S:

$$A_e = \frac{P_{rf}}{S} = \frac{P_{rf,0}}{S_{ref}} \frac{P_{tx,ref}}{P_{tx,0}}. \tag{5}$$

3. MEASUREMENT RESULTS

The antenna under test (AUT) is a modified planar inverted-F antenna (PIFA) that has been designed for RFID applications at 869 MHz [6]. The port impedance of the antenna should be Z_{in}= (7 + j170) Ω, to match the input impedance

of the Palomar RFID chip [5]. The antenna is designed to be attached on metal platforms. Hence the measurements were carried out on metal platforms of different sizes, and on a styrofoam support, to simulate the free space condition. The measurement system is presented in Fig. 2. The measurements were carried out in an anechoic chamber.

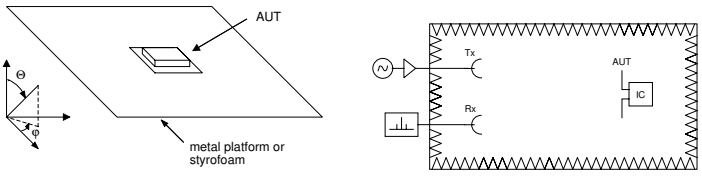

Figure 2: On the left: The AUT attached to a platform. On the right: Block diagram of the measurement system.

The antenna under test, with the oscillator IC connected to it, was placed on a metal plate or, in the free space situation, on a styrofoam support, which was then attached to a rotating mount. The AUT was illuminated by a single frequency signal transmitted via the Tx antenna. The receiver branch consists of an antenna and a spectrum analyzer.

3.1. Radiation pattern measurements

To measure the normalized power radiation pattern P_n, one does not have to know the reference power and power intensity in (5), assuming the references remain constant throughout the measurement. Because the antenna aperture is the measure of the power transfer between the antenna and the load, the radiation pattern can be calculated as

$$P_n(\varphi, \Theta) = \frac{A_e(\varphi, \Theta)}{A_{e,max}} = \frac{P_{tx,0,min}}{P_{tx,0}(\varphi, \Theta)}, \tag{6}$$

where the maximum aperture $A_{e,max}$ and the minimum critical transmitted power $P_{tx,0,min}$ take care of the normalization. Equation (6) holds, because the frequency remains constant during a radiation pattern measurement. The uncertainty in the measured power levels was 0.1 dB, which leads approximately to an overall error ΔP_n = 0.2 dB.

The radiation patterns measured with the aperture method are compared to the patterns acquired with a traditional setup, where transmission between a standard reference antenna and the antenna under test is measured. In the transmission measurements the AUT was fitted to a 50–Ω feedline with a stripline fitting network. The fitting network was connected to other measurement apparatus through an optical link. The antenna mounting, including the platform, was identical to the aperture measurement. The antenna was fed through the metal platform, so the disturbing effect of the feedline can mainly be seen in the back lobe of the antenna. The radiation patterns obtained are presented in Fig. 3.

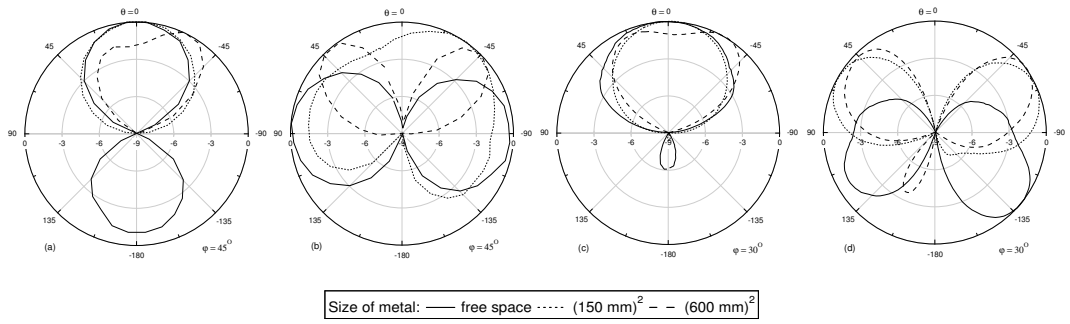

Figure 3: The measured radiation patterns. On the left: aperture method, co- (a) and cross-polarization (b). On the right: transmission method, co- (c) and cross-polarization (d).

Despite the measurement planes differ about 15°, the measurement methods give similar results, when the AUT is attached on big metal surfaces. In this case, the feedline does not disturb the transmission measurement and the similarity of the patterns validates the aperture measurement. On the other hand, as the metal platform is reduced, the back lobes become increasingly different due to the feedline disturbances in the transmission measurement. The dipole-like radiation pattern measured with the aperture method in free space complies with the simulations.

3.2. Bandwidth measurements

The critical power was measured in the AUT main lobe at frequency steps of few MHz near the application frequency to determine the frequency behavior of the AUT. The antenna aperture is calculated using (5). The error is mainly due to the uncertainty in the required power $P_{rx,0}$, about 10 %. Adding other error sources in squares, the overall relative error becomes $\Delta A_e/A_e$ = 11 %.

The antenna aperture vs. frequency is presented in Fig. 4. The bandwidth and the center frequency of the antenna can be seen from this fiure directly. At the center frequency the magnitudes of the reactances of the antenna and the chip are equal. Because chip reactance is known, the reactance of the antenna can be calculated on this single frequency. An approximation for the gain of the antenna can be easily calculated at the center frequency using relation $A_e = \lambda^2 G_A/(4\pi)$. This assumes a perfect match also in resistances of the antenna and the chip.

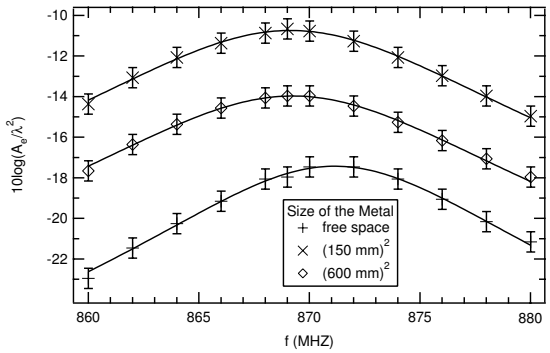

Figure 4: The bandwidth measurement results with a fit of (4) to aid the eye.

4. SUMMARY AND CONCLUSIONS

A new method utilizing backscatter data to characterize antenna radiation was presented. The method is based on antenna aperture measurement by modulating the load connected to the antenna under test. The oscillator modulates the backscattered signal. The measurement concentrates on the sidebands of the backscattered signal, which enables radiation pattern and bandwidth measurements even in noisy laboratory environment, although more accurate results are achieved in an anechoic chamber.

The method has been applied to characterize small RFID antennas at 869 MHz. The radiation pattern and bandwidth measurements are simple and robust. In radiation pattern measurements, the disturbing effect of a feedline when measuring small antennas with traditional transmission measurement technique was demonstrated.

Acknowledgments

This work has been supported by Tekes, The National Technology Agency of Finland. The authors would like to thank O. Jaakkola for his contribution to the concept of the study. The IC chips were manufactured by Atmel Germany Gmbh.

References

[1] J. Appel-Hansen, "Accurate determination of gain and radiation patterns by radar cross-section measurements", *IEEE Trans. Antennas Propagat.*, vol. AP-27, pp. 640–646, Sep. 1979.

[2] J. T. Mayhan, A. R. Dion and A. J. Simmons, "A technique for measuring antenna drive port impedance using backscatter data", *IEEE Trans. Antennas Propagat.*, vol. 42, pp. 526–532, Apr. 1994.

[3] R. F. Harrington, "Field measurements using active scatterers", *IEEE Trans. Microwave Theory Tech.*, vol. MTT-11, p. 454, Sep. 1963.

[4] J. D. Kraus, *Antennas*, New York: McCraw-Hill, pp. 41–56, 1950.

[5] U. Karthaus and M. Fischer, "Fully integrated passive UHF RFID transponder IC with 16.7-μW minimum RF input power", *IEEE J. Solid-State Circuits*, vol. 38, pp. 1602–1608, Oct. 2003.

[6] M. Hirvonen, P. Pursula, K. Jaakkola and K. Laukkanen, "Planar inverted-F antenna for radio frequency identification", *Electron. Lett.*, vol. 40, pp. 848–850, Jul. 2004.

A New Milestone Reached: The Hologram Based Compact Antenna Test Range Demonstrated at 650 GHz

Tomi Koskinen[(1)], Juha Ala-Laurinaho[(1)], Juha Mallat[(1)], Anne Lönnqvist[(1)], Janne Häkli[(1)], Jussi Tuovinen[(2)], and Antti V. Räisänen[(1)]

[(1)]MilliLab, SMARAD/ Radio Laboratory, Helsinki University of Technology
P. O. Box 3000, FI-02015 HUT, Finland
Tel: +358-9-4512255; Fax: +358-9-4512152
Email: tvkoskin@cc.hut.fi

[(2)]MilliLab, VTT Information Technology
P. O. Box 1202, FI-02044 VTT, Finland

Abstract

We have constructed a demonstrative compact antenna test range (CATR) and tested its performance at 650 GHz. An amplitude hologram of 0.93 meter in diameter was used as the focusing element of the CATR. The measured amplitude and phase ripples in the quiet-zone are ca. 2 dB and 15°, peak-to-peak. Good measurement results indicate that the hologram based CATR is applicable also for high submillimeter wave frequencies.

Keywords: Compact Antenna Test Range, Hologram, Submillimeter wavelength

1. INTRODUCTION

Since the early 1990's, the Radio Laboratory of the Helsinki University of Technology has been developing a novel type of compact antenna test range (CATR) that is based on the use of an amplitude hologram as the focusing element (see Fig. 1a that shows the layout of the CATR discussed in this paper) [1]. The hologram is used to transform an incoming spherical wave to a plane wave needed for antenna testing. It is manufactured by etching a computer-generated interference pattern on a thin metal-plated dielectric film (see Fig. 1b). The pattern consists of narrow, nearly vertical, slots and metal strips. The hologram is tensioned in a rigid frame that makes it flat. When the hologram is illuminated with a feed antenna (typically a corrugated horn) it diffracts several beams into different directions. One of the beams is the desired plane wave; the other beams are eliminated by absorbers. The hologram is designed typically so that the plane wave propagates in an angle of 33° in respect to the normal of the hologram. The antenna under test is placed in a high quality region of the plane wave called a quiet-zone.

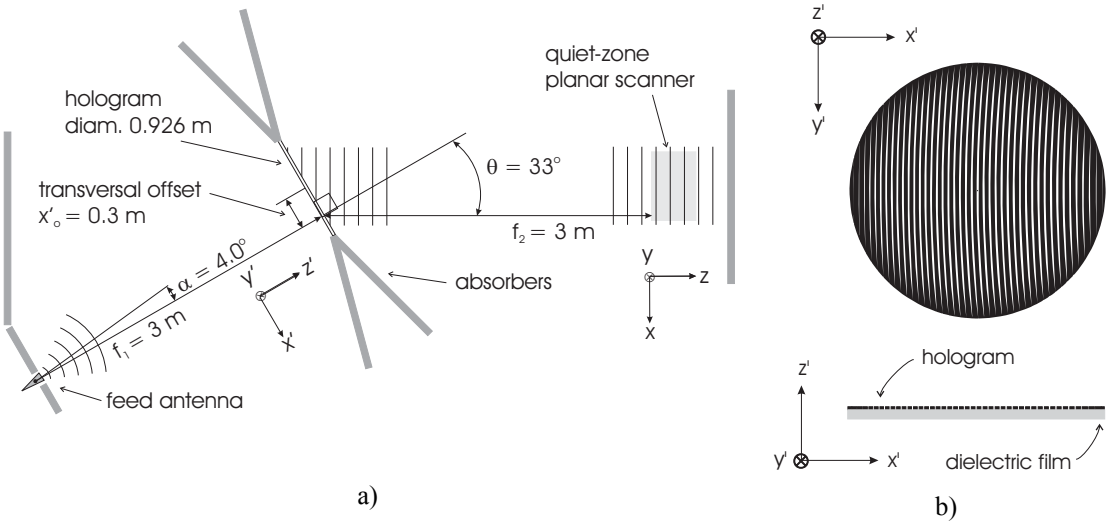

Fig. 1. a) Layout of the hologram based CATR at 650 GHz. b) An amplitude hologram. Radio transparent slots are in white, metal strips in black.

Due to the simple structure of the hologram, a tolerable surface accuracy requirement (~0.1λ [2]) and due to its relatively low manufacturing costs, the hologram based CATR is seen as a competitive alternative to the conventional reflector based CATR. Especially at sub-mm wavelengths, reflectors suffer from a very high surface accuracy requirement (~0.01λ [3]), which makes using of holograms appealing.

Previously, a hologram based CATR has been used successfully for testing large reflector antennas at 119 GHz and 322 GHz [4,5]. Many of the future scientific (e.g., ESA's Planck and Herschel) or remote sensing satellites will operate at high submillimeter wave frequencies (> 500 GHz). Development of a measurement method for testing the reflector antennas used in these satellites is an essential task. The hologram based CATR is seen as a potential measurement method.

2. THE 650 GHz HOLOGRAM

2.1. Design

A demonstrative amplitude hologram of 0.93 m in diameter was designed and manufactured for 650 GHz. The computer-generated hologram pattern was optimized by using a FDTD based simulation tool (developed in MilliLab), which has earlier been found useful at lower frequencies [1]. E.g., an adequate edge tapering of slots to prevent harmful edge diffraction was chosen on basis of the simulation results.

An appropriate substrate material was needed for the hologram. Previous experiments at lower frequencies have shown a copper-laminated Mylar film (with a relative permittivity of 3.3 for Mylar) to be an electrically good and mechanically durable substrate for holograms. According to simulations, the thickness of the Mylar film should not be greater than 50 μm at 650 GHz. Otherwise, the field within the film starts to resonate, which disturbs the field in the quiet-zone. Therefore, a 50 μm thick Mylar film with 17 μm copper laminate was chosen as the substrate material.

A corrugated horn antenna designed for 650 GHz was used as the feed and it was placed at a distance of 3 m from the hologram (see Fig. 1a). The feed was moved 0.3 m from the axis of the hologram and rotated 4.0° toward the center point of the hologram. In this way, the optimization of the hologram pattern becomes simpler, and the slots in the mid-section of the pattern are more uniform in width, which facilitates manufacturing. The quiet-zone was optimized at 3 m from the hologram and it was in an angle of 33° in respect to the normal of the hologram. According to the simulation, amplitude and phase deviations in the quiet-zone are at maximum 0.6 dB and 5°, peak-to-peak. The planarity of the field is satisfactory. The width of the simulated quiet-zone is ca. 0.53 m.

2.2. Manufacturing

The manufacturing method was based on direct laser writing of the hologram pattern on the photo resist on top of the substrate. After the laser writing, chemical wet etching was done to process the hologram pattern. A higher manufacturing accuracy can be achieved when laser writing is used instead of photo masks. According to the manufacturer, the nominal manufacturing accuracy of this method is 5 μm, which is sufficient at 650 GHz. The realized manufacturing accuracy was inspected with a camera microscope. The slots widths were measured along the horizontal centerline of the hologram with an interval of 20 mm (see Fig. 2). The estimated measurement accuracy was ±7 μm.

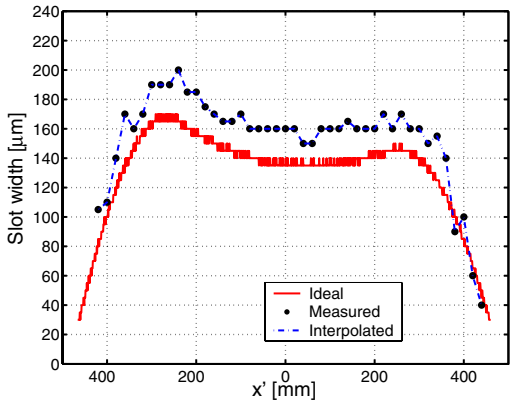

Fig. 2. Ideal and measured (and interpolated) slot widths along the horizontal centerline of the hologram.

The ideal slot widths are 135-170 μm in the mid-section of the hologram. Towards the edges of the hologram, slots are tapered down to 30 μm to prevent edge diffraction. The measured slot widths are systematically ca. 20 μm too wide, i.e., the pattern is slightly overetched. The random error is at maximum ±5 μm. The slots narrower than 105 μm are not perfectly etched on the left edge and the slots narrower than 40 μm are not etched on the right edge. Only one hologram was manufactured. Most likely, manufacturing error could have been reduced if more than one hologram had been manufactured and the manufacturing process had been tuned to its optimum.

To study the effect of the manufacturing error, a simulation for the measured slot widths was also done. The slot widths between the measurement points were linearly interpolated. For the measured slot widths, the maximum deviations from the plane wave are 2 dB and 6°, peak-to-peak.

3. MEASUREMENTS

3.1. Measurement Setup

The measurements were done in a small room with dimensions of 2.85 × 6.35 × 8.8 m^3 (height × width × depth). The quiet-zone field was probed using a planar scanner. Millimeter wave absorbers were used to eliminate reflections. Especially, all reflecting surfaces close to the feed and probe antennas were carefully covered with absorbers to avoid standing waves between the transmitter/ receiver and the hologram [6].

The amplitude and phase values of the field were measured with AB Millimètre MVNA-8-350 vector network analyzer. Corrugated horns (designed for 650 GHz) were used as the feed and probe antennas. An adequate dynamic range was achieved by using a powerful backward-wave oscillator (BWO) as the transmitter and a Schottky diode harmonic mixer as the receiver [6]. It was noticed that the BWO gives 3 dB more power at 644 GHz than at 650 GHz. Therefore, the measurements were done at 644 GHz where a dynamic range of 32 dB was achieved. A small change in the operating frequency (here the relative change is less than 1%) does not have a significant effect on the operation of the hologram. The change in the operating frequency only steered the direction of the plane wave slightly (from 33° to 33.35°).

3.2. Measurement Results and an Estimate of the Measurement Accuracy

Fig. 3 shows the measured horizontal and vertical cut of the quiet-zone field at 3 m from the hologram. Fig. 4 shows the *xy*-scan. According to the horizontal and vertical cuts, the amplitude and phase ripples are at maximum 2 dB and 15°, peak-to-peak. The measured amplitude ripple is of the same magnitude as the simulated one. In the whole quiet-zone area (see the *xy*-scan), the ripples are at maximum 3 dB and 40°, peak-to-peak. The width of the quiet-zone is about 0.6 m in the horizontal and vertical directions.

The amplitude and phase uncertainties of MVNA at a dynamic range of 32 dB are smaller than 0.35 dB and 1.5°. It was noticed that the measured phase value jittered about ±2.5° on the MVNA display. This was apparently caused by the phase locking loop of the BWO. Otherwise, measured amplitude and phase values were very stable, and no long-term drifting was seen. The total uncertainty of the phase values has been estimated to be less than 14° (the worst-case estimate), or 7.7° (RSS) [6].

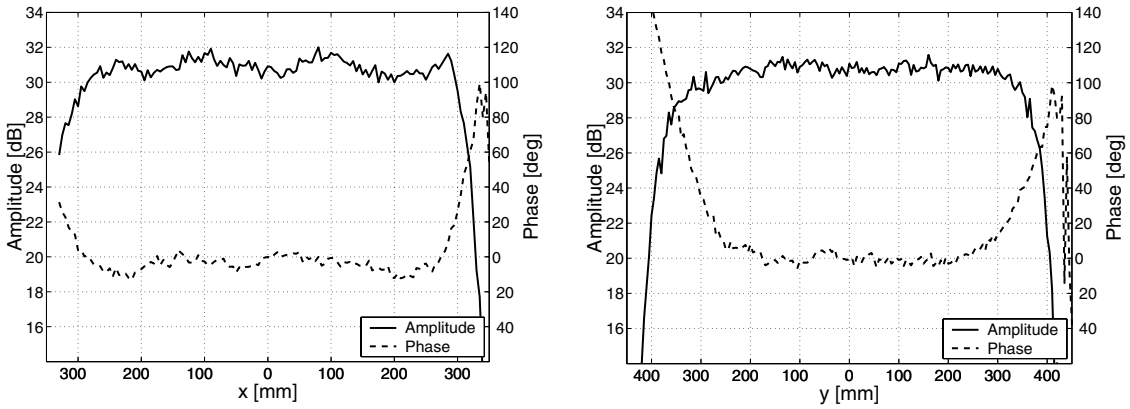

Fig. 3. A measured horizontal and vertical cut of the quiet-zone field at 3 m from the hologram.

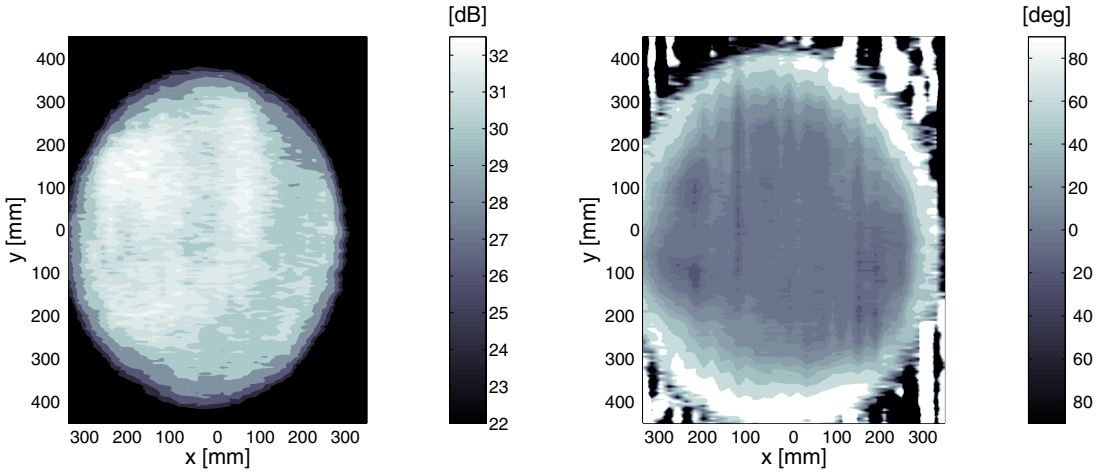

Fig. 4. *Xy*-scan of the quiet-zone field at 3 m from the hologram.

5. CONCLUSIONS

A 0.93-m amplitude hologram was designed and manufactured, and it was used as the focusing element of a CATR at 644 GHz. A suitable substrate material and manufacturing method was found. The measured ripples are ca. 2 dB and 15°, p-p. The hologram is the first of its kind manufactured. Most likely, the manufacturing quality could be improved by further tests. Performance of the hologram is very satisfactory, and it shows that the hologram based CATR is feasible at high sub-mm wave frequencies.

At lower frequencies (119 and 322 GHz), large holograms (diameter >1 m) have been manufactured from several pieces joining the pieces together by glueing or soldering [4,5]. Soldering has proved to be a good joining method. Accurate alignment of the pieces is the most difficult part in the manufacturing of large holograms. The alignment should be studied more if joining is going to be used for large holograms operating at frequencies above 322 GHz. The best quality is achieved by manufacturing the hologram in one piece. So far, the maximum size of a hologram manufactured in one piece is 1.35×3.2 m^2, which is limited by the manufacturing facility and the material available.

ACKNOWLEDGMENTS

This work was partly funded by ESA/ESTEC (Contract No. 13096/NL/SB), Tekes (National Technology Agency of Finland), and the Academy of Finland. The first author wishes to thank Nokia Foundation, Finnish Cultural Foundation and the Foundation of the Finnish Society of the Electronics Engineers for financial support. CSC, the Finnish IT center for science is acknowledged for computer resources.

References

[1] T. Hirvonen, J. Ala-Laurinaho, J. Tuovinen, A. V. Räisänen, "A compact antenna test range based on a hologram," *IEEE Trans. Antennas Propagat.*, Vol. 45, No. 8, 1997, pp. 1270–1276.

[2] J. Ala-Laurinaho, T. Hirvonen, A. V. Räisänen, "On the planarity errors of the hologram of the CATR," *Proceedings of the IEEE Antennas and Propagat. Intern. Symp.*, Orlando, Florida, USA, July 11–16, 1999, pp. 2166–2169.

[3] *IEEE Standard Test Procedure for Antennas*, IEEE Std 149-1979, published by IEEE, Inc., distributed by Wiley-Interscience, 1979, 143 p.

[4] J. Ala-Laurinaho, T. Hirvonen, P. Piironen, A. Lehto, J. Tuovinen, A.V. Räisänen, U. Frisk, "Measurement of the Odin telescope at 119 GHz with a hologram type CATR," *IEEE Trans. Antennas Propagat*., Vol. 49, No. 11, 2001, pp. 1264–1270.

[5] A.V. Räisänen, J. Ala-Laurinaho, T. Koskinen, A. Lönnqvist, J. Säily, J. Häkli, J. Mallat, V. Viikari, S. Ranvier, J. Tuovinen, "Computer-generated hologram and its use for submm-wave antenna measurement," *2004 IEEE Aerospace Conference Proceedings*, Big Sky, MO, USA, March 6−13, 2004, CD-ROM, ISBN: 0-7803-8156-4.

[6] T. Koskinen, J. Ala-Laurinaho, A.V. Räisänen, "Feasibility study of a hologram based compact antenna test range for 650 GHz," *Proceedings of the 26th Annual Meeting & Symposium of the Antenna Measurement Techniques Association (AMTA)*, Stone Mountain, GA., USA, Oct. 17-22, 2004, in press.

Dielectric-loaded Flat Reflector Test Antenna for Submillimetre Wave Antenna Measurements

Juha Mallat, Juha Ala-Laurinaho, Ville Viikari, Antti V. Räisänen

MilliLab, Radio Laboratory/SMARAD, Helsinki University of Technology
P.O. Box 3000, FI-02015 HUT, Finland
Email: juha.mallat@hut.fi

Abstract
An offset dielectric-loaded flat reflector antenna has been designed and realized for submillimeter wavelengths. The antenna has high directivity with a reasonable-sized aperture, and it is a suitable test object for the development work of antenna measurement techniques dedicated for high-gain antenna tests. The diameter of the dielectric loading on top of the flat main reflector is 120 mm and it is made of Teflon. To facilitate the manufacturing, the other surface of the dielectric loading is spherically shaped. The shape of the dielectric loading is optimised by adjusting the ray path lengths equal in the horizontal centreline of the antenna aperture. The ray path lengths are calculated with ray-tracing method. The antenna operation is verified at 310 GHz and the measured half-power beamwidth is 0.51°.

Keywords: Dielectric loading, reflector, submillimetre waves, antenna.

1. INTRODUCTION

A simple two-reflector antenna system with an offset dielectric-loaded flat main reflector is introduced in this paper. This low-cost antenna has suitable characteristics for use as a test object of submillimetre wave antenna measurement methods. The antenna is shown in the photograph of Fig. 1, with the dielectric-loaded main reflector seen as the white object in the upper part. The feed horn and the flat subreflector are seen near the centre. Much of the supporting framework is of acrylic, with cast acrylic in the sides for a strain-free structure. The antenna is designed to be connectable to the support collar of the feed horn and instrumentation receiver unit also seen in the photograph. The operation of the antenna has been tested at 310 GHz.

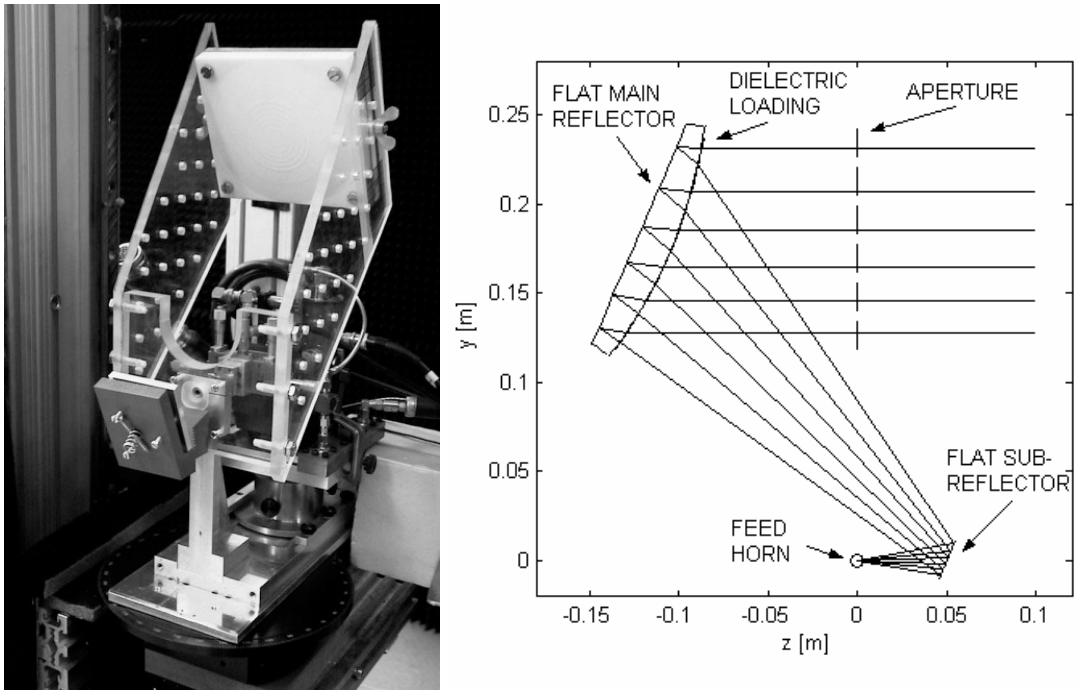

Fig. 1. (LHS) The antenna after connection to measurement instrumentation (a submillimetre wave vector network analyser extension receiver and on a rotator stage in an x-y-z-scanner). (RHS) Sketch of the antenna.

As usual in measurement techniques, there is always a need for suitable test objects to be used in verification of novel experimental or theoretical methods. Much measurement interest around submillimetre wave antennas is in large (diameter > 1 m) reflector antennas which are to be used at increasingly high frequencies, especially for satellite missions. Proposed measurement methods often rely on the use of compact antenna test ranges (e.g., the hologram CATR [1]) as they help to avoid many of the difficulties otherwise appearing due to large far-field distances, atmospheric effects, etc. The ultimate test object, in the form of an actual large reflector antenna, is indeed rather hard to come by and basically impractical as a test antenna, even when taking notice of the benefits of using a CATR.

In a recent special demonstration project a very large reflector test antenna has been successfully measured at 322 GHz in a hologram CATR [2]. However, an easily available low-cost test antenna option is needed for more everyday measurement technique development and research. Practicality in laboratory use, and the features of available submillimetre wave measurement instrumentation (here typically a millimetre wave vector network analyser with receiver and transmitter extensions) need to be taken into account in designing the test antenna system. The aperture of the antenna needs to be large enough with respect to the wavelength. This is because a relatively large aperture leads to high directivity and a radiation pattern that can be estimated to reveal the essential features and possible problems of any measurement method intended for even larger reflector antennas. The realised antenna for use at frequencies near 300 GHz or at wavelengths near 1 mm was chosen to have an aperture of 120 mm in diameter, leading high directivity and a minimum half-power beamwidth well below 1°.

The use of dielectric-loaded reflectors has been previously reported by some authors in other specific applications. For example, dielectric loading of subreflectors may be used for reducing sidelobes [3]. For main reflectors some other types of application benefits have been reported: dielectric loading of a parabola may offer advantages for millimetre wave receiver/transmitter front-end design [4], and a hemispherical lens has been used with a flat reflector for multisatellite reception scanning at relative low microwave frequencies [5].

Dielectric loading can be considered basically as an alternative (a supplement or a complement) to shaping reflector antenna surfaces when some desired radiation pattern is to be created or maintained. In our case, the introduced test antenna uses only dielectric loading by Teflon in order to control phase front curvature. This creates a directive effective aperture for the antenna system, while the reflectors remain flat so that they are light, inexpensive, and easy to manufacture, fix and position. The loss of the dielectric loading material, Teflon, is suitably very low. More importantly, the low relative dielectric constant (2.06) leads to noncritical overall manufacturing requirements, methods, and costs if compared to metal reflector shaping. As chosen in design goals, the achieved radiation pattern is directive with a good main beam and a clear sidelobe structure. Both of these are important features for comparing results obtained in using competing new and traditional measurement techniques, and also for development of correction techniques against environmental disturbances. From a mechanical viewpoint, the features of the antenna agree well with the structural capabilities of the RF and scanning instrumentation. The features of the antenna also facilitate the use of moderately sized test CATR elements (holograms in our case) for creating the antenna test zone, the so-called quiet-zone. The chosen offset reflector allows a compact structure feasible for use with the relatively small rotator and scanner stages that are available for accurate positioning as required in antenna measurements at submillimetre wavelengths. Disassembly and accurate reassembly of the light-weight reflector structure is easy for alternately carrying out other measurement tasks, such as quiet-zone scanning etc. The corrugated feed horn stays in its accurate scanner-relative position. This is favourable as the horn also serves as a probe antenna.

2. ANTENNA DESIGN

The basic design of the antenna is shown in the sketch of Fig. 1. The goal in the antenna design was to achieve a radiation pattern with a half-power beamwidth *HPBW* well below 1° at the operation frequency of 310 GHz. For an aperture antenna, the well-known approximate equation for the relation between the beamwidth and the antenna aperture diameter can be written as

$$HPBW \approx 1.2 \times \lambda/D \times (180°/\pi) \quad (1)$$

where λ is the wavelength and D is the antenna diameter. From (1) the required aperture diameter is calculated to be larger than 66.5 mm. The realised diameter of the dielectric loading was 120 mm resulting in an approximate *HPBW* of 0.55° at 310 GHz.

To facilitate the manufacturing, the shape of the dielectric loading surface was selected to be flat on one side and spherical on the other side. The optimisation parameters for the dielectric loading dimensions are the radius of the spherical surface (realised 273 mm) and the maximum thickness of the dielectric loading (realised 20 mm). Also, the focal length of the system (realised 300 mm) and tilting angles of the flat sub- and main reflectors (realised 67°) can be adjusted for optimum performance of the antenna. The dielectric loading parameters were chosen in such a way that the lengths of the ray paths were equal in the horizontal centreline of the antenna aperture. Due to the offset structure of the antenna and the spherical surface of the dielectric loading the phase is not flat in the vertical direction. This results in larger beamwidth in elevation plane than in azimuth plane. This designed feature is beneficial as it relaxes the pointing in the elevation direction.

A MATLAB-based code was written for calculating the lengths of the rays in the antenna aperture. The rays are originating from the feed focus. The first reflection occurs at the flat subreflector. The rays propagate from subreflector to the spherical dielectric loading surface. The rays refract in the air-Teflon interface and propagate in the dielectric loading material to the flat main reflector. After reflection at the flat main reflector, the rays propagate back to the dielectric loading surface, and refract to free space. The antenna aperture is situated in front of the dielectric loading in the same plane, where the feed focus is. The vectors for the ray directions are calculated with Snell's laws of refraction and reflection.

3. TEST AND VERIFICATION RESULTS

The antenna was tested by measuring the radiation pattern in a hologram CATR at 310 GHz. The repeatability after disconnection and reconnection to the instrumentation was also verified. The mechanical instrumentation included a horizontal rotator stage in an x-y-z-scanner. RF instrumentation was a submillimetre wave vector network analyser AB Millimètre MVNA 8-350 with an extension receiver ESA-2 in the antenna end, while the respective transmitter extension ESA-1 was in use for illuminating the hologram of the CATR for quiet-zone creation. The instrumentation provided ample dynamic range and good stability. The quiet-zone field quality was essentially equivalent to a far-field test condition for the antenna.

The radiation pattern measurement result in the azimuth plane is shown in Fig. 2. The figure also shows the repeatability between two measurements after and before a disconnection and reconnection of the test antenna system. The half-power beamwidth is 0.51°, which agrees well with the approximated design value.

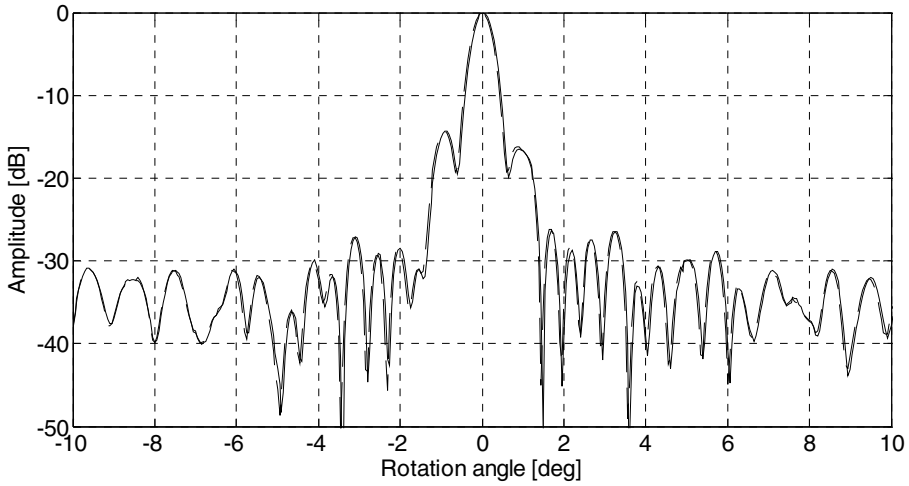

Fig. 2. Measured 310 GHz azimuth pattern of the antenna (two results, due to a repeatability test).

The near and far sidelobe structure has suitably variable features in order to allow comparison of measurement techniques and results as well in a broad angle range as at different sidelobe levels. As intended for future research applications, possible measurement technique dependent deformations are expected to become visible also in the main beam since it has a well-defined form. The repeatability of the radiation pattern features is good, with mostly less than 1 dB of error between the two test results. Deep zeroes show more discrepancy.

The vector network analyser measures radiation pattern phase simultaneously with the relative amplitude. At the test frequency of 310 GHz, one degree in phase would correspond to 2.7 µm in distance. As an indication of the achievable accuracy, the phase in the two pattern measurements of the repeatability test differed by 30° on average, and only by 11° on average in absolute value after a baseline correction of the average phase difference.

4. CONCLUSIONS

An offset dielectric-loaded flat reflector antenna has been designed and realized for submillimetre wavelengths. The antenna is designed to be used in the development work of antenna measurement techniques. The measurements at 310 GHz verify that this low-cost antenna has suitable characteristics for the use as a test object. The measured half-power beamwidth is 0.51°. The antenna structure is simple enabling low costs and easy manufacturing of the antenna. The antenna structure is also compatible with typical available instrumentation at these high frequencies.

ACKNOWLEDGMENTS

The authors wish to thank Mr. Eino Kahra for the help in the mechanical realisation of the antenna. The Academy of Finland and TEKES have supported the work through SMARAD - Centre of Excellence.

References

[1] A.V. Räisänen, J. Ala-Laurinaho, T. Koskinen, A. Lönnqvist, J. Säily, J. Häkli, J. Mallat, V. Viikari, S. Ranvier, and J. Tuovinen, "Computer-generated hologram and its use for submm-wave antenna measurement," *2004 IEEE Aerospace Conference Proceedings*, Big Sky, MO, March 6–13, 2004, CD-ROM, ISBN: 0-7803-8156-4.

[2] J. Ala-Laurinaho, J. Häkli, T. Koskinen, A. Lönnqvist, J. Mallat, S. Ranvier, A. V. Räisänen, J. Säily, J. Tuovinen, and V. Viikari, "Tests of the ADMIRALS antenna in a hologram compact antenna test range," *Proceedings of XXVIII National Convention on Radio Science & IV Finnish Wireless Communication Workshop*, October 16–17, 2003, Oulu, Finland, pp. 263–266.

[3] A. Prata, M.R. Barclay, W.V.T. Rusch, and D.C. Jenn, "Dual-reflector antenna sidelobe control through a dielectric loaded subreflector," *Digest of Antennas and Propagation Society International Symposium*, 1988, vol. 2, pp. 859–862.

[4] P.H. Siegel and R.J. Dengler, "The dielectric-filled parabola: a new millimeter/submillimeter wavelength receiver/transmitter front end," *IEEE Transactions on Antennas and Propagation*, vol. 39, pp. 40–47, January 1991.

[5] D.M. Harrison, M. Fujimoto, and G. Tabor, "A hemispherical lens antenna for multi-satellite reception," *Digest of Antennas and Propagation Society International Symposium*, 1992, vol. 3, pp. 1332–1335.

Composite Video Traffic over IEEE 802.15.3a Wireless Personal Area Networks

Livio Viggiano[(1)], Ulrico Celentano[(1)], Ian Oppermann[(1)]

[(1)]Centre for Wireless Communications, University of Oulu
Tutkijantie 2E, PO box 4500,
90014 Oulu, Finland
Email: { livio.viggiano, ulrico.celentano, ian.oppermann} @ee.oulu.fi

Abstract
In this paper, transmission of multidimensional video traffic over IEEE 802.15.3a WPANs is presented. First, a statistical model for the multidimensional video source is presented and validated by comparison with real traces. Then, different resource allocation strategies implemented on top of IEEE 802.15.3 MAC are presented and their performance compared.

Keywords: MAC, Modelling, QoS, UWB, Video, WPAN.

1. INTRODUCTION

This work is part of the research performed at CWC within ULTRAWAVES EU-IST project. The scope of the project is to provide a wireless home connectivity solution for audio and video entertainment devices, based on IEEE 802.15.3 architecture and exploiting an UWB radio interface. The work presented here deals with L2 issues of the protocol stack within the domain of ULTRAWAVES.
In this paper, transmission of multidimensional video traffic over IEEE 802.15.3a WPANs is presented. First, the composite ULTRAWAVES video source is represented by a statistical model based on analysis of the source's properties. This model is validated by comparison of its statistics with those of real traces. Then, different resource allocation strategies are presented and their performance is compared using implementation of both strategies and IEEE 802.15.3 MAC [1] in OPNET network performance analyzer.

2. MULTIDIMENSIONAL VIDEO SOURCE TRAFFIC

The video traffic source considered in this work consists of three MPEG-2 [2] streams, each being a part of a unique panoramic, scene (Fig. 1). Three screens are positioned along a polygon arc with spectators located approximately in the polygon's centre.

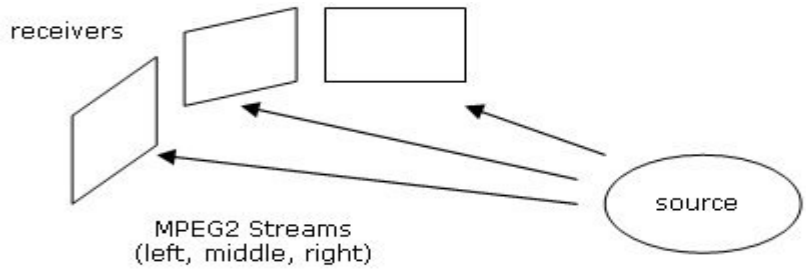

Fig. 1. The ULTRAWAVES scenario.

Since each triple of frames compose a snapshot of a single scene, those streams exhibit mutual correlation. Statistical properties of MPEG video traffic [3] show that using a Gamma probability distribution function (PDF) to model I, P, and B frame sizes gives good fitting with empirical data. The analyses performed in CWC on real multidimensional video streams confirm these results, and show how the three streams are correlated (Table 1).

Table 1. Correlation ρ between pairs of picture portions.

Video Stream 1	Video Stream 2	ρ
left	middle	0.9104
left	right	0.8699
middle	right	0.9187

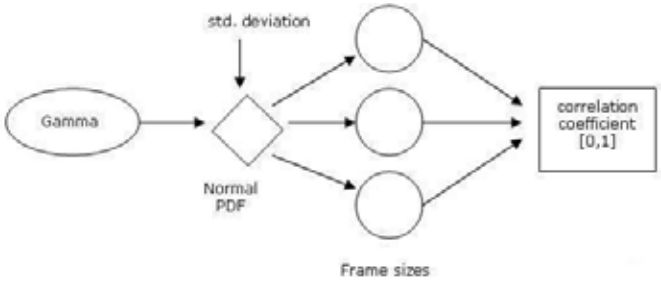

Fig. 2. The model for the multidimensional composite video source.

A proposed way to provide three different streams with identical distribution and with chosen correlation coefficient is presented in the following (Fig. 2). For each occurrence of an I, P, or B frame, a realization from a Gamma PDF with proper parameters is generated. Each realization is then used as arithmetic mean for a Normal PDF from which three different realizations are extracted. These values are the frame sizes of the three different streams generated by our model. Increasing and decreasing the standard deviation value of the Normal PDF between reasonable limits, allows us to obtain correlation coefficient be spread on all the interval [0,1]. Basically, the effect of this filtering is that the occurrences in the heaviest classes are shifted to the sides without being replaced by the same amount of occurrences coming from the closest classes. This means that the values are slightly more spread on the abscissa axis, with same mean but increased variance. Fig. 3 shows a graphic comparison of the original data with the one generated by filtering through a Normal PDF. It can be seen that the difference is reasonably small. Obviously, the larger the increase in the correlation between streams, the smaller are the changes in the shape of the streams.

This particular source has been implemented in OPNET network performance analyzer (version 6.0), allowing to simulate this multidimensional MPEG-2 video traffic according to the proposed procedure described above.

3. QOS SUPPORT IN IEEE 802.15.3 MAC

IEEE 802.15.3 MAC draft Standard presents a centralized, peer-to-peer communications system for short range applications [4]. In these wireless personal area networks (WPANs), interconnected devices (DEVs) are associated in a so-called piconet (PN). Among DEVs, the piconet coordinator (PNC) is selected. The PNC regulates in a centralized manner the traffic, which is however peer-to-peer. Both contention-based and contentionless accesses are available in the Standard. The IEEE 802.15.3 MAC superframe (SF) is shown in Fig. 4. With the beacon, the PNC informs each DEV on the composition of the fields following in the superframe, and on the allocation of the contentionless TDMA time slots. Channel time allocation (CTA) requests can be either asynchronous or isochronous. In the latter case, a dedicated pseudo static slot is granted to the device that has requested it to transmit high priority data. Resource allocation policies and quality of service (QoS) provision is on purpose left undefined in the Standard. This topic is addressed in this work.

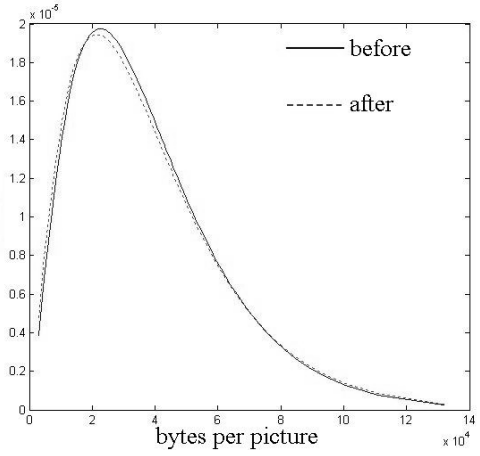

Fig. 3. Probability distribution function before and after filtering through the Gaussian PDF

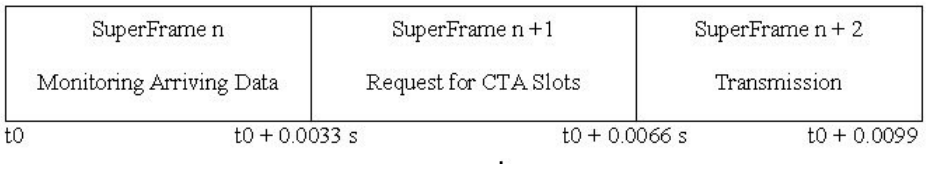

Fig. 4. The three-phase CTA negotiation procedure

In the scenario described in this paper, it is assumed that the same WPAN is used to carry delay-sensitive, high priority video traffic together with delay-insensitive, low priority background data. The latter traffic can be represented, e.g., by uploading or downloading data between a pair of DEVs of the WPAN. The scope of resource allocation schemes described here is to guarantee the requested quality to the video traffic whilst maximizing the throughput of background data traffic.
According to IEEE 802.1.D Informative Recommendation [5], when there are only two queues, QoS categories have to be intended for highest priority as Voice Traffic (i.e., requirement of less than 10ms delay), and for lowest priority as Best Effort. IEEE 802.15.3 suggests using isochronous channel time allocation (CTA) slots for high QoS categories (classes 3 to 6). In IEEE 802.15.3 MAC, despite the centralized policy, the acknowledgement of the required capacity is done by each device. A device that has to transmit a video stream is capable to choose how much capacity to ask to transmit its data. If the requested capacity is chosen equal to the peak of the video stream required bandwidth, then the delay will be close to zero, but there will be a huge waste of capacity. If the requested capacity is chosen equal to a value between the peak and the average of the traffic, then the efficiency of the allocation will increase, but this will introduce a delay that increases as much as the data comes with more jitter. An adaptive solution that increases the efficiency of time slots allocation until reaching the optimal performance, providing at the same time a QoS in terms of delay that respects Voice category specification is here presented. The superframe length is fixed in 0.0033 s. In each SF there is always at least one management CTA (MCTA) for each device. During each SF, the device is monitoring how many data need to be sent. In the following SF, an asynchronous channel time request command is sent by the devices within the assigned MCTA to inform the PNC of the needed amount of capacity. The PNC then counts the amount of high priority requests and if it is possible to satisfy all of them, allocates requested CTAs to each device for the upcoming SF. Since a cycle of monitoring-request-allocation is made by three SFs, if an high priority request can be satisfied, the delay introduced will be in the worst case (i.e., with data arrived at the beginning of the monitoring SF and scheduled at the end of the transmission SF) 0.0099. This value agrees with QoS specification above introduced. The efficiency of the resource allocation is optimal. Measuring the efficiency in terms of slots used to transmit packets over the number of allocated slots, η_m, it can be seen that with our proposed method this parameter reaches the maximum, which is the unit. An isochronous stream dimensioned on the peak will give η_p = (average value) / (peak value), while an isochronous stream dimensioned with a value between the average and the peak will give an η varying between η_p and η_m , but without any QoS guarantee. In implementing the resource allocation algorithm, reliability for the allocated streams is granted in the following way. Since IEEE 802.15.3 MAC suggests to use isochronous stream to grant a fixed amount of capacity, it ensures that an allocated stream will last as much as a device needs it. In order to provide this, the MAC is able to refuse isochronous streams when there is not enough capacity to satisfy the existing plus the new request, thus an ON-OFF policy. To emulate this behaviour using asynchronous requests, our MAC gives priority to the high priority streams already in service while deciding on a new allocation request. This means that in case of a very large request of resources, the last DEV trying to access the medium will be neglected service. (So, for example, in a home consumer electronic application scenario, a request to start a wireless videogame will not interrupt any portion of the movie watched possibly in the other room.) In addiction to that, there is a limit on the amount of capacity that each device can obtain. Since the radio interface that we are considering provides 110 Mbit/s, a fraction of the overall capacity is available to other devices in the piconet. Fairness is also provided in order to allow all the devices to transmit low-priority data with the same probability.

4. RESULTS

Evaluation of the performances of adaptive asynchronous allocation in terms of delay and efficiency are shown in the following.

In Fig. 5 are plotted the asymptotic values of the average end to end delay for several bit-rates. As shown, at 35Mbps the average delay is already pretty below the 0.1 s limit.
In Fig. 6 is shown how the dynamic allocation of the capacity minimizes the delay without wasting capacity. The comparison with a synchronous allocation at 110Mbps which gives delays pretty closes to the ones given by the dynamic allocation (Table 2) shows that using a dynamic allocation the average of occupied capacity decreases from the 58% to the 26%, freeing all the space wasted by the static allocation to other applications.

Table 2. Comparison between delays given by allocations of Fig. 6 at 110 Mbps

end to end delay (average)	DEV	SYNCH	DYN
	rcv 1	0.013	0.0074
	rcv 2	0.013	0.0120
	rcv 3	0.013	0.0160

5. CONCLUSIONS

In this paper, a statistical model for the multidimensional ULTRAWAVES video source has been presented. The model has been implemented in OPNET together with the model of IEEE 8021.5.3 MAC. On top of it, a resource allocation policy that provides reliable QoS for 802.1D data has been presented. The performance of this scheme has been studied and discussed. It has been shown that the proposed resource allocation scheme provides optimal performance in terms of allocation efficiency while having the delay kept within the category specification.

6. ACKNOWLEDGEMENTS

This work has been supported by the EC within IST project ULTRAWAVES IST-2001-35189, FW Pr. 5

7. REFERENCES

[1] IEEE, "Draft Standard for Telecommunications and Information Exchange Between Systems – LAN/MAN Specific Requirements – Part 15.3: Wireless Medium Access Control (MAC) and Physical Layer (PHY) Specifications for High Rate Wireless Personal Area Networks (WPAN)", Draft P802.15.3/D17, Feb 2003.
[2] MPEG-2 Motion Picture Expert Group, URL: http://www.chiariglione.org/mpeg/
[3] O. Rose, "Statistical properties of MPEG video traffic and their impact on traffic modeling in ATM systems", Proc. Local Comput. Netw., 16-19 Oct, pp. 397-407, 1995.
[4] U. Celentano, I. Oppermann, "Medium Access Control", in UWB Theory and Applications, Chapt. 7 in: I. Oppermann, M. Hämäläinen, J. Iinatti (eds.), 320 p., Wiley, Oct 2004.
[5] ANSI/IEEE Std 802.1D, Media Access Control (MAC) Bridges, 1998.
[6] A. Chodorek and R. R. Chodorek, "Characterization of the MPEG-2 video traffic generated by DVD applications", Proc. Eur. Conf. Universal Multiservice Netw., pp. 62-70, 2000.

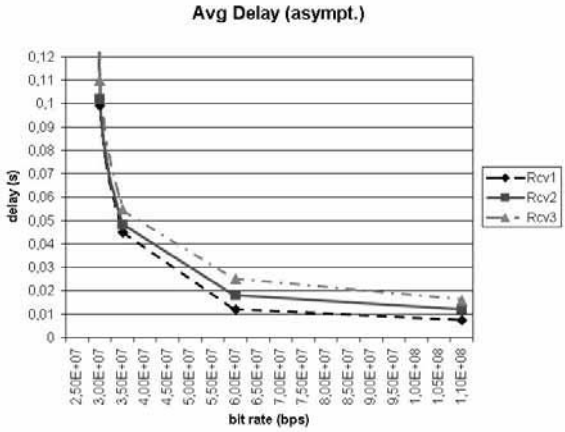

Fig. 5. End-to-end packet Delay for the three receivers with Dynamic Resource Allocation

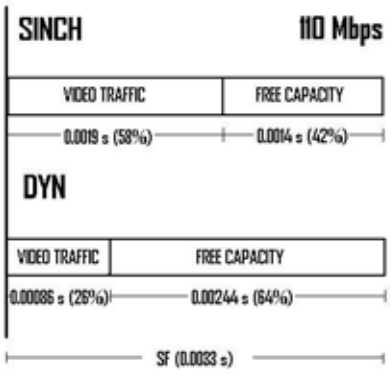

Fig. 6. Comparision between Synchronous and Dynamic Resource Allocation at 110 Mbps

Session 6a:
Sensors and Applications

Planck – Mission and Technology

Petri Jukkala[(1)], Nicholas Hughes[(1)], Mikko Laaninen[(1)], Ville-Hermanni Kilpiä[(1)], Jussi Tuovinen[(2)], Jussi Varis[(2)], Anna Karvonen[(2)]

[(1)]Ylinen Electronics Ltd.
Teollisuustie 9 A
02700 Kauniainen, Finland
Email:Petri.Jukkala@elektrobit.com

[(2)]Millilab, VTT Information Technology
Tietotie 3, Espoo
P.O. Box 12021, 02044 VTT, Finland
Email:Jussi.Tuovinen@vtt.fi

Abstract

An overview will be presented for the Planck Mission to measure Cosmic Microwave Background (CMB) radiation anisotropies with an accuracy better than ever. Special attention will be given to the development, manufacturing and performance of the 70 GHz receivers of the Low Frequency Instrument (LFI). Sensitivity of the receivers is based on state-of-the-art InP MMICs. Presently, the Engineering Model (EM) has been completed and manufacturing of the Proto Flight Model (PFM) is ongoing. The EM of LFI 70 GHz receivers have demonstrated performance with a 43 K noise temperature, 7 GHz effective noise bandwidth, and a 1/f knee frequency of 40 mHz. For the PFM a new MMIC run has been made and the amplifiers achieve a noise temperature of about 25 K, when cooled to 20 K.

Keywords: Cosmic Microwave Background, low noise receiver, MMIC

1. INTRODUCTION

The Planck Mission is part of the European Space Agency's (ESA) Cosmic Vision 2020 science program. After NASA's COsmic Background Explorer (COBE) and Wilkinson Microwave Anisotrophy Probe (WMAP) spaceprobes, Planck is the third generation mission dedicated for Cosmic Microwave Background (CMB) observations to map the full sky. Planck's final performance will be only limited by astrophysical constraints. Two multipixel and ultrasensitive instruments to determine the anisotropy (mK variations) of the CMB radiation will be on board of Planck: the Low Frequency Instrument (LFI) and the High Frequency Instrument (HFI). Both instruments will utilise a common passively cooled 1.5 m aperture off-set reflector antenna. The front-ends of the LFI and HFI receiver arrays are cooled to 20 K and 0.1 K, respectively. LFI, based on InP MMIC amplifiers, will have channels at 30, 44, and 70GHz. The corresponding number of receivers at each frequency is 4, 6, and 12. Both polarisations will be measured at all LFI frequencies. Therefore, each corrugated horn on the focal surface will be followed by an orthomode transducer (OMT) to separate the two polarisations. The number of feed horns is half of the number of receivers. HFI, based on bolometer technology, will have channels at 100, 143, 217, 353, 545, and 857 GHz and 4, 12, 12, 6, 6, and 6 detectors at each frequency, respectively. Planck will be launched in 2007 together with the Herschel telescope using the Ariane 5.

A passive millimeter wave imaging system

Mikko Kantanen, Manu Lahdes, Jussi Tuovinen

MilliLab, VTT Information Technology
P.O. Box 12021
FIN-02044 VTT
Finland
Email: mikko.kantanen@vtt.fi

Abstract
The millimeter wave imaging is useful for applications where conventional visible light and infrared sensor are inadequate. In this work a millimeter wave imaging system has been built to demonstrate millimeter wave imaging capabilities. Basic theory of millimeter wave imaging is presented and imaging system utilising a Dicke radiometer is described. Millimeter wave images taken with the system are shown.

Keywords: Passive millimeter wave imaging, passive millimeter wave imaging system, radiometry

1. INTRODUCTION

Progress in the manufacturing of the millimeter wave monolithic integrated circuits (MMICs) has increased the interest towards millimeter wave applications. The characteristic properties of millimeter waves enable some unique applications, one of which is the millimeter wave imaging. Millimeter wave imaging systems can be considered as an extension of imaging sensors working at visible light and infrared regions. Using millimeter waves, imaging can be performed when it is impossible to get pictures with visible light and infrared sensors. One great advantage of using millimeter waves is to be able to picture a scene under adverse weather conditions, for example through fog or dust. Possible applications for millimeter wave imaging sensors are automotive collision avoidance radars, enhanced vision systems, concealed weapon detection, and contraband detection.

2. PASSIVE MILLIMETER WAVE IMAGING THEORY

A millimeter wave image is created by measuring an antenna temperature map over the scene of interest using very sensitive radiometer. The antenna temperature of the object depends on the noise radiated from the object. This noise has two components; part of the noise is related to the physical temperature of the object and the other part is surrounding noise reflected by the object. Mathematically this can be formulated

$$T_A = \varepsilon T_P + \rho T_r , \tag{1}$$

where T_A and T_P are the antenna temperature and the physical temperature of the object, respectively. T_r is the noise temperature of the reflected radiation. Material parameters, emissivity ε and reflectivity ρ, describe how much radiation is coming from internal and external source, respectively. These two parameters are related by equation

$$\varepsilon + \rho = 1 . \tag{2}$$

Using (2), (1) can be re-written

$$T_A = T_r + \varepsilon(T_P - T_r) = T_r + (1-\rho)(T_P - T_r), \tag{3}$$

where it is seen that for two objects at same physical temperature, the difference in measured antenna temperatures depends only on the emissivity (or reflectivity) of the objects.

At millimeter wave region, the sky can be used as an external noise source for imaging. The antenna temperature of the sky is a function of the elevation angle and ranges between 30-290 K at 94 GHz. Thus,

objects reflecting noise from the sky appear colder than their surroundings, in a sense of antenna temperature [1, 2].

3. IMAGING SYSTEM

3.1. Scanner

To obtain an informative image of the scene of interest large number of pixels is needed. In infrared imagers, full staring arrays with one receiver for each pixel are used. In a millimeter wave imager, this kind of array is also possible but extremely expensive. Thus, imaging is normally performed using small number of receivers and scanning the main lobe of an antenna over the scene of interest.

Scanning can be mechanical or electronic. In mechanical scanning, entire antenna or focusing elements are moved step-by-step or continuously. Mechanical scanning is relatively easy to realize, but its drawback is slowness, which is present in mechanical movement. Also, antenna system may be quite heavy, which makes scanning system designing very challenging [3]. In electronic scanning, the main lobe of an antenna is moved by adjusting electrical properties of the antenna or a feed network. The main options for electronic scanning are multiplexing techniques, correlation radiometers and phased array antennas [4]. Electronic scanning systems require very precise components, such as switches and phase shifters. They may also need quite complex signal processing algorithms. For these reasons, millimeter wave imaging systems have so far used mechanical scanning mainly.

The purpose of this work has been to build a simple imager that demonstrates the capabilities of millimeter wave imaging. The main emphasis has been on the quality of images, while the imaging speed has been with less importance. Thus, a mechanical scanning has been used. In this scanner, the entire radiometer system is moved in azimuth and elevation planes using two computer controlled stepper motors. The scene of interest is scanned in a step-by-step fashion.

3.2. Radiometer

Another main issue to create an informative image is the ability to measure antenna temperature accurately. This is done using a very sensitive radiometer. The most well known radiometer topologies are total power, Dicke and noise adding radiometers. In an ideal case, best antenna temperature resolution is achieved using a total power radiometer. However, gain instability of the radiometer degrades its performance. The gain instability issue is more important as the total imaging time is longer. The errors due the gain instability are reduced by calibrating the radiometer constantly, either by reference load as in Dicke radiometer or by added noise as in noise adding radiometer [5, 6].

In this work, a Dicke radiometer has been used. The block diagram and a photo of the radiometer are presented in Fig. 1 and Fig. 2, respectively. A 30 cm diameter horn antenna, with two focusing lenses is used to get a narrow main lobe. The beamwidth is 0.7°. Antenna is followed by single pole double throw (SPDT) switch that connects either the antenna or the reference load to the first amplifier with 1 kHz frequency. The amplifier chain consists of two low noise amplifiers (LNA) and isolators to reduce possible mismatch problems. The millimeter wave signal is transformed directly to DC using a detector diode and a low frequency amplifier. The operational frequency of the radiometer is 94 GHz with 4 GHz bandwidth.

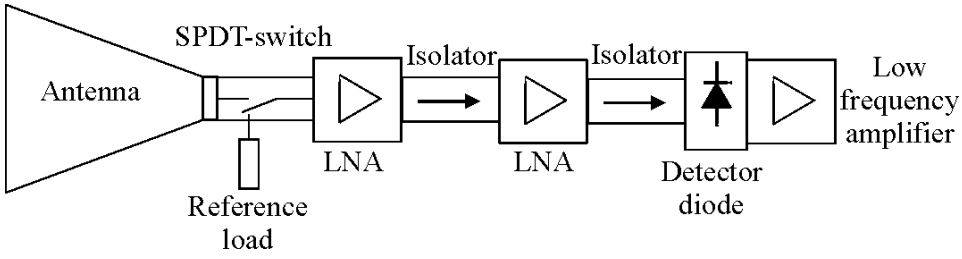

Fig. 1. The block diagram of the Dicke radiometer.

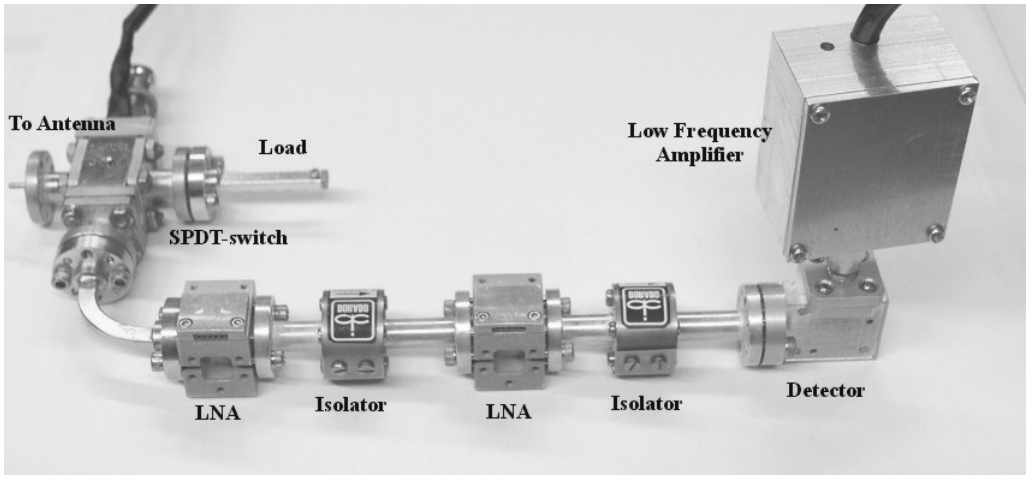

Fig. 2. A photo of the Dicke radiometer.

3.3. Data processing

The resulting two level 1 kHz signal from the detector diode is fed to 12-bit A/D-converter. The raw waveform data is read to the computer and reference and antenna signals are separated. Using the reference signal to track gain variations, a corrected antenna temperature reading is calculated. From the resulting data an appropriately scaled grayscale picture is created. The pictures can be further improved using commercial photo editing programs.

4. PASSIVE MILLIMETER WAVE IMAGES

In the following, some millimeter wave images taken with the imager described above are presented. In the images, colder objects appear brighter.

In Fig. 3, concealed weapons detection capability is demonstrated. A person is holding a metallic handgun silhouette inside a newspaper. Reflection of the cold sky is clearly noticeable. There are also additional reflections from shoulders, chest and arms.

Fig. 3. A millimeter wave image and a photo of a person carrying a handgun silhouette inside the newspaper.

In Fig. 4, millimeter wave image is used for enhanced vision purposes. Main objects in the millimeter wave image are two trash containers. One in front and the other further back. Also, signs indicating visitor parking slots and the tree line are detectable from the millimeter wave image. The strongest reflection comes from the trash container frame. Reflection from the tarmac creates a millimeter wave "shadow" for the container.

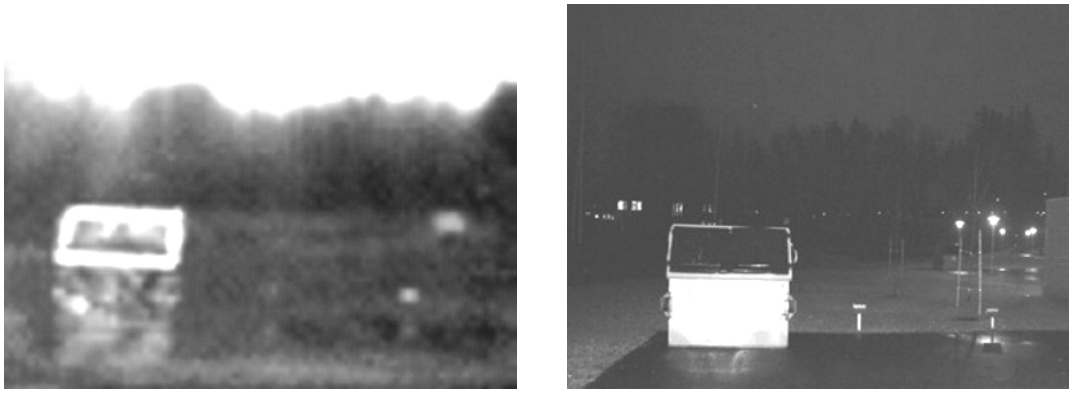

Fig. 4. A millimeter wave image and a photo of a night time scenery.

5. ACKNOWLEDGMENT

This work has been supported by Finnish Defence Forces Technical Research Centre.

6. REFERENCES

[1] L. Yujiri, M. Shoucri, and P. Moffa, "Passive millimeter wave imaging," *IEEE Microwave Magazine*, vol. 4, no. 3, pp. 39-50, 2003.

[2] R. M. Smith, K. D. Trott, B. M. Sundstrom, and D. Ewen, "The passive mm-wave scenario," *Microwave Journal*, vol. 39, no. 3, pp. 22-34, 1996.

[3] D. G. Gleed, R. Appleby, N. A. Salmon, S. Price, G. N. Sinclair, R. N. Anderton, J. R. Borrill, and M. R. M. Wasley, "Operational issues for passive millimeter wave imaging system," *Proceedings of SPIE on Passive Millimeter-Wave Technology*, vol. 3064, Orlando, FL, 1997, pp. 23-33.

[4] A. R. Harvey, R. Appleby, P. M. Blanchard, and A. H. Greenaway, "Beam-steering technologies for real time passive millimeter wave imaging," *Proceedings of SPIE on Passive Millimeter-Wave Technology II*, vol. 3378, Orlando, FL, 1998, pp. 63-72.

[5] L. A. Klein, *Millimeter Wave and Infrared Multisensor Design and Signal Processing*, Norwood, Artech House Inc. 1997.

[6] F. T. Ulaby, R. K. Moore, and A. K. Fung, *Microwave Remote Sensing*, Reading, Mass., Addison-Wesley Publishing Company, 1981.

Development of SQUID Amplifier and AC-biased Bolometer for Detection of Sub-mm Radiation

Jari S. Penttilä[(1)], Antti Virtanen[(1)], Minna Nevala[(2)], Kimmo Kinnunen[(2)], Arttu Luukanen[(1)], Juha Hassel[(1)], Mikko Kiviranta[(1)], Panu Helistö[(1)], Ilari Maasilta[(2)], and Heikki Seppä[(1)]

[(1)]VTT Information Technology
P.O. Box 1207
FI-02044 VTT, Finland
Email: jari.s.penttila@vtt.fi

[(2)]University of Jyväskylä
P.O. Box 35
FI-40351 Jyväskylä, Finland
Email: ilari.maasilta@phys.jyu.fi

Abstract
We report development on submillimeter wavelength detection system based on ac-biased superconducting antenna-coupled transition-edge microbolometer operated at 4 K. The sensor is read out by low noise superconducting quantum interference device (SQUID) followed by room temperature ac electronics. Based on dc measurements, the should be below room temperature photon noise. Multiplexed readout enables construction of multi-pixel arrays with capability to sense subkelvin temperature differences at video frequency.

Keywords: bolometers, superconductors, cryogenics, multiplexing

1. INTRODUCTION

The demand for improved radiation detectors especially in the submillimeter is increasing rapidly. Many promising applications require, instead of single pixel detectors, large detector arrays or cameras. Most of the spectral lines of materials lie in the submillimeter band. New detector and source concepts have made possible the survey of this interesting but so far little studied frequency region. In security applications, the potential of submm frequencies has been demonstrated in detection of concealed weapons [1]. Submm frequencies are also suitable for medical applications, atmosphere monitoring and studies of the anisotropy of the cosmic background.
For fundamental reasons, the best thermal detectors in terms of the noise equivalent power are superconducting detectors. The low temperature decreases thermal noise, the steep superconducting transition decreases the contribution of Johnson noise compared to the inevitable phonon noise. In non-thermal photon-counting detectors the small energy gap of superconductors makes ample number of charge carries available compared to semiconducting detectors. Superconducting transition-edge sensors (TES) are thus one major branch of ultra-high resolution detectors for both submm and X-ray energies. One advantage of TES sensors is their scalability: large matrices of such sensors can in principle be fabricated with micro- or nanolithography, just like semiconducting detector arrays. However, brute-force scaling up of the detector and readout rapidly results in increased complexity and heat problems. Although a SQUID is a low power device (1-10 nW/device) compared to semiconductors, the power consumption of a large number of SQUIDs is considerable. In addition, each wire from room to cryogenic temperature introduces noise and conducts heat. The cooling capacity at low temperatures is highly limited. Thus multiplexing schemes to read out a number of detector pixels are intensively searched now around the world.

2. TRANSITION-EDGE SENSOR

The sensor consists of an antenna-coupled niobium vacuum-bridge bolometer [2] in which the thermal isolation is obtained by a vacuum gap between the bridge and the substrate (see Fig.1). Antenna coupling extends the detectable range of wavelengths to millimeter waves and further. Thus, the temperature sensing element can be made much smaller than the wavelength of the detected signal allowing smaller thermal mass. So far the best reported power resolution at 4 K is 14 fW/√Hz [2].

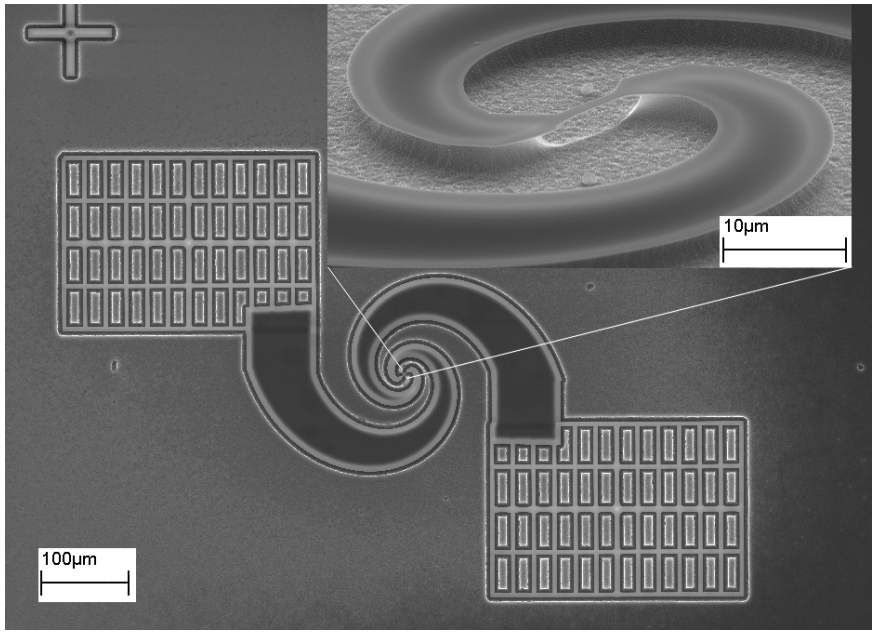

Fig. 1. Antenna-coupled microbolometer fabricated at University of Jyväskylä. The niobium bridge is located at the center of the spiral. The inset shows a magnified view of the bridge.

The most popular readout technique is to voltage bias the TES to a suitable point in the transition curve and couple it inductively to a SQUID, a current sensitive amplifier, which naturally matches the small impedance of the TES. The change in resistance due to heat absorbed is read out as a change in the current. Voltage bias also introduces so-called electrothermal feedback (ETF) [3]: the dissipated power becomes a constant, so that an amount of incoming radiative power will replace the same amount of bias power. ETF leads to decreased response time and increased dynamic range. In the limit of large ETF, the electrical responsivity of bolometer current to the applied power, $S_I \equiv dI/dP$, approaches $S_I \propto -1/V$. The responsivity increases as the bias voltage is lowered. However, at very low bias voltages the electrical circuit becomes unstable. This instability occurs when electrical time constant $\tau_{ele} = L_{in}/R$ becomes of the order of the intrinsic thermal time constant $\tau = C/G$. Here R is the bolometer resistance at the bias point, C is the heat capacity and G is the thermal conductance of the bolometer.

3. READOUT ELECTRONICS

Superconducting quantum interference device, SQUID, is the most sensitive magnetometer known. A SQUID can be used as an ultra low noise current amplifier by placing a superconducting planar coil above the SQUID loop. As current signal flows through the coil, changing magnetic field is induced through the SQUID producing current or voltage signal at the SQUID output.
SQUID-based readout electronics for weak current signals has been developed and tested at VTT [4]. Owing to Pd shunt resistors, the SQUID can be cooled down to millikelvin temperatures. In the SQUID electronics, the current signals coming from a bolometer-based submm detector are sensed by current biased SQUIDs. A simple schematic of the measurement setup is shown in Fig. 2. Two transformers are used for impedance and noise matching at the SQUID output. The first transformer matches the low output impedance of a SQUID to the 50 Ω characteristic impedance of the twisted pair used to bring the signal to room temperature. The second transformer performs noise matching between the 50 Ω input and a room-temperature amplifier stage based on parallel-coupled discrete JFETs. The room temperature amplifier is a narrowband amplifier tuned at the center frequency of 5 MHz.

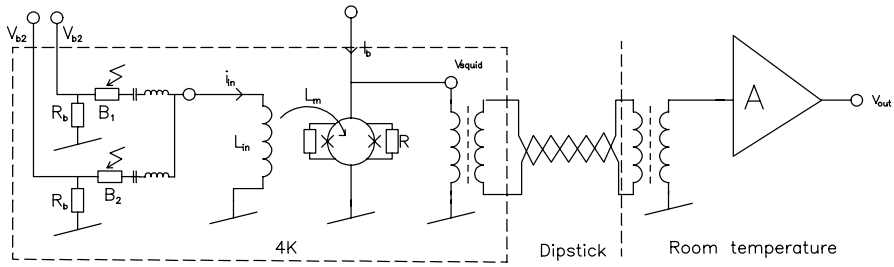

Fig. 2. A simple schematic of the squid-based read out electronics

Bolometers B_1 and B_2 are voltage biased with a bias resistors $R_b << R_{1,2}$, where $R_{1,2}$ is the resistance of bolometer $B_{1,2}$. One SQUID can be used to measure signal from several bolometers by using frequency domain multiplexing [5]. Each bolometer is biased with a carrier signal at an individual frequency. Signal detected by bolometers is then multiplied by the carrier signal and passed through a bandpass filter with has the same center frequency as the carrier signal. Signal is then amplified and can be demodulated by multiplying it with the carrier signal again.

The SQUID based readout amplifier was tested without bolometers at 4.2 K. Frequency response was tested by feeding a current signal to the input coil L_{sq} through a 100 kΩ resistor at room temperature. Voltages were measured at the output and input to determine the amplification of the system. Measured current gain v_{out}/i_{in} is shown in Fig. 3a. Current gain at 5 MHz was 78 mV/μA. The increase at high frequencies is due to capacitive leakage in the bias lines.

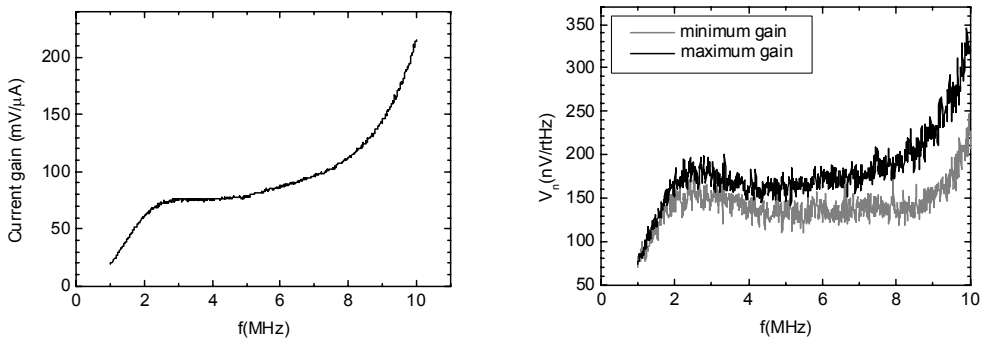

Fig. 3. a) Measured frequency response v_{out}/i_{in} of SQUID-based readout amplifier, b) measured noise voltage at the amplifier output. The white noise at the maximum gain corresponds to a current noise of 2.2 pA/rtHz at the SQUID input coil.

Output noise of the SQUID based amplifier was measured at amplifier output. Fig. 3b shows the noise voltage when SQUID is biased to a point of maximum and zero gain. Zero gain measurement indicates the noise floor of the setup, which is about 130 nV/√Hz at the amplifier output. The current noise reduced to the SQUID input coil is 2.2 pA/rtHz corresponding to flux noise of 0.6 $\mu\Phi_0/\sqrt{Hz}$ at the SQUID loop.

4. DC MEASUREMENTS OF BOLOMETERS

We have measured the dc current-voltage characteristics of the vacuum-bridge bolometers using the SQUID electronics by shorting the bandpass filter in Fig. 2 and by measuring the SQUID output voltage using a dc-coupled preamplifier. The setup is build on ^{4}He flow cryostat equipped with optical windows. Fig. 5 shows the bolometer current as a function of bias voltage. The data is fitted to theoretical IV-curve

$$I(V) = \frac{4G(T_c - T_0)}{V} + \frac{V}{R_n}, \qquad (2)$$

where G is the thermal conductance, T_c and T_0 are the critical and bath temperatures, and R_n is the normal state resistance of the bolometer. The minimum voltage bias was limited by the measurement setup and

the actual low voltage instability is estimated to be at even lower voltages. From the minimum bias voltage and the measured parameters we calculate the typical responsivity of –2000 A/W and NEP of about 2 fW/√Hz. In the calculation, we have taken into account both SQUID current noise and the Johnson noise and phonon noise of the bolometer.

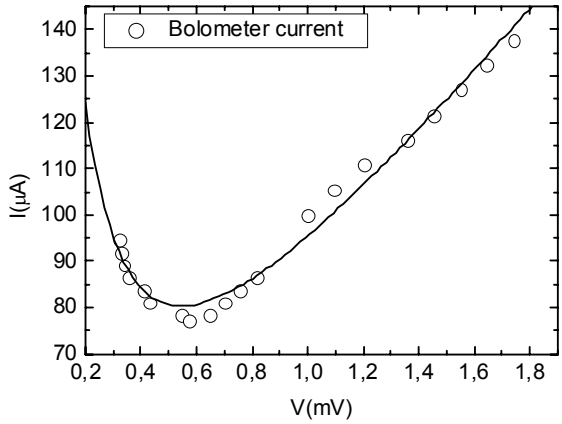

Fig. 5. Current-voltage characteristics of vacuum-bridge microbolometer. The solid line is the fit based on theoretical curve (2).

5. CONCLUSIONS

The estimated noise equivalent power of 2 fW/rtHz of our bolometer setup implies that it is possible to reach performance limited by the room temperature photon noise. We are currently preparing the ac biased bolometer setup in order to verify this assumption made using measured dc responsivity. In the setup, it is also possible to use frequency domain multiplexing the read out several bolometers with one SQUID.

Financial support from National Technology Agency of Finland is gratefully acknowledged.

References

[1] E. N. Grossman, A. K. Bupathiraju, A. K. Miller, C. D. Reintsema, "Concealed weapons detection using an uncooled millimeter-wave microbolometer system", *Proc. SPIE*, vol. 4719, pp. 364-369, 2002.

[2] A. Luukanen and J.P. Pekola, "A superconducting antenna-coupled hot-spot microbolometer," *Appl. Phys. Lett.*, vol. 82, pp. 3970-3972, June 2003.

[3] K. D. Irwin, "An application of electrothermal feedback for high resolution cryogenic particle detection", *Appl. Phys. Lett.*, vol. 66, pp. 1998-2000, April 1995.

[4] M. Kiviranta, J.S. Penttilä, L. Grönberg, H. Seppä, and I. Suni, "Dc and un SQUIDs for readout of ac-biased transition-edge sensors", *IEEE Trans. Appl. Supercond.*, vol. 13, pp. 614-617, June 2003.

[5] M. Kiviranta, H. Seppä, J. van der Kuur and P. de Korte, "SQUID-based readout schemes for microcalorimeter arrays", *AIP conference proceedings*, vol 605, pp. 295-300, (2002).

Session 7a:
Remote Sensing II

Feasibility of HUT Snow Covered Area Estimation Method for Operative Use

Luojus, K., Pulliainen, J., Hallikainen, M.

Laboratory of Space Technology, Helsinki University of Technology
PO Box 3000, FIN-02015 HUT, Finland
Email: kari.luojus@hut.fi, tel: +358 9 4512377

Abstract
The feasibility of HUT Snow Covered Area (SCA) estimation method for operative use is studied. The HUT SCA method is a two-step procedure for estimating Snow Covered Area for boreal forest regions. The analysis of the method is conducted using ERS-2 SAR, Envisat ASAR and Radarsat images. The test area consists of Northern Finland and for the ERS-2 images an area of 14 sub-drainage basins is studied. The analysis is carried out for several affecting factors. The ERS-2 images are used for overall accuracy analysis of the method, and the Envisat and Radarsat images are used to determine the suitability of the method for operative use.

Keywords: Remote sensing, Snow Covered Area, SCA, snow melt season, space-borne radar

1. INTRODUCTION

Monitoring the snow melt season is important for various environmental, hydrological and meteorological applications. Information on snow cover during the snow melt season can be directly used for predicting and preventing floods and for optimising hydropower industry operations. Space-borne Synthetic Aperture Radars (SAR) have shown their usability in snow monitoring during the snow melt season and especially in monitoring of wet snow. Various methods for Snow Covered Area estimation using Space-borne SARs have been developed. The HUT SCA method has been developed for the boreal forest zone. The accuracy assessment with 24 ERS-2 SAR images for the method is conducted using a test region dominated by boreal forest. The assessment of the SCA method is vital in order to integrate the HUT SCA method with the Finnish Environment Institute SYKE's Watershed Simulation and Forecasting System (WSFS) [1]. The integration of SCA estimates derived from Space-borne SARs is expected to increase the overall accuracy of the operative WSFS model. The suitability of the HUT SCA method for operative use is studied with Envisat ASAR WSM and Radarsat SCW images. The WSM and SCW images have large spatial coverage and are thus more suitable than ERS-2 images for operative use.

2. TEST SITE, SATELLITE DATA AND REFERENCE DATA

The accuracy analysis with the ERS-2 images was conducted for a test site consisting of 14 River Kemijoki sub-drainage basins, located, in Northern Finland near Lokka. The studies with Envisat and Radarsat images are conducted with the test area covering the whole of northern Finland. Sub-drainage basins are used as calculational units to ensure operative compatibility with the WSFS model. Each sub-drainage basin is analysed independently to allow the analyses to be compared with the sub-drainage basin characteristics. The satellite data consists of 24 ERS-2 C-band SAR intensity images acquired during the years 1997, 1998, 2000, 2001 and 2002. The Envisat SCW data consist of 19 images acquired from 2003 and 2004 and the Radarsat data consist of 5 SCW images from 2004. The SCA estimation results are compared with data from model simulations of the WSFS.

3. HUT SNOW COVERED AREA ESTIMATION METHOD

The Snow Covered Area (SCA) method developed at HUT is a two-step procedure for obtaining the SCA estimate from SAR intensity images during the snow melt season. The procedure requires the knowledge of the forest stem volume distribution of the target area and two reference images are needed for the SCA estimation. One reference image describes the wet snow situation in the beginning of snow melt season and one reference image describes the snow-free situation at the end of the snow melt season. The first step of the method is a forest canopy compensation, which is done using forest stem volume information. The second step is the employment of pixel-wise linear interpolation algorithm that uses the reference images to calculate the snow covered area estimate. The radar backscattering coefficient is a sum of

backscattering signatures from different contributors. Some contributions are caused by the snow and ground layers, some are caused by the backscattering from forest and forest canopy. The contribution from forest canopy is not related to the SCA and it is therefore a source of error. This error can be minimised by using the forest compensation method. The method is based on the boreal forest backscattering model developed at HUT and has been presented by [2] and [3]. Using the forest backscattering model the contribution of backscattering of forest canopy is calculated, and this contribution is reduced from the total observed backscattering coefficient. The corrected value is then used in the second step of the method. The boreal forest backscattering model describes the backscattering coefficient (σ^o) as a function of stem volume:

$$\begin{aligned}\sigma^\circ(V,\chi) &= \sigma^\circ_{surf}\cdot\exp\left(\frac{-2\kappa_e(A(\chi))\cdot V}{\cos\theta}\right)+\frac{\sigma_V(B(\chi))\cos\theta}{2\kappa_e(A(\chi))}\left[1-\exp\left(\frac{-2\kappa_e(A(\chi))\cdot V}{\cos\theta}\right)\right] \\ &\equiv \sigma^\circ_{surf}\cdot t(V,\chi)^2+\sigma^\circ_{can}(V,\chi),\end{aligned} \tag{1}$$

where V is the forest stem volume [m³/ha] and A(χ) defines the canopy extinction coefficient κ_e [1/m³/ha] and B(χ) defines the canopy backscattering coefficient σ_v [1/m³/ha]. σ^o_{surf} is the backscattering coefficient of the ground or snow layer, and θ is the angle of incidence. The first term of (1) defines the backscattering contribution from ground or snow layer σ^o_{surf} and the two-way transmittivity through the forest canopy t^2. The second term of (1) σ^o_{can} defines the forest canopy backscattering contribution. The values for κ_e and σ_v are dependent on weather conditions and are obtained by:

$$\kappa_e(A(\chi)) = a_0 \cdot \chi \tag{2}$$
$$\sigma_v(B(\chi)) = b_0 \cdot \chi^2 , \tag{3}$$

where constant coefficients $a_0 = 2.78\cdot10^{-3}$ ha/m³ and $b_0 = 9.99\cdot10^{-4}$ ha/m³. The values are derived for dry summer conditions where χ =1. For wet snow situation during the melt season the value for χ needs to be solved.

Using (1) – (3) the backscattering contribution for forest canopy can be solved by extracting backscattering coefficients representing different stem volume classes from the satellite images by using the forest stem volume information. The solving is a done by non-linearly fitting the observed backscattering coefficients to the model, where the parameters χ and σ^o_{surf} are the variables to be optimised. For the optimisation the backscattering for each stem volume class need to be calculated. The minimisation problem is written by:

$$\min_{\chi,\sigma^\circ_{surf}} \sum_{i=1}^{N} w_i \cdot \left(\left\langle\sigma^\circ_{OBSERVED i}\right\rangle - \sigma^\circ(V_i,\chi,\sigma^\circ_{surf})\right)^2, \tag{4}$$

where N is the number of volume stem classes, $\left\langle\sigma^\circ_{OBSERVED,i}\right\rangle$ is the observed backscattering coefficient for the stem volume class V_i and σ^o is the calculated backscattering coefficient. The weighing factor w_i is used if the stem volume classes are unevenly distributed. When the minimisation has been conducted and the parameters for the backscattering coefficient are known, the solved variables σ^o_{surf} and χ can be used with (1) to calculate the backscattering coefficient without the contribution from the forest canopy, corresponding to the backscattering with stem volume of 0 m³/ha. This is the forest compensated backscattering coefficient that is used in the second step; the linear interpolation phase of SCA estimation.

The linear interpolation algorithm uses a pixel-wise comparison of the observed backscattering coefficient to the backscattering coefficients from the two reference situations [4]. The outcome is the SCA estimate in percentage, obtained by:

$$SCA = 100\% \cdot \frac{\sigma^\circ_{surf} - \sigma^\circ_{ground,ref}}{\sigma^\circ_{snow,ref} - \sigma^\circ_{ground,ref}}, \tag{5}$$

where σ^o_{surf} is the observed or estimated surface backscattering coefficient, $\sigma^o_{ground,\ ref}$ is the reference backscattering coefficient from the snow-free ground and $\sigma^o_{ground,\ snow}$ is the reference backscattering

coefficient from the wet snow covered ground. In the case of forest compensated SCA evaluation, the used reference backscattering coefficients are the forest compensated values. The estimates for open areas are calculated by using the backscattering values from open areas. In this study the algorithm was used with averaged backscattering coefficients from the observed sub-drainage basins and the sub-drainage basins each contained several thousands of pixels.

4. RESULTS

The accuracy analysis with ERS-2 data was conducted with the main focus on the overall accuracy assessment for the SCA method. The analysis was conducted independently for open areas and forested areas. The HUT method is dependant on the selection of the reference images so this was the starting point for the analysis. The effect of reference image selection was conducted by choosing a large set of reference images with loose selection criteria and analysing the accuracy for all reference image combinations for all the cases. This provided a very large database for statistical accuracy analysis. There were 7280 individual SCA estimates for different reference image combinations and 268 estimates for the best reference image pair. The accuracy characteristics were obtained by comparing the SCA estimates with the WSFS reference data, i.e. the RMSE shows the average Root Mean Squared Error of all the estimates when compared to the corresponding WSFS reference data. The correlation coefficient shows the correlation between the SCA estimates and the WSFS reference data.

The results for all the reference image combinations were compared with the results obtained with the best reference image combination. As shown in Table 1 the reference image selection has a significant effect on the SCA estimation results. This is an important factor concerning the overall usage of HUT SCA method. The results acquired with the best reference pair combination can be considered as the accuracy for the SCA estimation when the reference image selection is conducted successfully.

Table 1. Overall accuracy characteristics and the influence of reference image selection analysed with ERS-2 data.

	Open areas		**Forested areas**	
	All combinations	**Best pair**	**All combinations**	**Best pair**
RMSE	0.278	0.213	0.204	0.179
Mean abs. error	0.209	0.137	0.154	0.119
Bias	+0.180	+0.095	+0.043	-0.049
Correlation coefficient	0.830	0.874	0.860	0.896

In addition to the effect of reference image selection, the accuracy analysis with ERS-2 data contained multiple other factors, including the effect of satellite flight path, the effect of topography and the effect of forest compensation on the estimation accuracy. The effect of forest compensation, which is a key element of the HUT SCA method is examined here. The effect was studied by calculating the SCA estimates without using the forest compensation algorithm. The estimates obtained with and without the forest compensation were then compared in the analysis. The RMSE showed an average improvement of 8,5% and an improvement of 11,8% in the case of the best reference image.

An example of the SCA estimation with ERS-2 data is illustrated in Fig. 1 by a map of SCA distribution for the 14 sub-drainage basins of Lokka area.

Studies for the operative suitability of the method are currently ongoing. The main factor concerning the operative use is the effect of incidence angle variation on large images to the SCA estimation. Also the functionality of the method with Radarsat data, which are HH-polarised is studied. The validation of the HUT SCA method for operative use will be conducted with a similar statistical accuracy analysis that was carried out for the ERS-2 data. The preliminary results of these studies include a spatial presentation of SCA estimation for Northern Finland with a Radarsat SCW image from 5 May 2004 shown in Fig. 1.

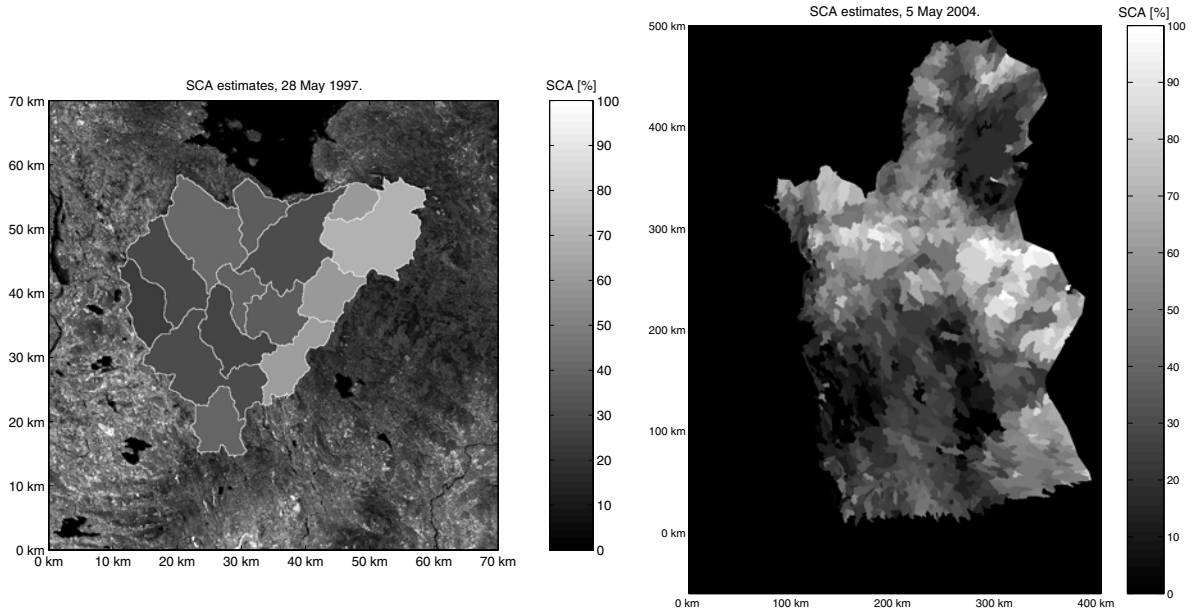

Fig. 1. On the left, an illustration of SCA estimation with ERS-2 data for 28 May 1997. On the right, an illustration of SCA estimation with Radarsat SCW data for 5 May 2004, covering most of northern Finland.

5. CONCLUSIONS

The main goal of analysing the statistical accuracy for the SCA method was reached. The analysis presents the accuracy of the method with the ERS-2 SAR data. For the statistical analysis the total number of test cases was 7280. The results show that the HUT SCA method works well in boreal forest region, which was expected. The analysis shows high correlation coefficients between the SCA estimates and the WSFS reference data and RMSE values of 0.213 for open areas and 0.179 for forested areas.

The data analysis with Envisat ASAR and Radarsat data for the operative use is currently underway. The preliminary results, however, suggest that the method is suitable for operative use, possibly with certain limitations caused by the variation of incidence angle in large images. The analysis for the variation of incidence angle and the overall accuracy are still ongoing.

6. REFERENCES

[1] Vehviläinen, B. (1994), ”The watershed simulation and forecasting system in the National Board of Waters and Environment”, Publications of the Water and Environment Research Institute, No.17, National Board of Waters and the Environment, Finland.

[2] Pulliainen, J., Kurvonen, L., Hallikainen, M. (1999), ”Multi-temporal behavior of L- and C-band SAR observations of boreal forest”, IEEE Trans. Geosci. Remote Sensing, vol. 37, pp. 927-937.

[3] Pulliainen, J., Koskinen, J., and Hallikainen, M. (2001), ”Compensation of forest canopy effects in the estimation of snow covered area from SAR data”, Proc. IGARSS'01, Sydney, Australia, 9-13 July 2001.

[4] Koskinen, J., Pulliainen, J., and Hallikainen, M. (1997), ”The use of ERS-1 SAR data in snow melt monitoring”, IEEE Trans. Geosci. Remote Sens. 35:601-610.

Snow Melt Detection Using Neural Networks

Matias Takala[(1)], Jouni Pulliainen[(1)], Markus Huttunen[(2)], Martti Hallikainen[(1)]

[(1)]Laboratory of Space Technology
Helsinki University of Technology
P.O. Box 3000, FIN-02015 HUT
FINLAND
Tel.: +358-9-451 6077
Fax.: +358-9-451 2898
Email: Matias.Takala@hut.fi

[(2)]Finnish Environment Institute
P.O.Box 140, FIN-00251 Helsinki
Finland

Abstract

The authors of this paper have developed earlier a simple model called CDA (Channel Difference Algorithm) to estimate the beginning of snow melt. A new algorithm using a an artificial neural network called Self Organizing Map (SOM) is constructed. The name of the new algorithm is SDA (SOM Detection Algorithm). The new algorithm is tested using SSM/I data and hydrological predictions are used as reference data, which covers years 1997 and 1998 and represents the boreal forest zone in Finland. In this paper preliminary results from the SDA are presented. The detection results are promising.

Keywords: Radiometer, SSM/I, snow melt detection, neural networks, SOM

1. INTRODUCTION

Remote sensing radiometer measurements are sensitive to liquid water content in snowpack. In consequence the space-borne observations from a radiometer system such as SSM/I (Special Sensor Microwave Imager) are very well suited for the spatial mapping of wet snow. Many applications such as run-off and river discharge forecasting are important applications in northern countries. These forecasting models require a reasonably accurate estimate when the melting of the snow cover takes place. Until recently only a sparse network of ground based weather stations could provide this information.

The advantage of a microwave instrument over an optical instrument in remote sensing is that the microwaves penetrate the cloud cover and are operational at night time. Microwave radiometers are also well suited for global monitoring due to their low spatial resolution.

Until now the microwave radiometer estimation algorithms have succesfully estimated the snow melt beginning in open areas like arctic tundra and glaciers. The CDA (Channel difference algorithm) results by from an earlier paper authors [3] suggested that the estimation is also possible in the boreal forest areas. In this paper preliminary results from the new SDA (SOM detection algorithm) are presented and their ability to estimate the snow melt beginning is discussed.

2. MATERIALS AND METHODS

The radiometer data consist of daily averaged brightness temperature grids from the SSM/I [1] instrument. Channels at 19, 22 and 37 GHz are used with either vertical or horizontal polarization. The 22 GHz channel uses only horizontal polarization. Reference data consists of snow liquid water content predictions and temperature predictions calculated by an operative hydrological run-off model by Finnish Environment Institute.

The basis of the SDA-algorithm is an artificial neural network called SOM [2] (Self Organized Map). The network is a non-supervised network which means that the network classifies the input data internally. The input data vector during the training was the brightness temperature vector. In [3] it was proposed that the detection is feasible only when snow water equivalent (SWE) values are high and the temperature remains in the region between -5° and 5° C. This was used as a rule for the selection of the training

vectors. After the training one must determine which of the internal classes responds to the input that has the property one wishes to detect. This was done by choosing only a set of vectors where the liquid water content was high.

3. RESULTS

Fig. 1 presents a preliminary test run using the SDA-algorithm. The test site is located in northern Finland in the river Kemijoki drainage area. The data are from the year 1997.

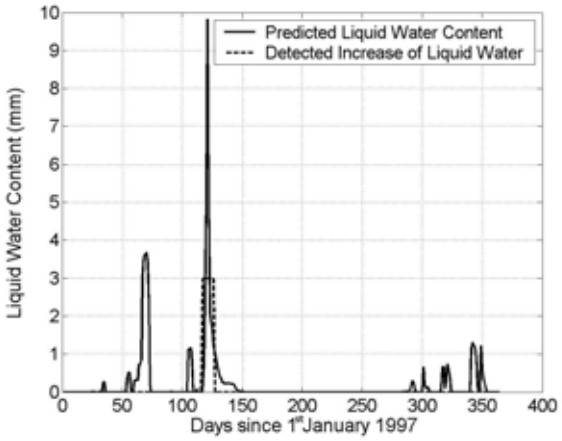

Fig. 1 Preliminary melt detection results from a test site in northern Finland. The output of the detection is binary, value 3 means that melt is detected , value 0 means that no melt has been detected.

The obtained result in fig. 1 are very promising. The SDA estimates the melting spike in spring very well but does not detect the minor spikes as wished. The CDA [3] detects the increased liquid content well but cannot distinguish the major spike from the others. However, other results indicate that the accuracy of the detection decreases if the value of the snow water equivalent (SWE) is low during the winter. This is reasonable, because the volume of the snow affects directly the amount of the liquid water.

4. DISCUSSION

The advantages of the new SDA algorithm over CDA are clear. The SDA can accurately estimate the beginning of the snow melt in most cases. Both the CDA and SDA are developed using data from the boreal forest areas in contrary to the other algorithms by other researchers which are applicable in arctic tundra and glacier conditions. Compared to the CDA the SDA can distinguish the major spring time melting from the other wet snow situations.

The results in this papers are indroductory and preliminary in nature and the subject still needs more research. At the moment the authors are working with a manuscript which will give detailed information about the SDA. The operational aspects of the SDA are further discussed.

5. REFERENCES

[1] DMSP F-11 & F-13 SSM/I Brightness Temperature Grids, Polar Regions, National Snow and Ice Data Center, University of Colorado, Boulder. http://www.nsidc.org

[2] Kohonen, T. (1982). Self-organized formation of topologically correct feature maps, *Biological Cybernetics*, vol. 43, pp. 59-69, 1982.

[3] Takala, M., Pulliainen, J., Huttunen, M. and Hallikainen, M. (2003), Estimation of the beginning of snow melt period using SSM/I data. *IEEE 2003 International Geoscience and Remote Sensing Symposium (IGARSS'03)*, Toulouse, France, 21-25 July, 2003.

Harmonic Balance Simulation of a Tunnel Diode Oscillator Circuit

K.-A. Hovitie

Unigraf Oy
Ruukintie 3, 02320 Espoo
Email: kalle.hovitie@unigraf.fi

Abstract
In this work the curveform of an Esaki Tunnel Diode (TD) oscillator circuit is simulated with the Harmonic Balance (HB) method incorporated in APLAC 7.20 circuit simulator. The I-V characteristic of the TD is modeled with a physics derived equation. Both the load line of the simulated oscillator circuit and the TD-model parameters are adjusted to fit the used components. Finally the obtained HB-simulation results are compared with the measured ones.

1. INTRODUCTION

Oscillators using a TD as an active element belong to the class of (strongly) nonlinear negative resistance oscillators. Traditionally, the Negative Differential Resistance (NDR) component is described with an algebraic equation of odd order symmetry suitable for further analytic study,

$$i = -Au + Bu^3 \tag{1}$$

where A and B are positive constants. The origin, now at the center of the NDR-region, can easily be shifted by a change of the coordinates. The analytic equation for the oscillator circuit (fig.1) is found from (1) and the condition,

$$i_C + i_L + i = 0 \tag{2}$$

where $i_C = Cdu/dt$, $i = -Au + Bu^3$ and $u = Ldi_L/dt + Ri_L$. Usually, in practice, R is small enough so it can be neglected. This simplifies considerably the resulting equation , which can be written,

$$d^2u/dt - \varepsilon(1-\alpha u^2)\omega_o du/dt + \omega_o{}^2 u = 0 \tag{3}$$

where $\varepsilon = A/C\omega_o$, $\alpha = 3B/A$ and $\omega_o{}^2 = 1/LC$. Equation (3) is the classical Van der Pol's nonlinear differential equation [1] except for the extra parameters α and ω_o.

The damping term, i.e. the coefficient of du/dt, is negative for small displacements and positive for large displacements u. The nature of the solution depends upon the value of ε. In this context we are interested only for solutions when ε >>1, i.e. relaxation oscillation type operation. Van der Pol type equations has traditionally been solved either graphically with e.g. the isocline method or analytically applying different type of analysis methods like perturbation method and variation of parameters. But for large values of ε (ε >>1) the use of these methods is not justified although the results are qualitatively correct. A different approach to find the curveform of the TD oscillator even for large values of ε is to use the method of Harmonic Balance incorporated in some circuit simulator programs. The simulation results obtained with HB show a very good similarity with the measured ones of the actual circuit.

2. TUNNEL DIODE MODEL

Instead of using the algebraic equation (1) for modeling of p-n type TD static I-V characteristic we apply physics-based equation for this task. Using the notations and ideas given in [2] the I-V characteristic is the result of three current components; band to band tunneling current Jt,

$$J_t = J_p(V/V_p)e^{(1-V/V_p)} \tag{4a}$$

excess current Jx,

$$J_x = J_v e^{(A2(V-Vv))} \tag{4b}$$

and thermal current Jth,

$$J_{th} = J_o(e^{(qV/kT)} - 1) \tag{4c}$$

where Jp and Jv are the peak and valley current densities, Vp and Vv the peak and valley voltages respectively, Jo the saturation current density and A2, the exponent prefactor, is a function of several physical parameters. Thus the complete static I-V characteristic is the sum of these three current components,

$$J = J_t + J_x + J_{th} \tag{5}$$

3. OSCILLATOR CIRCUIT

The oscillator circuit used in this simulation is presented in figure 1. The capacitor Ctd comprises of the TD-capacitance + parasitics. Inductance L is chosen after the frequency range and conductance G = 1/R represents the load. The lumped element values in the model circuit are; L=72 nH, Ctd = 20 pF, Vdc = 0,24 V and R = 16 ohm. Vdc is for bias purposes and current source Iosc, with certain amplitude and frequency, is necessary for successful steady state (SS) analysis.

4. SIMULATION RESULTS

In the simulation all TD parameters, Jo, Jv, Jp, Vv, Vp, kT/q and A2 can be independently and freely varied to adjust the I-V characteristic as well as possible to match the used TD, in this case a Russian made Ge TD 1I308K. This particular TD has Ip = 50+-5mA, Iv <= 10mA Vp <= 0,18V and Vv = 0,45-0,48V. The simulated I-V characteristic is presented in figure 2, where Ip = 49,94mA @ Vp = 150mV and Iv = 8,73mA @ Vv = 470 mV. These values correspond the actual tunnel diode reasonable well. The condition for relaxation oscillations is fulfilled because G=1/R =1/16 A/V = 0,0625A/V

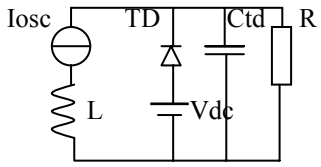

Figure 1. Circuit model used in the simulations.

≤ 0,184 A/V = 1/5,44 V/A = magnitude of the Negative Differential Conductance (NDC) at Vdc = 0,24 V. Decreasing R below 6 ohm makes the curveform more and more rounded and sinusoidal, figure 5. The duty cycle can be adjusted from near 10 % to almost 100 % by varying the bias voltage Vdc.

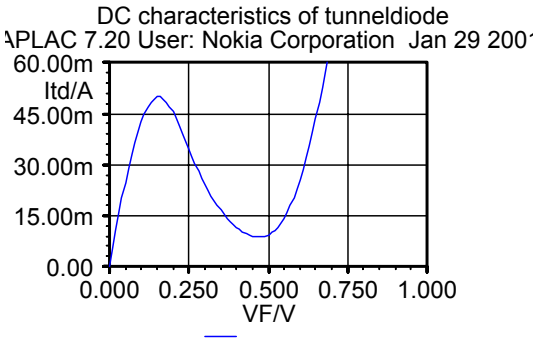

Figure 2. Simulated I-V curve of the p-n TD.

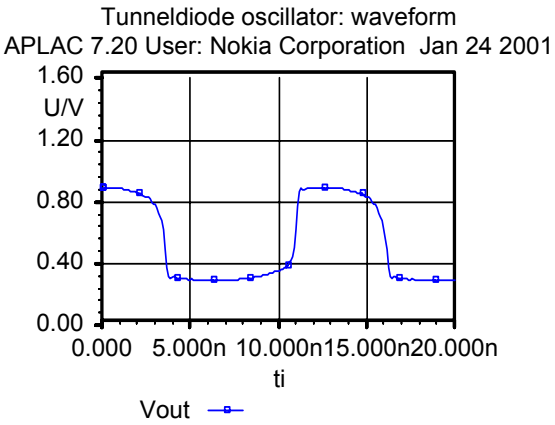

Figure 3. HB-simulation of TD-oscillator. R=16 , Vbias = 240 mV. >>1.

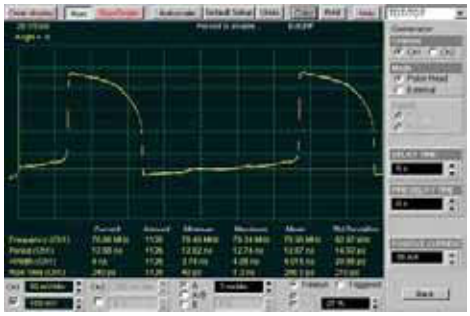

Figure 4. Measured curveforms of the TD- oscillator circuit.

A higher Vdc gives greater duty cycle, figure 6, which clarifies the situation when Vdc = 460 mV. To get a rough estimate of the size of ε implicit in the simulations we can take advantage of equation,

$$f \approx (2\pi / 1{,}62)\, f_0 / \varepsilon \qquad (\varepsilon >> 1) \tag{5}$$

where $f_o = 1/2\pi\sqrt{1/LC_{td}}$ = 132 MHz and f, the real frequency, is 80 MHz. Solving (5) gives $\varepsilon \geq 6$. The rise time in the simulated curve, fig. 3, is about 300ps-400ps. This is in accordance with the measured rise time, fig. 4, 280 ps. In practice rise times down to 40 ps can relatively easily be achieved with p-n TD-generators. Neither the simulated nor the measured curve reflects the attainable situation in this respect. But the simulated and measured amplitudes match each others anyway because the latter, 290 mV, must be multiplied with factor 2 due to the 6dB attenuation involved in the measurement coupling.

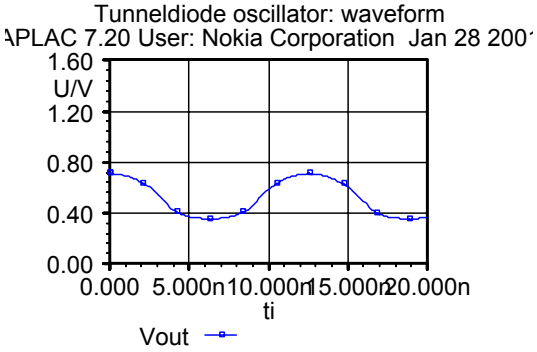

Figure 5. Effect of the load (G) on the curve-form. Vbias=240 mV, R = 3 Ω . ε <<1.

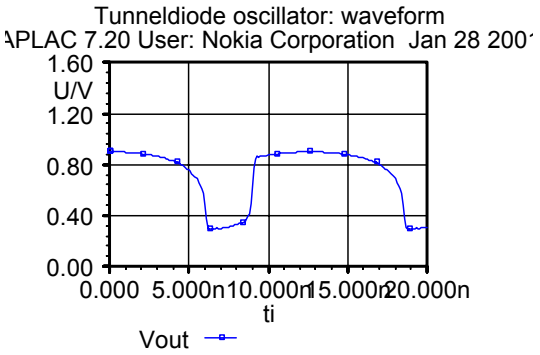

Figure 6. Effect of Vdc on the duty cycle. Vbias = 460 mV, R = 16 Ω .

5. CONCLUSIONS

Numerically generated curves of a p-n tunnel diode oscillators have been used along the experimental results to judge the feasibility of the Harmonic Balance method used in simulations. The number of harmonics used in all HB-simulations is 32.

During the simulations two type of convergent problems have arised. For the first, oscillations around a local minima or maxima, which may due to the fact that the algorithm (Newton-Raphson) used in HB is only locally convergent. For the second no convergence at all or false convergence to a wrong solution may and will occure if frequency f or current Iosc, the optimizing variables, are too far from the correct ones.

The cause for the latter phenomenon is unknown but it is supposed that if positive or negative conductance values of the I-V characteristic become close to the slope of the load line, unrealistically large current and/or voltages are generated during the iterations with the result that simulations fail.

One remedy to the aforementioned is to restrict the range of variables f and Iosc as close as possible to the final, expected values of the circuit.

Keeping the above restrictions in mind the HB-method is relative fast, simple and accurate enough for SS-analysis of strongly nonlinear (TD) circuits. Also fitting the TD-characteristics to a given component data using physics-based equations is straightforward and results in an excellent match.

References

[1] Nicholas Minorsky. Nonlinear oscillation. D. Van Nostrand Company, Inc, 1962.

[2] S.M. Sze. Physics of Semiconductor Devices. Second Edition, John Wiley and Sons, 1981.

Published by

Series title, number and report code of publication

VTT Symposium 235
VTT–SYMP–235

Author(s)
Lahdes, Manu (ed.)

Title

URSI/IEEE XXIX Convention on Radio Science

Espoo, Finland, November 1–2, 2004

Abstract

XXIX URSI Convention on Radio Science was held at Dipoli Congress Centre in Espoo, Finland, on November 1–2, 2004. The convention was organized by the Finnish National Committee of URSI, VTT Information Technology, and Finland IEEE Section and IEEE AP/ED/MTT Chapter. The convention provided a forum for discussion of advances in the broad field of radio science and radio communications. The program included contributed and invited presentations. This book contains the program of the conference and the written articles of the presentations.

Keywords
communication technology, remote sensing, antennas, electromagnetic theory, electromagnetic materials, circuits and components, wireless communications, sensors, defence and security

Activity unit
VTT Information Technology, Tietotie 3, P.O.Box 12021, FIN–02044 VTT, Finland

ISBN	Project number
951–38–6295–X (soft back ed.) 951–38–6296–8 (URL: http://www.vtt.fi/inf/pdf/; CD-rom)	

Date	Language	Pages	Price
October 2004	English	154 p. + CD-rom	D

Name of project	Commissioned by
	Nokia Research Centre, IEEE Finland Section

Series title and ISSN	Sold by
VTT Symposium 0357–9387 (soft back ed.) 1455–0873 (URL: http://www.vtt.fi/inf/pdf/; CD-rom)	VTT Information Service P.O.Box 2000, FIN–02044 VTT, Finland Phone internat. +358 9 456 4404 Fax +358 9 456 4374

XXIX URSI Convention on Radio Science was held at Dipoli Congress Centre in Espoo, Finland, on November 1–2, 2004. The convention was organized by the Finnish National Committee of URSI, VTT Information Technology, and Finland IEEE Section and IEEE AP/ED/MTT Chapter. The convention provided a forum for discussion of advances in the broad field of radio science and radio communications. The program included contributed and invited presentations. This book contains the program of the conference and the written articles of the presentations.

Tätä julkaisua myy

VTT TIETOPALVELU
PL 2000
02044 VTT
Puh. (09) 456 4404
Faksi (09) 456 4374

Denna publikation säljs av

VTT INFORMATIONSTJÄNST
PB 2000
02044 VTT
Tel. (09) 456 4404
Fax (09) 456 4374

This publication is available from

VTT INFORMATION SERVICE
P.O.Box 2000
FIN–02044 VTT, Finland
Phone internat. + 358 9 456 4404
Fax + 358 9 456 4374

ISBN 951–38–6295–X (soft back ed.)
ISSN 0357–9387 (soft back ed.)

ISBN 951–38–6296–8 (URL: http://www.vtt.fi/inf/pdf/; CD-rom)
ISSN 1455–0873 (URL: http://www.vtt.fi/inf/pdf/)